



**HAL**  
open science

# Mg/transition-metal nanomaterials for efficient hydrogen storage

Pavel Rizo

► **To cite this version:**

Pavel Rizo. Mg/transition-metal nanomaterials for efficient hydrogen storage. Material chemistry. Université Paris-Est, 2018. English. NNT : 2018PESC1050 . tel-02134889

**HAL Id: tel-02134889**

**<https://theses.hal.science/tel-02134889v1>**

Submitted on 20 May 2019

**HAL** is a multi-disciplinary open access archive for the deposit and dissemination of scientific research documents, whether they are published or not. The documents may come from teaching and research institutions in France or abroad, or from public or private research centers.

L'archive ouverte pluridisciplinaire **HAL**, est destinée au dépôt et à la diffusion de documents scientifiques de niveau recherche, publiés ou non, émanant des établissements d'enseignement et de recherche français ou étrangers, des laboratoires publics ou privés.



UNIVERSITÉ —  
— PARIS-EST

## **THÈSE**

pour obtenir le grade de Docteur de l'Université Paris-Est

Spécialité : Sciences des matériaux

présentée et soutenue publiquement par

**Pavel RIZO-ACOSTA**

le 19 décembre 2018

# **Mg/transition-metal nanomaterials for efficient hydrogen storage**

## **Nanomatériaux à base de magnésium et de métaux de transition pour un stockage efficace de l'hydrogène**

Devant le Jury :

**M<sup>r</sup> Jean-Louis BOBET**  
**M<sup>r</sup> Salvatore MIRAGLIA**  
**M<sup>r</sup> José -Francisco FERNÁNDEZ**  
**M<sup>r</sup> Michel LATROCHE**  
**M<sup>r</sup> Fermín CUEVAS**

Université de Bordeaux (Examineur)  
Institut Néel, Grenoble (Rapporteur)  
UAM, Madrid (Rapporteur)  
ICMPE, Thiais (Co-directeur de thèse)  
ICMPE, Thiais (Directeur de thèse)



## Acknowledgments

*First and foremost, I want to say, “thank you”, to my supervisors Fermin Cuevas and Michel Latroche, for giving me the opportunity to work on this project and carrying out my Ph.D. Thesis in the ICMPE (Institut de Chimie et des Matériaux Paris-Est) laboratory, and for their expert guidance, supporting, instructions, and encouragement*

*I would like to express my special thanks to Mr. Jean-Louis BOBET (University of Bordeaux), Mr. Salvatore MIRAGLIA (Institute Néel of Grenoble), and Mr. José Francisco FERNÁNDEZ (Universidad Autónoma de Madrid) to have kindly accepted to be the members of the jury for my Ph.D. dissertation.*

*Je souhaite également exprimer ma plus grande gratitude à tous les membres de CMTR (Chimie Métallurgie des Terres Rares) pour m'avoir accueilli aimablement dans leur groupe et pour leur soutien. Il ne serait pas juste de mentionner leurs noms, car j'ai reçu de l'aide et le soutien de tous, directement ou indirectement. Je suis également reconnaissant aux gens de l'ICMPE au cours de ces trois années, j'ai rencontré des gens formidables ici.*

*Gracias al departamento de física de materiales de la Universidad Autónoma de Madrid por su amigable acogida y por la amable ayuda que recibí durante una semana y después por correo electrónico.*

*I would like to thanks to all my Friends from all the nationalities that I have done during this time for their support and their friendship.*

*A really special thanks to my family, for always trusting and supporting me in every task of my life, allowing me to achieve great goals such as this dissertation.*

*I want to express my sincere thanks to all the people who made it possible for me to successfully complete my graduate study.*

*Finally, I would like to acknowledge the financial support from the Consejo Nacional de Ciencia y Tecnología, y la Secretaria de Energía.*



## Abstract

### Mg/transition-metal nanomaterials for efficient hydrogen storage

Magnesium metal is a prominent element for solid-state hydrogen storage due to its large abundance in earth's crust and its high weight and volumetric hydrogen uptakes. However, hydrogen sorption suffers from sluggish kinetics and the formed hydride is too stable for applications working under ambient conditions. The former issue can be solved by developing composites combining two hydrides,  $MgH_2$  and  $TiH_2$  at the nanoscale. These materials are synthesized by mechanical milling under reactive atmosphere. By this technique, the formation of nanocomposites and their hydrogenation can be obtained in a single-step. Moreover, these materials can be produced at large scale for application purposes.

The work focused on three topics: i) the optimization of the  $TiH_2$  content in the  $(1-y)MgH_2+yTiH_2$  system. This was accomplished by optimizing the titanium content ( $0.0125 \leq y \leq 0.3$  mole), while keeping good kinetics, hydrogen reversibility and cycle-life. The data show that  $y=0.025$  is the best compromise to fulfill the most practical properties; ii) the extension to other transition metals for the system  $0.95MgH_2+0.05TMH_x$  ( $TM$ : Sc, Y, Ti, Zr, V and Nb), evaluating the contribution of each additive to kinetics, hydrogen reversibility and cycle-life; iii) the conception of an automatic cycling device able to carry out hundreds of sorption cycles with the aim of measuring the cycle-life of metal hydrides.

The work was done using manifold experimental methods. For synthesis, reactive ball milling under hydrogen atmosphere was primarily used. The crystal structure and the chemical composition of nanomaterials was determined from X-ray diffraction (XRD) analysis. Particle size and morphology were obtained by Scanning Electron Microscopy / Energy Dispersive X-Ray Spectroscopy (SEM/EDS). Thermodynamic, kinetic and cycling properties toward hydrogen sorption were determined by the Sieverts method.

Keywords : magnesium hydride, hydrogen storage, nanocomposites, metal hydrides.



## Résumé

### Nanomatériaux à base de magnésium et de métaux de transition pour un stockage efficace de l'hydrogène

Le magnésium est un élément de choix pour le stockage de l'hydrogène à l'état solide en raison de sa grande abondance dans la croûte terrestre et de ses fortes capacités de sorption massique et volumétrique de l'hydrogène. Cependant, la réaction de sorption souffre d'une cinétique lente et l'hydrure formé est trop stable pour des applications fonctionnant sous conditions ambiantes. Le premier problème peut être résolu en développant des composites associant deux hydrures,  $MgH_2$  et  $TiH_2$ , à l'échelle nanométrique. Ces matériaux sont synthétisés par broyage mécanique sous atmosphère réactive. Cette technique permet la formation des nanocomposites et leur hydrogénation en une seule étape. De plus, ces matériaux peuvent être produits à grande échelle pour les besoins des applications.

Les travaux ont été menés en trois parties : i) l'optimisation de la teneur en  $TiH_2$  dans le système  $(1-y)MgH_2+yTiH_2$ . Ceci a été accompli en ajustant la teneur en titane ( $0,0125 \leq y \leq 0,3$  mole), tout en conservant une bonne cinétique, une réversibilité de l'hydrogène et une durée de vie utile. Les données montrent que la valeur  $y = 0,025$  offre le meilleur compromis pour développer les propriétés les plus adéquates; ii) l'extension à d'autres métaux de transition pour le système  $0,95MgH_2 + 0,05TMH_x$  ( $TM$ : Sc, Y, Ti, Zr, V et Nb), en évaluant la contribution de chaque additif sur la cinétique, sur la réversibilité de l'hydrogène et sur la durée de vie en cyclage; iii) la conception d'un dispositif de cyclage automatique capable de réaliser des centaines de sorption/désorption dans le but de mesurer la durée de vie des hydrures métalliques.

Le travail a été effectué à l'aide de nombreuses méthodes expérimentales. Pour la synthèse, le broyage réactif sous atmosphère d'hydrogène a été principalement utilisé. La structure cristalline et la composition chimique des nanomatériaux ont été obtenues à partir de l'analyse par diffraction des rayons X (DRX). La taille et la morphologie des particules ont été déterminées par microscopie électronique à balayage et spectroscopie de rayons X à dispersion d'énergie (SEM / EDS). Les propriétés thermodynamiques, cinétiques et cycliques de la sorption d'hydrogène ont été déterminées par la méthode de Sieverts.

Mots clés : hydrure de magnésium, stockage de l'hydrogène, nanocomposites, hydrures métalliques.



## Preface

Nowadays the world faces an environmental issue, which derives of global warming. The exhaust gases, containing mainly CO<sub>2</sub> generated from agriculture, industries, and combustion of fuels, have been critically increased. It is a reality that energy in the present should be sustainable and therefore it must change towards a cleaner and more efficient direction. The European Union has set a target by 2050 of renovating the energy sector into a low-carbon one, with the intention of reducing greenhouse gases [1].

An alternative for a sustainable energy world is the use of hydrogen. By the way, hydrogen is an energetic vector. It is not a primary source of energy. Nevertheless, hydrogen can be produced from renewable sources working for clean energy systems. It is known that hydrogen can generate more energy per mass compared with the conventional sources. The chemical energy per mass of hydrogen (142 MJ/Kg) is three times larger than that of other chemical fuels, e.g. liquid hydrocarbons (47.16 MJ/Kg) [2]. One critical issue for using hydrogen in practical applications is its efficient storage.

Different methods and phenomena are commonly used for hydrogen storage, such as, i) high-pressure gas cylinders (up to 80 MPa)[3], ii) liquid hydrogen in cryogenic tanks (at -253 °C)[4], iii) adsorbed hydrogen on solid materials with very large specific surface area (at T <-173 °C)[5], iv) absorbed hydrogen at interstitial sites in a host metallic structure (some metal hydrides working at ambient pressure and temperature), v) chemically bonded in covalent and ionic compounds (at ambient pressure)[6]. Figure I shows the summary of different technologies mentioned before. It can be seen that metal and complex hydrides (blue area) have volumetric capacities far superior to that of liquid hydrogen.

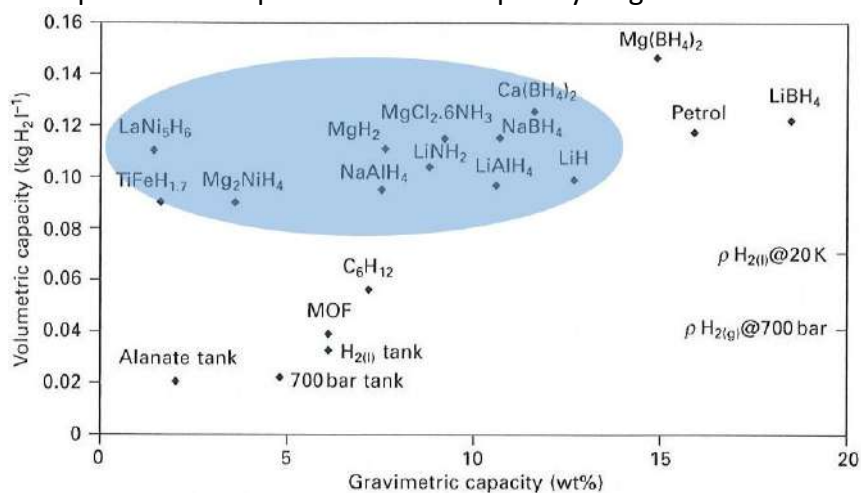
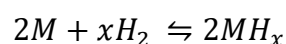


Figure I . Hydrogen storage capacities for different storage media[3]

The most common materials for reversible hydrogen storage is metal hydrides MH<sub>x</sub>. Many metals and alloys can reversibly react with H<sub>2</sub> to form hydrides through the general reaction:



The reverse reaction (*i.e.* metal *M* reformation) can be accomplished by either increasing the temperature or reducing the hydrogen pressure. The stored hydrogen can be released by

reducing the hydrogen pressure in a closed system to a level below the plateau pressure ( $P_p$ ) of the  $M/MH_x$  equilibria. A hydride stable under a certain temperature and hydrogen pressure will decompose when the temperature is increased to a level where  $P_p$  is higher than the system pressure. The temperature needed for a hydride to release hydrogen at 1 bar,  $T(P_p = 1 \text{ bar})$ , is a critical parameter as it indicates the minimum working temperature for a hydrogen system based on that material. Unfortunately, the known metals and alloys with  $T(P_p = 1 \text{ bar})$  lower than 80 °C are based on high weight transition metals and rare earths (e.g. LaNi<sub>5</sub> and FeTi) and therefore have low gravimetric hydrogen storage capacities (< 3 wt.%).

Because of the low gravimetric capacity for these interstitial metal hydrides (Fig I), the interest of materials with higher capacity has been increasing. This is the case of magnesium hydride which has a storage capacity of 7.6 wt. %. Even though MgH<sub>2</sub> has a high  $T(P_p = 1 \text{ bar}) = 280 \text{ °C}$  and sluggish kinetics, research on this hydride has deserved a great interest because of its high abundance and low cost. Many efforts have been done to improve the slow kinetics of MgH<sub>2</sub>.

One of the most common approaches to improve the hydrogen sorption kinetics of MgH<sub>2</sub> is by nanostructuring through mechanical milling methods. Bulk coarse magnesium hydride, with a particle size of ten of micrometers need at least some hours to fully decompose at 350 °C. By milling, the crystal and particle sizes of magnesium hydride reduce at the nanoscale and the surface roughness and area increase. This leads to a reduction in desorption time to some minutes at 350 °C [7].

By combining the last approach with the use of selected additives, further improvement of sorption kinetics can be attained. Hydrogen molecules can easily dissociate at the surface of some catalytic additives. Then, the nascent hydrogen atoms can permeate through them if they exhibit high diffusion coefficients for hydrogen and facilitate hydrogen transport toward the magnesium metal. It is important to find good candidates for magnesium hydride systems, which allows enhancing the kinetics of both absorption and desorption reactions.

Previous studies have demonstrated that Ti is an attractive additive to improve Mg hydrogenation properties [8,9]. It is a lightweight transition metal *TM* and at relatively low cost. Moreover, the *fcc* fluorite-type structure of titanium hydride is characterized by a fast diffusion coefficient. The catalytic properties of the TiH<sub>2</sub> phase on reversible hydrogenation of MgH<sub>2</sub>/Mg have already been previously reported by our group at ICMPE/CNRS [10]. In this previous work, the H-cycling properties of a 70MgH<sub>2</sub>-30TiH<sub>2</sub> nanocomposite were characterized and compared to those of Ti-free MgH<sub>2</sub> synthesized by the same mechanochemical method (reactive ball milling, RBM). The Ti-containing nanocomposite exhibited outstanding sorption kinetics with absorption/desorption reaction times below 100 seconds at 300 °C. Furthermore, such fast kinetics remain stable over more than 30 cycles. In contrast, pure MgH<sub>2</sub> obtained by the same RBM method exhibited sorption reaction times over 60 min and slowed down on H-sorption cycling.

This thesis targets three objectives. First one, to find out and understand whether there is an optimum TiH<sub>2</sub> amount in the MgH<sub>2</sub>-TiH<sub>2</sub> system. The second aim is to screen other transition metals additives forming hydrides; namely *TM* = Sc, Y, Zr, V, and Nb. Finally, this thesis aims to design and built-up an experimental system for studying the hydrogen sorption properties of MgH<sub>2</sub>-*TM*H<sub>x</sub> systems over hundreds of cycles.

Following these objectives, this Thesis is organized in five chapters. In the first chapter is presented an overview of hydrogen storage technologies as well as some previous studies of  $\text{MgH}_2$  with different additives. In the second chapter, the experimental methods carried out for producing and characterizing  $\text{MgH}_2$ - $\text{TMH}_x$  systems are discussed. The third chapter is devoted to the  $\text{MgH}_2$ - $\text{TiH}_2$  system and the optimization of  $\text{TiH}_2$  amount. It presents results on material synthesis, thermodynamic, kinetic and cycling analysis. The rate controlling mechanism for both absorption and desorption reactions is also examined. The fourth chapter is focused on the study of different  $\text{MgH}_2$ - $\text{TM}/\text{TMH}_x$  systems aiming to identify better additives and a better understanding of their role. In the fifth chapter, the design and implementation of an automatic cycling device used for analyzing the cycling life of metal hydrides are reported. Finally, a short summary of the most important outcomes of this Thesis and potential guidelines for future investigation is presented.

- [1] COM (2011) 112 - A Roadmap for moving to a competitive low carbon economy in 2050. Eur Environ Agency n.d. <https://www.eea.europa.eu/policy-documents/com-2011-112-a-roadmap> (accessed March 13, 2018).
- [2] Weast R, Astle M, Beyer W. CRC Handb. Chem. Phys. Ready-Ref. Book Chem. Phys. Data, Boca Raton, Fla: CRC Press; 1984.
- [3] Walker G, editor. Front matter. Solid-State Hydrog. Storage, Woodhead Publishing; 2008, p. i–iii. doi:10.1533/9781845694944.frontmatter.
- [4] Flynn TM. A liquification of gases. vol. 10. 7th ed. New York: 1992.
- [5] Panella B, Hirscher M. Physisorption in Porous Materials. Handb. Hydrog. Storage, Wiley-Blackwell; 2010, p. 39–62. doi:10.1002/9783527629800.ch2.
- [6] Züttel A. Hydrogen storage methods. Naturwissenschaften 2004;91:157–72. doi:10.1007/s00114-004-0516-x.
- [7] Huot J, Liang G, Boily S, Van Neste A, Schulz R. Structural study and hydrogen sorption kinetics of ball-milled magnesium hydride. J Alloys Compd 1999;293–295:495–500. doi:10.1016/S0925-8388(99)00474-0.
- [8] Shao H, Felderhoff M, Schüth F. Hydrogen storage properties of nanostructured  $\text{MgH}_2/\text{TiH}_2$  composite prepared by ball milling under high hydrogen pressure. Int J Hydrog Energy 2011;36:10828–33. doi:10.1016/j.ijhydene.2011.05.180.
- [9] Choi YJ, Lu J, Sohn HY, Fang ZZ. Hydrogen storage properties of the Mg–Ti–H system prepared by high-energy–high-pressure reactive milling. J Power Sources 2008;180:491–7. doi:10.1016/j.jpowsour.2008.02.038.
- [10] Cuevas F, Korablov D, Latroche M. Synthesis, structural and hydrogenation properties of Mg-rich  $\text{MgH}_2$ - $\text{TiH}_2$  nanocomposites prepared by reactive ball milling under hydrogen gas. Phys Chem Chem Phys 2011;14:1200–11. doi:10.1039/C1CP23030A.



## Table of contents

Abstract.....	I
Résumé.....	III
Preface.....	V

### Chapter 1. Introduction

Introduction.....	3
Hydrogen as an Energetic carrier.....	3
1.1 Hydrogen Generalities.....	4
1.2 Hydrogen storing methods.....	4
1.2.1 High pressure gas storage.....	4
1.2.2 Liquid hydrogen.....	5
1.2.3 Physisorption of hydrogen.....	5
1.2.4 Metal hydrides.....	6
1.2.5 Complex hydrides.....	6
1.2.6 Chemical reaction with water.....	7
1.3 Metal Hydrides overview.....	7
1.3.1 Thermodynamic of metal hydrides .....	7
1.3.1.1 Hysteresis.....	9
1.3.1.2 Reversible Capacity.....	10
1.3.2 Kinetic of metal hydrides.....	11
1.3.2.1. Activation.....	11
1.3.3 Cycling life.....	11
1.4 Magnesium.....	12
1.4.1 Thermodynamic properties of the Mg–H system.....	12
1.4.1.1 Modification of Mg-H thermodynamics.....	13
1.4.2 Kinetic properties of the Mg–H system.....	13
1.5 Ti-Mg system.....	14
1.6 Zr-Mg system.....	17
1.7 Sc-Mg system.....	20
1.8 Y-Mg system.....	23
1.9 V-Mg system.....	26
1.10 Nb-Mg system.....	29
References.....	32

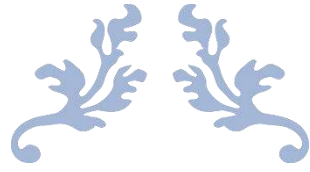
### Chapter 2. Synthesis and characterization techniques

2.1 Materials and samples handling.....	39
2.2 Synthesis of metal hydrides and alloys.....	39
2.2.1 Reactive Ball Milling (RBM).....	39
2.2.2 Electromagnetic processing of materials by induction melting.....	40
2.3 Structural, morphological and chemical characterization.....	41
2.3.1 X-Ray Diffraction (XRD).....	41
2.3.1.1 The Rietveld and Loppstra method.....	41
2.3.1.2 Structure refinements - the Rietveld method.....	42

2.3.2 Scanning Electron Microscopy (SEM).....	44
2.3.3 Inductively Coupled Plasma Optical Emission Spectrometry (ICP-OES).....	45
2.3.4 Electron Probe Micro-Analysis (EPMA).....	45
2.4 Characterization of hydrogenation properties.....	47
2.4.1 The Sieverts' method.....	47
2.4.1.1 Pressure-Composition-Isothermal (PCI), kinetic and cyclic measurements.....	47
2.4.1.2 Temperature-Programmed Desorption (TPD).....	47
2.4.1.3 Temperature-programmed absorption (TPA).....	48
References.....	48
 <b>Chapter 3. Effect of TiH<sub>2</sub> additive on the hydrogen storage properties of magnesium hydride</b>	
3.1 Synthesis and chemical characterization of MgH <sub>2</sub> -TiH <sub>2</sub> nanocomposites.....	53
3.2 Microstructural characterization.....	55
3.3 Hydrogen sorption properties.....	59
3.4 Effect of hydrogen cycling on the microstructure of MgH <sub>2</sub> -TiH <sub>2</sub> nanocomposites.....	66
3.5 Analysis of hydrogen sorption kinetics.....	72
3.6. Discussion.....	77
References.....	83
 <b>Chapter 4. Effect of hydride-forming <i>TM</i> additives (<i>TM</i> = Ti, Zr, Sc, Y, V, and Nb) on sorption properties of MgH<sub>2</sub>-based nanocomposites</b>	
4.1 MgH <sub>2</sub> with 4 transition metals Ti and Zr.....	89
4.1.1 Synthesis and structural characterization.....	89
4.1.2 Hydrogen sorption properties.....	94
4.1.3 Effect of hydrogen cycling on the microstructure of MgH <sub>2</sub> -TiH <sub>2</sub> and MgH <sub>2</sub> -ZrH <sub>2</sub> NCs.....	97
4.2 MgH <sub>2</sub> with group 3 transition metals Sc and Y.....	99
4.2.1 Synthesis and structural characterization.....	99
4.2.2. Hydrogen sorption properties.....	102
4.2.3 Effect of hydrogen cycling on the microstructure of MgH <sub>2</sub> -ScH <sub>2</sub> and MgH <sub>2</sub> -YH <sub>3</sub> NCs.....	105
4.3 MgH <sub>2</sub> with group 5 transition metals V and Nb.....	107
4.3.1 Synthesis and structural characterization.....	107
4.3.2 Hydrogen sorption properties.....	109
4.3.3 Effect of hydrogen cycling on the microstructure of MgH <sub>2</sub> -VH.....	112
4.4 Discussion.....	113
References.....	121
 <b>Chapter 5. Conception of an automatic cycling device to measure the cycle-life of metal hydrides</b>	
5.1 Principle of the Automatic cycling device.....	127
5.1.1 Thermochemical hydride compressors.....	127

5.1.1.1 Development of hydride compressors.....	127
5.1.1.2 Hydrogen cycling devices.....	128
5.1.2 Principle of <i>AC-device</i> .....	129
5.2 Setting of the operation conditions.....	130
5.3 Selection of the hydride forming alloy.....	131
5.3.1 Synthesis of $\text{LaNi}_{4.66}\text{Sn}_{0.34}$ .....	136
5.3.1.1 Characterization of $\text{LaNi}_{4.66}\text{Sn}_{0.34}$ .....	136
5.4 Blueprint of AC-device.....	138
5.5 Connections and software of control and measure.....	141
5.6 Measurements.....	142
5.7 Conclusion.....	145
References.....	146
<b>Conclusions and future works</b>	
Conclusions.....	151
Future works.....	153
Annex.....	155





---

# CHAPTER 1

---

Introduction





## Chapter 1. Introduction

The European Union has set a target by 2050 of renovating the energetic sector into low-carbon one, with the intention of reducing greenhouse gas emissions, upholding a strong growth for a global position as well as increasing energy security [1].

The European Commission presented in “EU 2020 Strategy” [2] puts forward three reinforcing priorities:

- Smart growth: developing an economy based on knowledge and innovation.
- Sustainable growth: promoting a more resource efficient, greener and more competitive economy.
- Inclusive growth: fostering a high-employment economy delivering social and territorial cohesion.

Both hydrogen and fuel cell technologies are key factors for each point presented above. An innovative economy would involve a new and broad hydrogen market. Meanwhile, a greener economy should be linked with a low-carbon emission society. Finally, with an innovative and green economy, a territorial cohesion work accomplishes the inclusive growth.

According to International Energy Agency (IEA) report scenario by 2050 [3], hydrogen will likely expand the market over the coming decades if three hydrogen costs fall: production, distribution, and end-use (hydrogen storage). Also, effective policies shall be put in place to increase energy efficiency and improve energy security.

### Hydrogen as an Energetic carrier

An energy carrier is a substance for delivering mechanical work or heat transfer. Examples of energy carriers include: solid, liquid or gaseous fuels (e.g., biomass, coal, oil, natural gas, hydrogen)

As an energy carrier, hydrogen provides a unique opportunity to contribute to all major European policy objectives in the transport and energy sectors:

- Hydrogen is a nontoxic gas with a high mass-energy density (between 120 and 142 MJ/kg) and is one of the most abundant elements in the biosphere, though scarce in pure form.
- It can be produced from water, biomass, biogas, natural gas or from any other fossil fuel,
- Used in conjunction with fuel cells, hydrogen provides an efficient decentralized solution for combined heat and power generation, both at an industrial and a domestic level;
- Hydrogen is an efficient way to store electricity, especially the renewable electricity generated by intermittent sources (solar, wind, hydroelectricity)
- Hydrogen can be used as an alternative fuel for clean mobility using fuel cell electric vehicles, including passenger cars, buses, light-duty and material handling vehicles
- Hydrogen offers a significant reduction of greenhouse gases emissions – hydrogen oxidation only produces water at the point of use – and a reduction in air pollution and noise.

Hydrogen can be produced using renewable sources working for clean energy systems. The main interests for hydrogen as an energy vector is due to the flexibility related to both its production and more important its use as a fuel. Since some years, the use of hydrogen as a fuel has been stronger, even with the severe competition with fossil fuels. To be more competitive, hydrogen as to deal with some drawbacks, such as effective and safe store reducing the cost processes.

Fuel cells can generate electricity from various feedstocks and can be used not only in connection with an electricity grid but also as a stand-alone power generator. Fuel cells have broader applications than any other power source currently available. The power produced can be used in many portable, stationary and transport applications and the heat, a by-product, can also be used for heating and cooling [4].

## 1.1 Hydrogen Generalities

Hydrogen (chemical symbol H) is the lightest element of the periodic table (atomic weight 1.00794 a.m.u), with atomic number  $Z=1$ . The origin of its name comes from the combination of the Greek words 'hydor' meaning 'water' and 'geinomai' meaning 'to bring forth', i.e. the element that brings forth water. Hydrogen is the ninth most abundant element on Earth's crust, as well as, the second most abundant element in Earth's sea after oxygen. Under normal conditions of temperature and pressure (at a temperature of 20°C and pressure of 1 atm), it is a colorless, odorless, tasteless, and flammable gas. Hydrogen was discovered by Henry Cavendish in England in 1766 and named by Lavoisier [5,6].

## 1.2 Hydrogen storing methods

The attractiveness of hydrogen is focused on its electron which is accompanied by only one proton (for charge neutrality), i.e. hydrogen has the highest ratio number of valence electrons to protons (and neutrons) of all the elements in the periodic table. [7].

Hydrogen storage technique basically implies the huge volume reduction of the hydrogen gas; 1 kg of hydrogen at ambient temperature and atmospheric pressure takes a volume of 11 m<sup>3</sup>. To increase the hydrogen density in a storage system, work must either be applied to compress hydrogen, or the temperature should be decreased below its critical temperature.

Different methods and phenomena are commonly used for hydrogen storage: i) high-pressure gas cylinders (up to 80 MPa), ii) liquid hydrogen in cryogenic tanks (at -253 °C), iii) adsorbed hydrogen on solid materials with a large specific surface area (typically at  $T < -173$  °C), iv) absorbed on interstitial sites in a host metal (usually near ambient pressure and temperature), v) chemically bonded in covalent and ionic compounds (at ambient pressure) [8].

### 1.2.1 High-pressure gas storage

The most common hydrogen storage solution currently uses pressurized cylinders to store hydrogen. Cylinders lighter than metal are used, typically working at 350 bar, though it exists other tanks working at 700 bar. The construction of cylinder consists in a liner (made from aluminum, steel or polymer) around which carbon fibers are wound and sealed in a polymer resin. The gravimetric storage capacity of the 700 bar tanks is 4.5 %, however, the volumetric

capacity is only 0.025 kgH<sub>2</sub>/l. The energy required for 700 bar compressions is 15 % of lower heating value (LHV) of the hydrogen stored in the vessel.

On-board, compressed gas storage is currently the best compromise. For applications where space is not an issue, for example, stationary storage at a fueling station, compressed gas is a relative cheap solution. For portable applications, compressed gas is too bulky, especially in cars where a significant amount of space must be sacrificed because of the cylindrical shape of the tank [9].

### 1.2.2 Liquid hydrogen

Cryogenic storage of hydrogen is another mature technology. It works at very low temperature (-253 °C) at ambient pressure. Due to the low liquid-vapor critical temperature of hydrogen (-240 °C), liquid hydrogen can only be stored in open systems because there is no liquid phase existing above the critical temperature. The volumetric density of liquid hydrogen is 70.8 kg·m<sup>3</sup>, comparable to that of solid hydrogen (70.6 kg·m<sup>3</sup>). The challenges of liquid hydrogen storage are the energy-efficient liquefaction process and the thermal insulation of the cryogenic storage vessel to reduce the boil-off of hydrogen. The simplest liquefaction cycle is the Joule–Thompson cycle (Linde cycle). The gas is first compressed and then cooled in a heat exchanger, before it passes through a throttle valve where it undergoes an isenthalpic Joule–Thomson expansion, producing some liquid. The cooled gas is separated from the liquid and returned to the compressor via the heat exchanger [10].

The boil-off rate of hydrogen from a liquid hydrogen storage vessel due to heat leaks is a function of the size, shape and thermal insulation of the vessel. Large-sized spherical containers are expensive because of their manufacturing difficulty. Since boil-off losses due to heat leaks are proportional to the surface to volume ratio, the evaporation rate diminishes drastically as the storage tank size increases. The relatively large amount of energy needed for the liquefaction and the continuous boil-off of hydrogen limit the possible applications for liquid hydrogen storage systems to utilizations where the cost of hydrogen is not an important issue and the hydrogen is consumed in a relatively short time, e.g. air and space applications.

### 1.2.3 Physisorption of hydrogen

Physical adsorption is the process where hydrogen is stored in molecular form (that means, without dissociating H<sub>2</sub> molecule) on the surface of a solid (carbon materials (3.5 wt. %H<sub>2</sub>), metal-organic frameworks (4 %H<sub>2</sub>), zeolites (1.5 wt. %H<sub>2</sub>)[9]. The molecular adsorption of H<sub>2</sub> is done through van der Waals forces, between the gas molecules and the atoms at the solid surface.

Adsorption is an exothermic process, where, heat is released during the adsorption of gas molecules on the surface. Owing to the low polarizability of H<sub>2</sub> molecule, the interaction is very weak (with an enthalpy of adsorption of between 40 and 10 KJ/mol) These weak interactions mean low temperature is needed to obtain significant amounts of adsorbed gas, so that the hydrogen molecules do not have too much thermal energy which easily overcomes the van der Waals interaction.

In general, porous materials show excellent cyclability as the material itself does not undergo any significant change through the adsorption/desorption process. A cryo-tank is needed as for liquid hydrogen and there are similar issues with boil-off. However, there is a significant energy saving in having to keep the store at  $-200\text{ }^{\circ}\text{C}$  as opposed to  $-253\text{ }^{\circ}\text{C}$ . These combined reasons make porous hydrogen storage materials less attractive for automobile on-board storage [11].

#### 1.2.4 Metal hydrides

Metal hydrides are promising materials for both stationary and mobile hydrogen storage applications. These materials are formed by one or several metals (alloys and intermetallic compounds) able to react with hydrogen gas. Hydrogen reacts with many transition metals and their alloys to form those hydrides. The electropositive transition metals (i.e. scandium, yttrium, the lanthanides, the actinides, and the members of the titanium and vanadium groups) form stable hydrides. The binary hydrides of the transition metals are predominantly metallic in character and are usually referred to as metal hydrides. The lattice structure is that of a typical metal with atoms of hydrogen in interstitial sites; for this reason, they are also called interstitial hydrides [12]. Ternary systems  $AB_xH_n$  have an important interest due to the variety of elements which allows tailoring of the hydride properties (see Table 1.1).

The *A* element is usually either an alkaline-earth metal (elements group two), a transition or a rare earth metal which tends to form a stable hydride. The *B* element is often a last transition metal and forms only unstable hydrides. Some well-defined ratios of *B* to *A* in the intermetallic compound  $x = 0.5, 1, 2, 3$  and  $5$  have been found to form hydrides with a hydrogen to metal ratio of up to 2. Metal hydrides are successfully effective for large amounts of hydrogen storing ( $\text{MgH}_2$  7.6 wt. %), in both a safe and compact way. Up to now, all the reversible hydrides working around ambient temperature and atmospheric pressure consist of transition metals. Therefore, the gravimetric hydrogen density is limited to 3 mass%. It remains a challenge to find out novel lightweight metal hydrides that react reversibly with hydrogen near normal thermodynamic conditions [13].

#### 1.2.5 Complex hydrides

Complex metal hydrides are normally formed by elements of the first and second groups of the periodic table. They are especially interesting because of their light weight and the number of hydrogen atoms per metal atom, which is in a few cases 2. The main difference between the complex hydrides and the metallic hydrides is that the former are ionically and/or covalently bounded. The hydrogen in the complex hydrides is often located in the corners of a tetrahedron with boron or aluminum in the center. The negative charge of the complex anion,  $[\text{BH}_4]^-$  and  $[\text{AlH}_4]^-$ , is compensated by a cation, e.g.  $\text{Li}^+$  or  $\text{Na}^+$ .

**Table 1.1** The most important hydride-forming intermetallic compounds families including both the prototype and the structure.

Intermetallic compound	Prototype	Hydrides	Structure
$AB_5$	LaNi <sub>5</sub>	LaNiH <sub>6</sub>	Haucke phases, hexagonal
$AB_2$	ZrV <sub>2</sub> , ZrMn <sub>2</sub> , TiMn <sub>2</sub>	ZrV <sub>2</sub> H <sub>5.5</sub>	Laves phase, hexagonal or cubic
$AB_3$	CeNi <sub>3</sub> , YFe <sub>3</sub>	CeNi <sub>3</sub> H <sub>4</sub>	Hexagonal, PuNi <sub>3</sub> -type
$A_2B_7$	Y <sub>2</sub> Ni <sub>7</sub> , Th <sub>2</sub> Fe <sub>7</sub>	Y <sub>2</sub> Ni <sub>7</sub> H <sub>3</sub>	Hexagonal, Ce <sub>2</sub> Ni <sub>7</sub> -type
$A_6B_{23}$	Y <sub>6</sub> Fe <sub>23</sub>	Ho <sub>6</sub> Fe <sub>23</sub> H <sub>12</sub>	Cubic, Th <sub>6</sub> Mn <sub>23</sub> -type
$AB$	TiFe, ZrNi	TiFeH <sub>2</sub>	Cubic, CsCl- or CrB-type
$A_2B$	Mg <sub>2</sub> Ni, Ti <sub>2</sub> Ni	Mg <sub>2</sub> NiH <sub>4</sub>	Cubic, Ti <sub>2</sub> Ni-type

### 1.2.6 Chemical reaction with water

Hydrogen can be generated from metals and chemical compounds reacting with water. The most common experiment – shown in many chemistry classes – where a piece of sodium floating on water produces hydrogen, demonstrates such a process. The sodium is transformed into sodium hydroxide in this reaction. The reaction is not directly reversible, but the sodium hydroxide could later be removed and reduced in a solar furnace back to metallic sodium. Two sodium atoms react with two water molecules and produce one hydrogen molecule. The hydrogen molecule produces again a water molecule in the combustion, which can be recycled to generate more hydrogen gas. However, the second water molecule necessary for the oxidation of the two sodium atoms must be added. Therefore, sodium has a gravimetric hydrogen density of 3 mass%. The same process carried out with lithium leads to a gravimetric hydrogen density of 6.3 mass%. The major challenge with this storage method is the reversibility and the control of the thermal reduction process in order to produce the metal in a solar furnace[14].

### 1.3 Metal Hydrides overview

As it was shown above metal hydrides can be successfully employed as efficient and safe storage media of hydrogen gas. In these materials, storage sometimes takes place under moderate pressure and temperature conditions. In that respect, metal hydrides have a significant advantage over classical hydrogen storage methods, which suffer from either extremely high pressures or very low temperatures. Storage in metal hydrides is, therefore, one of the key factors, facilitating *e.g.* hydrogen-driven fuel cells and Nickel-Metal Hydride batteries [15]. To unravel the hydrogen storage process in metals, a more detailed understanding is, however, essential.

#### 1.3.1 Thermodynamic of metal hydrides

Pressure-composition isotherms are widely used for determining the thermodynamic aspects of hydride formation between hydrogen gas and a solid, here a metal. The most important part of these isotherms is the plateau zone. The amount of hydrogen storage is directly associated with the plateau length. The host metal firstly dissolves hydrogen as a solid solution ( $\alpha$ -phase) up to a solubility limit  $\alpha$ . At that point, increasing the hydrogen pressure will induce the nucleation and growth of a novel hydride phase ( $\beta$ -phase) at the expense of the former  $\alpha$ -

phase (see Fig. 1.1). The two-phase region expands from  $\alpha$  to  $\beta$ , the plateau width decreases with temperature and eventually disappears above a critical point  $T_c$ . Beyond this temperature the transition from the  $\alpha$  to  $\beta$  phases is continuous. The plateau pressure,  $P_p$ , is related to the enthalpy ( $\Delta H$ ) and entropy ( $\Delta S$ ), as a function of temperature  $T$  by the van't Hoff equation:

$$\ln P_p = \frac{\Delta H}{RT} - \frac{\Delta S}{R} \quad \text{Eq. 1.1}$$

where,  $P_p$  is the plateau pressure, and  $R$  the gas constant. From this equation, the slope of the line in  $1/T$  is equal to the formation enthalpy divided by the gas constant (first term), therefore the intercept at the origin is equal to the formation entropy divided by the gas constant (Figure 1.1).

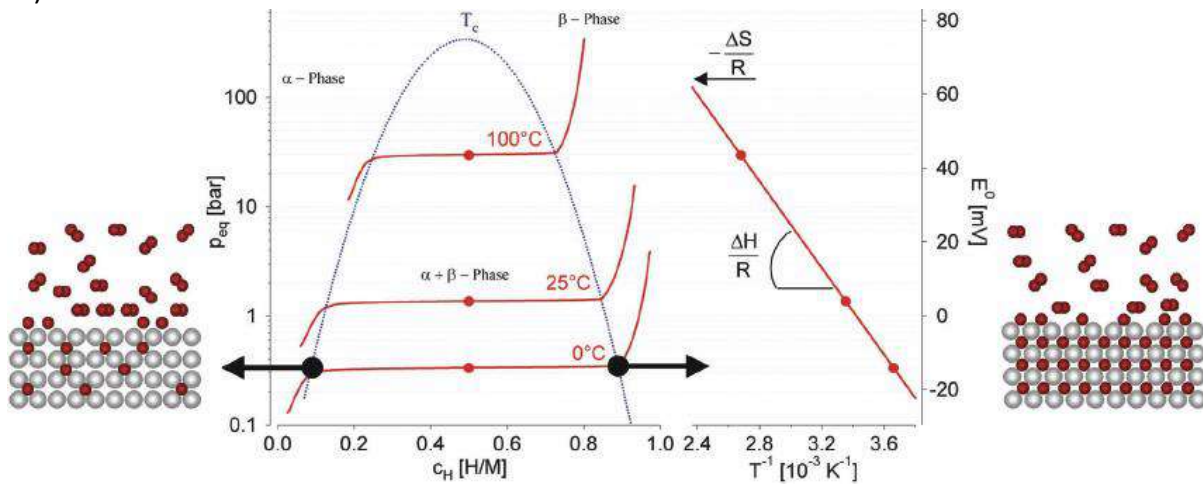


**Fig. 1.1** Left-hand side: Typical Pressure-Composition isotherms of a Metal-Hydrogen system. Right-hand side: related van't Hoff plot.

$\Delta H$  is a measure of the metal-hydrogen bond energy (and therefore of the hydride stability) meanwhile the entropy change corresponds mostly to the change from molecular hydrogen gas to dissolved solid hydrogen. The latter approximately corresponds to the standard entropy of hydrogen and therefore,  $\Delta S_f \approx -130 \text{ J}\cdot\text{K}^{-1}\text{mol}^{-1}\text{H}_2$  for most of the metal-hydrogen systems. As for the hydride stability, it is characterized by the enthalpy term. To reach a plateau pressure of 1 bar at 300 K,  $\Delta H_f$  should amount to  $-39.2 \text{ kJ mol}^{-1}\text{H}_2$ . The term entropy formation for metal hydrides leads to a significant heat evolution  $\Delta Q = T\cdot\Delta S_f$  (exothermic reaction) during hydrogen absorption.

The same heat must be provided to the metal hydride to desorb the hydrogen (endothermic reaction). In the case hydrogen desorbs below  $RT$ , this heat can be delivered by the environment. However, if the desorption occurs above  $RT$ , the necessary heat has to be delivered from an external source, such as the combustion of hydrogen[16].

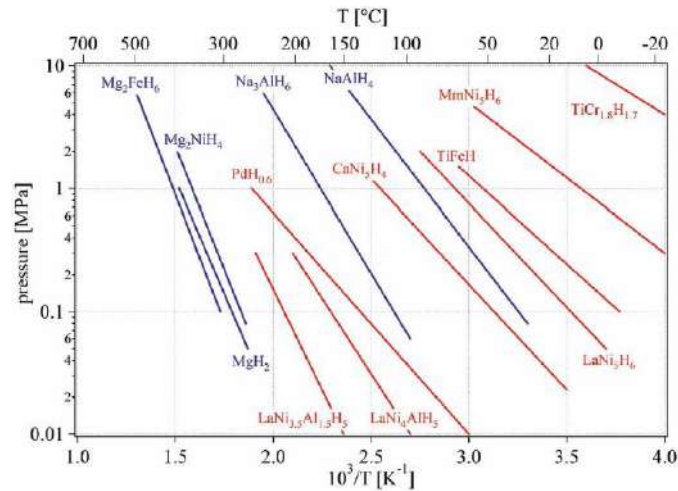


Figure 1.2 van't Hoff plots of some selected hydrides [16]

### 1.3.1.1 Hysteresis

Hysteresis is observed for nearly all metal hydrides: the pressure  $P_f$  needed for hydride formation is greater than the hydride decomposition pressure  $P_d$  (Figure 1.3). In practical applications, hysteresis represents a loss of efficiency. Another manifestation of this phenomenon is that the maximum hydrogen solubility in the solute phase  $a_{max}$  is higher for hydride formation  $a'$  than for hydride decomposition  $a''$ . A similar behavior takes place for the minimum solubility in hydride phase  $\beta_{min}$ .

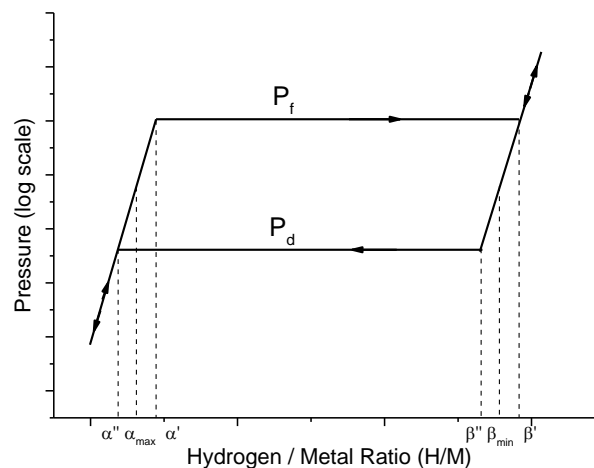


Fig. 1.3 Schematic representation of hysteresis for a metal hydride system

One explanation of hysteresis was proposed by Lacher [17] who suggested that it may result from the effect of particle size (i.e. either small nuclei of the dilute phase  $\alpha$  in the hydride phase or small nuclei of hydride phase) on the equilibrium hydrogen pressures.

Hysteresis is an important feature for practical applications as it impacts the service pressure of a storage tank. In fact, it represents a loss of efficiency because of the irreversible

deformation of hydrogen sorption. Hysteresis should be as small as possible, which can be achieved by element substitution in the alloy and heat treatment.

### 1.3.1.2 Reversible Capacity

Reversible capacity  $C_{rev}$  is defined as the difference between the hydrogen amount absorbed and the desorbed one, which can be considerably less than the maximum capacity  $(M/H)_{max}$  (Figure 1.4). A clear example is vanadium. At  $T= 25\text{ }^{\circ}\text{C}$  and  $P_{H_2} = 10^{-7}\text{MPa}$ , it forms a monohydride (VH), whereas a dihydride (VH<sub>2</sub>) is formed above 1 MPa at the same temperature. Under standard conditions ( $T= 0^{\circ}\text{C}$  and  $P= 0.1\text{ MPa}$ ), the dehydrogenation of the monohydride is thermodynamic impossible, so the reversible capacity of vanadium at these conditions is between VH<sub>≈1</sub> and VH<sub>≈2</sub>. Hydrogen capacity,  $C_H$ , can be reported in different units: i) as the atomic ratio (H/M) between hydrogen and metal atoms; ii) in weight percent (wt. %), denoting the weight of hydrogen stored over the weight of the hydride phase and iii) another way to hydrogen capacity is the volumetric capacity (g/l), expressed by the number of hydrogen atoms per unit volume [18].

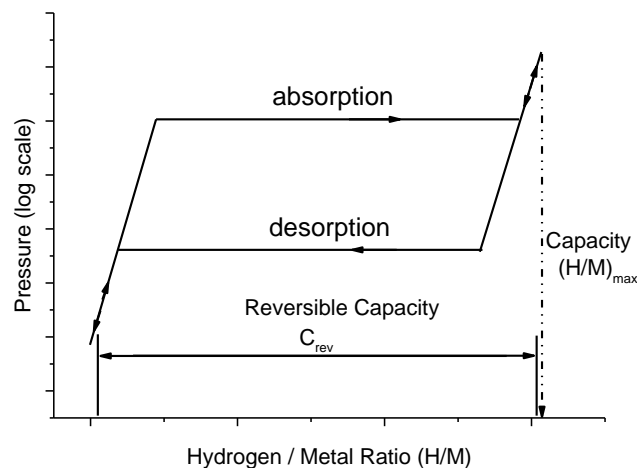


**Fig. 1.4** Schematic representation of reversible capacity for a metal hydride

### 1.3.2 Kinetic of metal hydrides

For hydrogen storage in solids, sorption kinetics are of paramount importance. The reaction between metal and hydrogen is a heterogeneous phase transformation. Formation of a metal hydride occurs through several steps taking place in series: H<sub>2</sub> transport to the surface, H<sub>2</sub> dissociation, H chemisorption, surface-bulk migration, H diffusion and finally, nucleation and growth of the hydride phase. Inverse reactions occur on hydride decomposition. For a reaction in series, the slowest step is defined as the rate-determining step.

Hydrogen reaction kinetics for a given material depends on many sensitive parameters such as activation conditions, structural defects, crystallinity and occurrence of catalytic phases. For example, nanostructured materials including secondary catalytic phases can be synthesized by mechanical ball milling. In this way, nanocomposites material with fast kinetics

are obtained thanks to short diffusion lengths for hydrogen diffusion and catalyzed surface reactions [19–26]. Both, the sample temperature and the hydrogen pressure should remain constant. No one of these conditions is easily fulfilled in the case of the metal-hydrogen reaction. Metal particles suffer from fragmentation during absorption and sintering during desorption. Sample temperature changes because of the heat of reaction and, except for constant pressure experiments, the absorption and desorption of hydrogen induce a related decrease or increase of pressure. In order to obtain reliable kinetics data, care should be taken to minimize all these effects [27].

The applicability of a hydrogen storage system is highly dependent on the kinetic parameters (rate and time of full desorption and absorption). The identification of the rate controlling mechanism gives the possibility to understand and thus to improve the kinetic properties. As hydride formation is a multi-step process, the reaction rate is dependent on many individual parameters. Since there are too many parameters describing the hydride formation, usually three different approximates are applied to model the measured  $\alpha(t)$  functions [28].

The surface-controlled process assumes that the slowest step of the reaction is the chemisorption. In the case of the contracting volume model, the main assumption is that the initial nucleation on the surface is fast compared to the overall growth kinetics and the nucleation zone is thin compared to the particle diameter. The third model, the Johnson-Mehl-Avrami (JMA), applies to cases where the nucleation and growth of the new phase begin randomly in the bulk and at the surface. From adjusting the measured  $\alpha$  functions to the model predicted ones, the rate control mechanisms can be determined [29].

#### **1.3.2.1. Activation**

The metal surface is covered with a native layer of oxide that acts as a hydrogen barrier. It must be overcome to start metal hydrogenation. The time that hydrogen lasts to cross the oxide film is called in literature incubation time [30]. Therefore, the first hydrogenation treatment is normally performed at high temperature and pressure to facilitate hydrogen penetration through the oxide layer. Upon hydrogenation, the metal lattice volume increases significantly while on dehydrogenation, the lattice reverts to its original size. This expansion-contraction breaks the metal particles, exposing fresh metal surface, reducing particle size and enhancing reaction kinetics.

#### **1.3.3 Cycling life**

For practical applications, it is of great importance to maintain the sorption properties (capacity, kinetics, reversibility, plateau pressure, etc.) of the hydrogen storage system during the whole life of the device. Typically, it can run from a few hundred to several thousand cycles. Cycling life depends on many parameters such as impurities in the hydrogen gas leading to poisoning, agglomeration of particles, and structural relaxation, etc. Nevertheless, magnesium and magnesium-based compounds could sustain a few thousand cycles without drastic changes in hydrogen sorption properties. A special way to improve cycling stability is by element substitution in the alloy [31].

## 1.4 Magnesium

Considering that metal hydrides could become outstanding energy carriers for both mobile and stationary applications, the hydrogen storage mass should be reduced. An important promising candidate is magnesium for this mobile mass sensitive application, Mg-based hydrides have drawn much attention due to Mg low density and cost [32]. MgH<sub>2</sub> is an outstanding hydrogen store due to its high hydrogen content both specific (7.6 wt. % H) and volumetric (0.109 kg<sub>H2</sub>/l).

Metallic magnesium has a hexagonal crystal structure (space group:  $P6_3/mmc$ ) crystal structure with lattice parameters  $a= 3.2094 \text{ \AA}$  and  $c=5.2108 \text{ \AA}$ . it forms a stoichiometric dihydride MgH<sub>2</sub> which can crystallize in two polymorphic forms. Stable at ambient conditions,  $\beta$ -MgH<sub>2</sub> has a tetragonal TiO<sub>2</sub> rutile-type (space group:  $P4_2/mnm$ ), with lattice parameters  $a =4.517 \text{ \AA}$  and  $c=3.0205 \text{ \AA}$ . This hydride, at mechanical pressure exceeding 390 MPa transforms into a metastable  $\gamma$ -MgH<sub>2</sub> modification that crystallizes with an orthorhombic PbO<sub>2</sub>-type structure [33].

Hydrogen accumulates within the magnesium body in the form of stoichiometric magnesium hydride MgH<sub>2</sub> [34]. The absorption process occurs in several steps, generally defined as follows [35]:

- 1) adsorption of hydrogen molecules on the surface of a magnesium particle, followed by their dissociation into hydrogen atoms  $H_2 \rightarrow 2H$ ;
- 2) diffusion of dissolved hydrogen atoms into the Mg - bulk ( $\alpha$ -phase);
- 3) formation of the magnesium hydride MgH<sub>2</sub> ( $\beta$ -phase) at the  $\alpha$ - $\beta$  interface  $Mg + 2H \rightarrow MgH_2$ .

The desorption process occurs in the reverse order, namely [36]:

- 1) magnesium hydride decomposes at the  $\alpha$ - $\beta$  interface and hydrogen atoms dissolve in the metallic bulk  $MgH_2 \rightarrow Mg + 2H$ ;
- 2) the dissolved hydrogen atoms move to the surface of the particle by diffusion transport;
- 3) the chain of several surface reactions (association of hydrogen atoms on the surface followed by the release of gaseous molecular hydrogen from the surface of powder particle  $2H \rightarrow H_2$ ) provides the surface degassing [37]

Fernandez and Sanchez [27] found that the rate-determining step for this desorption is hydrogen diffusion through the  $\beta$  phase. The diffusion of H in MgH<sub>2</sub> is very slow, and the diffusion coefficient of H in magnesium hydride at 300°C-100°C lies between  $10^{-18}$  and  $10^{-24} \text{ m}^2/\text{s}$  [38].

### 1.4.1 Thermodynamic properties of the Mg–H system

Magnesium hydride is a stable hydride, with a heat of formation of  $-74.5 \text{ kJmol}^{-1}H_2$  and an entropy variation of  $-135 \text{ Jmol}^{-1}H_2 \text{ K}^{-1}$ . Figure 1.5 shows the variation of the desorption plateau pressure as a function of temperature for magnesium hydride. For desorbing hydrogen under  $P_{H_2} = 1 \text{ bar}$  (0.1MPa) (lower blue line), magnesium hydride must be heated to at least 277°C. Similarly, magnesium could not absorb hydrogen below a pressure of 10 bar (upper blue line) if the temperature is higher than 370 °C. Therefore, magnesium hydride reversibly stores hydrogen only at  $\sim 300 \text{ }^\circ\text{C}$  for hydrogen pressures compatible with the feeding of fuel cells

(typically around 0.1 MPa). For room temperature applications, the challenge is to reduce the operation temperature of this system while keeping as high as possible its hydrogen storage capacity.

#### 1.4.1.1 Modification of Mg-H thermodynamics

One solution to destabilize magnesium hydride is to alloy magnesium with another element, usually a late transition metals, besides Sc, Y, and La. One classic example is  $Mg_2Ni$  where the heat formation of the ternary hydride is reduced to  $-64.5 \text{ kJ mol}^{-1} \text{ H}_2$ . Unfortunately, hydride destabilization is accompanied by a severe reduction of mass capacity to 3.6 wt.%. Alloying with other elements has been studied, as pointed out by Dornheim *et al.* [39].

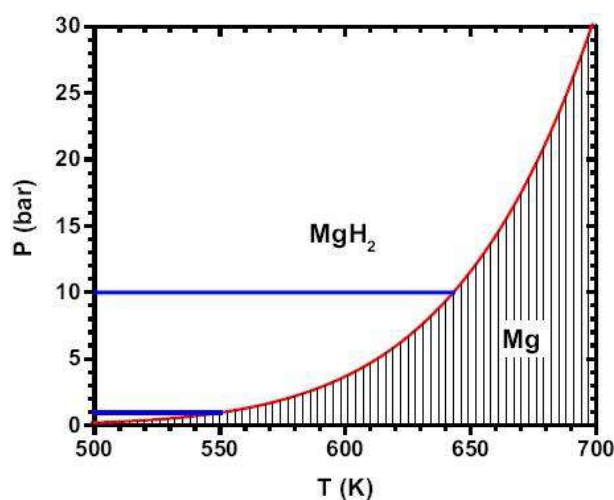
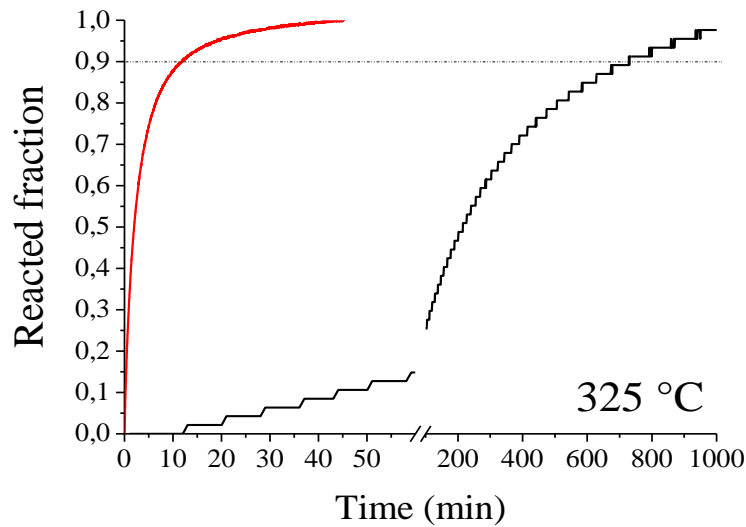


Fig. 1.5 Dependence of the desorption plateau pressure of  $MgH_2$  with temperature [39].

Several magnesium-based alloys have been investigated for reversible hydrogen storage, and the alloying elements include rare earth metals [40], transition metals [41], and other metals such as Al, Sn, In and Pd [20].

#### 1.4.2 Kinetic properties of the Mg–H system

During the last years, many efforts have been done to improve the sluggish kinetics of Mg/ $MgH_2$  sorption. A quite effective technique is to use mechanical ball milling, creating clean and enhanced surface areas and reducing the crystallite size to the nanoscale [42]. Figure 1.6 shows the drastic effect of milling on the hydrogen kinetics of magnesium. Ninety percent of the reaction occurs in 12 min for milled magnesium, meanwhile, for the non-milled one, the absorption time takes more than 10 h. This improvement is attributed to a high density of defects that act as nucleation sites for the hydride phase and by grain boundaries that facilitate hydrogen diffusion to the matrix. Increasing in the specific surface area by milling also plays a significant role. In different investigations, it has been shown that reduction in crystallite size is probably the dominant factor of the enhanced kinetics [21,43,44]. Another way to enhance reaction kinetics is the use of catalysts or additives that facilitate hydrogen transport toward and/or hydride nucleation in Mg matrix.



**Fig .1.6** Hydrogen absorption curves of both non-milled (micrometric) (black line) and ball-milled (red line) Mg at 325 °C

### 1.5 Ti-Mg system

Owing to its light weight among the transition metals and its relatively low cost, titanium is an attractive additive to improve Mg hydrogenation properties. The Ti-Mg phase diagram is reported by Murray [45]. Figure 1.7 shows the very little mutual solubility of Mg and Ti in any phase, and no intermetallic compounds occur. Thus, the equilibrium solid phases are the low-temperature cph (rt Ti) and (Mg) solid solutions and the bcc solid (ht Ti) based on the high-temperature form of pure Ti.

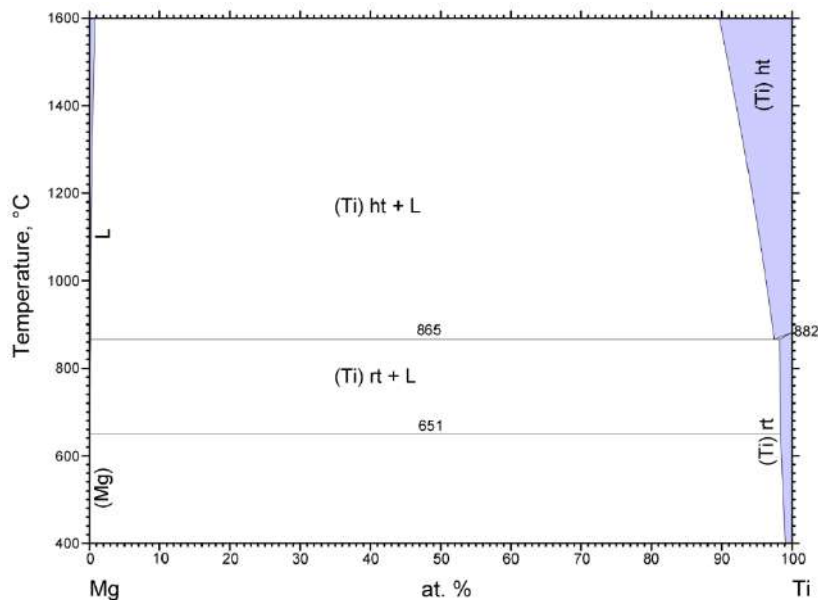


**Figure 1.7** Ti-Mg Phase Diagram by Murray [45]

The Ti-H phase diagram (Figure 1.8) is summarized by San Martin [46]. It depicts a gradual hydrogen absorption above 300 °C, titanium changes from a hexagonal (hcp) *ht* solid solution phase through a cubic (bcc) *ht* hydride with a composition close to TiH and to a cubic (fcc) *rt*

hydride phase with a maximum hydrogen content of  $\text{TiH}_2$ . Crystal structure data are presented in Table 1.2.

**Table 1.2.** Ti-H Crystal structure data

Phase label	Formula	Prototype	Pearson symbol	Density (mg/m <sup>3</sup> )	Volume (nm <sup>3</sup> )	Cell parameter (nm)	Cell parameters (°)	Ref.
<b>TiH<sub>2</sub> rt</b> (ε)	TiH <sub>1.97</sub>	ThH <sub>2</sub>	tI6 <i>I4/mmm</i>	3.76	0.044	a=0.3177 b=0.3177 c=0.4363	α=90 β=90 γ=90	[47]
<b>(Ti) ht</b> (βTi)	Ti	W	cI2 <i>Im-3m</i>	4.37	0.0364	a=0.33149 b=0.33149 c=0.33149	α=90 β=90 γ=90	[47]
<b>TiH<sub>2</sub> ht</b> (δ)	TiH <sub>2</sub>	CaF <sub>2</sub>	cF12 <i>Fm-3m</i>	3.56	0.0932	a=0.45345 b=0.45345 c=0.45345	α=90 β=90 γ=90	[47]
<b>(Ti) rt</b> (αTi)	TiH <sub>0.17</sub>	Mg	hP2 <i>P6<sub>3</sub>/mmc</i>	4.54	0.0352	a=0.29472 b=0.29472 c=0.46758	α=90 β=90 γ=120	[47]

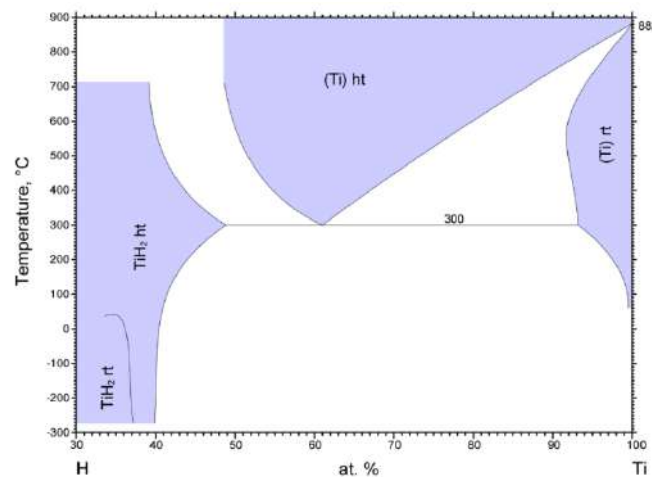


**Figure 1.8.** Ti-H diagram phase by San Martin [46]

The TiH diffusion data were collected by Zhou [48] in the temperature range of 25 °C to 400°C, and the pressure is referred as 1 atm (0.1 MPa). The values of hydrogen diffusion ( $D_H$ ) of  $\text{TiH}_{1.71}$  are lower than those of  $\text{TiH}_{1.66}$  and metallic ht-Ti.

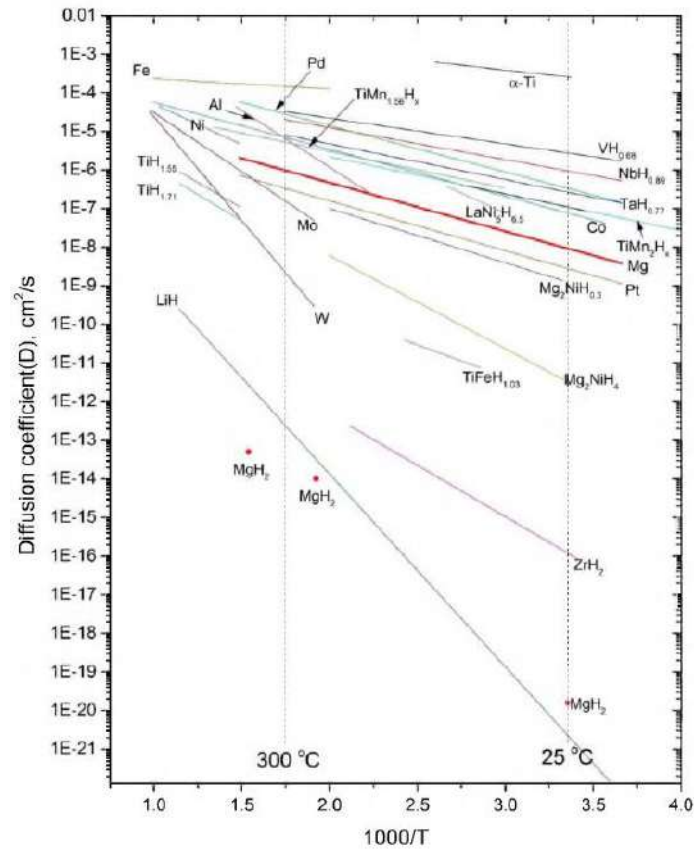


**Figure 1.9.** Intrinsic diffusion coefficients ( $D_H$ ) for some transition metals, intermetallic, and hydrides [48].

PCI curves of the Ti-H system (Fig. 1.10) were measured by Arita [49], at 300 °C and  $1.4 \times 10^{-3}$  MPa, the  $n_H/n_{Ti}$  ratio measured was 1.953, which means that the system shows to be pretty stable at this operation conditions.

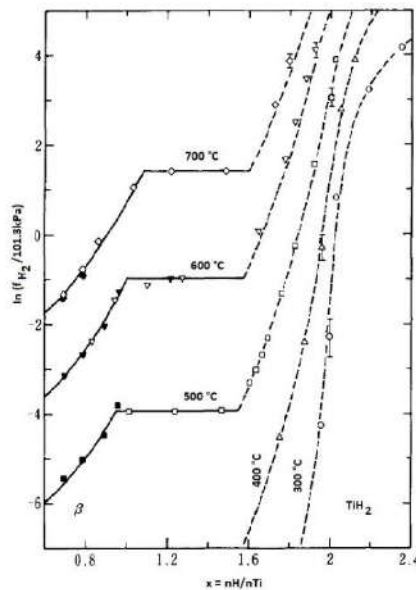


**Figure 1.10.** Fugacity vs  $x$  in  $TiH_2$  [49].  $f_{H_2}/P_{H_2} = 3.6 \times 10^{-4}$

Mg-Ti binary alloys were studied by Liang & Schulz[50], they synthesized Mg and Ti by reactive ball milling (RBM) getting a Mg-Ti nanocrystalline alloy with an extended solubility of Ti in Mg. It was observed that Mg(Ti) solid solution is stable at temperatures below 250 °C and phase decomposition becomes fast after 300 °C. Mg(Ti) solid solution transforms to MgH<sub>2</sub> and TiH<sub>2</sub> upon hydrogen sorption. Because of such decomposition, a destabilization of MgH<sub>2</sub> was not reached. Lu *et al.* [22] investigated hydrogen sorption properties of MgH<sub>2</sub>-0.1TiH<sub>2</sub> mixtures produced by RBM of MgH<sub>2</sub>-TiH<sub>2</sub> powder mixtures. They observed that this material has reversible hydrogen storage with a cycling hydrogen storage of 6 wt.%. There is no loss of cycling capacity over 80 sorption process. They conclude that both the nano-size and the addition of TiH<sub>2</sub> contributed to a significant improvement of the kinetics of both (de)hydrogenation of MgH<sub>2</sub>. Improvement of the kinetic in Mg-Ti system is also reported by Pasquini *et al.* [51], they synthesized Mg nanoparticles (size range 100 nm to 1 nm) by inert gas condensation and decorated by titanium clusters via *in situ* vacuum deposition. They observed a complete hydrogenation as well as good cycling stability working at 330 °C and  $P_{H_2} = 1.8$  MPa. Ponthieu *et al.* [52] investigated the Mg-Ti-H system focusing on MgH<sub>2</sub>-TiH<sub>2</sub> nanocomposites. The samples were prepared by RBM of Mg and Ti mixtures under hydrogen pressure to form (1-x)MgH<sub>2</sub>+xTiH<sub>2</sub> nanocomposites with molar ratio  $0 < x < 0.5$ . They consist of MgH<sub>2</sub> (with the coexistence of  $\beta$ - and  $\gamma$ -polymorphs) and  $\epsilon$ -TiH<sub>2</sub> homogeneously distributed with crystallite sizes below 15 nm. A study of the sorption properties showed that only the hydrogen stored in magnesium hydride is reversible under moderate conditions ( $T < 330$  °C,  $P_{H_2} < 1$  MPa). The presence of the titanium hydride leads to very fast hydrogen sorption kinetics for the magnesium system. TiH<sub>2</sub> inclusions are found homogeneously distributed within the MgH<sub>2</sub> matrix. They are claimed to enhance hydrogen mobility in Mg by preserving short diffusion paths for hydrogen. Indeed, TiH<sub>2</sub> inclusions are shown to limit grain growth of both Mg and MgH<sub>2</sub> phases. Furthermore, TiH<sub>2</sub> is expected to favor the diffusivity of hydrogen through the existence of a coherent coupling between TiH<sub>2</sub> and Mg/MgH<sub>2</sub> [53]. As an additive, Ti-hydride shows remarkable performance in improving the hydrogen storage properties of Mg, especially at moderate temperatures (300 °C). Cuevas *et al.* found that during milling of Mg-Ti powder mixtures under hydrogen atmosphere (8 MPa), TiH<sub>2</sub> phase was firstly formed ( $t < 15$  min) before MgH<sub>2</sub> [23] They also established that the milled 0.7Mg-0.3Ti composite can keep stable cyclic capacity of 3.7 wt.% H at 300 °C for at least 30 cycles .

## 1.6 Zr-Mg system

Figure 1.11 presents the calculated Mg-Zr phase diagram at the temperature range of 300 to 1000 °C by Hämäläinen [54]. Experimental phase diagram data exist in a very limited composition range from 0 to 1 at. % Zr. The melting point of magnesium was assessed at 650 °C and zirconium at 1855 °C. There was evidence of a peritectic reaction near the magnesium-rich end. The maximum solid solubility of 1.042 at.% Zr in (*rt*Mg) is reported. The solid solubilities of magnesium in both (*ht*Zr) and (*rt*Zr) are negligible.

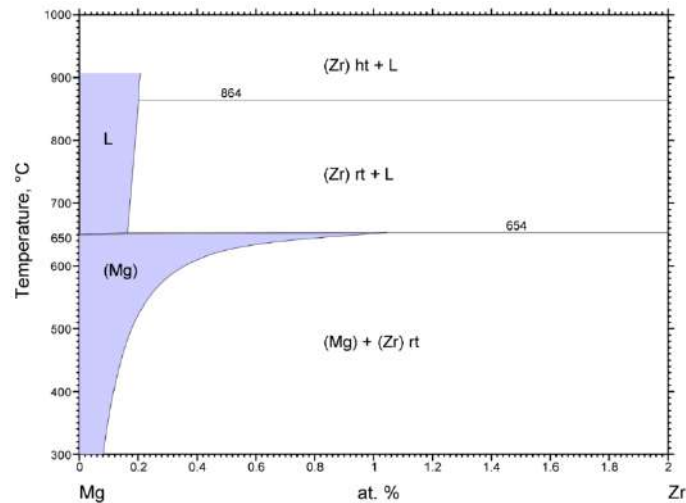
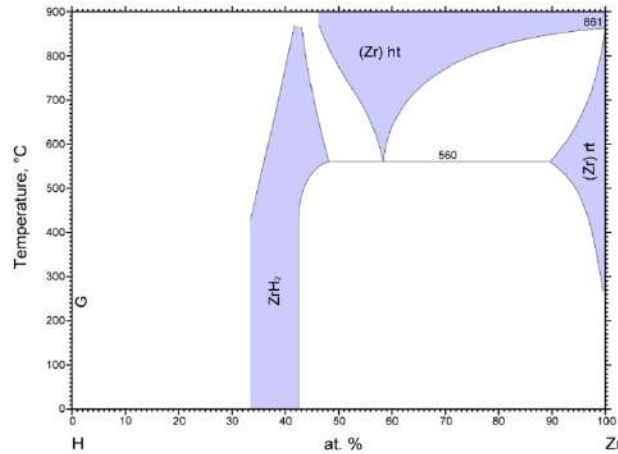


Figure 1.11. Magnesium-Zirconium Binary Phase Diagram [54].

The Zr-H equilibrium phase diagram depicted by Zuzec *et al.* [55] consists of the following phases: (i) the *cph* terminal (random interstitial) solid solution, ( $ZrH_2$ ), which shows a maximum H solubility of 5.9 at.% H ( $X=0.063$ ) at 560 °C. ( $X=H/Zr$  is the H/Zr atomic ratio.); (2) The *bcc* terminal (random interstitial) solid solution, (*htZr*), with a eutectoid decomposition at 560 °C and 37.5 at.% H ( $X=0.60$ ); (3) the *fcc* *rt* phase. Crystal structure data are presented in Table 1.3.

Table 1.3. Zr-H Crystal structure data

Phase label	Formula	Prototype	Pearson symbol	Density (mg/m <sup>3</sup> )	Volume (nm <sup>3</sup> )	Cell parameter (nm)	Cell parameters (°)	Ref.
(Zr) rt $\alpha, (\alpha Zr)$	Zr	Mg	hP2 <i>P6<sub>3</sub>/mmc</i>	6.49	0.04665	a=0.32333 b=0.32333 c=0.51523	$\alpha=90$ $\beta=90$ $\gamma=120$	[56]
ZrH <sub>2</sub> $\epsilon$	ZrH <sub>2</sub>	ThH <sub>2</sub>	tI6 <i>I4/mmm</i>	5.63	0.055	a=0.35179 b=0.35179 c=0.4447 T=294 K	$\alpha=90$ $\beta=90$ $\gamma=90$	[57]
(Zr) ht $\beta, (\beta Zr)$	Zr	W	cI2 <i>Im-3m</i>	6.42 6.42	0.0472 0.0472	a=0.3614 b=0.3614 c=0.3614 T=1173 K	$\alpha=90$ $\beta=90$ $\gamma=90$	[58]
ZrH <sub>1.6</sub> $\delta$	ZrH <sub>1.8</sub>	CaF <sub>2</sub>	cF12 <i>Fm-3m</i>	5.66	0.1091	a=0.4779 b=0.4779 c=0.4779 T=1173 K	$\alpha=90$ $\beta=90$ $\gamma=90$	[59]



**Figure 1.12.** The H-Zr System [55].

In figure 1.13, Russel *et al.* [60] measured the solubility of hydrogen in zirconium as a function of hydrogen pressure (range 1 to 760 mm. of Hg) and temperature (range 600 to 900 °C). Inside Figure, the temperature is represented by letters as follows: A, 600 °C; B, 700°C; C, 750°C; D, 800°C; E, 825°C; F, 850°C; G, 875°C; H, 900°C. As it can be noted for the operation conditions ZrH<sub>2</sub> system is more stable than TiH<sub>2</sub>.

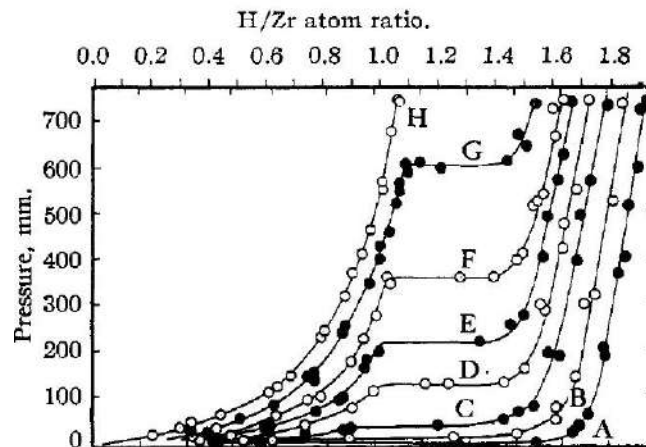


**Figure 1.13.** Isothermal pressure-volume curves [60].

Hydrogen diffusion in ZrH, ( $1.58 < x < 1.98$ ) was studied by Majer *et al.* [61] (Figure 1.14) in the temperature range 327 to 700 °C, measured by means of pulsed field-gradient nuclear magnetic resonance. It can be seen in this image that  $D_H$  is slower than for TiH<sub>2</sub>, as the number of hydrogen increases,  $D_H$  decreases.

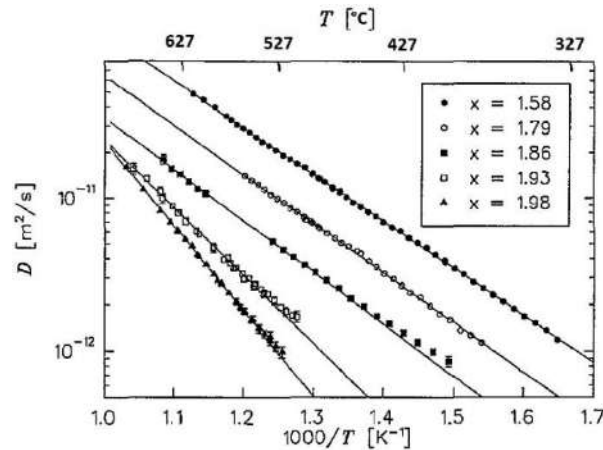
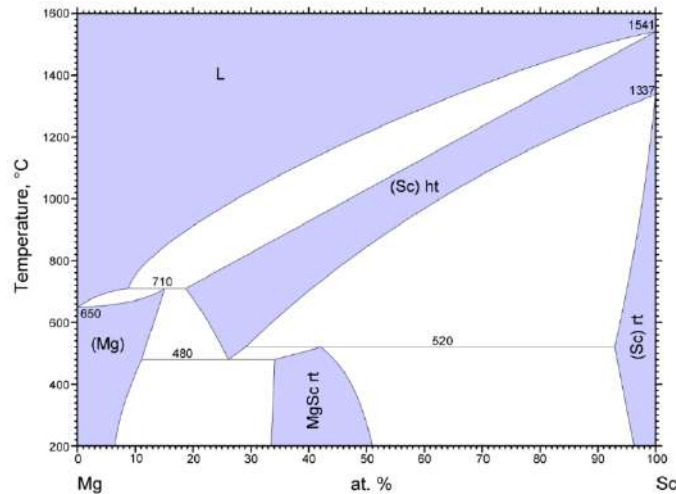


**Figure 1.14.** The temperature dependence of the hydrogen diffusivity in ZrH, measured by PFC NMR [61].

Korablov *et al.* [62] selected hydrides ( $\text{TiH}_2$ ,  $\text{ZrH}_2$ ), chlorides ( $\text{VCl}_3$ ,  $\text{ScCl}_3$ ) and oxides ( $\text{V}_2\text{O}_5$ ) as additives facilitating hydrogen release and uptake for magnesium hydride. Mechanism of hydrogen release and uptake in magnesium hydride system at 270 °C, 10 MPa, were assessed. The weakest kinetic effect for hydrogen desorption is provided by  $\text{TiH}_2$ , whereas the strongest influence was provided by  $\text{V}_2\text{O}_5$ . Zirconium hydride has an intermediate kinetic effect. A similar analysis of additive effect was also performed at a higher temperature of 320 °C, 10 MPa. The additive ability to accelerate the reaction kinetics follows the sequence:  $\text{ScCl}_3 < \text{TiH}_2 < \text{ZrH}_2 < \text{VCl}_3 < \text{V}_2\text{O}_5$ . Czujko *et al.*[63] studied the effects of metal additives on the hydrogen desorption properties of magnesium hydride ( $\beta\text{-MgH}_2$ ) formed after hydrogenation of the  $\text{Mg}+10\text{wt. \%X}$  ( $X = \text{V}, \text{Y}, \text{Zr}$ ) synthesized by RBM. TGA studies of the powders at 350 °C shows that the  $\text{Mg}+10\text{wt. \%Zr}$  composite desorbs hydrogen within the highest and simultaneously narrowest temperature range. Furthermore, the Mg composites with V and Y exhibit a two-step desorption. Finally, hydrogen desorption in a Sieverts-type apparatus at 300, 325 and 350 °C under atmospheric pressure of hydrogen shows that the  $\text{Mg}+10\text{wt. \% V}$  composite exhibits the most rapid kinetics.

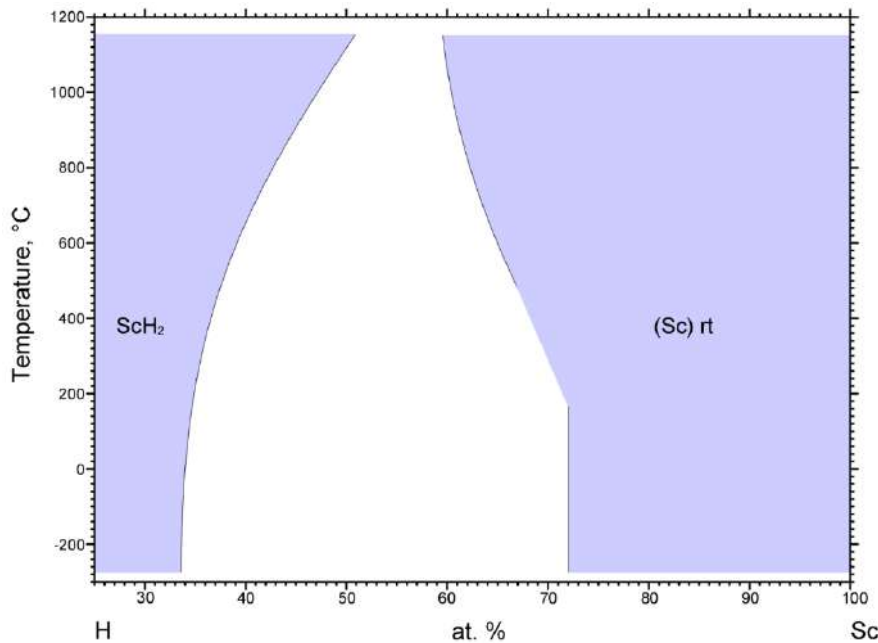
### 1.7 Sc-Mg system

Mg-Sc phase diagram (Figure 1.15) drawn by Nayed [64] consists of: the liquid, L; the terminal (Mg) solid solution; the high-temperature bcc (*htSc*) solid solution; the intermediate CsCl-type solid solution designated *MgSc rt* the terminal low-temperature cph (*rtSc*) solid solution; a peritectic reaction at 710 °C a peritectoid reaction at 520 °C and a eutectoid reaction at 480 °C.



**Figure 1.15.** Magnesium-Scandium Binary Phase Diagram [64].

The hydrogen-scandium system is plotted in Figure 1.16. For  $(ScH_2)$ , the upper limit for its existence would most probably be the  $\alpha \leftrightarrow \beta$  transformation temperature of pure Sc at 1337 °C. However, the range of presently available measurements of equilibrium isotherms for the absorption of H in Sc does not extend as far as this temperature, the highest measured isotherm being that for 1100 °C. The  $\alpha_{Sc}$  phase field being the widest of all; the  $(\alpha_{Sc})/[(\alpha_{Sc})+rt]$  boundary extends to  $x=0.40$  (28.6 at.% H) at 22 °C (i.e.,  $0.35 < x < 0.43$ ). At close to this concentration the  $(\alpha_{Sc})/[(\alpha_{Sc})+rt]$  boundary follows a path essentially independent of  $x$  down to very low temperatures. Crystal structure data are presented in Table 1.4.

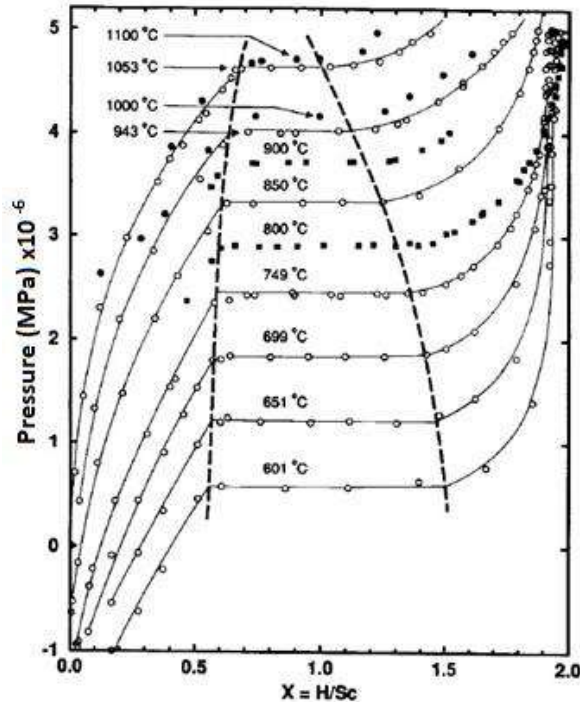


**Figure 1.16.** The H-Sc System [64].

**Table 1.4.** Sc-H Crystal structure data

Phase label	Formula	Prototype	Pearson symbol	Density (mg/m <sup>3</sup> )	Volume (nm <sup>3</sup> )	Cell parameter (nm)	Cell parameters (°)	Ref.
<b>ScH<sub>2</sub></b> $\delta$	ScH <sub>2</sub>	CaF <sub>2</sub>	cF12 <i>Fm-3m</i>	2.85	0.1095	a=0.47844	$\alpha=90$	[65]
						b=0.47844	$\beta=90$	
						c=0.47844	$\gamma=90$	
<b>(Sc) rt</b> $(\alpha\text{Sc})$	ScH <sub>0.39</sub>	Mg	hP2 <i>P6<sub>3</sub>/mmc</i>	2.95	0.05111	a=0.334	$\alpha=90$	[66]
						b=0.334	$\beta=90$	
						c=0.529	$\gamma=120$	

Manchester et Pitre [67] drew the PCI curves shown in Figure 1.17, which depicts the high stability of ScH<sub>2</sub>, the researchers also reported the inexistence of hysteresis for this hydride.

**Figure 1.17.** Pressure-composition isotherms for H-Sc system [67]

The Mg-Sc system was studied by Latroche *et al.* [68], these researchers found that thin films of Mg<sub>0.65</sub>Sc<sub>0.35</sub> exhibited a relatively high reversible hydrogen storage capacity (4.1 wt.%) with improved kinetics. They reported an equilibrium pressure at 300 °C (573 K) close to 0.06 MPa on the plateau. They also mentioned that faster kinetics are achievable due to the change from the rutile structure of MgH<sub>2</sub> to the fluorite structure of Mg<sub>0.65</sub>Sc<sub>0.35</sub> hydride, which enhances the mobility of hydrogen. Luo *et al.* [69] studied the thermodynamic of Mg<sub>0.65</sub>Sc<sub>0.35</sub> alloy at different temperatures 320, 340 and 350 °C founding a plateau pressure in desorption at 0.213, 0.355 and 0.452 MPa respectively. From PCI curves, the reversible hydrogen storage capacity was measured (4.2 ± 0.1 wt.%), close to the theoretical value of

4.4 wt.%. They observed two plateaus, the main one appeared over the capacity range 0.6–3.5 wt.%, while the lower plateau was present when capacity was below 0.6 wt.%. A total of 55 cycles were carried out and the hydrogen storage capacity remained unchanged after the initial 2 cycles, indicating the good cycling stability of the 0.65MgH<sub>2</sub>/0.35ScH<sub>2</sub> system. These same researchers studied the hydrogen storage properties of ball-milled  $x\text{MgH}_2/(1-x)\text{ScH}_2$  ( $x=0.65-1$ ) samples [70]. They found that a small addition of ScH<sub>2</sub> (6 mol.%) effectively improved the kinetics of MgH<sub>2</sub> by reducing the activation energy value from  $159 \pm 1 \text{ kJ mol}^{-1}$  of the as-received MgH<sub>2</sub> to  $99 \pm 6 \text{ kJ mol}^{-1}$ . It was also observed that the samples in which the ScH<sub>2</sub> content ranged from 6 to 12 mol.% and underwent ball milling for a longer duration (20 and 40 h) showed the most improved dehydrogenation kinetics of MgH<sub>2</sub> over cycling. They suggested that the nano-sized ScH<sub>2</sub> could help the dissociation of H<sub>2</sub> as well as functioning as nucleation sites for the growth of Mg during dehydrogenation.

### 1.8 Y-Mg system

The Mg-Y phase diagram (Figure 1.18) was drawn by [71], in which the phase boundaries of (*ht*Y) and (*rt*Y) were estimated due to lack of experimental data, by optimization of thermodynamic and phase diagram data.

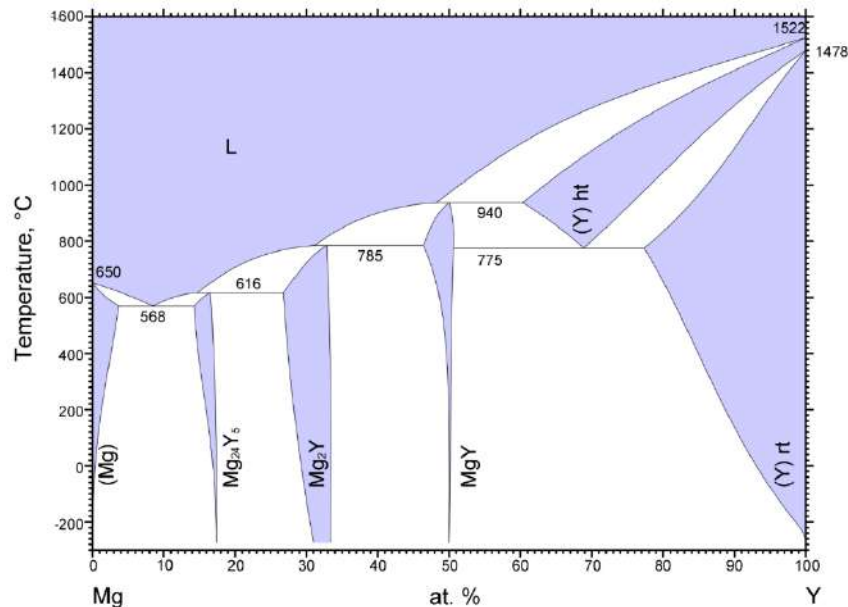
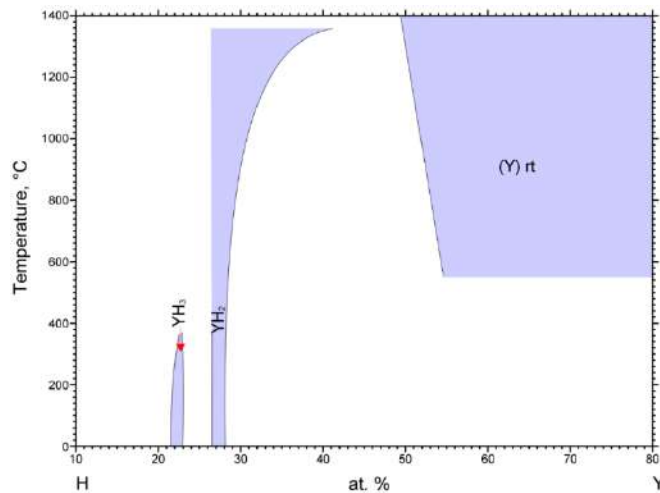


Figure 1.18. Magnesium-Yttrium Binary Phase Diagram [71].

Hydrogen yttrium phase diagram, Figure 1.19. Khatamian [72] refers to a "solid solution phase," *i.e.*, the phase with the pure metal as one boundary and the mixed phase region as the other boundary. For the Y-H system at room temperature this boundary is located at 20 at.% H; in the present evaluation, this phase has been designated  $\alpha$ . Greek letters are preferable to lose terminology (such as "the hydride phase") if a general agreement on the choice of Greek letters can be established; *e.g.*, the phase centered around the YH<sub>2</sub> composition, which has been variously labeled  $\beta$  phase,  $\gamma$  phase, or hydride phase. The present evaluators suggest that this phase is designated  $\delta$ , to conform to the phase nomenclature used for the Ti-H system. The  $\alpha$  phase of the Y-H system retains the *cph* structure, the  $\delta$  phase has *fcc* structure, and the phase above the approximate composition YH<sub>3</sub> has a hexagonal structure. Crystal structure data are presented in Table 1.5.

**Table 1.5.** Y-H Crystal structure data

Phase label	Formula	Prototype	Pearson symbol	Density (mg/m <sup>3</sup> )	Volume (nm <sup>3</sup> )	Cell parameter (nm)	Cell parameters (°)	Ref.
(Y) rt	Y	Mg	hP2	4.47	0.066	a=0.36474	α=90	[73]
			<i>P6<sub>3</sub>/mmc</i>	4.47	0.066	b=0.36474 c=0.57306	β=90 γ=120	
(αY)	Y	Mg	hP2 <i>P6<sub>3</sub>/mmc</i>			a=0.36474 b=0.36474 c=0.57306	α=90 β=90 γ=120	
YH <sub>3</sub>	YH <sub>3</sub>	HoH <sub>3</sub>	hP24 <i>P-3c1</i>	3.96	0.2313	a=0.63587 b=0.63587 c=0.66068	α=90 β=90 γ=120	[74]
YH <sub>3</sub>								
YH <sub>2</sub>	YH <sub>2</sub>	CaF <sub>2</sub>	cF12 <i>Fm-3m</i>	4.28	0.1412	a=0.5207 b=0.5207 c=0.5207	α=90 β=90 γ=90	[75]
δYH <sub>2</sub>								

**Figure 1.19.** Hydrogen-Yttrium Binary Phase Diagram [72].

Yannopoulos *et al.* [76] published the isothermal equilibrium data for the yttrium-hydrogen system which are represented in Figure 1.20 for the temperature range from 601.4 to 949.4 °C. From the shape of the isotherms, it is inferred for the condensed state the existence of two single-phase regions separated by a two-phase field. In the dilute region of the Y-H system up to 0.1 g.-atom of hydrogen/g.-atom of yttrium. Reversibility of the measurements for the composition range demonstrates that it fits with the isothermal desorption points in the righthand portion and the desorption points (●) in the left of the figure.

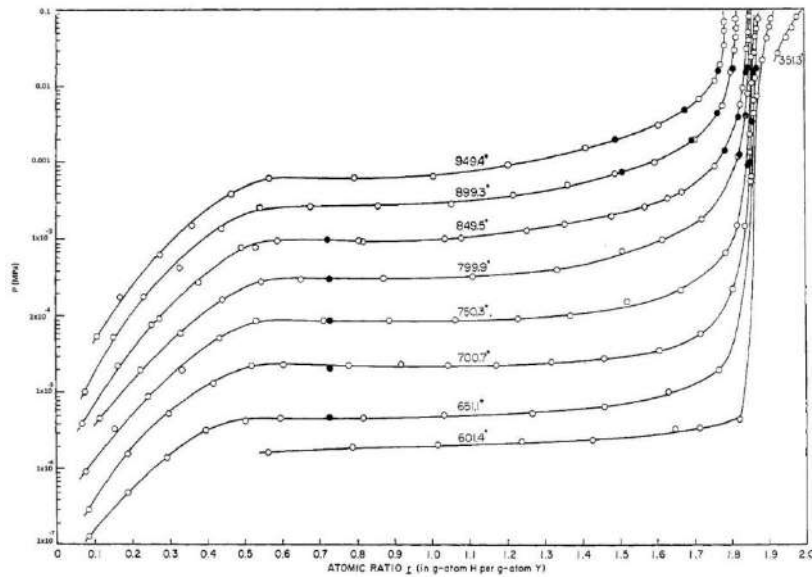


**Figure 1.20.** Experimental isotherms for the system yttrium-hydrogen: o, absorption points; ●, desorption points [76]

The data, shown in Figure 1.21, show a definite hysteresis loop in the absorption vs desorption measurements. Phase boundary estimates are indicated by the dashed lines on the figure. The estimated uncertainty in visually defining these boundaries are  $\pm 0.05$  (H/Y) and  $\pm 0.10$  (H/Y) units, respectively. In the latter case, it is assumed that a two-phase field exists even though thermodynamic irreversibility is demonstrated.

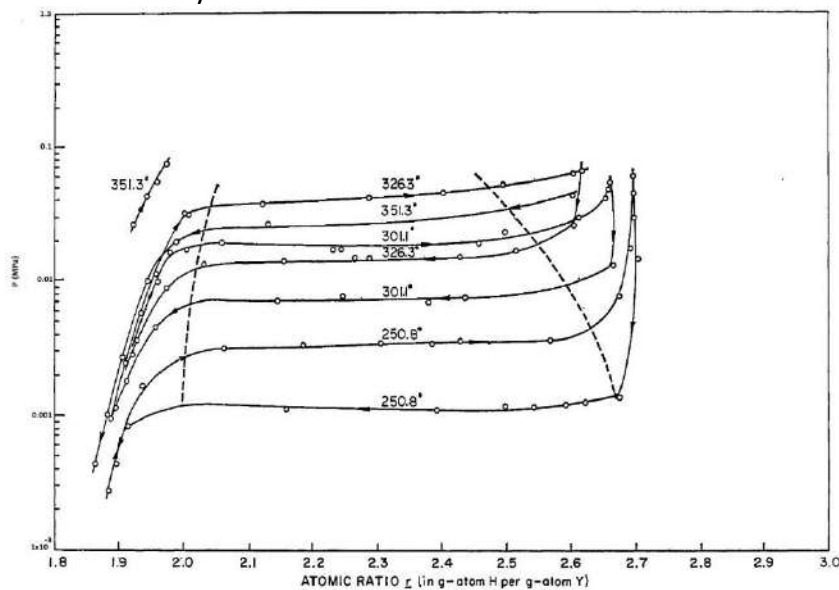


**Figure 1.21.** Experimental isothermal curves for the system yttrium-hydrogen. Absorption and desorption reproducible, irreversible curves are designated by the right and left-hand arrows, respectively [76].

$YH_x$  is commonly used as a switchable mirror, real-time transitions from metallic ( $YH_2$ ) to semiconducting ( $YH_3$ ) behavior occur in  $YH_x$  films during continuous absorption of hydrogen, accompanied by pronounced changes in their optical properties [77].

Several thermodynamically unstable transition metal aluminum hydrides with a high hydrogen content like  $Y(\text{AlH}_4)_3$  have been studied because of the relatively high stability of  $Y(\text{AlH}_4)_3$ .  $Y(\text{AlH}_4)_3$  was reported to be quite stable and starts to decompose at 50 °C.  $Y(\text{AlH}_4)_3$  has a high theoretical hydrogen content of 6.6 wt%, while until now no further information is known about its hydrogen storage properties and reversibility [78].

### 1.9 V-Mg system

The Mg-V is presented by Smith [79] in Figure 1.22, who explains that there are no intermediate phases in the system, however, extensive immiscibility was observed in both liquid and solid state.

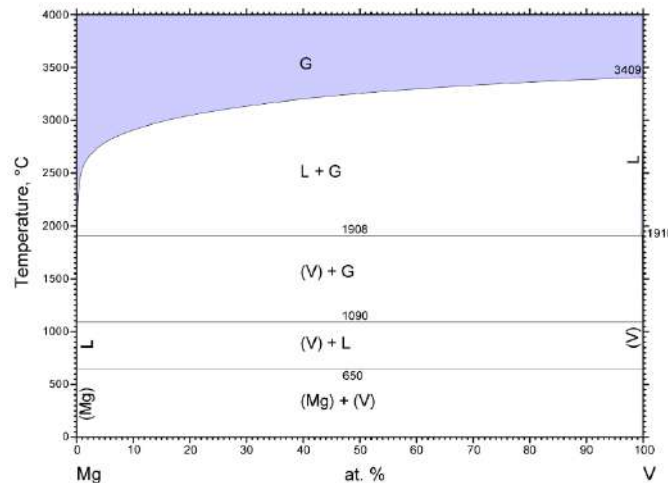


**Figure 1.22.** Magnesium-Vanadium Binary Phase Diagram [79].

Vanadium, which crystallizes in the *bcc* cubic structure at 0.1 MPa, absorbs interstitial H up to an atomic H/V ratio of about two. For H/V ratios up to unity, the phase diagram is shown in Figure 1.23. Above 200°C (473 K), the  $\alpha$ -phase with *bcc* structure of vanadium is observed. Only a lattice expansion accompanies the increase of the hydrogen concentration in this cubic phase (solid-solution behavior). At lower temperatures, the  $\beta$ -hydride phase, in which the V atoms form a body-centered tetragonal lattice, appears. Depending on whether the cubic phase has a lower or higher hydrogen concentration than the tetragonal  $\beta$ -phase, it is usually denoted by  $\alpha$  or  $\alpha'$ -phase, respectively. At room temperature, pure  $\beta$ -phase exists for H/V ratios between 0.45 and 0.9. The lower concentration is in equilibrium with the  $\alpha$ -phase containing H/V = 0.05. However, for H/V ratios exceeding 0.9, a new phase, the  $\gamma$ -phase, appears in coexistence with the  $\beta$ -phase. The  $\gamma$ -phase has a *fcc* arrangement of vanadium atoms and contains a hydrogen concentration of H/V = 2. Crystal structure data are presented in Table 1.6.

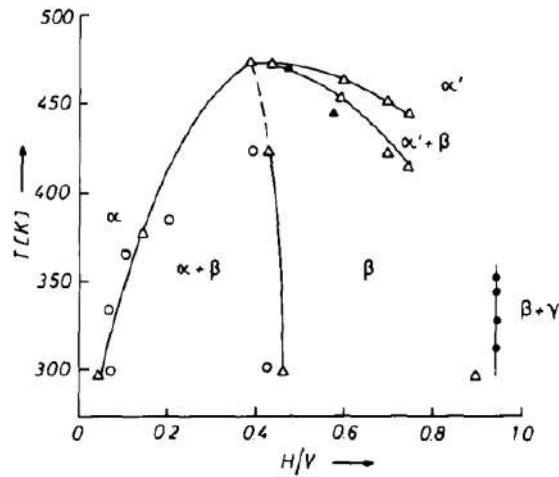


Fig. 1.23 V-H phase diagram [79]

Table 1.6. V-H Crystal structure data

Phase label	Formula	Prototype	Pearson symbol	Density (mg/m <sup>3</sup> )	Volume (nm <sup>3</sup> )	Cell parameter (nm)	Cell parameters (°)	Ref.
(V)	V	W	cI2 <i>Im-3m</i>	6.08	0.0278	a=0.303 b=0.303 c=0.303	$\alpha=90$ $\beta=90$ $\gamma=90$	[80]
$\alpha$	VH <sub>2</sub>	CaF <sub>2</sub>	cF12 <i>Fm-3m</i>	4.52	0.0779	a=0.4271 b=0.4271 c=0.4271	$\alpha=90$ $\beta=90$ $\gamma=90$	[81]
$\gamma$	V <sub>2</sub> H <sub>1.10</sub>	V <sub>2</sub> H <sub>1.1</sub>	tI56 <i>I4<sub>1</sub>/amd</i>	5.47	0.25029	a=0.6035 b=0.6035 c=0.6872	$\alpha=90$ $\beta=90$ $\gamma=90$	[82]
$\beta$								

Figures 1.24 shows a series of pressure-composition isotherms on vanadium films over the whole concentration range V-VH<sub>2</sub>. Pressure plateaus indicate regions where two hydride phases coexist with the gas phase. The phase diagrams in the inserts [83] are determined by temperature variations of sealed samples. The hysteresis is negligible for  $0.5 < x < 1.0$ . For  $1.0 < x < 1.8$ , the plateau pressures for hydriding are a factor of 2-3 higher than the dehydriding pressures shown here. Values given against the full curves are in °C.

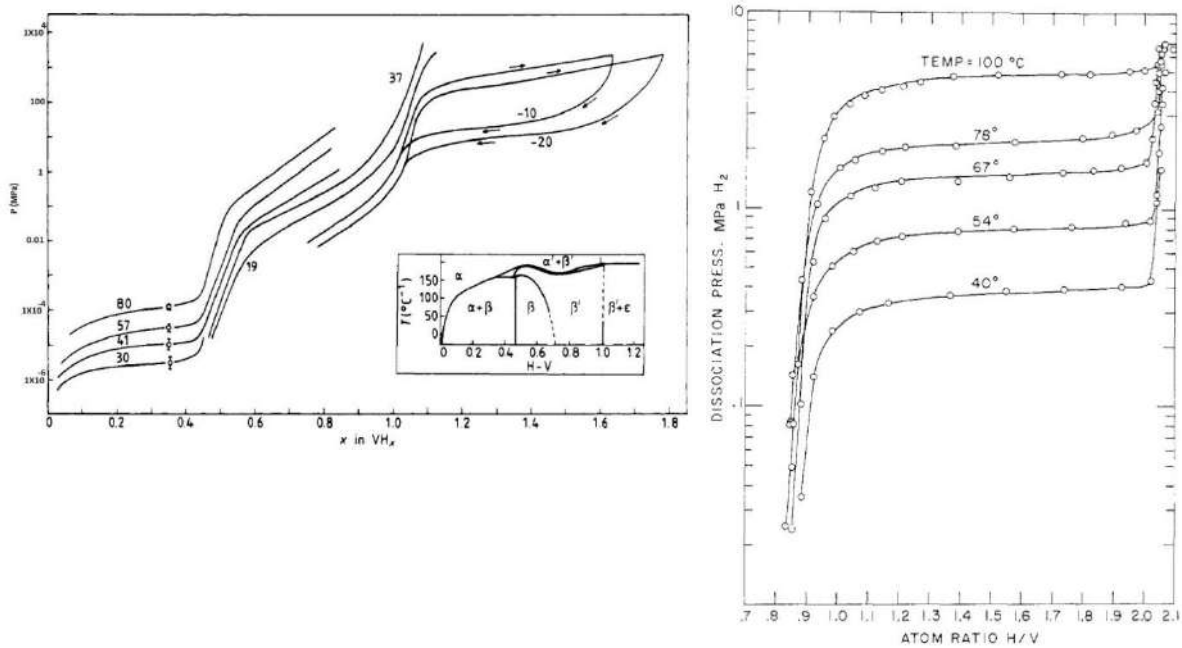


Figure 1.24. Pressure-composition isotherms for VH [83].

Several pressure-composition isotherms of the V-H system exists in the region  $VH_{0.8}$  to  $VH_{2.0}$  [84]. The initiation of a pressure plateau at a composition approximating  $VH_{0.95}$  marks the point at which the  $\gamma$  phase appears in the previously existing  $\beta$  phase. At  $40^\circ\text{C}$ , the plateau extends from  $VH_{0.95}$  to  $VH_{2.00}$  at which point the isotherm rises sharply, marking the composition at which the  $\beta$  phase disappears and only the  $\gamma$  phase exists. As indicated in Figure 1.24, hydrogen may dissolve in the  $\gamma$  phase and H: V atomic ratios above 2.00 are possible. It will be noticed that the  $67^\circ\text{C}$  and  $78^\circ\text{C}$  isotherms cross one another in the single-phase ( $\gamma$ ) region; this is a consequence of the non-stoichiometry of the system in which the higher temperature isotherm was obtained using a sample which had a greater initial hydrogen content (ie.,  $VH_{2.08}$  vs.  $VH_{2.01}$  at room temperature).

Figure 1.25 shows the diffusion coefficients for H and D in V, Nb, and Ta that have been determined and plotted by Schaumann [85] as a function of the reciprocal temperature. VH has the fastest  $D_H$  value among the others, then V-H and finally Ta-H.

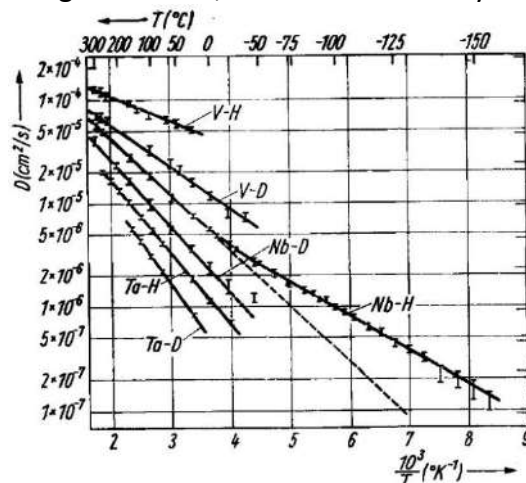
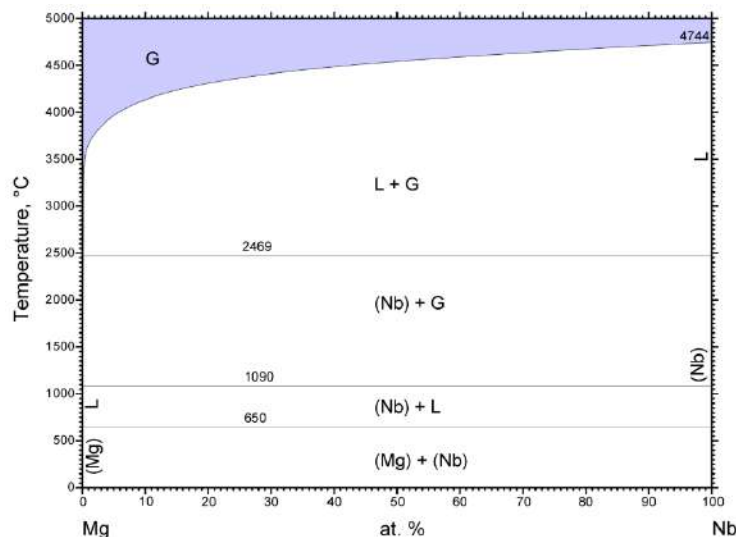


Figure 1.25 Logarithm of the diffusion coefficients of H respectively D in V, Nb, and Ta as a function of the reciprocal temperature [85]

Liang *et al.* [86] have prepared a composite  $\text{MgH}_2+5 \text{ at.}\% \text{ V}$  by RBM leading to a nanocomposite mixture of  $\beta\text{-MgH}_2 + \gamma\text{-MgH}_2 + \text{VH}_{0.8}$ , which can desorb hydrogen at  $200 \text{ }^\circ\text{C}$  under vacuum and re-absorb hydrogen quickly even at room temperature. The re-hydrogenation of this nanocomposite is extremely fast. In fact, at  $P_{\text{H}_2} = 1 \text{ MPa}$ , it can absorb 2wt. % in 16 min at  $29^\circ\text{C}$ , 4 wt. % in 2 min at  $100 \text{ }^\circ\text{C}$  and 5.6 wt. in 4 min at  $200 \text{ }^\circ\text{C}$ . They concluded that the enthalpy and entropy of the composite are identical to that of pure magnesium. Ren *et al.*[87] analyzed the effects of pure vanadium and V-based solid solution alloys ( $\text{V}_{75}\text{Ti}_5\text{Cr}_{20}$ ,  $\text{V}_{80}\text{Ti}_8\text{Cr}_{12}$ ,  $\text{V}_{80}\text{Ti}_{20}$ , and  $\text{V}_{80}\text{Cr}_{20}$ ) on the sorption kinetics of magnesium hydride. 5 mol % of V-based additive was used. In all cases, dehydrogenation temperatures of  $\text{MgH}_2$  with V-based additive were approximately  $100 \text{ }^\circ\text{C}$ , 0.1MPa lower than that of pure  $\text{MgH}_2$ . Among the V-based additives,  $\text{V}_{75}\text{Ti}_5\text{Cr}_{20}$  provides the lowest dehydrogenation temperature ( $217^\circ\text{C}$ ). Samples with  $\text{V}_{75}\text{Ti}_5\text{Cr}_{20}$ ,  $\text{V}_{80}\text{Ti}_8\text{Cr}_{12}$ , and pure V as additives fully dehydrogenate within 6 min. As compared to the pure  $\text{MgH}_2$  sample, which did not dehydrogenate at all at this low temperature. These results demonstrate a significant improvement in the kinetics of dehydrogenation of  $\text{MgH}_2$  with V-based alloys additives. The significant hydrogen absorption of  $\text{MgH}_2$  with V-based additives (1 bar hydrogen pressure and room temperature) suggests a strong effect of V-based additives on the hydrogenation of Mg. As concerns thermodynamics, they reported that the V-based additives do not affect the thermodynamic stability of magnesium hydride.

### 1.10 Nb-Mg system

The Mg-Nb phase diagram was drawn by Smith [80], which is very similar to Mg-V (Figure 1.22 being more stable Nb than V.



**Figure 1.26.** Magnesium-Niobium Binary Phase Diagram [80].

It is known that hydrogen is dissolved in large amounts into niobium, the maximum capacity ( $C_{max} \sim 2 \text{ H/M}$ ) doing it in tetrahedral interstitial sites. The phase diagram of the Nb-H system is depicted in Figure 1.27. At room temperature, the solubility limit  $\alpha_{max}$  of hydrogen in Nb extends approximately to  $x = 0.04$ . In the concentration range of  $0.7 < x < 1.1$ , the hydride ( $\beta$ -phase) occurs with the hydrogen atoms ordered in chains along a (110) direction. The next

higher phase corresponds roughly to the  $\text{NbH}_2$ -phase ( $\delta$ -phase). Crystal structure data are presented in Table 1.7.

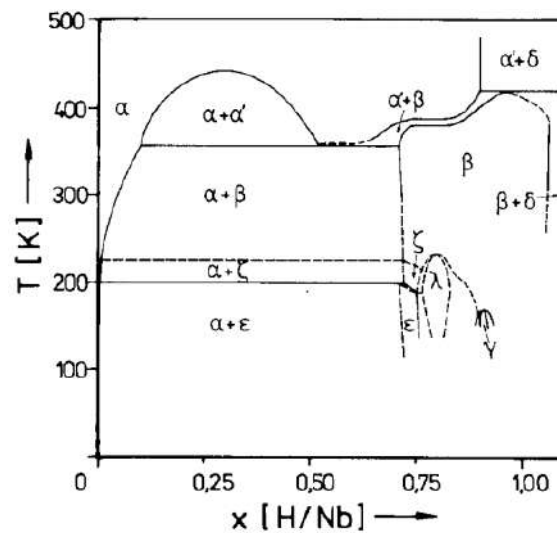


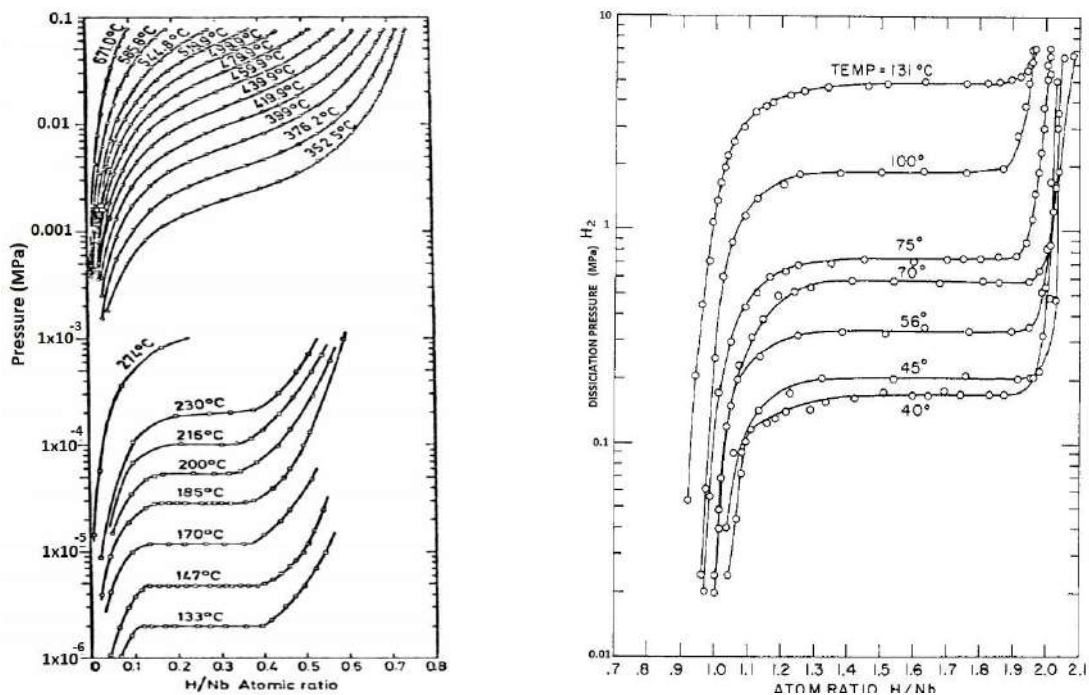
Fig 1.27 Nb-H phase diagram [80].

Table 1.7. Nb-H Crystal structure data

Phase label	Formula	Prototype	Pearson symbol	Density (mg/m <sup>3</sup> )	Volume (nm <sup>3</sup> )	Cell parameter (nm)	Cell parameters (°)	Ref.
<b>NbH<sub>0.85</sub> rt</b>	NbH	TaH <sub>0.5</sub>	oS8	7.56	0.08256	a=0.3467	α=90	[81]
			C222				β=90	
β						c=0.4917	γ=90	
<b>(Nb)</b>	NbH <sub>0.03</sub>	W	cl2	8.55	0.0361	a=0.33053	α=90	[89]
			<i>Im-3m</i>				β=90	
α						c=0.33053	γ=90	
<b>Nb<sub>2</sub>H /t2</b>					(no data)			
ζ								
<b>NbH<sub>0.72</sub> lt</b>					(no data)			
ε'								

Hydrogen is extremely mobile in niobium, in the  $\alpha$ -phase the diffusion coefficient  $D$  depends only slightly on temperature and at  $-173$  °C it still has a value of some  $10^{-8}$  cm<sup>2</sup>/s [90].

The Nb-H<sub>2</sub> system behaves in a manner similar to the V-H<sub>2</sub> system [84,91]. In Figure 1.28 is shown several pressure-composition isotherms for the region extending from Nb<sub>0.1</sub> to Nb<sub>0.8</sub> on the left and NbH<sub>0.9</sub> to NbH<sub>2.0</sub> on the right. The isotherms rise steeply on the left until a composition of NbH<sub>1.1</sub> is reached where the  $\gamma$ -dihydride phase appears. At 40 °C the  $\beta$ + $\gamma$  mixed phase region extends to NbH<sub>1.9</sub> where the isotherm begins a steep ascent indicating the disappearance of the  $\beta$  phase. It may be noted that the lower temperature isotherms indicate an appreciable solubility of hydrogen in the pure  $\gamma$  phase which resulted in hydrogen contents up to a composition corresponding to NbH<sub>2.081</sub>, niobium dihydride, as are other group Va hydrides, is a nonstoichiometric compound. Here, too, it is possible for the isotherms to cross one another in the single-phase ( $\gamma$ ) region because of the variable initial hydrogen content.



**Figure 1.28.** Pressure-composition isotherms for NbH<sub>0-0.8</sub> (left) and NbH<sub>0.9-2.1</sub> (right) [84,91].

Some studies have shown that Nb additive can intensively enhance the hydrogen sorption kinetics of magnesium [92], [93]. On the basis of the first principle calculations, Song *et al.* [94] confirmed that the alloying element Nb could destabilize magnesium hydride because it makes the bond energies between magnesium and hydrogen weaker from a kinetic viewpoint. Huot *et al.* [95] established that the ball milled MgH<sub>2</sub> + 5 atom% Nb composite could absorb 5.2 wt % H<sub>2</sub> at 300 °C within 5 min at  $P_{abs} = 0.1$  MPa and  $P_{des} = 0.015$  MPa. Yavari *et al.* [96] also confirmed an increase of hydrogen desorption kinetics when Nb was added to MgH<sub>2</sub>. De Castro *et al.* [24] reported that the desorption temperature of the ball milled Mg + 5 atom% Nb nanocomposite was 270 °C, the dehydrogenation behavior was studied by differential scanning calorimetry (DSC). Thus, Nb is considered as an effective additive not only for significantly reinforcing hydrogen sorption kinetics but also reserving the superior hydrogen sorption capacity of the Mg-based composite, due to a result indicating that Mg promoted the hydrogenation of Nb in the same way that Nb promoted the hydrogenation of Mg. With respect to the catalytic mechanism of Nb, Huot *et al.* [95] claimed that the formation of NbH<sub>x</sub>

( $x \approx 0.9$ ) phase during dehydrogenation acted as a gateway to accelerate the hydrogen release from  $\text{MgH}_2$ . Considering the good catalytic effect of Nb on the hydrogen sorption of the milled Mg–Nb composite, Liu *et al.* [97] intended to fabricate the Mg–Nb nanocomposite by hydrogen plasma-metal reaction, the Mg-7.5 wt % Nb nanocomposite was successfully prepared by this method. Nb nanoparticles of 12 nm are homogeneously decorated on the surfaces of the Mg nanoparticles and effectively prevent the Mg nanoparticles from growing during both the synthesis stage and the hydrogenation/dehydrogenation process. The Mg–Nb nanocomposite showed fast hydrogen absorption/desorption kinetics and high hydrogen storage capacity. The Mg–Nb nanocomposite can quickly uptake 4.0 wt %  $\text{H}_2$  in 10 min and reach a saturation value of 5.7 wt %  $\text{H}_2$  in 60 min at 200 °C. Furthermore, it can also release 4.0 wt %  $\text{H}_2$  in 60 min at 300 °C. The reversible hydrogen storage capacity is as high as 7.0 wt. % at 400 °C. The enhanced hydrogen storage capacities and the reduced apparent activation energies are due to the prominent catalytic effect of Nb nanoparticles and the nanosizing effects of both Mg and Nb.

## References

- [1] COM (2011) 112 - A Roadmap for moving to a competitive low carbon economy in 2050. Eur Environ Agency n.d. <https://www.eea.europa.eu/policy-documents/com-2011-112-a-roadmap> (accessed March 13, 2018).
- [2] COM(2010) 2020 final, Europe 2020: A strategy for smart, sustainable and inclusive growth. Eur Environ Agency n.d. <https://www.eea.europa.eu/policy-documents/com-2010-2020-europe-2020> (accessed March 13, 2018).
- [3] Publication: IEA Energy Technology Essentials: Hydrogen Production & Distribution n.d. <https://www.iea.org/publications/freepublications/publication/iea-energy-technology-essentials-hydrogen-production--distribution.html> (accessed March 13, 2018).
- [4] Fuel cells and Hydrogen technologies in Europe | [www.fch.europa.eu](http://www.fch.europa.eu) n.d. <http://www.fch.europa.eu/node/787> (accessed March 13, 2018).
- [5] Haynes WM. CRC Handbook of Chemistry and Physics, 95th Edition. CRC Press; 2014.
- [6] Tzimas E, Europäische Kommission, editors. Hydrogen storage: state-of-the-art and future perspective. Luxembourg: Office for Official Publications of the European Communities; 2003.
- [7] Weast R, Astle M, Beyer W. CRC Handb. Chem. Phys. Ready-Ref. Book Chem. Phys. Data, Boca Raton, Fla: CRC Press; 1984.
- [8] Züttel A. Hydrogen storage methods. *Naturwissenschaften* 2004; 91:157–72. doi:10.1007/s00114-004-0516-x.
- [9] Walker G. Solid-State Hydrogen Storage: Materials and Chemistry. Elsevier; 2008.
- [10] Flynn TM. A liquification of gases. vol. 10. 7th ed. New York: 1992.
- [11] Panella B, Hirscher M. Physisorption in Porous Materials. *Handb. Hydrog. Storage*, Wiley-Blackwell; 2010, p. 39–62. doi:10.1002/9783527629800.ch2.
- [12] Huot J. Metal Hydrides. *Handb. Hydrog. Storage*, Wiley-Blackwell; 2010, p. 81–116. doi:10.1002/9783527629800.ch4.
- [13] Schlapbach L, Züttel A. Hydrogen-storage materials for mobile applications. *Nature* 2001; 414:353–8. doi:10.1038/35104634.
- [14] Griessen R, Züttel A. Science and technologie of hydrogen in metals. Amsterdam: 2003.
- [15] Notten PHL, Latroche M. Secondary batteries – Nickel systems | Nickel–Metal Hydride: Metal Hydrides A2 - Garche, Jürgen. *Encycl. Electrochem. Power Sources*, Amsterdam: Elsevier; 2009, p. 502–21.
- [16] Züttel A. Materials for hydrogen storage. *Mater Today* 2003; 6:24–33. doi:10.1016/S1369-7021(03)00922-2.

- [17] Lacher JR. A theoretical formula for the solubility of hydrogen in palladium. *Proc R Soc Lond A* 1937; 161:525–45. doi:10.1098/rspa.1937.0160.
- [18] Sandrock G. A panoramic overview of hydrogen storage alloys from a gas reaction point of view. *J Alloys Compd* 1999;293–295:877–88. doi:10.1016/S0925-8388(99)00384-9.
- [19] Perejón A, Sánchez-Jiménez PE, Criado JM, Pérez-Maqueda LA. Magnesium hydride for energy storage applications: The kinetics of dehydrogenation under different working conditions. *J Alloys Compd* 2016; 681:571–9. doi:10.1016/j.jallcom.2016.04.191.
- [20] Zhong HC, Wang H, Ouyang LZ, Zhu M. Microstructure and hydrogen storage properties of Mg–Sn nanocomposite by mechanical milling. *J Alloys Compd* 2011; 509:4268–72. doi:10.1016/j.jallcom.2010.11.072.
- [21] Varin RA, Czujko T, Chiu C, Wronski Z. Particle size effects on the desorption properties of nanostructured magnesium dihydride ( $MgH_2$ ) synthesized by controlled reactive mechanical milling (CRMM). *J Alloys Compd* 2006; 424:356–64. doi:10.1016/j.jallcom.2005.12.087.
- [22] Lu J, Choi YJ, Fang ZZ, Sohn HY, Rönnebro E. Hydrogen Storage Properties of Nanosized  $MgH_2-0.1TiH_2$  Prepared by Ultrahigh-Energy–High-Pressure Milling. *J Am Chem Soc* 2009; 131:15843–52. doi:10.1021/ja906340u.
- [23] Cuevas F, Korablov D, Latroche M. Synthesis, structural and hydrogenation properties of Mg-rich  $MgH_2-TiH_2$  nanocomposites prepared by reactive ball milling under hydrogen gas. *Phys Chem Chem Phys* 2011;14:1200–11. doi:10.1039/C1CP23030A.
- [24] de Castro JFR, Santos SF, Costa ALM, Yavari AR, Botta F WJ, Ishikawa TT. Structural characterization and dehydrogenation behavior of Mg–5 at.%Nb nano-composite processed by reactive milling. *J Alloys Compd* 2004; 376:251–6. doi:10.1016/j.jallcom.2004.01.021.
- [25] Hanada N, Ichikawa T, Fujii H. Catalytic effect of Ni nano-particle and Nb oxide on H-desorption properties in  $MgH_2$  prepared by ball milling. *J Alloys Compd* 2005;404–406:716–9. doi:10.1016/j.jallcom.2004.12.166.
- [26] Zhang J, Cuevas F, Zaïdi W, Bonnet J-P, Aymard L, Bobet J-L, et al. Highlighting of a single reaction path during reactive ball milling of Mg and TM by quantitative  $H_2$  gas sorption analysis to form ternary complex hydrides (TM = Fe, Co, Ni). *J Phys Chem C* 2011; 115:4971–9. doi:10.1021/jp2005293.
- [27] Fernández JF, Sánchez CR. Rate determining step in the absorption and desorption of hydrogen by magnesium. *J Alloys Compd* 2002; 340:189–98. doi:10.1016/S0925-8388(02)00120-2.
- [28] Mintz MH, Zeiri Y. Hydriding kinetics of powders. *J Alloys Compd* 1995;216:159–75. doi:10.1016/0925-8388(94)01269-N.
- [29] Daniel F. Hydrogen storage in Mg-based alloys. *Anyagfizikai Tanszek*, 2010.
- [30] Fernández JF, Cuevas F, Sánchez C. Surface activation and hydrogenation kinetics of Ti sponge. *Int J Hydrog Energy* 1996; 21:765–8. doi:10.1016/0360-3199(96)00010-9.
- [31] Dehouche Z, Klassen T, Oelerich W, Goyette J, Bose TK, Schulz R. Cycling and thermal stability of nanostructured  $MgH_2-Cr_2O_3$  composite for hydrogen storage. *J Alloys Compd* 2002; 347:319–23. doi:10.1016/S0925-8388(02)00784-3.
- [32] Jain IP, Lal C, Jain A. Hydrogen storage in Mg: A most promising material. *Int J Hydrog Energy* 2010; 35:5133–44. doi:10.1016/j.ijhydene.2009.08.088.
- [33] Crivello J-C, Dam B, Denys RV, Dornheim M, Grant DM, Huot J, et al. Review of magnesium hydride-based materials: development and optimization. *Appl Phys A* 2016;122. doi:10.1007/s00339-016-9602-0.
- [34] Stampfer JF, Holley CE, Suttle JF. The Magnesium-Hydrogen System1-3. *J Am Chem Soc* 1960;82:3504–8. doi:10.1021/ja01499a006.
- [35] Bloch J, Mintz MH. Kinetics and mechanisms of metal hydrides formation—a review. *J Alloys Compd* 1997;253–254:529–41. doi:10.1016/S0925-8388(96)03070-8.
- [36] Gabis IE, Voit AP, Evard EA, Zaika YV, Chernov IA, Yartys VA. Kinetics of hydrogen desorption from the powders of metal hydrides. *Proc 9th Int Symp Met-Hydrog Syst Fundam Appl MH2004* 2005;404–406:312–6. doi:10.1016/j.jallcom.2005.02.090.

- [37] Drozdov IV, Vaßen R, Stöver D. Modelling and evaluation of hydrogen desorption kinetics controlled by surface reaction and bulk diffusion for magnesium hydride. *RSC Adv* 2015; 5:5363–71. doi:10.1039/C4RA08089K.
- [38] Xu Q, Kobayashi T. *Advanced materials for clean energy*. CRC Press; 2015.
- [39] Dornheim M, Doppiu S, Barkhordarian G, Boesenberg U, Klassen T, Gutfleisch O, et al. Hydrogen storage in magnesium-based hydrides and hydride composites. *Scr Mater* 2007;56:841–6. doi:10.1016/j.scriptamat.2007.01.003.
- [40] Darriet B, Pezat M, Hbika A, Hagenmuller P. Application of magnesium rich rare-earth alloys to hydrogen storage. *Int J Hydrog Energy* 1980;5:173–8. doi:10.1016/0360-3199(80)90094-4.
- [41] Pozzo M, Alfè D. Hydrogen dissociation and diffusion on transition metal (= Ti, Zr, V, Fe, Ru, Co, Rh, Ni, Pd, Cu, Ag)-doped Mg (0001) surfaces. *Int J Hydrog Energy* 2009; 34:1922–30. doi:10.1016/j.ijhydene.2008.11.109.
- [42] Huot J, Liang G, Boily S, Van Neste A, Schulz R. Structural study and hydrogen sorption kinetics of ball-milled magnesium hydride. *J Alloys Compd* 1999;293–295:495–500. doi:10.1016/S0925-8388(99)00474-0.
- [43] Wronski Z, Varin RA, Chiu C, Czujko T, Calka A. Mechanochemical synthesis of nanostructured chemical hydrides in hydrogen alloying mills. *J Alloys Compd* 2007;434–435:743–6. doi:10.1016/j.jallcom.2006.08.301.
- [44] Liang G, Huot J, Boily S, Van Neste A, Schulz R. Catalytic effect of transition metals on hydrogen sorption in nanocrystalline ball milled  $MgH_2$ -Tm (Tm=Ti, V, Mn, Fe and Ni) systems. *J Alloys Compd* 1999;292:247–52. doi:10.1016/S0925-8388(99)00442-9.
- [45] Murray JL. The Mg-Ti (Magnesium-Titanium) system. *Bull Alloy Phase Diagr* 1986;7:245–8. doi:10.1007/BF02868999.
- [46] San-Martin A, Manchester FD. The H-Ti (Hydrogen-Titanium) system. *Bull Alloy Phase Diagr* 1987; 8:30–42. doi:10.1007/BF02868888.
- [47] *A Handbook of Lattice Spacings and Structures of Metals and Alloys*. Elsevier; 1958. doi:10.1016/C2013-0-08243-6.
- [48] Zhou C. A study of advanced magnesium-based hydride and development of a metal hydride thermal battery system. PhD Thesis 2015.
- [49] Arita M, Shimizu K, Ichinose Y. Thermodynamics of the Ti-H system. *Metall Trans A* 1982; 13:1329–36. doi:10.1007/BF02642869.
- [50] Liang G, Schulz R. Synthesis of Mg-Ti alloy by mechanical alloying. *J Mater Sci* 2003; 38:1179–84. doi:10.1023/A:1022889100360.
- [51] Luca Pasquini EC. Magnesium nanoparticles with transition metal decoration for hydrogen storage. *J Nanoparticle Res* 2011; 13:5727–37. doi:10.1007/s11051-011-0509-6.
- [52] Ponthieu M, Cuevas F, Fernández JF, Laversenne L, Porcher F, Latroche M. Structural Properties and Reversible Deuterium Loading of  $MgD_2$ - $TiD_2$  Nanocomposites. *J Phys Chem C* 2013; 117:18851–62. doi:10.1021/jp405803x.
- [53] Crivello J-C, Denys RV, Dornheim M, Felderhoff M, Grant DM, Huot J, et al. Mg-based compounds for hydrogen and energy storage. *Appl Phys A* 2016;122. doi:10.1007/s00339-016-9601-1.
- [54] Hämäläinen M, Zeng K. Thermodynamic evaluation of the Mg-Zr system. *Calphad* 1998; 22:375–80. doi:10.1016/S0364-5916(98)00037-6.
- [55] Zuzek E, Abriata JP, San-Martin A, Manchester FD. The H-Zr (hydrogen-zirconium) system. *Bull Alloy Phase Diagr* 1990; 11:385–95. doi:10.1007/BF02843318.
- [56] Hydrogen-Zirconium Binary Alloy Phase Diagram (based on 1990 Zuzek E.) - ASM International n.d. [https://www.asminternational.org/home/-/journal\\_content/56/10192/APD-H-ZR-901266/APD-DATA-SHEET](https://www.asminternational.org/home/-/journal_content/56/10192/APD-H-ZR-901266/APD-DATA-SHEET) (accessed September 14, 2018).
- [57] Okamoto H, editor. *Desk handbook: phase diagrams for binary alloys*. 2nd ed. Materials Park, Ohio: ASM International; 2010.
- [58] Kittel JH, Ayer JE, Beck WN, Brodsky MB, O’Boyle DR, Zegler ST, et al. Plutonium and plutonium alloys as nuclear fuel materials. *Nucl Eng Des* 1971; 15:373–440. doi:10.1016/0029-5493(71)90076-8.

- [59] Niedźwiedź K, Nowak B, Żogał OJ.  $^{91}\text{Zr}$  NMR in non-stoichiometric zirconium hydrides,  $\text{ZrH}_x$  ( $1.55 \leq x \leq 2$ ). *J Alloys Compd* 1993; 194:47–51. doi:10.1016/0925-8388(93)90643-2.
- [60] Solid Solution Equilibria in the Zirconium-Hydrogen System1 n.d. <https://pubs.acs.org/doi/pdf/10.1021/ja01610a074> (accessed September 14, 2018).
- [61] Majer G, Renz W, Barnes RG. The mechanism of hydrogen diffusion in zirconium dihydrides. *J Phys Condens Matter* 1994; 6:2935–42. doi:10.1088/0953-8984/6/15/015.
- [62] Korablov D, Nielsen TK, Besenbacher F, Jensen TR. Mechanism and kinetics of early transition metal hydrides, oxides, and chlorides to enhance hydrogen release and uptake properties of  $\text{MgH}_2$ . *Powder Diffr* 2015; 30:59–15. doi:10.1017/S0885715615000056.
- [63] Czujko T, Varin RA, Chiu C, Wronski Z. Investigation of the hydrogen desorption properties of  $\text{Mg}+10\text{wt.}\%X$  ( $X=\text{V}, \text{Y}, \text{Zr}$ ) submicrocrystalline composites. *J Alloys Compd* 2006; 414:240–7. doi:10.1016/j.jallcom.2005.07.009.
- [64] Nayeb-Hashemi AA, Clark JB. The  $\text{Mg}-\text{Sc}$  (Magnesium-Scandium) system. *Bull Alloy Phase Diagr* 1986; 7:574–8. doi:10.1007/BF02869876.
- [65] Venturini EL, Morosin B. Low temperature anomaly in  $\text{Sc}_{0.995}\text{Gd}_{0.005}\text{H}_{1.9}$ . *Phys Lett A* 1977; 61:326–8. doi:10.1016/0375-9601(77)90630-2.
- [66] Azarkh ZM, Funin VN. X-ray structural phase analysis of the scandium-hydrogen system. *Sov Phys Crystallogr Krist* 1965; 10:21–4.
- [67] Manchester FD, Pitre JM. The  $\text{h}-\text{sc}$  (Hydrogen- Scandium) system. *J Phase Equilibria* 1997; 18:194–205. doi:10.1007/BF02665706.
- [68] Latroche M, Kalisvaart P, Notten PHL. Crystal structure of  $\text{Mg}_{0.65}\text{Sc}_{0.35}\text{D}_x$  deuterides studied by X-ray and neutron powder diffraction. *J Solid State Chem* 2006; 179:3024–32. doi:10.1016/j.jssc.2006.05.032.
- [69] Luo X, Grant DM, Walker GS. Hydrogen storage properties of nano-structured  $0.65\text{MgH}_2/0.35\text{ScH}_2$ . *Int J Hydrog Energy* 2013; 38:153–61. doi:10.1016/j.ijhydene.2012.10.025.
- [70] Luo X, Grant DM, Walker GS. Catalytic effect of nano-sized  $\text{ScH}_2$  on the hydrogen storage of mechanically milled  $\text{MgH}_2$ . *J Alloys Compd* 2015; 622:842–50. doi:10.1016/j.jallcom.2014.10.161.
- [71] Okamoto H.  $\text{Mg}-\text{y}$  (magnesium-yttrium). *J Phase Equilibria* 1992;13:105–6. doi:10.1007/BF02645395.
- [72] Khatamian D, Manchester FD. The  $\text{H}-\text{Y}$  (Hydrogen-Yttrium) system. *Bull Alloy Phase Diagr* 1988; 9:252–60. doi:10.1007/BF02881276.
- [73] IUCr. *Acta Crystallographica* Volume 9, Part 7, July 1956. [Http://journals.iucr.org/journalswebproductionsitescjo-Testqissues19560700indexhtml](http://journals.iucr.org/journalswebproductionsitescjo-Testqissues19560700indexhtml) 2015. <http://journals.iucr.org/q/issues/1956/07/00/> (accessed September 14, 2018).
- [74] Fedotov VK, Antonov VE, Bashkin IO, Hansen T, Natkaniec I. Displacive ordering in the hydrogen sublattice of yttrium trihydride. *J Phys Condens Matter* 2006; 18:1593–9. doi:10.1088/0953-8984/18/5/012.
- [75] Beavis LC, Blewer RS, Guthrie JW, Nowak EJ, Perkins WG. The Formation and Properties of Rare-Earth and Transition Metal Hydrides. In: Veziroğlu TN, editor. *Hydrog. Energy Part A*, Boston, MA: Springer US; 1975, p. 659–74. doi:10.1007/978-1-4684-2607-6\_46.
- [76] Yannopoulos LN, Edwards RK, Wahlbeck PG. The Thermodynamics of the Yttrium-Hydrogen System1. *J Phys Chem* 1965;69:2510–5. doi:10.1021/j100892a004.
- [77] Huiberts JN, Griessen R, Rector JH, Wijngaarden RJ, Dekker JP, Groot DG de, et al. Yttrium and lanthanum hydride films with switchable optical properties. *Nature* 1996; 380:231–4. doi:10.1038/380231a0.
- [78] Cao Z, Ouyang L, Wang H, Liu J, Felderhoff M, Zhu M. Reversible hydrogen storage in yttrium aluminum hydride. *J Mater Chem A* 2017; 5:6042–6. doi:10.1039/C6TA10928D.
- [79] Smith J.F., and Lee K.J.,  $\text{Mg}-\text{V}$  (Magnesium-Vanadium), *Binary Alloy Phase Diagrams*, II Ed., Ed. T.B. Massalski, Vol. 3, 1990, p 2566-2567 n.d.
- [80] Lomnitska YF.  $\text{V}-\text{Si}-\text{Sb}$  phase diagram. Isothermal section at 1070 K. *Powder Metall Met Ceram* 2007;46:461–6. doi:10.1007/s11106-007-0072-y.

- [81] Müller H, Weymann K. Investigation of the ternary systems Nb-V-H and Ta-V-H. *J Common Met* 1986;119:115–26. doi:10.1016/0022-5088(86)90201-8.
- [82] Kajitani T., Hirabayashi M. Neutron Diffraction Study of  $\beta$ 1-V<sub>2</sub>H and  $\beta$ -V<sub>2</sub>D\*. *Z Für Phys Chem* 1985;145:27. doi:10.1524/zpch.1985.145.1\_2.027.
- [83] Alefeld G, Völkl J, editors. *Hydrogen in Metals II: Application-Oriented Properties*. Berlin Heidelberg: Springer-Verlag; 1978.
- [84] Reilly JJ, Wiswall RH. Higher hydrides of vanadium and niobium. *Inorg Chem* 1970;9:1678–82. doi:10.1021/ic50089a013.
- [85] Schaumann G, Völkl J, Alefeld G. The diffusion coefficients of hydrogen and deuterium in vanadium, niobium, and tantalum by gorsky-effect measurements. *Phys Status Solidi B* 1970;42:401–13. doi:10.1002/pssb.19700420141.
- [86] Liang G, Huot J, Boily S, Van Neste A, Schulz R. Hydrogen storage properties of the mechanically milled MgH<sub>2</sub>-V nanocomposite. *J Alloys Compd* 1999;291:295–9. doi:10.1016/S0925-8388(99)00268-6.
- [87] Ren C, Fang ZZ, Zhou C, Lu J, Ren Y, Zhang X. Hydrogen Storage Properties of Magnesium Hydride with V-Based Additives. *J Phys Chem C* 2014; 118:21778–84. doi:10.1021/jp504766b.
- [88] Smith J.F., Mg-Nb (Magnesium-Niobium), *Binary Alloy Phase Diagrams, II Ed.*, Ed. T.B. Massalski, Vol. 3, 1990, p 2526 n.d.
- [89] Drake A, Finlayson TR, Harris IR. An X-ray diffraction study of hydride precipitation in the systems, Nb-H and Nb-5at.%Mo-H. *J Common Met* 1987;129:123–31. doi:10.1016/0022-5088(87)90039-7.
- [90] Welter J-M, Johnen FJ. Superconducting transition temperature and low temperature resistivity in the niobium-hydrogen system. *Z Für Phys B Condens Matter* 1977; 27:227–32. doi:10.1007/BF01325532.
- [91] J A Pryde and C G Titcomb. Phase equilibria and kinetics of evolution of dilute solutions of hydrogen in niobium. *J Phys C Solid State Phys* 1972; 5:1293.
- [92] Cui J, Liu J, Wang H, Ouyang L, Sun D, Zhu M, et al. Mg-TM (TM: Ti, Nb, V, Co, Mo or Ni) core-shell like nanostructures: synthesis, hydrogen storage performance and catalytic mechanism. *J Mater Chem A* 2014; 2:9645–55. doi:10.1039/C4TA00221K.
- [93] Bazzanella N, Checchetto R, Miotello A. Catalytic effect on hydrogen desorption in Nb-doped microcrystalline MgH<sub>2</sub>. *Appl Phys Lett* 2004; 85:5212–4. doi:10.1063/1.1829155.
- [94] Song Y, Guo ZX, Yang R. Influence of selected alloying elements on the stability of magnesium dihydride for hydrogen storage applications: A first-principles investigation. *Phys Rev B Condens Matter Mater Phys* 2004;69:094205.1-094205.11.
- [95] Huot J, Pelletier JF, Lurio LB, Sutton M, Schulz R. Investigation of dehydrogenation mechanism of MgH<sub>2</sub>-Nb nanocomposites. *J Alloys Compd* 2003; 348:319–24. doi:10.1016/S0925-8388(02)00839-3.
- [96] Yavari AR, de Castro JFR, Vaughan G, Heunen G. Structural evolution and metastable phase detection in MgH<sub>2</sub>-5%NbH nanocomposite during in-situ H-desorption in a synchrotron beam. *J Alloys Compd* 2003; 353:246–51. doi:10.1016/S0925-8388(02)01199-4.
- [97] Liu T, Ma X, Chen C, Xu L, Li X. Catalytic Effect of Nb Nanoparticles for Improving the Hydrogen Storage Properties of Mg-Based Nanocomposite. *J Phys Chem C* 2015; 119:14029–37. doi:10.1021/acs.jpcc.5b03442.



---

# CHAPTER TWO

---

Synthesis and characterization techniques





## Chapter 2: Synthesis and characterization techniques

### 2.1 Materials and samples handling

All the elements involved in this research have been gotten commercially. The sources and forms of all used raw metals are listed in Table 2.1. They have been used as-received without further purification. The rare earth metals used in the automatic cycling device were filed down right before melting to remove the native oxide layer at the surface. The raw elements were carefully weighted to desire stoichiometric proportion with a precision of  $\pm 0.001$  mg. All samples handling, weighting, and loading were performed in an argon-filled glove box with a controlled amount of oxygen ( $<2$  ppm) and moisture ( $\text{H}_2\text{O} < 45$  ppm). For the synthesis of hydrides, 6 N Alphagaz (99,9999 % purity) was used.

**Table 2.1** Characteristics of the starting metallic materials

Element	Supplier	Purity	State	Mesh
Mg	Alfa-Aesar	99.8%	Powder	-20+100
Ti	Alfa-Aesar	99.9%	Powder	-150
Zr	CERAC	99.7%	Powder	-325
V	Stream Chemicals	99.5%	Powder	-325
Nb	Chem Pur	99.9%	Powder	-150
Sc	China Rare Metals	99.9%	Pieces, irregularly shaped	-100 (post crushed)
Y	Stream Chemicals	99.9%	Powder	-40
La	Alfa-Aesar	99.9%	Pieces under mineral oil	-
Ni	Alfa-Aesar	99.9%	Pieces, irregularly shaped	-
Sn	Alfa-Aesar	99.9%	Rod	-

### 2.2 Synthesis of metal hydrides and alloys

#### 2.2.1 Reactive Ball Milling (RBM)

Mechanochemical synthesis of metal hydrides using ball milling has become a very frequently used method. Different kind of planetary ball mills such as rotational, vibratory or attritor mills is commonly used. The different types of mills differ in their milling efficiency and capacity as well as arrangements for cooling, heating, gas loading *etc.* Planetary ball mills are used wherever the highest degree of fineness is required. In addition to well-proven mixing and size reduction processes, these mills also meet all technical requirements for colloidal grinding and provide the energy input necessary for mechanical alloying. The extremely high centrifugal forces of a planetary ball mill result in very high pulverization energy and therefore short grinding times. Typically, a few grams of material and balls are placed in a planetary ball mill to give a ball-to-powder weight ratio of 10:1–60:1.

Several parameters can be varied for the ball-milling synthesis: milling speed, total milling time, vial and ball composition, powder-to-ball weight ratio, vial diameter, ball diameter and density, milling temperature, milling atmosphere and pressure of the reactive gas. Most planetary mills only allow controlling the speed of the main support disk. The speed of the planets, on which the milling vials are mounted, is usually fixed relative to the speed of the main disk. However, for mills, such as the Fritsch Vario-

Planetary Mill Pulverisette 4, both the speed of the support disk and the planets can be varied freely. Thereby, the trajectory of the balls within the vial may be controlled at least when the number of balls is low. Ideally, the milling can be continuously changed from the high-energy mode dominated by high-energy ball–vial impacts to a grinding mode where the balls mainly follow the circumference of the vial[1].

Different  $MgH_2$ - $TMH_x$  nanocomposites had been prepared by reactive ball milling during this work. The systems are listed in Table 2.2. RBM experiments under hydrogen gas (6 N Alphasgaz) were performed in a high-pressure milling vial (Evicomagnetics, Germany) equipped with gas pressure and temperature sensors [2]. The commercial vial was connected to a manometric hydrogenation device equipped with calibrated volumes. Using this device, we established the starting hydrogen pressure in the vial (typically 8 MPa) and the volume occupied by the gas in the vial (typically 166 cm<sup>3</sup>). The milling process was performed in a Fritsch Pulverisette 4 planetary mill at disk and vial rotation speed of 400 rpm and 800 rpm (relative to disk), respectively, with a ball-to-powder mass ratio of 60:1. Stainless steel balls of 12 mm in diameter were used. Milling was carried out in two subsequent cycles, 120 min milling time and 120 min rest each.

**Table 2.2**  $MgH_2$ - $TMH_x$  nanocomposites prepared by RBM

Nanocomposites	Composition (mol %)
$MgH_2$ -TiH <sub>2</sub>	Ti = 0.0125-0.3
$MgH_2$ -ZrH <sub>2</sub>	Zr= 0.05
$MgH_2$ -VH <sub>2</sub>	V= 0.05
$MgH_2$ -NbH <sub>2</sub>	Nb= 0.05
$MgH_2$ -ScH <sub>2</sub>	Sc= 0.05
$MgH_2$ -YH <sub>2</sub>	Y= 0.05

### 2.2.2 Electromagnetic processing of materials by induction melting

Electromagnetic processing of material is a technology which works with different interactions between material and electromagnetic field. The high-frequency induction heating and melting are one of the first applications of electromagnetic fields [3]. The alloys are prepared by co-melting according to the technique of high-frequency induction melting, also called levitation in cold crucible. An induction coil is connected to the power supply so that a magnetic field is generated from the current flow. The starting metals with stoichiometric quantities are placed in the copper crucible with inner water-cooling circulation. The crucible is surrounded by a water-cooled alternating current solenoid coil of copper. An aperiodic generator provides a maximum power of 50 kW and delivers a high-frequency alternating current (up to 120 kHz).

The  $LaNi_{4.66}Sn_{0.34}$  alloy was prepared by the co-fusion of the elements in a high-frequency induction furnace. A non-inductive copper melting-pot cooled by water circulation was put into a vacuum enclosure incorporated by a silica tube. The magnetic field applied to the sample is created by an external solenoid. The primary and second pumps allow to reach a pressure of  $7 \times 10^{-10}$  MPa, the residual pressure is measured by a vacuum gauge, the temperature is measured by an optical pyrometer.

The three high purity metals were cleaned on the surface and weighted in an accuracy of  $\pm 0.0001$  mg. to produce a 112 g final product. The target was to synthesize more material than calculated before to prevent loss of material during synthesis as well as to have extra material for its characterization. Both nickel and tin were manipulated under air, meanwhile, lanthanum was prepared inside the gloves box due to its high reactivity with the oxygen. The fusion was carried out increasing slowly the temperature to allow the metals to degas. To limit the nickel and tin vaporization, it was performed a reduction with argon. The final product was cracked into several pieces and put inside a silica tube under primary vacuum ( $1 \times 10^{-7}$  MPa) and annealing was performed at 850 °C for 8 days. Finally, the silica tube was cooled by water quenching. The alloy was recovered inside the glove box and stored for characterization.

## 2.3 Structural, morphological and chemical characterization

### 2.3.1 X-Ray Diffraction (XRD)

Because of the availability and properties of X-rays, diffraction is one of the most common techniques for phase identification and structural characterization of crystalline materials. This technique allows determining crystalline structures on powdered materials. X-rays wavelengths used for crystallographic studies are typically in the range 0.5-2.5 Å. X-ray is scattered by electrons of the atoms and the important consequences of this are that [4]:

- The atomic scattering factor of elements,  $f_i$  in Eq. (2.3) increases linearly with the atomic number  $Z$ ;
- The  $f_i$  factors have a significant dependence on the scattering angle, the maximum value (equal to the number of electrons) is at zero scattering angle and decreases with increasing scattering angles;
- X-rays interact strongly with matter.

In this work, the XRD analyses were carried out with a Bruker D8 Advance  $\theta$ - $\theta$  Diffractometer with Cu-K $\alpha$  Radiation ( $w_{K\alpha 1}=1.54051$  Å,  $\lambda_{K\alpha 2}= 1.54433$  Å) and graphite rear monochromator. A value of  $2\theta$  ranging from 25 to 70 degrees was used during this procedure. Because of the nanocomposites reactivity, a special air-tight sample-holder was used to avoid their exposition with air and moisture. XRD sample-holder was loaded with about 200 mg of powder inside the glove box and hermetically closed with an X-ray transparent lid.

#### 2.3.1.1 The Rietveld and Loppstra method

X-ray powder diffraction is an efficient method for determining the phase content of a polycrystalline material. Every material exhibits a typical 'X-ray fingerprint', which is stored in databases such as the ICDD PDF2 or PDF4. This fingerprint is utilized in the DIFFRAC.EVA software for reliable phase identification. Once the phases and their structure had been identified, the XRD experimental profile can be fitted to a calculated profile by means of the Rietveld's method [5,6]. For this work, diffraction patterns were analyzed using the Fullprof Suite software [7].

### 2.3.1.2 Structure refinements - the Rietveld method

The final step in a structure solution is to fit the experimental diffraction pattern with a calculated pattern while refining the crystallographic parameters of all detected phases. Loopstra and Rietveld [6] suggested using the whole experimental powder diffraction diagram in the refinements by fitting a calculated diagram to the observed data. It should be emphasized that the Rietveld method is a structure refinement method and not a method to solve unknown structures. An adequate structure model must be known in advance.

The minimizing function in the Rietveld method is:

$$M = \sum_{i=1}^n w_i (y_i^{obs} - y_i^{calc})^2 \quad [2.1]$$

$n$  is the number of measured data points,  $y_i^{obs}$  and  $y_i^{calc}$  are the observed and calculated intensity at point  $i$  of the powder diffraction pattern, respectively, and  $w_i$  is the weight of the point given by  $w_i = 1/\sigma_i^2$  where  $\sigma_i$  is the variance. The calculated intensity (assuming a single-phase sample) can be described by:

$$y_i^{calc} = b_i + S_i \sum_{hkl} M_{hkl} \cdot L_i \cdot P_i \cdot A_{hkl} \cdot T_{hkl} \cdot |F_{hkl}|^2 \cdot \Phi(2\theta_{hkl} - 2\theta_i) \quad [2.2]$$

$b_i$  is the background at point  $i$ . It can be either determined manually or by interpolation between selected points or described by a polynomial. The sum covers all reflections contributing to Bragg scattering at point  $i$ .  $S_i$  is the scale factor,  $L_i$  is the Lorentz factor that is defined by the geometry diffraction,  $P_i$  is the polarization factor accounting for the partial polarization of the scattered electromagnetic wave,  $M_{hkl}$  is the multiplicity factor accounting for the presence of multiple symmetrically equivalent points in reciprocal space  $A_{hkl}$ ,  $T_{hkl}$  is the preferred orientation factor,  $\Phi$  is the profile function coming from instrumental and sample broadening in the diffraction pattern,  $2\theta_{hkl}$  is the ideal Bragg angle for reflection  $hkl$ ,  $2\theta_i$  is the scattering angle corresponding to point  $i$ , the structure factor  $F_{hkl}$  is the structure factor defined by:

$$F_{hkl} = \sum_{j=1}^N f_j \exp(2\pi i(hx_j + ky_j + lz_j)) \exp(-B_j \sin^2 \theta / \lambda^2) \quad [2.3]$$

$f_j$  is the atomic scattering factor that is strongly dependent of both radiation type and elements,  $N$  is the number of atoms in the unit cell,  $x_j$ ,  $y_j$ ,  $z_j$  are the atomic fraction coordinates of factor  $j$  in the unit cell,  $B_j$  is the isotropic displacement parameter of atom  $j$  defined as  $B_j = 8\pi^2(\bar{u}^2)^j$ ,  $(\bar{u}^2)^j$  is the root mean square deviation of atom  $j$  from the equilibrium position in  $\text{\AA}^2$ .

Several factors influence the shape and width of the measured Bragg peaks, the most important are those related with the X-ray apparatus: collimation of the beam,

degree of mosaicity of the monochromator, detector resolution; and the related to the nature of the sample: size and in addition to imperfection/mosaicity. The resulting profile shape is a convolution of all these components. The measured profiles show both a Gaussian and Lorentzian contribution. The Rietveld method was developed with a pure Gaussian distribution which well fits data from low-resolution neutron powder diffractometer, but with improved resolution, and X-Ray diffraction in general, a significant Lorentzian contribution is present.

Nowadays the so-called pseudo-Voigt profile function is a commonly used profile function. It is a linear combination of a Gaussian and a Lorentzian function. The peak broadening is measured by the “full-width-at-half-maximum” (FWHM). The Gaussian contribution is given by:

$$FWHM_{Gaussian} = \sqrt{U \tan^2 \theta + V \tan \theta + W} \quad [2.4]$$

And Lorentzian:

$$FWHM_{Lorentzian} = \frac{Y}{\cos \theta} + X \tan \theta \quad [2.5]$$

Table 2.3 are summarized the typical parameters which are refined in the Rietveld method. The starting point for the refinement should be an adequate structure model. Many software programs are available for Rietveld refinements, such as Fullprof [7], GSAS [8] and TOPAS-Academic [9].

**Table 2.3** Parameters for Rietveld refinements for a single-phase compound based on constant wavelength X-ray

Scale factor (S)
Zero-shift
Background (when refined as a polynomial function)
Lattice parameters: $a, b, c, \alpha, \beta, \gamma$
Profile parameters: $U, V, W, X, Y$
Coordinates of atoms: $x_j, y_j, z_j$
Isotope displacement parameters: $B_j$
Occupation parameters: $O_j$

The figure of merit to evaluate the quality of the refinements are the weight profile  $R$ -factor:

$$R_{wp} = \left[ \frac{\sum_{i=1}^n w_i (y_i^{obs} - y_i^{calc})^2}{\sum_{i=1}^n w_i (y_i^{obs})^2} \right]^{1/2} \quad [2.6]$$

And the goodness of fit:

$$\chi^2 = \frac{\sum_{i=1}^n w_i (y_i^{obs} - y_i^{calc})^2}{n - p} = \left[ \frac{R_{wp}}{R_{exp}} \right]^2 \quad [2.7]$$

where  $p$  is the number of free least square parameters and  $R_{exp}$  is the so-called expected profile R-factor.

An important application of the Rietveld method is the determination of relative amounts of different phases in a sample with a so-called *quantitative phase analysis*. Based on multiphase refinements the molar-, weight-, and volume- fractions can be calculated from the individual scale factors and the unit cells contents and volume.

Finally, the accurate analyses of the profile parameters and their dependence on the scattering angle  $2\theta$  can give information about strain and particle sizes in the sample. The term  $U$  in Eq.2.4 describes strain contribution to peak broadening, while the term  $Y$  in Eq. 2.5. corresponds to the crystal size distribution. The term  $U$  in Eq.2.4 describes strain contribution to peak broadening, while the term  $Y$  in Eq. 2.5. corresponds to the crystal size distribution [10].

### 2.3.2 Scanning Electron Microscopy (SEM)

By irradiating a sample with a monochromatic electron beam, scanning electron microscopy (SEM) takes advantage of the diverse interactions between the electrons and the sample to obtain chemical and morphological information on the material.

The images in secondary electrons give information on the surface morphology of the sample. The angular emission of backscattered electrons (BSE) is characteristic of the atomic number on the probe path. Heavy atoms (large atomic number  $Z$ ) induce stronger elastic scattering between the incident electron and the nucleus. Therefore, BSE images can provide a chemical contrast of the specimen. Qualitative analysis is a routine test on interesting samples to verify chemical compositions. Energy dispersive spectroscopy (EDS) quantitative analysis is performed using a Zeiss Ultra field emission scanning electron microscope equipped with a Bruker SDD EDS analyzer [11].

The morphological characterization of the materials was performed using scanning electron microscopy for imaging. The microscope was provided by the company Carl Zeiss, it is a MERLIN SEM. It has a field effect gun (FEG) to obtain an electronic probe of very small diameter (of the order of one nanometer at the sample), nevertheless carrying a large current (of the order of the nanoampere). This current is constant (variation less than 0.5% per hour), which allows easier and more reliable analyzes. The design of the column and especially of the objective lens of this microscope takes full advantage of this beam by significantly reducing the aberrations of the electromagnetic optical system, even at low electron acceleration voltages. This, together with an annular secondary electron detector located above the objective lens, makes possible to obtain morphological observations with excellent resolution at any acceleration voltage: the guaranteed resolutions are 0.8 nm to 15 kV and 1.4 nm at 1 kV on gold. A second annular detector allows the detection of backscattered electrons with low acceleration voltage, to obtain chemical contrast images with a very good spatial resolution. The secondary and backscattered electron detectors arranged this time in the object chamber, improving the observation capabilities of the microscope. Particle size was measured with the specialized software ImageJ, this software allows to

configure the image on a known scale, then to calculate the area of the particles on the image, finally, the size can be measured from the given area [12].

### 2.3.3 Inductively Coupled Plasma Optical Emission Spectrometry (ICP-OES)

ICP-OES, an abbreviation for Inductively Coupled Plasma, is a method of optical emission spectrometry. ICP/OES is one of the most powerful and popular analytical tools for the determination of trace elements. The technique is based upon the spontaneous emission of photons from atoms and ions that have been excited in a radiofrequency discharge. Liquid and gas samples may be injected directly into the instrument, while solid samples require extraction or acid digestion so that the analyses will be done in solution. The sample solution is converted to an aerosol and directed into the central channel of the plasma. At its core, the inductively coupled plasma (ICP) sustains a temperature of approximately 10 000 °C, so the aerosol is quickly vaporized. Elements are liberated as free atoms in the gaseous state. Further collisional excitation within the plasma imparts additional energy to the atoms, promoting them to excited states. Sufficient energy is often available to convert the atoms to ions and subsequently promote the ions to excited states. Both the atomic and ionic excited state species may then relax to the ground state via the emission of a photon. These photons have characteristic energies that are determined by the quantized energy level structure for the atoms or ions. Thus, the wavelength of the photons can be used to identify the elements from which they originated. The total number of photons is directly proportional to the concentration of the originating element in the sample.

The instrumentation associated with an ICP/OES system is relatively simple. A portion of the photons emitted by the ICP is collected with a lens or a concave mirror. This focusing optic forms an image of the ICP on the entrance aperture of a wavelength selection device such as a monochromator. The wavelength exiting the monochromator is converted to an electrical signal by a photodetector. The signal is amplified and processed by the detector electronics, then displayed and stored on a computer [13].

The analyses were performed with a Varian Vista-Pro ICP-OES. For that purpose, MgH<sub>2</sub>-TiH<sub>2</sub> samples (~20 mg) were solubilized with acids (3 mL HCl 37%+ 2 mL HNO<sub>3</sub> 65% for samples containing Ti, whereas 2 ml HNO<sub>3</sub> was used for samples without Ti) and pure water.

### 2.3.4 Electron Probe Micro-Analysis (EPMA)

The electron microprobe, also known as the electron probe micro-analyzer (EPMA), uses X-ray spectrometry to both identify and measure concentration of elements in microscopic volumes of the specimen. This technique was used to determine the phase composition of induction-melted La(Ni, Sn)<sub>5</sub>-type alloys used in the automatic cycling device. With EPMA, a finely focused electron beam interacts with the sample to generate back-scattered electrons, secondary electrons, characteristic X-rays and light known as cathodoluminescence. By scanning the electron beam over a surface of the sample, these signals can be used to obtain high resolution scanning electron images, X-ray maps showing spatial distribution of elements, and cathodoluminescence

images for phase (element and compound) identification, estimation of phase distribution and proportions, trace element compositional variation and surface textural analysis of multi-phase composites. Characteristic X-rays generated from a microscopic volume in spot mode (i.e., beam not scanning) are utilized to obtain a complete quantitative chemical analysis. Sample preparation is minimal, but a well-polished surface is required for accurate quantitative analysis. The EPMA is mostly used for studying inorganic materials [14].

This is a non-destructive *in situ* analysis technique that detects all elements from beryllium in a cubic micron volume with a sensitivity of about 100 ppm. For this purpose, it relies on the measurement of the characteristic X-ray intensity emitted by a given element under excitation conditions.

The features of this device are:

- Model: SX 100 CAMEC
- Wavelength Dispersive Spectroscopy (WDS) analyzer;
- 3 vertical spectrometers with LPC1, LPC2, LPC3, Lalit, LPET and TAP crystals;
- 1 inclined spectrometer with LiF, PET, TAP, PC2 crystals;
- 1 EDS SDD spectrometer for EDS-WDS coupled analysis.

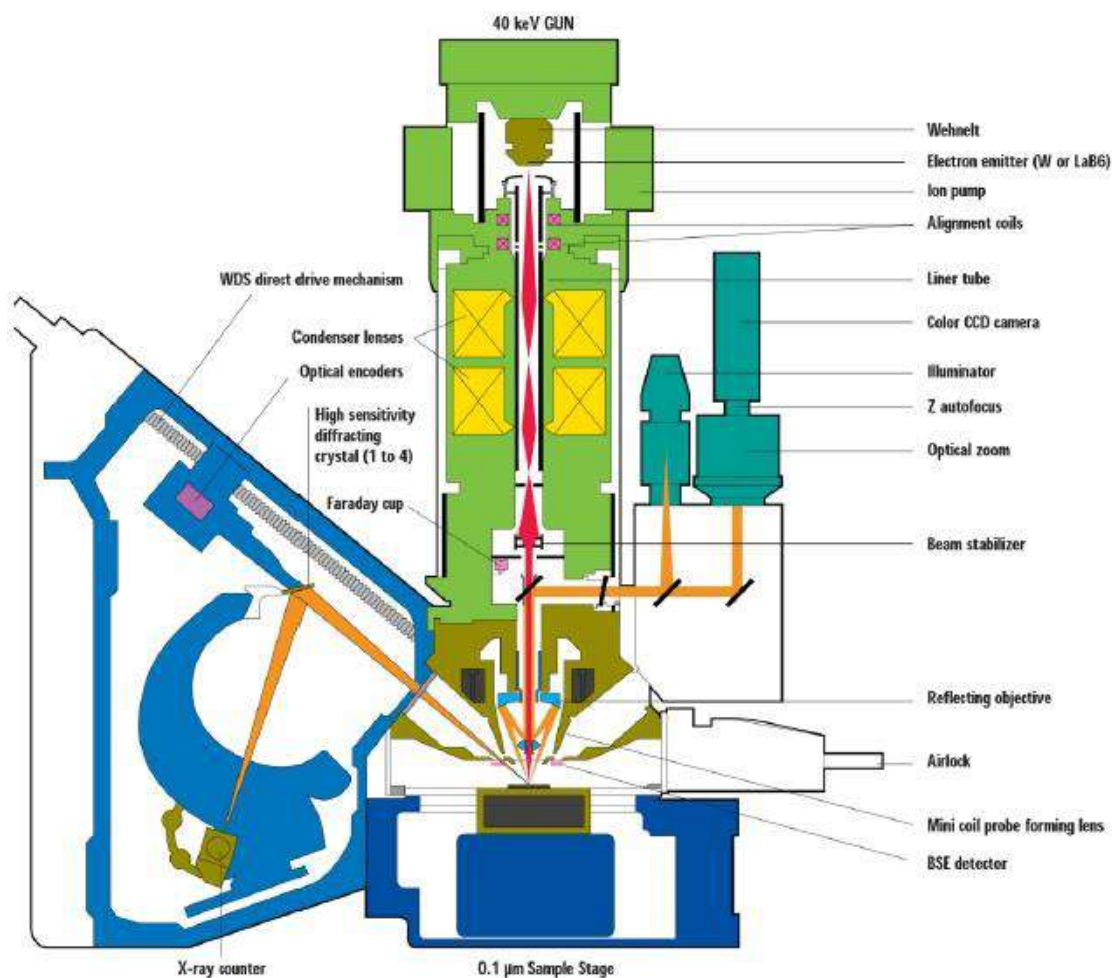


**Figure 1.1.** Technical drawing of the Cameca SX-100 EPMA instrument

## 2.4 Characterization of hydrogenation properties

### 2.4.1 The Sieverts' method

The Sieverts' method [15] is a volumetric measurement technique that was commonly used to measure the sorption of gaseous hydrogen into materials [16]. In the literature, the detailed description of this measurement method can be found [17]. The amount of hydrogen absorbed by a sample can be calculated using the real gas law:

$$PV = nZRT \quad [2.8]$$

where,  $P$  is the pressure,  $V$  is the volume,  $n$  is the value of moles,  $Z$  is the gas compressibility,  $R$  is the universal gas constant, and  $T$  is the temperature.

H-sorption measurements were made in a home-built Sieverts apparatus operated manually. This device is thermalized in water at 25 °C. It is equipped with two reservoirs of different volume each, a supplier hydrogen valve, one release valve to the atmosphere, a primary vacuum pump (1 Pa) and a connection to the sample holder which is heated to the operation temperature by an electric tubular oven.

#### 2.4.1.1 Pressure-Composition-Isothermal (PCI), kinetic and cyclic measurements

As is has been explained in Section 1.3.1, PCI measurements are used to characterize the thermodynamics of hydrogen sorption/desorption in a solid. Experiments are performed at isothermal conditions while measuring the amount of hydrogen absorbed/desorbed (Eq. 2.8) at an equilibrium hydrogen pressure. PCI measurements on absorption-desorption were carried out for all  $\text{MgH}_2\text{-TMH}_x$  systems ( $TM = \text{Ti, Zr, Sc, Y, V, and Nb}$ ) with the target of determining their thermodynamics.

Isothermal sorption kinetic measurements were performed at 300 °C in the same system at quasi-constant pressure using large reservoirs. Applied absorption and desorption pressures were set to  $P_{\text{abs}} = 0.8$  and  $P_{\text{des}} = 0.03$  to provide similar driving forces for absorption and desorption. At 300°C, the equilibrium plateau pressure of  $\text{MgH}_2/\text{Mg}$  system is 0.16 MPa. Therefore, driving forces were fixed to  $\ln(P_{\text{abs}}/P_p) = \ln(P_p/P_{\text{des}}) \approx 1.6$ .

Hydrogen cycling experiments were performed manually for all  $\text{MgH}_2\text{-TMH}_x$  systems for 20 cycles. Same conditions as for kinetic measurements were applied. In all cases, sorption time both on absorption and desorption sweeps was constrained to 15 min.

#### 2.4.1.2 Temperature-Programmed Desorption (TPD)

TPD technique is a characterization method for the determination of the kinetic parameters in desorption processes or hydride decomposition reaction [18]. A hydrogenated sample is placed in a closed system and heated up with a temperature program  $\beta(t) = dT/dt$  (with the temperature  $T$  usually being a linear function of the time  $t$ ) at low partial pressure of hydrogen. The amount of hydrogen desorbed from the sample as a function of the temperature is measured by the Sieverts' method. Hydrogen

gas desorption experiments were performed at initial  $P_{\text{des}} = 0.03$  MPa, by heating from RT to 300°C at a heating rate of 2°C/min.

#### 2.4.1.3 Temperature-programmed absorption (TPA)

The TPA technique is similar to the TPA but with the aim of determining kinetic parameters of the absorption processes. A hydrogen-free sample is placed in a closed system and heated up under a high partial pressure of hydrogen. The amount of hydrogen absorbed by the sample as a function of the temperature is measured by the Sieverts Method. Hydrogen gas absorption experiments were performed at  $P_{\text{abs}} = 0.8$  MPa by heating from RT to 300°C at a heating rate of 2°C/min.

#### References

- [1] Huot J, Ravnsbæk DB, Zhang J, Cuevas F, Latroche M, Jensen TR. Mechanochemical synthesis of hydrogen storage materials. *Prog Mater Sci* 2013; 58:30–75. doi:10.1016/j.pmatsci.2012.07.001.
- [2] Doppiu S, Schultz L, Gutfleisch O. In situ Pressure and Temperature Monitoring During the Conversion of Mg into MgH<sub>2</sub> by High-Pressure Reactive Ball Milling. *ChemInform* 2007;38. doi:10.1002/chin.200714019.
- [3] ASM Handbook, Volume 4A: Steel Heat Treating Fundamentals and Processes - ASM International.
- [4] Walker G. Solid-State Hydrogen Storage: Materials and Chemistry. Elsevier; 2008.
- [5] Rietveld HM. A profile refinement method for nuclear and magnetic structures. *J Appl Crystallogr* 1969; 2:65–71. doi:10.1107/S0021889869006558.
- [6] Loopstra BO, Rietveld HM. The structure of some alkaline-earth metal uranates. *Acta Crystallogr Sect B* 1969; 25:787–791. doi:10.1107/S0567740869002974.
- [7] Carvajal J. FULLPROF: A Program for Rietveld Refinement and Pattern Matching Analysis. *Physica B* 1993; 192:55–69.
- [8] H TB, B VDR. GSAS-II: the genesis of a modern open-source all-purpose crystallography software package. *J Appl Crystallogr*; 46:544–9. doi:10.1107/S0021889813003531.
- [9] TOPAS-R V. 4.0; Bruker AXS: Karlsruhe, Germany, 2006.
- [10] Ares JR, Cuevas F, Percheron-Guégan A. Mechanical milling and subsequent annealing effects on the microstructural and hydrogenation properties of multisubstituted LaNi<sub>5</sub> alloy. *Acta Mater* 2005; 53:2157–67. doi:10.1016/j.actamat.2005.01.030.
- [11] Hai X. Magnetocaloric materials for magnetic refrigeration at room temperature. Université Grenoble Alpes, 2016.

- [12] Rueden CT, Schindelin J, Hiner MC, DeZonia BE, Walter AE, Arena ET, et al. ImageJ2: ImageJ for the next generation of scientific image data. *BMC Bioinformatics* 2017; 18:529. doi:10.1186/s12859-017-1934-z.
- [13] Xiandeng H, S AR, T JB, L DG. Inductively Coupled Plasma Optical Emission Spectrometry. *Encycl. Anal. Chem.*, American Cancer Society; 2016, p. 1–25. doi:10.1002/9780470027318.a5110.pub3.
- [14] Chatterjee N. Electron Microprobe Facility. *Course Notes. MIT Camb* 2012:43.
- [15] Sieverts A. Absorption of Gases by Metals. *Z Für Met* 1929;21:37–46.
- [16] Blach TP, Gray EM. Sieverts apparatus and methodology for accurate determination of hydrogen uptake by light-atom hosts. *J Alloys Compd* 2007; 446–447:692–7. doi:10.1016/j.jallcom.2006.12.061.
- [17] Policicchio A, Maccallini E, Kalantzopoulos GN, Cataldi U, Abate S, Desiderio G, et al. Volumetric apparatus for hydrogen adsorption and diffusion measurements: Sources of systematic error and impact of their experimental resolutions. *Rev Sci Instrum* 2013; 84:103907. doi:10.1063/1.4824485.
- [18] Reilly JJ, Wiswall RH. Reaction of hydrogen with alloys of magnesium and copper. *Inorg Chem* 1967; 6:2220–3. doi:10.1021/ic50058a020.





---

# CHAPTER THREE

---

Effect of  $\text{TiH}_2$  additive on the hydrogen storage properties of magnesium  
hydride





### 3. Effect of TiH<sub>2</sub> additive on the hydrogen storage properties of magnesium hydride

In this chapter, the system  $(1-y)\text{MgH}_2+y\text{TiH}_2$  has been analyzed with the objective of having a better understanding of the role that TiH<sub>2</sub> addition plays during hydrogen sorption process of MgH<sub>2</sub>.  $(1-y)\text{MgH}_2+y\text{TiH}_2$  composites were synthesized by reactive ball milling. Their morphology and structural properties were determined by XRD and SEM in the as-milled state and after hydrogen cycling. Pressure Composition Isotherm (PCI) measurements were done to determine thermodynamics modifications in the Mg–H system by TiH<sub>2</sub> addition. Hydrogen cycling properties were determined using Sieverts' type apparatus for twenty absorption and desorption cycles. The evolution of the reversible storage capacity on cycling for a limited reaction time of 15 minutes has been measured with significant variations as a function of the additive quantity. Finally, hydrogenation kinetics were analyzed using available solid-state kinetic models and the rate-limiting step was determined both for absorption and desorption.

#### 3.1 Synthesis and chemical characterization of MgH<sub>2</sub>-TiH<sub>2</sub> nanocomposites

$(1-y)\text{MgH}_2+y\text{TiH}_2$  composites with Ti molar ratio  $y = 0, 0.0125, 0.025, 0.05, 0.1, 0.2,$  and  $0.3$  were synthesized by RBM under hydrogen atmosphere as described in chapter 2. For example, Figure 3.1 shows the evolution of hydrogen pressure and vial temperature during the synthesis of the composite with  $y = 0.3$ . The synthesis was performed in two cycles of 120 minutes milling and 120 minutes pause between them. At the beginning of milling, the vial temperature increases because of the collisions and frictions between the milling balls and the vial walls. This also leads to an increment of pressure due to gas confinement. Then, the pressure drops down due to the hydrogen absorption by both Mg and Ti metals leading to the formation of MgH<sub>2</sub> and TiH<sub>2</sub> phases[1], respectively. Once the hydride formation is completed, a pressure plateau is observed. At the end of the first milling cycle, both pressure and temperature decrease to equilibrium during the pause time. The second cycle does not entail any additional hydrogen absorption, being the change in pressure due to thermal variations induced by milling and rest. Thus, the second cycle can be used to calibrate the gas temperature that differs from the measured vial temperature [2]. This allows determining the hydrogen uptake ( $C_H$ ) corresponding to the pressure change observed during the first cycle. Hydrogen contents  $C_H$  for all synthesized composites are shown in Table 3.1. Experimental  $C_H$  values concur well with the nominal ones (according to the expected formation of MgH<sub>2</sub> and TiH<sub>2</sub> di-hydrides) with a maximum discrepancy of 9% for  $y = 0.2$ .

**Table 3.1.** Chemical composition of as-milled nanocomposites. H-content, C<sub>H</sub>, measured with Evicomagnetics device. Metal content determined by ICP-OES analysis for y=0 and 0.3 (the measured errors are less than 1%).

Composite	C <sub>H</sub> (wt. %)		Metal-content (at.%)		
	Nominal	Measured	Mg	Ti	Fe
y					
0	7.66	7.6	99.67	0	0.33
0.0125	7.57	7.6	-	-	-
0.025	7.48	7.6	-	-	-
0.05	7.32	6.8	-	-	-
0.1	7.02	6.7	-	-	-
0.2	6.49	5.9	-	-	-
0.3	6.03	5.9	70.19	29.15	0.66

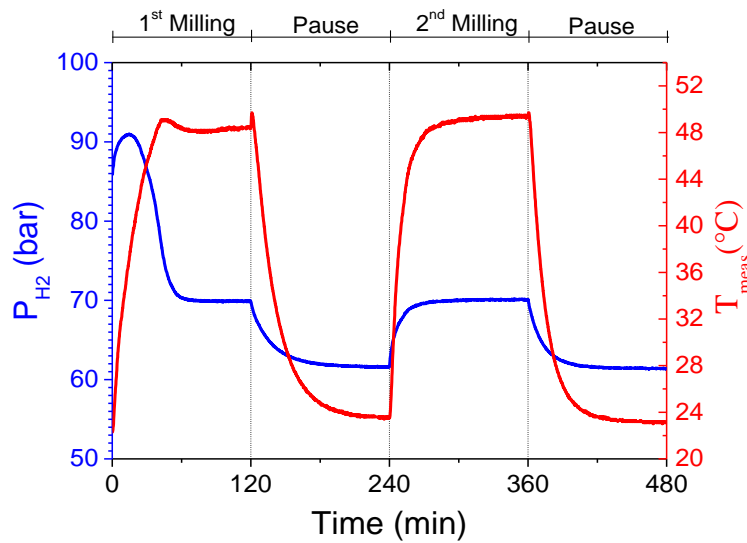


**Figure 3.1.** Evolution of the hydrogen pressure (blue line) and the vial temperature (red line) as a function of milling time during the synthesis of the composite 0.7MgH<sub>2</sub>+0.3TiH<sub>2</sub>

Hydrogen uptake curves collected during the synthesis of composites  $y = 0, 0.05$  and  $0.1$  are displayed in Figure 3.2. They were obtained from pressure and temperature data variations of the first milling cycle. For all samples, complete hydrogenation reaction takes less than 80 min. Hydrogenation starts within the first minutes of the milling process and is much faster for Ti-added composites ( $y = 0.05$  and  $0.1$ ) than for pure Mg ( $y=0$ ). The hydrogen uptake at  $t \leq 20$  min corresponds to the Ti dihydride formation.

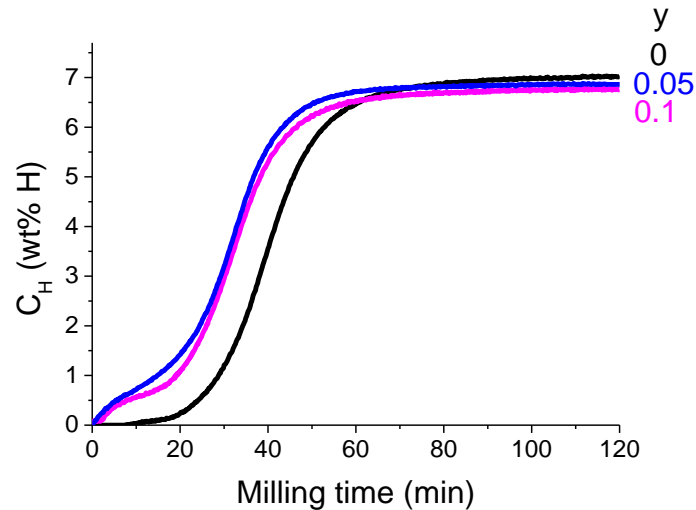


**Figure 3.2.** Hydrogen uptake curves during the first milling cycle of powder mixtures  $(1-y)\text{Mg} + y\text{Ti}$  with  $y = 0, 0.05$  and  $0.1$

The metal composition of as-milled composites was determined by ICP-OES for  $y=0$  and  $0.3$ . Results are gathered in Table 3.1. Minor Fe contamination ( $\leq 0.6$  at. %) from milling tools was detected. For  $y = 0.3$ , there is a good agreement between the nominal Ti-atomic ratio (30 at.%) and the experimental value (29.2 at.%).

### 3.2 Microstructural characterization

XRD patterns were collected for all as-milled composites to determine their crystallographic properties. Results are shown in Figure 3.3. All patterns exhibit broad diffraction peaks evidencing nanostructured materials. For  $y = 0$ , the pattern can be indexed with two phases: the rutile-type  $\beta\text{-MgH}_2$  (S.G.  $P42/mnm$ , C.P.  $a = 4.506(3)$   $c = 3.042(4)$ ) phase and high-pressure  $\gamma\text{-MgH}_2$  (S.G.  $Pbcn$ , C.P.  $a = 4.541(1)$ ,  $b = 5.444(1)$ ,  $c = 3.973(1)$ ) commonly found in ball milled MgH<sub>2</sub> [3]. For the other samples, three different phases are observed: the two previous MgH<sub>2</sub> polymorphs and  $\epsilon\text{-TiH}_2$  (S.G.  $I4/mmm$ , C.P.  $a = 3.171(2)$ ,  $c = 4.420(1)$ ). As expected, the intensity of the diffraction peaks belonging to the TiH<sub>2</sub> phase increases with the Ti-molar ratio  $y$ . No formation of ternary Mg-Ti-H phases is observed.

Rietveld analysis of XRD patterns is presented in Figure 3.4. Phase amounts and their average crystallite sizes are gathered in Table 3.3. The ratio between  $\gamma$  and  $\beta$  MgH<sub>2</sub> polymorphs remains stable ( $24 \pm 3$  wt.%) for all composites and the TiH<sub>2</sub>-content agrees well, though slightly in excess, as compared to nominal values. As concerns crystallite sizes, they are evaluated in the interval of 5-8 nm for both  $\beta\text{-MgH}_2$  and  $\gamma\text{-MgH}_2$  polymorphs, while they range from 8 to 13 nm for  $\epsilon\text{-TiH}_2$ . Note that the crystal size of both MgH<sub>2</sub> phases gradually decreases with TiH<sub>2</sub> content. Based on the formation of binary MgH<sub>2</sub> and TiH<sub>2</sub> phases as well as on their nanostructured state, the synthesized  $(1-y)\text{MgH}_2 + y\text{TiH}_2$  samples are hereafter named as nanocomposites (NCs).

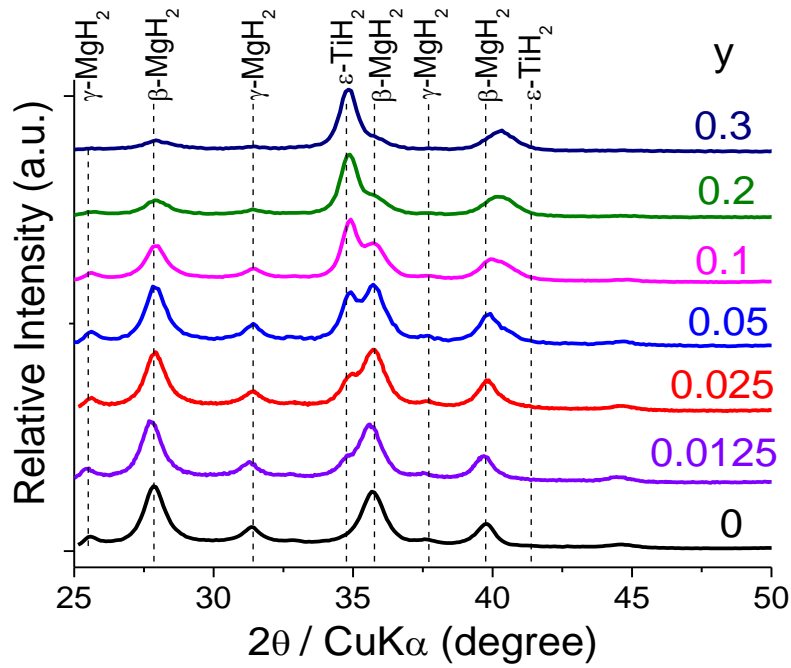


**Figure 3.3.** XRD patterns of nanocomposites (1-y)MgH<sub>2</sub>+yTiH<sub>2</sub> after RBM synthesis.

**Table 3.2.** Phase amounts, crystallite sizes and Rietveld agreement factors determined by XRD for the phases observed in as-milled NCs (1-y)MgH<sub>2</sub>+yTiH<sub>2</sub>.

NC (y)	Phase abundance (wt.%)				Crystal size(nm)			Rwp%
	γ-MgH <sub>2</sub>	γ/(γ+β)-MgH <sub>2</sub>	β-MgH <sub>2</sub>	ε-TiH <sub>2</sub> meas./nominal	γ-MgH <sub>2</sub>	β-MgH <sub>2</sub>	ε-TiH <sub>2</sub>	
0	22	22	78	-	8	8	-	11
0.0125	22	22	75	2/2	7	7	12	11
0.025	23	24	72	5/5	6	7	12	11
0.05	24	27	65	11/9	5	7	8	15
0.1	21	26	59	20/17	6	7	13	12
0.2	14	23	46	40/32	6	6	9	14
0.3	11	22	38	51/45	5	5	9	11

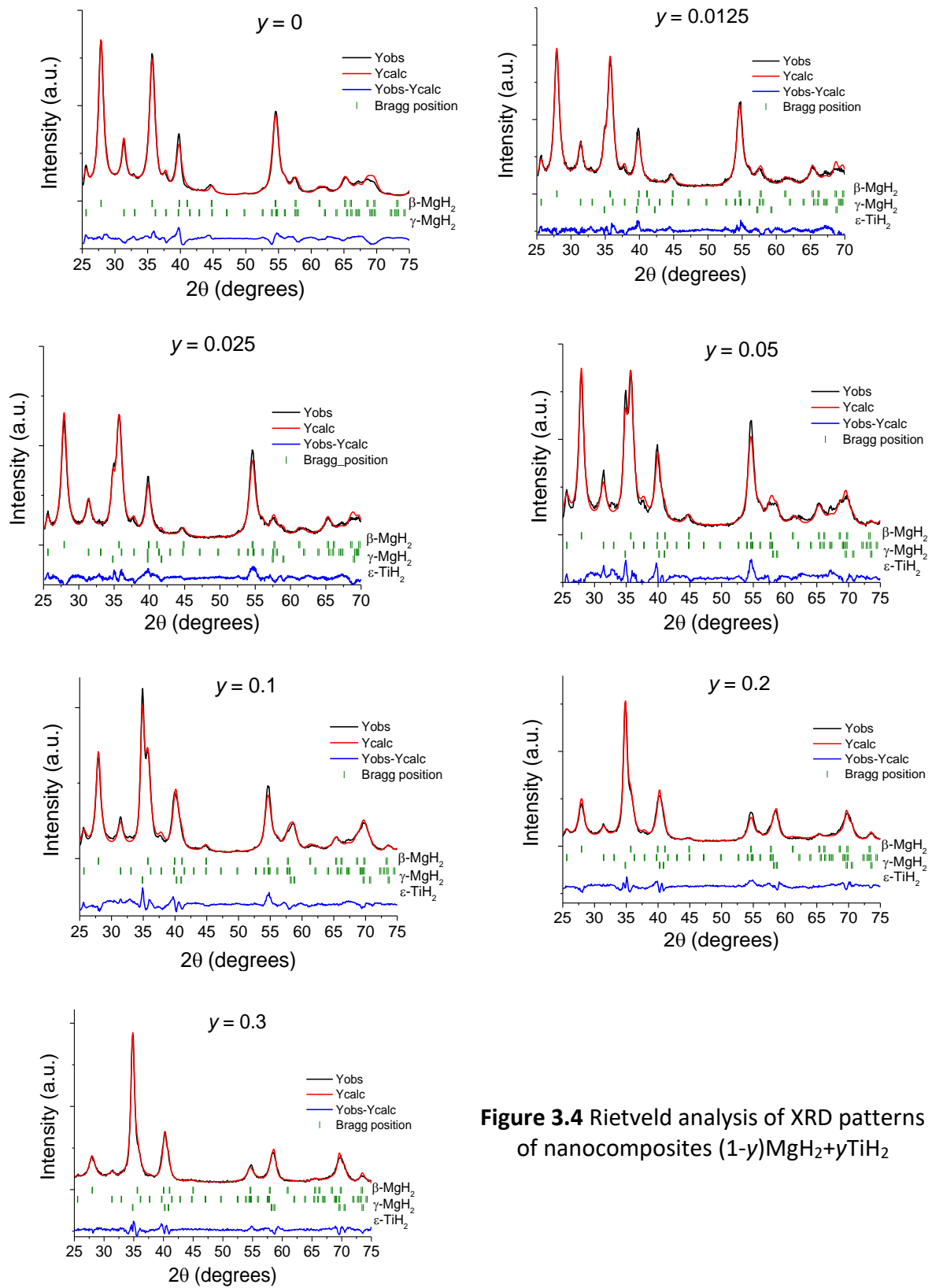


**Figure 3.4** Rietveld analysis of XRD patterns of nanocomposites  $(1-y)\text{MgH}_2 + y\text{TiH}_2$

SEM images of three different as-milled NCs ( $y=0$ , 0.0125 and 0.3) and their related particle size distribution are shown to the left and right of Figure 3.5, respectively. The particle size has been calculated by ImageJ software[4] and the particle size distribution has been fitted with a log-normal distribution (mean value and standard deviation values are inlets the graph). For pure Mg sample ( $y=0$ ), mean particles size is 1.2  $\mu\text{m}$  with a standard deviation of 1.9  $\mu\text{m}$ . For the NCs with  $y=0.0125$  and 0.3, the mean particle size is slightly higher (2.3  $\mu\text{m}$ ) with same standard deviation.

Figure 3.6 shows the morphology of as-milled NCs. The particles are agglomerates formed by tiny ( $\sim 100$  nm) primary particles. They have flake-like shape. For pure Mg ( $y = 0$ ), the agglomerates have a dense aspect and flat surface. For the Ti-containing NCs, the aspect is more porous, and the surface is rougher.

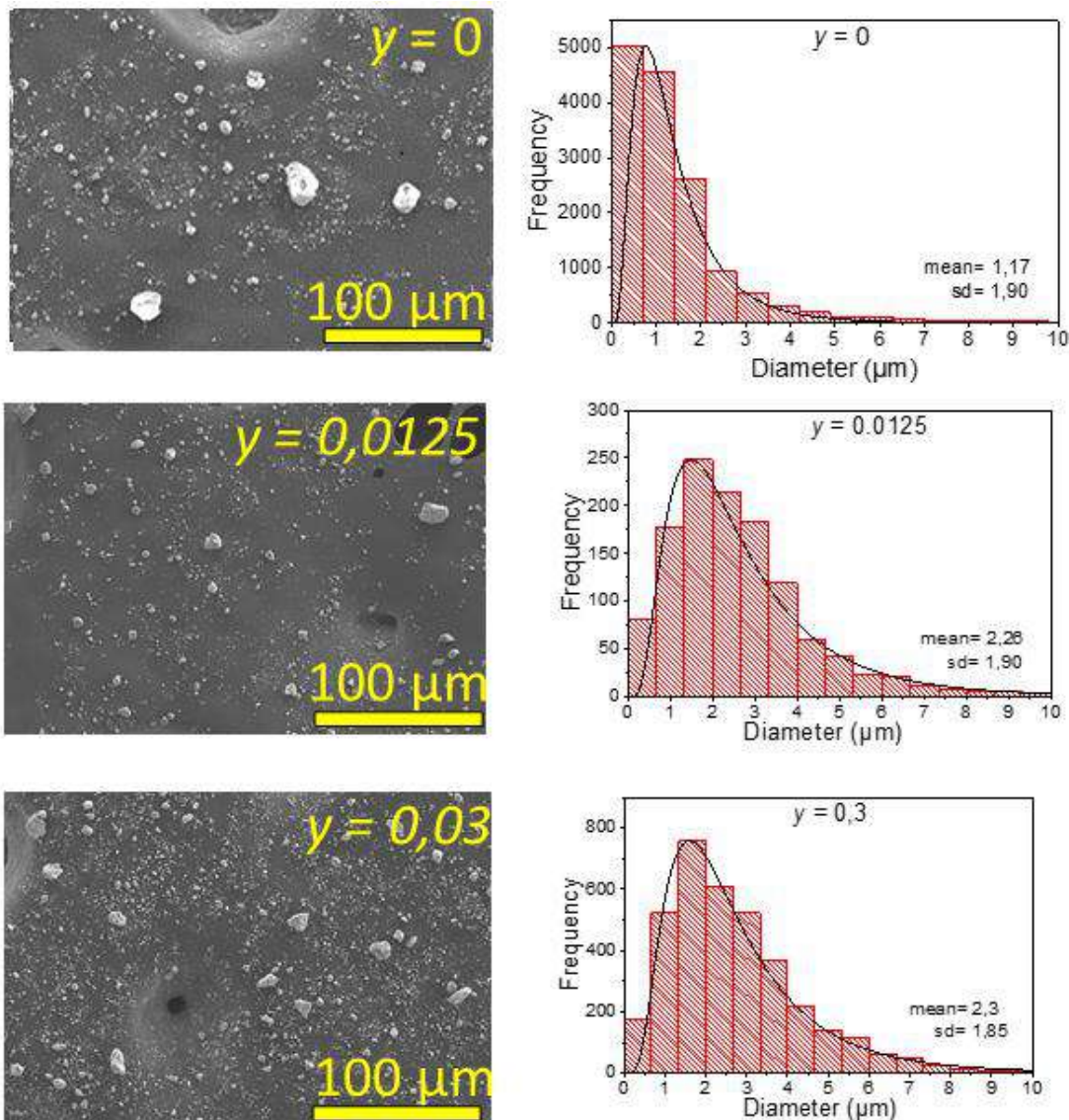


**Figure 3.5** Left) SEM images of as-milled powder samples. Right) particle size distribution (histograms) and best fit to a log-normal distribution (solid line) for  $y=0$ , 0.0125 and 0.3.

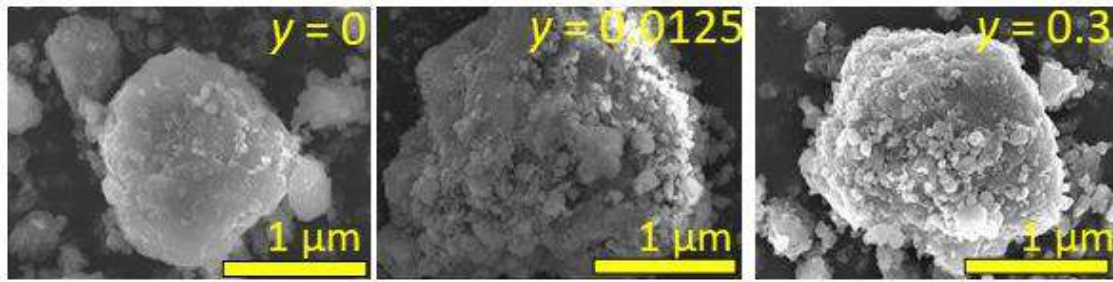


**Figure 3.6.** SEM images showing the particle morphology of as-milled samples for  $y=0$ , 0.0125 and 0.3.

### 3.3 Hydrogen sorption properties

All hydrogenation experiments were performed using a manometric manual Sieverts type apparatus described in Chapter 2. About 200 mg of each milled powder was loaded into a stainless-steel sample holder placed in a tubular electrical oven. The temperature of the oven was controlled by a PID system, using a type K thermocouple.

#### a) H-Thermodynamics

Pressure Composition Isotherm (PCI) measurements were carried out at 548, 573 and 598 K for the NC having the highest TiH<sub>2</sub> amount ( $y=0.3$ ) to ascertain possible changes of Mg-H thermodynamics by TiH<sub>2</sub> addition. The temperature of the sample was held constant ( $\pm 2$  K). Results are displayed in Figure 3.7. PCI isotherms are characterized by flat plateau pressures extending from 2 to 5.9 wt.%H and exhibiting low hysteresis. Both (de)hydrogenation enthalpy and entropy were determined from Van't Hoff plots depicted in the inset graph. The hydrogenation and dehydrogenation enthalpies are  $-73.6 \pm 0.9$  and  $75.5 \pm 0.6$  kJmolH<sub>2</sub><sup>-1</sup>, respectively; while the corresponding entropy values are  $-133 \pm 2$  and  $135 \pm 1$  JK<sup>-1</sup>molH<sub>2</sub><sup>-1</sup>.

These data are in agreement with the reported thermodynamic properties of magnesium hydride [5]. Therefore, TiH<sub>2</sub> additive does not modify the thermodynamic stability of magnesium toward hydrogen sorption. It should also be noted that 1.9 wt.% H remains trapped in the nanocomposite for pressures below 10<sup>-3</sup> MPa. This is attributed to hydrogen irreversibly stored in the TiH<sub>2</sub> phase under the studied thermodynamic conditions. Indeed, at 300 °C and  $P_{H_2} = 10^{-3}$  MPa, the equilibrium hydrogen content is as high as 1.95 H/Ti[6]. This implies that reversible hydrogen sorption in NCs nanocomposites (1- $y$ )MgH<sub>2</sub>+ $y$ TiH<sub>2</sub> at the used operation conditions is limited to the MgH<sub>2</sub>/Mg phase transformation.

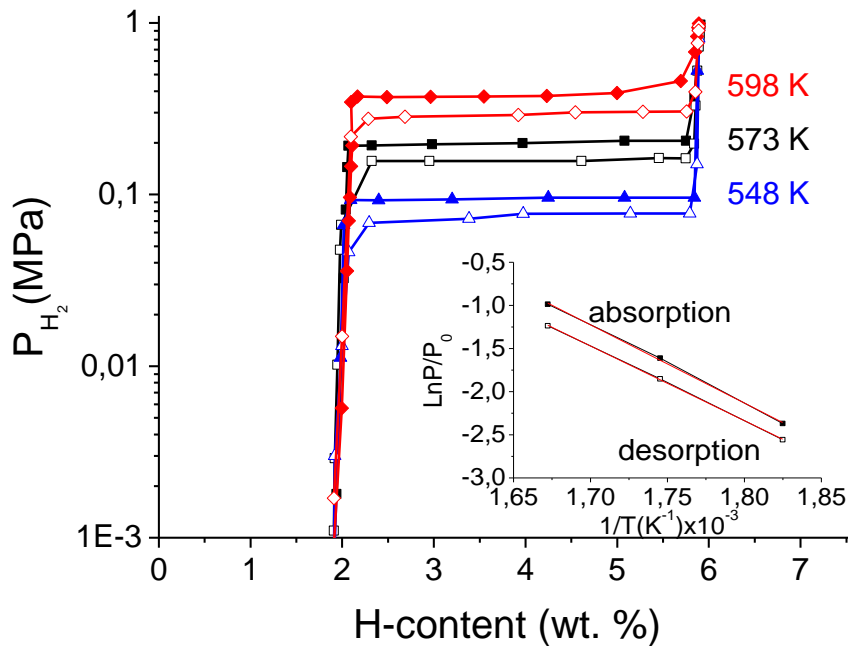


**Figure 3.7.** PCl absorption (full symbols) and desorption (empty symbols) curves for NC  $y=0.3$  at three different temperatures. Van't Hoff plots are given as inset.

### ***b) Temperature programmed desorption and absorption***

Temperature programmed desorption (TPD) characterization was carried out for as-synthesized pure MgH<sub>2</sub> and TiH<sub>2</sub>-containing NCs (Figure 3.8 a). The samples were heated up from room temperature to 350 °C at 2 °C/min in a closed volume. The desorption of pure MgH<sub>2</sub> sample starts at 250 °C while for Ti-containing NCs it starts at lower temperatures (< 200 °C). These results indicate that Ti-addition enhances the kinetics of hydrogen desorption as compared to pure MgH<sub>2</sub>. Moreover, in agreement with the previous thermodynamic results, hydrogen desorption does not cross the thermodynamic limit of the Mg-H system depicted in Fig. 3.8 a by a continuous red line.

Temperature programmed absorption (TPA) curves were monitored for the same samples as described before after TPD measurements (Figure 3.3, b). Experiments were carried out at a hydrogen pressure of 0.8 MPa with a heating rate of 2 °C/min. For the pure Mg sample, hydrogen absorption starts at 100 °C whereas a significant absorption rate occurs for all TiH<sub>2</sub>-containing NCs at room temperature. This result clearly evidences the enhancement of the hydrogen absorption properties of MgH<sub>2</sub> with TiH<sub>2</sub> addition.

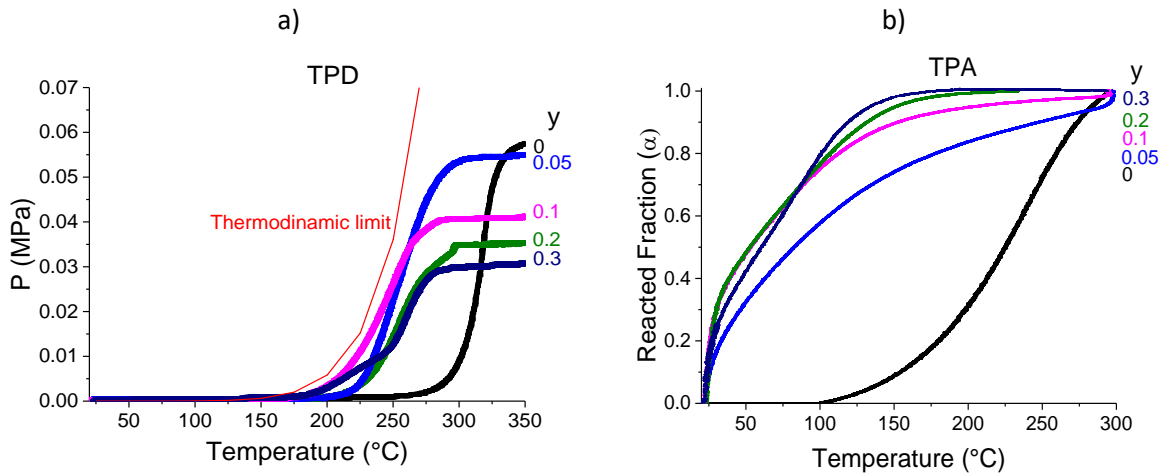


**Figure 3.8.** a) Temperature Programmed Desorption (TPD) and b) Temperature Programmed Absorption (TPA) for as-milled MgH<sub>2</sub> ( $y = 0$ ) and TiH<sub>2</sub>-containing NCs. In the TPD graph, the thermodynamic limit of the Mg-H system is depicted by a red line.

### c) Evolution of the reversible hydrogen capacity with cycling under constrained reaction time

To further characterize the sorption properties of the here studied nanocomposites, manometric cycling measurements over 20 cycles at a constant temperature have been performed in the same Sieverts' type apparatus. The operation temperature was fixed to 300 °C (573 K) as at this temperature the Mg-H system provides a significant plateau pressure ( $P_{p, H_2} = 0.16$  MPa) to feed a fuel cell system. In addition, H-cycling sorption experiments have been arbitrarily constrained to 15 min, a characteristic practical time for refilling hydrogen storage tanks [7]. These sorption measurements were performed at quasi-constant pressure by using large reservoirs compared to the sample holder volume. The same driving force,  $g$ , was used for absorption and desorption. This was accomplished by adjusting the applied hydrogen pressure in the system to both a higher value (for absorption) and lower (for desorption) than the plateau pressure so that  $g = \ln(P_{abs}/P_p) = \ln(P_p/P_{des}) \approx 1.6$ . For experiments at 300°C, absorption and desorption were set to  $P_{abs} = 0.8$  and  $P_{des} = 0.03$  MPa.

Figure 3.9 shows the evolution of the reversible capacity,  $C_{rev}$ , on cycling at 300 (Fig. 9a) and 340 °C (Fig. 9b) for representative NCs. The purpose was to determine the influence of sorption temperature on the cycling life. At 300 °C (Fig. 9a), the pure MgH<sub>2</sub> sample (*i.e.*  $y = 0$ ) exhibits in the first cycle very low reversible capacity,  $C_{rev} = 0.5$  wt.%, with a gradual decrease after 20 cycles:  $C_{rev} = 0.2$  wt.%. For TiH<sub>2</sub>-containing NCs,  $C_{rev}$  is much higher in the first cycle,  $C_{rev} > 4$  wt.%, and keeps rather stable on cycling, especially at high TiH<sub>2</sub> contents ( $y = 0.2$  and  $0.3$ ). After 20 cycles, the highest reversible H-capacity,  $C_{rev} = 4.9$  wt.%, is observed for the lowest TiH<sub>2</sub> amount ( $y = 0.025$ ). On increasing the temperature to 340 °C (Fig. 9b), the pure MgH<sub>2</sub> sample exhibits a slightly higher capacity,  $C_{rev} = 0.9$  wt.%, which decreases down to 0.5 wt.% after 20 cycles. Meanwhile, for Ti-containing NCs the initial capacity is very high at low TiH<sub>2</sub> amount:  $C_{rev} = 5.2$  and  $5.8$  wt.% for  $y = 0.05$  and  $0.1$ , respectively. However,  $C_{rev}$  gradually decreases on cycling. In contrast, the cycle-life of NCs with the highest TiH<sub>2</sub> amount ( $y = 0.2$  and  $0.3$ ) keeps stable on cycling. Therefore, excluding pure MgH<sub>2</sub>, the reversible

capacity increases on lowering the TiH<sub>2</sub> amount but the cycle-life deteriorates. This behavior exacerbates on increasing the sorption temperature.

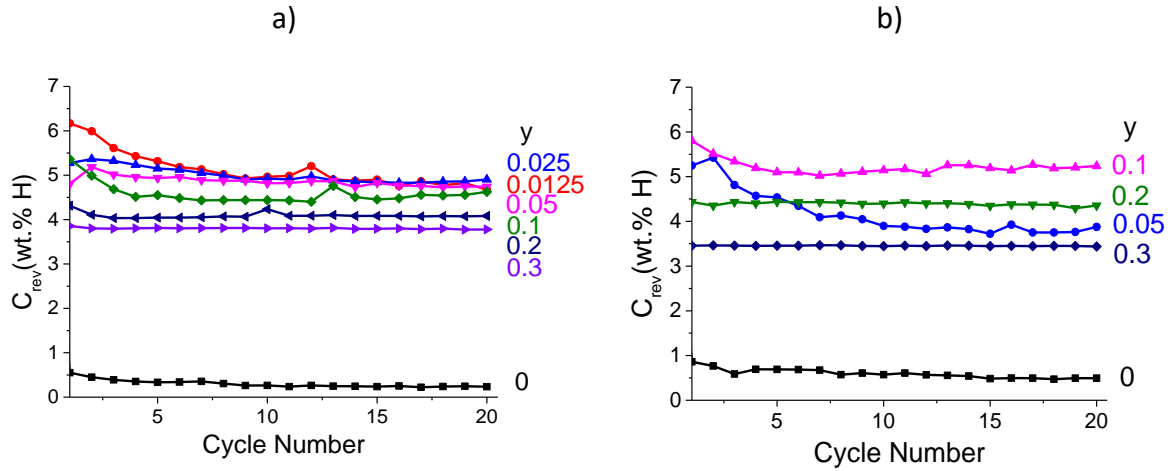


**Figure 3.9.** Reversible capacity on cycling of  $(1-y)\text{MgH}_2+y\text{TiH}_2$  NCs at a) 300 °C and b) 340 °C. Reaction time limited to 15 min.  $P_{abs} = 0.8$  and  $P_{des} = 0.03$  MPa.

#### d) Evolution of hydrogen kinetics on cycling

Figure 3.10 displays the hydrogen desorption curves during the 1<sup>st</sup> (Fig. 3.10a) and 20<sup>th</sup> cycle (Fig. 3.10b) for doped and undoped NCs. At the used desorption pressure,  $P_{des} = 0.03$  MPa, hydrogen desorption is exclusively attributed to the MgH<sub>2</sub> to Mg transformation. Full desorption (*i.e.* reacted fraction  $\alpha = 1$ ) is defined with respect to the hydrogen stored as MgH<sub>2</sub> within the nanocomposite. For the 1<sup>st</sup> desorption (Figure 3.10a), the slope of the desorption curves at short reaction time increases with the TiH<sub>2</sub> amount. This reveals that H-desorption kinetics strongly increases with TiH<sub>2</sub>-content. At the end of reaction time ( $t_{end} = 15$  min), the MgH<sub>2</sub> to Mg transformation is almost completed ( $\alpha \geq 0.85$ ) and reaction rates slow down for high TiH<sub>2</sub>-amount ( $y \geq 0.1$ ). In contrast, for low TiH<sub>2</sub>-amount ( $y \leq 0.05$ ) H-desorption rate is still significant at  $t_{end}$  and the reacted fraction is lower,  $\alpha = 0.7$ . The non-reacted fraction at  $t_{end}$ ,  $1 - \alpha = 0.3$ , is attributed to kinetically retained MgH<sub>2</sub>. Figure 3.10b shows the H-desorption curves at the 20<sup>th</sup> cycle. By comparison to the 1<sup>st</sup> cycle, the same beneficial effect of TiH<sub>2</sub> is observed on H-desorption kinetics. In addition, at a given TiH<sub>2</sub> content, H-desorption kinetics accelerate upon cycling leading. Thus, higher reacted fractions at  $t_{end}$  are observed for all NCs at cycle 20th as compared to the 2<sup>nd</sup> cycle.

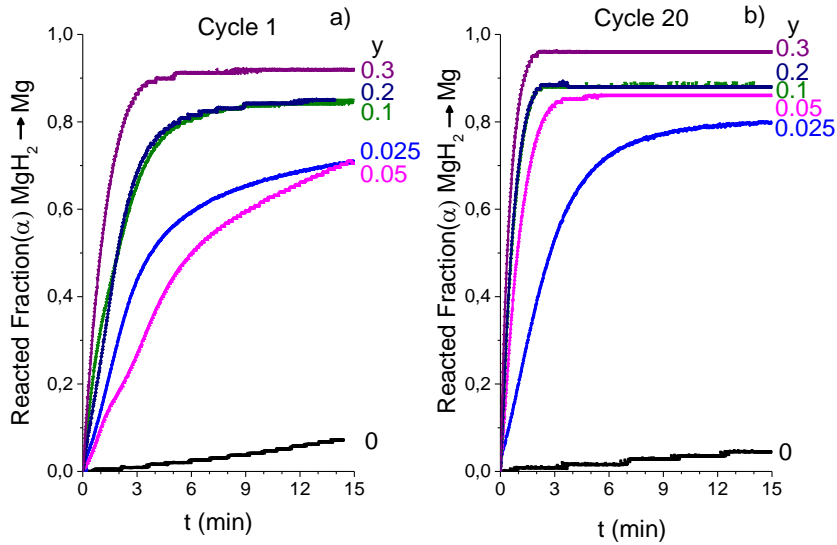


Figure 3.10. H-desorption curves at cycle one (a) and twenty (b) of  $(1-y)\text{MgH}_2+y\text{TiH}_2$  nanocomposites at 573 K for reaction time limited to  $t_{end} = 15$  min.  $P_{des} = 0.03$  MPa.

Figure 3.11 displays the H-absorption curves at the 2<sup>nd</sup> and 20<sup>th</sup> cycle. Note that 1<sup>st</sup> hydrogen absorption is assigned to the RBM sample synthesis. Absorption curves correspond to the reversible transformation of previously reformed Mg into MgH<sub>2</sub>. The full reacted fraction with  $\alpha = 1$  is defined as the quotient between the amount of hydrogen absorbed in the sweep compared to the total hydrogen stored as MgH<sub>2</sub> within the nanocomposite. Thus, values lower than 1 indicate that some Mg remains unreacted. Reaction rates for the 2<sup>nd</sup> cycle (Fig. 3.11a) are faster than for the 1<sup>st</sup> desorption (Fig. 3.10a) with most of the transformed fraction occurring at  $t \leq 3$  min. However, at longer reaction times, the absorption rate slows down, and  $\alpha$  approaches the values of the first desorption. H-absorption kinetics at short time does not change significantly on cycling: H-absorption curves are very similar at the 2<sup>nd</sup> and 20<sup>th</sup> cycle except for  $y = 0.1$  and  $0.2$ , which hardly saturate at  $t_{end} = 15$  min.

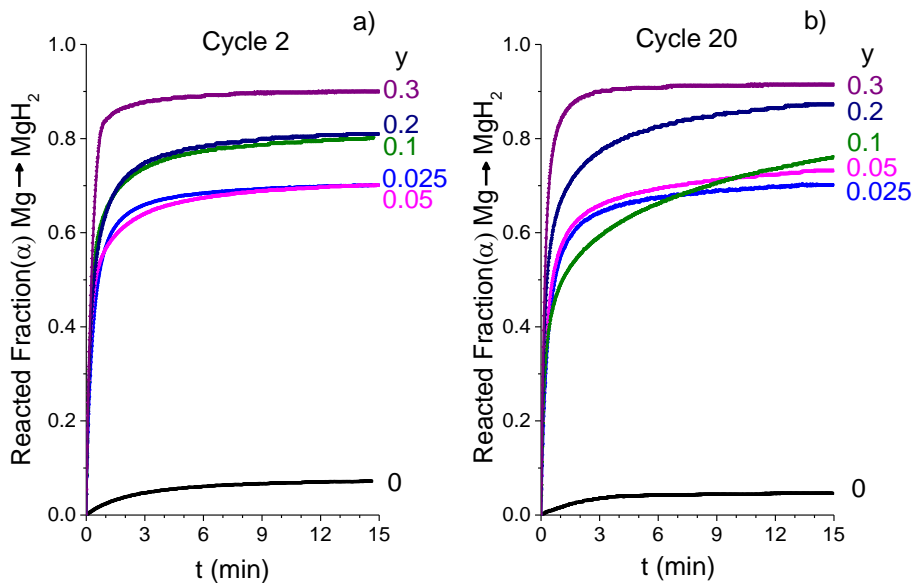


Figure 3.11. H-absorption curves at cycle two (a) and twenty (b) of  $(1-y)\text{MgH}_2+y\text{TiH}_2$  nanocomposites at 573 K for reaction time limited to  $t_{end} = 15$  min.  $P_{abs} = 0.8$  MPa.

### e) Evolution of hydrogen amount on cycling

Based on the previous thermodynamic and kinetic data, the hydrogen content in all NCs has been evaluated for each absorption and desorption sweep and results are displayed in Figure 3.12. The hydrogen content can be split into four contributions (from bottom to top in each graph): the hydrogen irreversibly stored in TiH<sub>2</sub>, the hydrogen retained as MgH<sub>2</sub> (*i.e.* not desorbed at  $t \leq t_{end}$ ), the hydrogen reversibly stored through the MgH<sub>2</sub>/Mg phase transformation,  $C_{rev}$ , and the unreacted Mg (*i.e.* not rehydrogenated at  $t \leq t_{end}$ ). Details for selected compositions are given in the following.

For pure MgH<sub>2</sub> sample ( $y = 0$ ), very little hydrogen is desorbed in the first cycle. Thus, in the desorption state, much of the material (~94 %) remains as MgH<sub>2</sub>. On the 2<sup>nd</sup> absorption, most formed Mg reverts to MgH<sub>2</sub> in the absorbed state, but the reversible capacity is extremely low:  $C_{rev} \approx 0.5$  wt. %. Then, only a little amount of hydrogen desorbs/absorbs and much of the sample remains as MgH<sub>2</sub> on cycling.

For NC  $y = 0.0125$ , *i.e.* with a little amount of TiH<sub>2</sub> addition (irreversible part), drastic changes are observed: the reversible capacity  $C_{rev}$  increases more than tenfold ( $\approx 6$  wt %) thanks to a large diminution of retained MgH<sub>2</sub>. However, a significant amount of unreacted Mg occurs. In addition, it should be noted that the amounts of both unreacted Mg and retained MgH<sub>2</sub> gradually increase through cycling and consequently  $C_{rev}$  decreases. After 20 cycles, the reversible capacity is 4.7 wt.%.

For NCs  $0.025 \leq y \leq 0.1$ , during desorption not only some hydrogen from MgH<sub>2</sub> has not been desorbed but also part of it is not absorbed to reform MgH<sub>2</sub> during cycling. Therefore, there is an increase in unreacted Mg and the amount of MgH<sub>2</sub> decreases with cycling. As a result, the  $C_{rev}$  is gradually decreasing only during the first cycles due to the increasing amount of unreacted Mg. It is important to mention that  $C_{rev}$  decreases also because the TiH<sub>2</sub> which is irreversible at this operation conditions.

For NCs with  $y \geq 0.2$ , the amount of both unreacted Mg and retained MgH<sub>2</sub> decreases drastically, showing that the Mg/MgH<sub>2</sub> phase transformation is practically complete. Furthermore, the reversible capacity  $C_{rev}$  keeps constant on cycling. One should note that the contribution of hydrogen stored as irreversible TiH<sub>2</sub> is high: 1.2 and 1.7 wt.% for  $y = 0.2$  and 0.3, respectively.

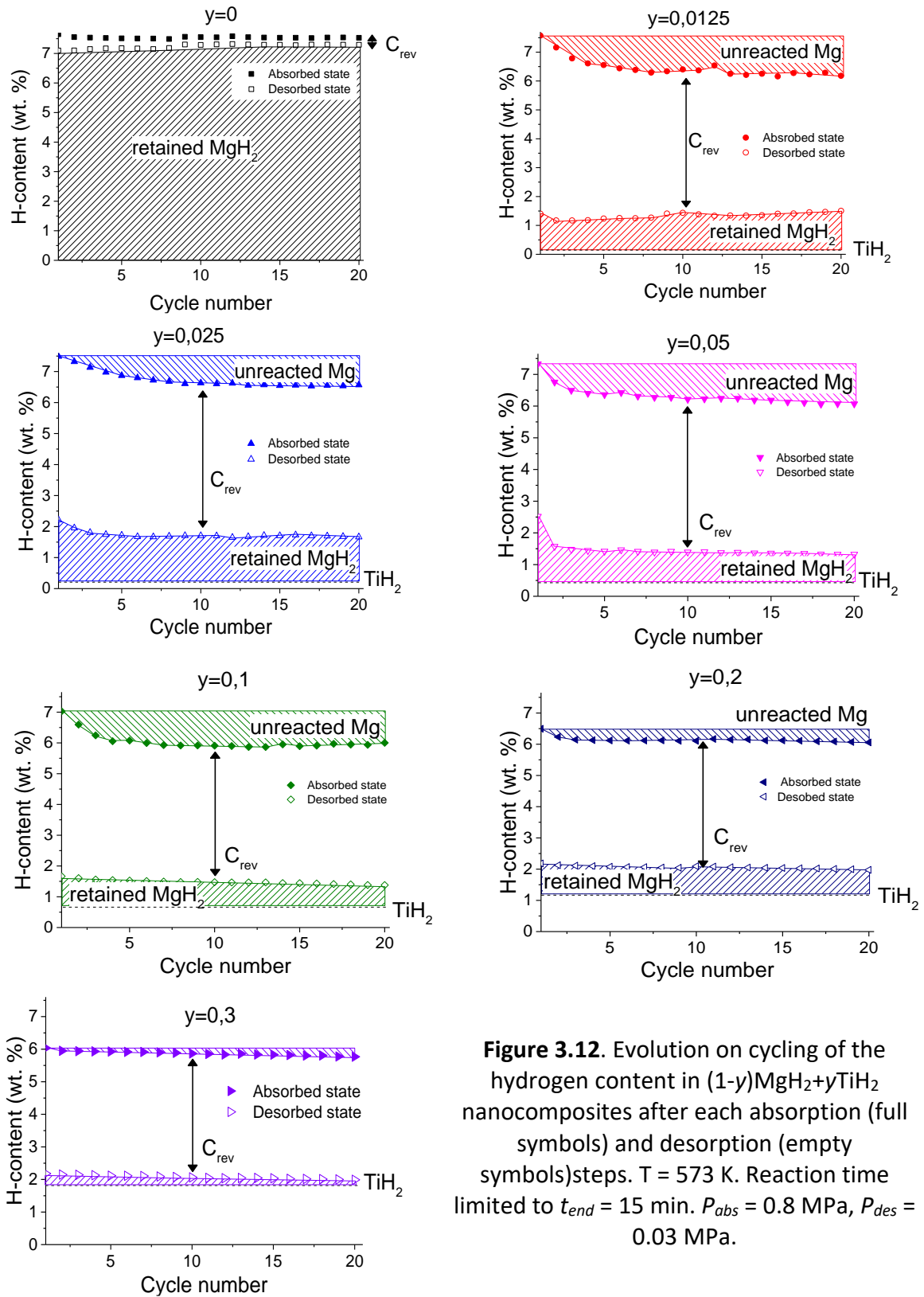


**Figure 3.12.** Evolution on cycling of the hydrogen content in  $(1-y)\text{MgH}_2 + y\text{TiH}_2$  nanocomposites after each absorption (full symbols) and desorption (empty symbols) steps.  $T = 573 \text{ K}$ . Reaction time limited to  $t_{\text{end}} = 15 \text{ min}$ .  $P_{\text{abs}} = 0.8 \text{ MPa}$ ,  $P_{\text{des}} = 0.03 \text{ MPa}$ .

### 3.4 Effect of hydrogen cycling on the microstructure of MgH<sub>2</sub>-TiH<sub>2</sub> nanocomposites

#### a) Crystallographic properties

XRD analysis was performed for all NCs after twenty sorption cycles in absorbed and desorbed states. XRD patterns are shown in Figure 3.13 and relevant crystallographic data from Rietveld analysis are gathered in Table 3.3. Diffraction patterns can be indexed in three phases:  $\beta$ -MgH<sub>2</sub>,  $\epsilon$ -TiH<sub>2</sub>, and Mg. The phase  $\gamma$ -MgH<sub>2</sub>, detected in as-synthesized samples, is fully transformed into  $\beta$ -MgH<sub>2</sub> after sorption experiments as a result of thermally induced strain relaxation [8]. As concerns  $\epsilon$ -TiH<sub>2</sub>, its amount and crystallinity both in absorbed and desorbed states do not change significantly as compared to as-synthesized NCs. In contrast, MgH<sub>2</sub> undergoes drastic changes in content and crystal size. Taking apart TiH<sub>2</sub>, MgH<sub>2</sub> is the main phase (>85 wt.%) in the absorbed state and the minor one (< 15 wt.%) in the desorbed state. Pure MgH<sub>2</sub> ( $y = 0$ ) is not considered as it exhibits extremely low reversibility on cycling staying almost fully hydrogenated in the desorption state. For Ti-containing samples, the MgH<sub>2</sub> amount variation between absorption and desorption reflects the reversibility of the MgH<sub>2</sub>/Mg transformation. The extent of this transformation is shown in Figure 3.14 as determined by XRD analysis as well as from reacted fractions in H-sorption experiments (Fig. 3.11b). A good agreement is found between XRD and kinetic data, which validates the hypothesis that incomplete Mg/MgH<sub>2</sub> transformation is due to kinetic effects. As evidenced in Figure 3.14, the reversibility of the MgH<sub>2</sub>/Mg transformation increases with Ti-amount.

It is also worth to comment on crystallite size changes of MgH<sub>2</sub> after H-sorption experiments (Table 3.3). Indeed, significant grain coarsening occurs after 20 cycles. For  $\beta$ -MgH<sub>2</sub>, the crystallite size enlarges from  $6 \pm 2$  to  $45 \pm 15$  nm between the as-milled and cycled samples. Such enlargement is mainly attributed to thermally driven effects (holding temperature at 300 °C) and not to cycling between Mg and MgH<sub>2</sub> phases. Indeed, pure MgH<sub>2</sub> sample, which does not desorb hydrogen significantly, undergoes similar grain growth. Also, from this table, it can be noted that, as the amount of TiH<sub>2</sub> is increasing, the crystal size of both  $\beta$ -MgH<sub>2</sub> and Mg after cycling is decreasing. It is reported that the presence of the TiH<sub>2</sub> phase minimizes grain coarsening of both  $\beta$ -MgH<sub>2</sub> and Mg phases [1].

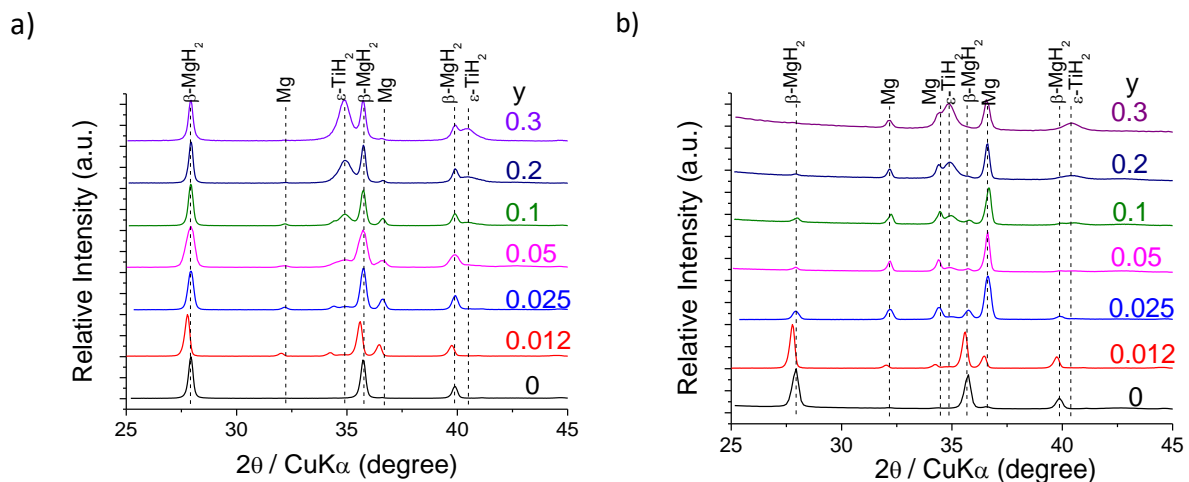


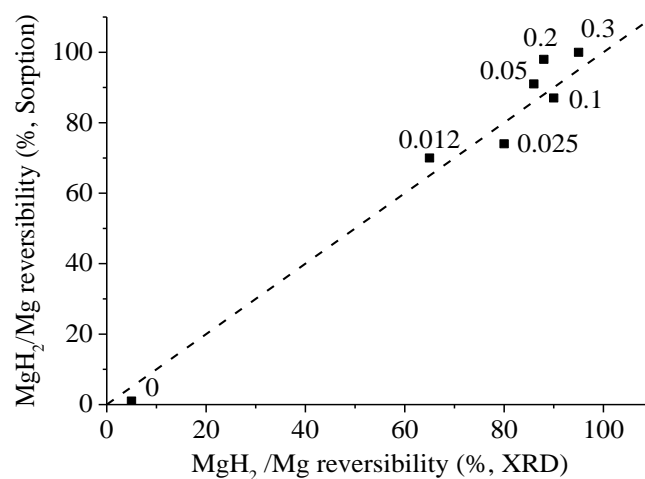
**Figure 3.13.** XRD patterns of  $(1-y)\text{MgH}_2+y\text{TiH}_2$  nanocomposites after 20 H-sorption cycles: a) absorbed state, b) desorbed state.

**Table 3.3.** Phase amount, crystal size and weight-profile Rietveld agreement factor of (1-y)MgH<sub>2</sub>+yTiH<sub>2</sub> nanocomposites after 20 H-sorption cycles at the absorbed and desorbed states.

Absorbed state							
Sample	Phase amount (wt. %)			Crystal size(nm)			Rwp%
	$\beta$ -MgH <sub>2</sub>	$\epsilon$ -TiH <sub>2</sub>	Mg	$\beta$ -MgH <sub>2</sub>	$\epsilon$ -TiH <sub>2</sub>	Mg	
y=0	100	-	-	42	-	-	15
y=0.012	83	3	14	77	6	-	15
y=0.025	83	4	13	58	12	-	15
y=0.05	83	10	7	31	8	-	13
y=0.1	71	20	9	65	13	-	10
y=0.2	59	40	1	46	9	-	14
y=0.3	49	51	1	47	9	-	10

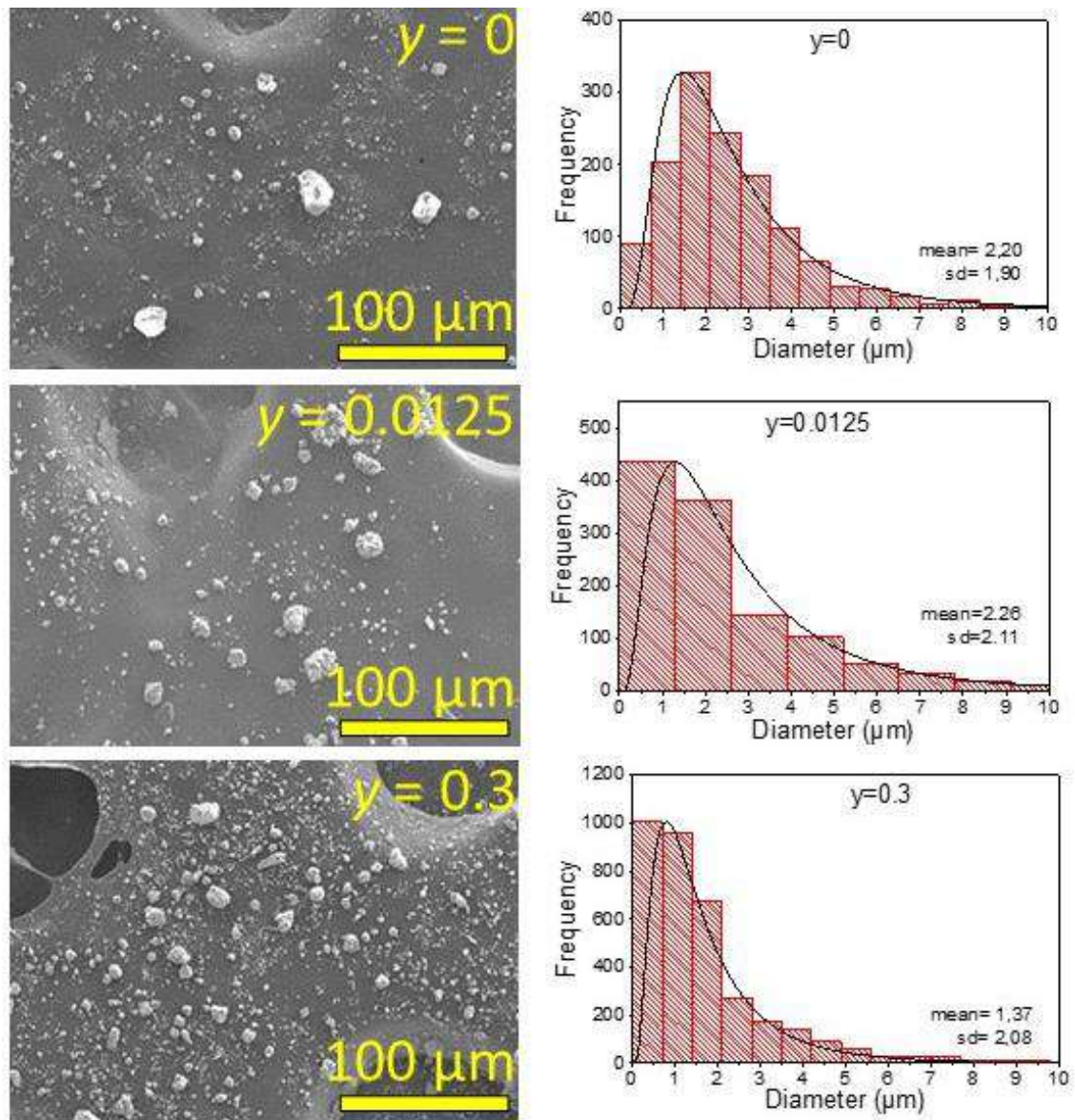
  

Desorbed State							
Sample	Phase amount (wt. %)			Crystal size(nm)			Rwp%
	$\beta$ -MgH <sub>2</sub>	$\epsilon$ -TiH <sub>2</sub>	Mg	$\beta$ -MgH <sub>2</sub>	$\epsilon$ -TiH <sub>2</sub>	Mg	
y=0	99	-	1	30	-	-	13
y=0.012	23	2	75	-	12	105	16
y=0.025	14	6	80	-	12	105	19
y=0.05	9	14	77	-	8	87	14
y=0.1	13	23	64	-	13	69	12
y=0.2	3	45	53	-	11	94	12
y=0.3	0.5	56	44	-	9	67	13


**Figure 3.14.** Reversibility of the MgH<sub>2</sub>/Mg phase transformation for (1-y)MgH<sub>2</sub>+yTiH<sub>2</sub> nanocomposites determined from H-sorption curves and XRD measurements. The dashed line stands for full agreement between H-sorption and XRD data. Data labels stand for y amount.

### b) Particle size and morphological properties

Morphological studies after cycling were carried out by SEM for three representative NCs ( $y = 0, 0.0125$  and  $0.3$ ) in both absorbed and desorbed state. SEM images and particle size distribution histograms are shown in Figure 3.15 and 3.16 for desorbed and absorbed states, respectively. For all NCs, particle size distributions obey log-normal distribution: mean and standard variations are shown in histograms insets and gathered in Table 3.4. The size of agglomerates is similar to absorption and desorption as well as compared to the as-milled state and has no significant dependence with  $\text{TiH}_2$  content. Indeed, the particle size is comprised between  $1.2$  and  $2.9 \mu\text{m}$  with a standard deviation of  $2 \mu\text{m}$



**Figure 3.15** SEM images showing the particle size distribution in  $(1-y)\text{MgH}_2+y\text{TiH}_2$  NCs after 20 cycles at the desorbed state

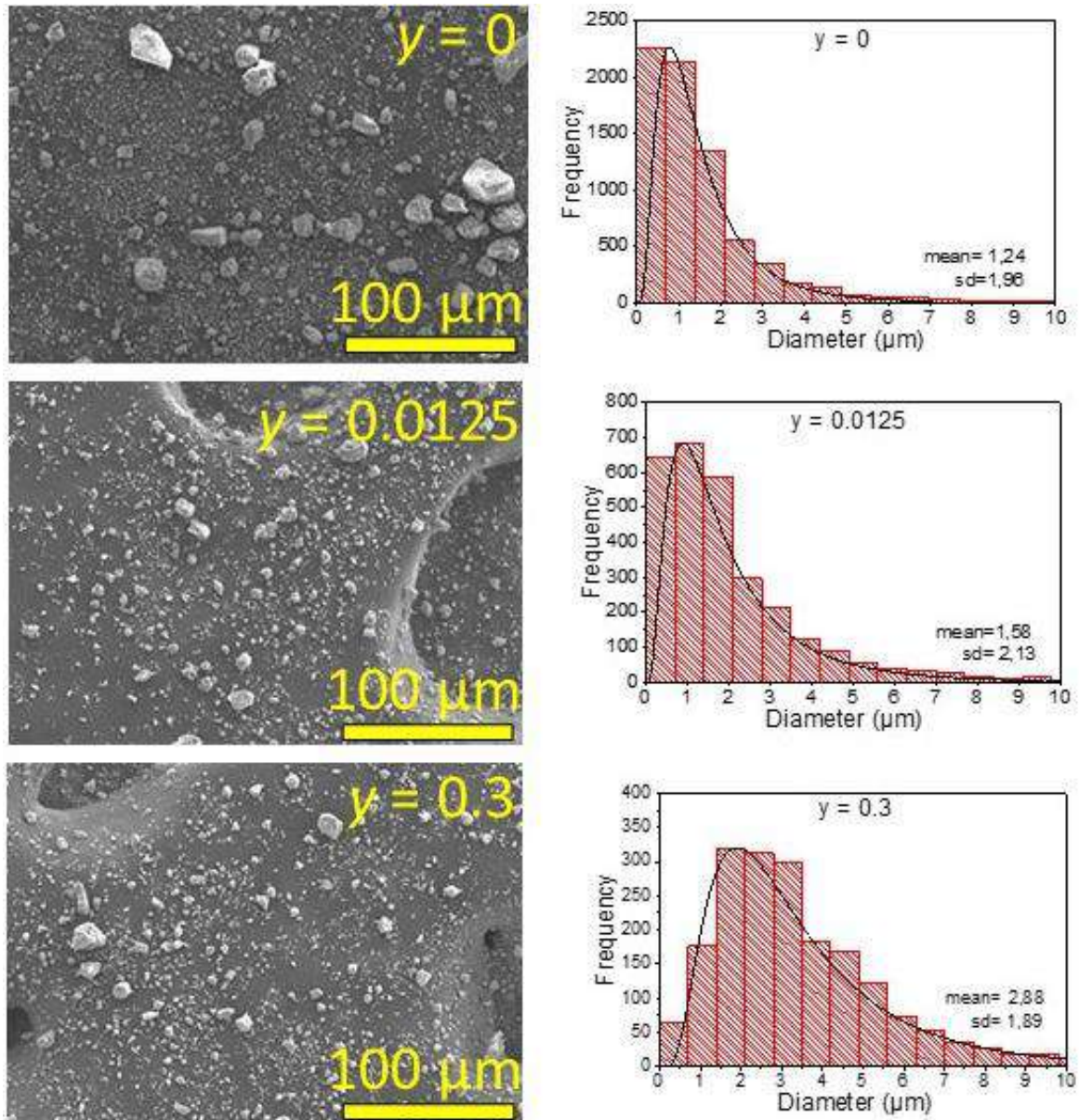


**Figure 3.16** SEM images showing the particle size distribution in  $(1-y)\text{MgH}_2+y\text{TiH}_2$  NCs after 20 cycles at the absorbed state

**Table 3.4.** Mean particle size ( $P_s$ ), of  $(1-y)\text{MgH}_2+y\text{TiH}_2$  NCs after 20 H-sorption cycles at the absorbed, desorbed and as-milled states.

NC ( $y$ )	$P_s$ ( $\mu\text{m}$ ) as-milled	$P_s$ ( $\mu\text{m}$ ) desorption	$P_s$ ( $\mu\text{m}$ ) absorption
0	1.2	2.2	1.2
0.0125	2.3	2.3	1.6
0.3	2.3	1.4	2.9

Figure 3.17 shows the morphology of the NCs after cycling in both absorbed and desorbed states. For  $y = 0$ , the agglomerates are formed by primary tiny slate-like particles both in the absorbed and desorbed states, which differs with the as-milled one, for which a flat surface was observed. For Ti-poor NC ( $y = 0.0125$ ), the agglomerate is dense in the absorbed state with tiny primary particles stick on it. The morphology resembles that of the as-milled one. In contrast, the morphology of the desorbed state shows the formation of protrusions [9]. For Ti-rich NC ( $y = 0.3$ ), both absorbed and desorbed states show the same

morphology. It is a dense agglomerate with cracks and small particles stick to it. The morphology resembles that of the as-milled sample but with cracking. This cracking could be attributed to the repeated volume change of the dense agglomerates upon repeated absorption and desorption cycles.

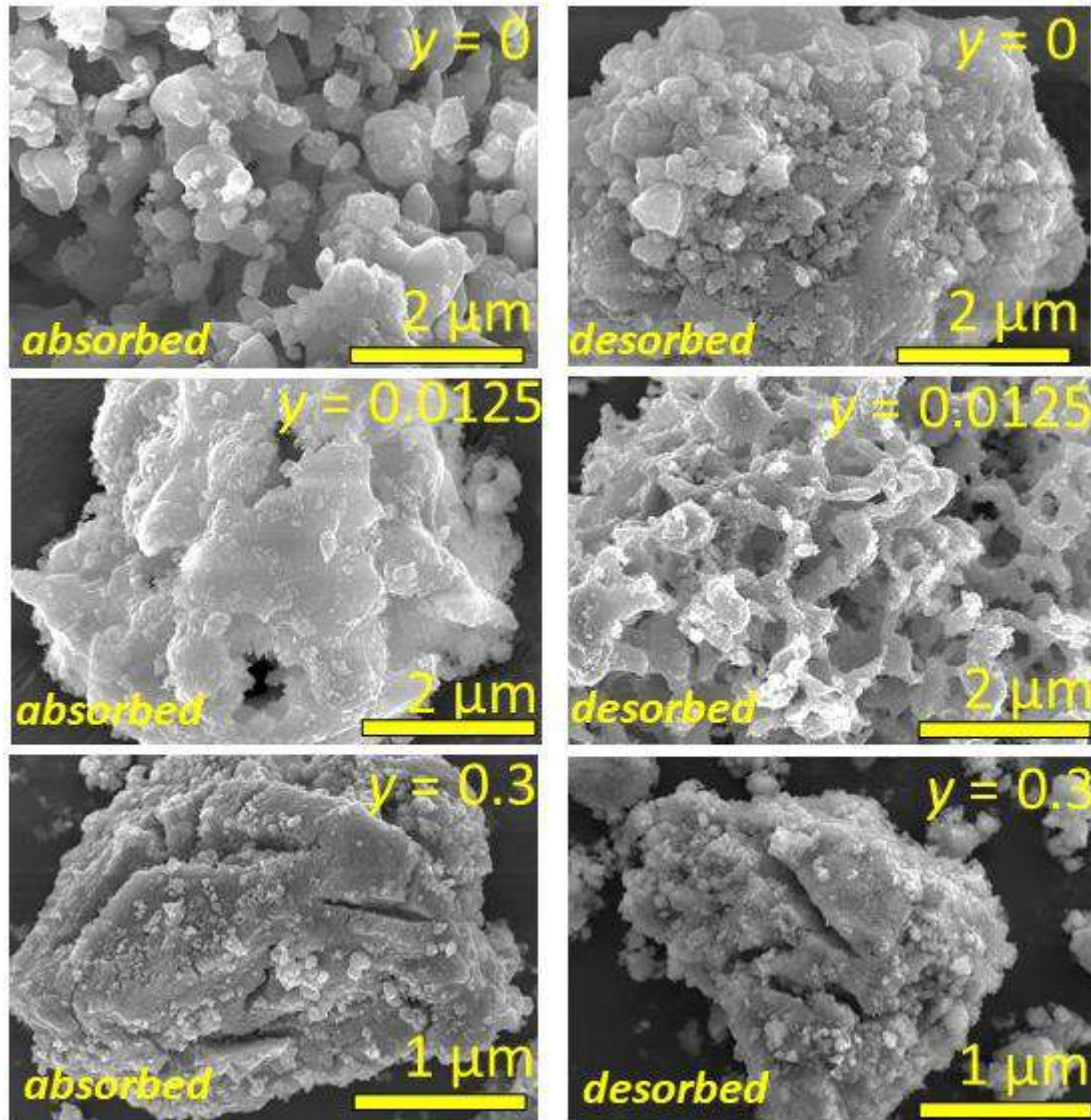


**Figure 3.17.** SEM images showing the morphology of  $(1-y)\text{MgH}_2+y\text{TiH}_2$  NCs after cycling in both absorbed and desorbed state

### c) Phase distribution

As shown in Figs. 3. 10 to 3.12, reaction kinetics and cyclability of  $(1-y)\text{MgH}_2+y\text{TiH}_2$  NCs improve when increasing the TiH<sub>2</sub> content. To obtain a better understanding on these results, the chemical composition in Ti-rich NC ( $y = 0.3$ ) has been analyzed by SEM-EDS at two different agglomerate locations: at the center and close to the edges. As-milled and cycled NC were analyzed for both absorbed and desorbed states. As an example, Figure 3.18 displays the SEM image and EDX analysis for an agglomerate. Results are summed up in Table 3.5.

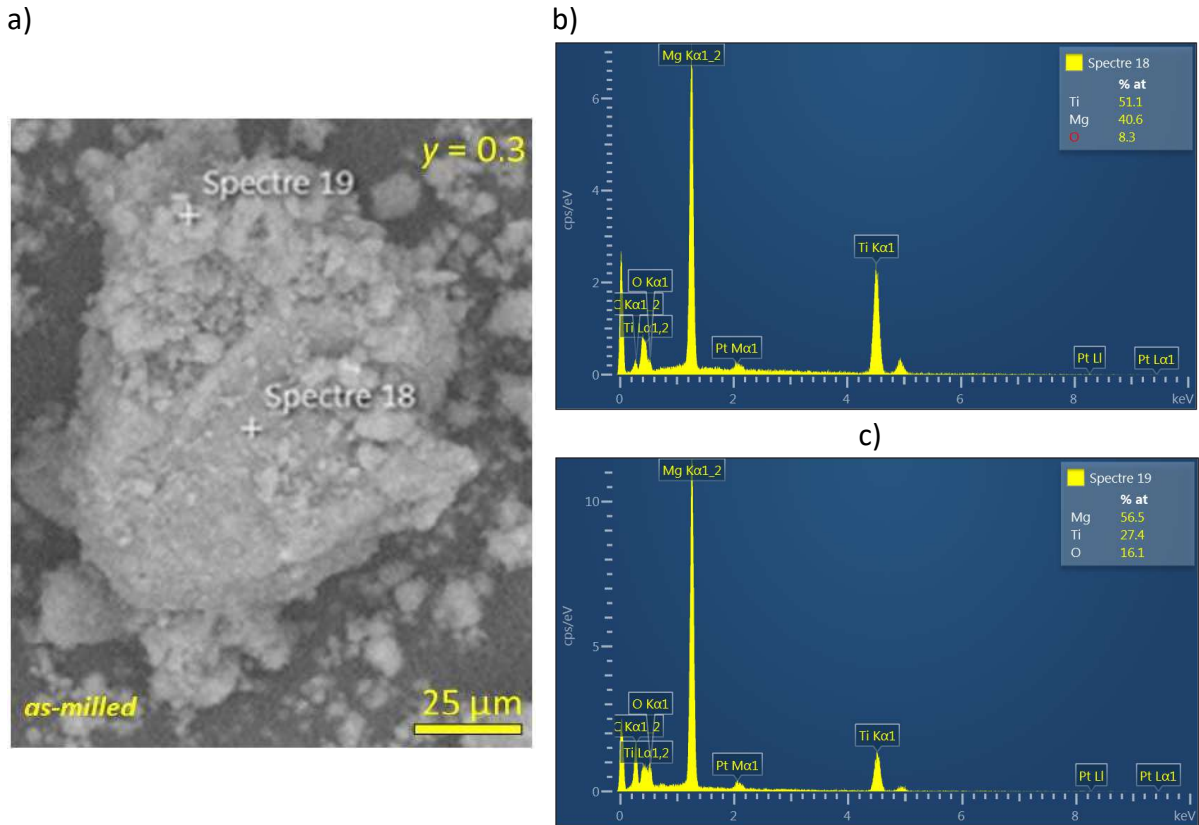


**Figure 3.18.** SEM-EDS analysis of as-milled  $(1-y)\text{MgH}_2+y\text{TiH}_2$  NC with  $y = 0.3$ , center (spectre 18) and edge (spectre 19)

**Table 3.5.** Ti and Mg content at the center and particle edge for as-milled and cycled (absorbed and desorbed) NC with  $y = 0.3$ .

Element	As-milled		Desorbed		Absorbed	
	Center	Edge	Center	Edge	Center	Edge
Ti (at.%)	22	25	13	25	10	27
Mg (at.%)	78	75	87	75	90	73

For the as-milled composite, Ti and Mg contents are similar at the center and edge of the agglomerate and close to the nominal value (30 at.% Ti). This reflects that there is a homogeneous dispersion of the MgH<sub>2</sub> and TiH<sub>2</sub> phases at the spatial resolution of EDX analysis ( $\sim 1 \mu\text{m}$ ). This agrees with microstructural data obtained by Transmission Electron Microscopy by Berti *et al.* on RMB MgH<sub>2</sub>-TiH<sub>2</sub> NCs [10]. These authors found that MgH<sub>2</sub> and TiH<sub>2</sub> phases are homogeneously distributed at the nanoscale.

For the cycled composite, similar atomic compositions are found at the agglomerate edges in both absorption and desorption states. They concur with the nominal value (30 at. % Ti). However, much lower Ti-contents are observed at the center of agglomerates. This reflects a partial migration of TiH<sub>2</sub> from the center to the edge during the cycling process.

### 3.5 Analysis of hydrogen sorption kinetics

As largely shown in this chapter, TiH<sub>2</sub> plays a major role in the reaction kinetics of hydrogen sorption in Mg. As shown in Fig. 3.10 and 3.11, isothermal sorption curves at 300 °C have been measured for different TiH<sub>2</sub> contents and at different cycling stages. Using these data, this section provides a kinetic analysis aiming to identify which kinetic model fits the best sorption curves to determine the controlling mechanism of the reaction.

A model is a theoretical, mathematical description of what occurs experimentally. In solid-state reactions, a model can describe a particular reaction type and translate that mathematically into a rate equation. Many models have been proposed in solid-state kinetics, and these models have been developed based on certain mechanistic assumptions. Other models are more empirically based, and their mathematics facilitates data analysis with little mechanistic meaning. Therefore, different rate expressions are produced from these models.

In homogeneous kinetics (e.g., gas or solution phases), kinetic studies are usually directed toward obtaining rate constants that can be used to describe the progress of a reaction. Additionally, the reaction mechanism is typically investigated and rate constant changes with temperature, pressure, or reactant/product concentrations are often helpful in uncovering mechanisms.

These mechanisms involve to varying degrees the detailed chemical steps by which a reactant is converted to product. However, in solid-state kinetics, mechanistic interpretations usually involve identifying a reasonable reaction model because information about individual reaction steps is often difficult to obtain[11].

In a typical hydrogenation experiment, the reacted fraction,  $\alpha$ , i.e. the amount of metal that becomes hydride in absorption or the amount of hydride that transforms to metal in desorption is recorded as a function of time,  $t$ , sample temperature,  $T$ , H<sub>2</sub> pressure,  $P_{H_2}$ , and for different sample shape. In most cases, the relationship between all the parameters takes the simple form:

$$F(\alpha) = k(P, T, r) * t \quad \text{Ec. 3.1}$$

where the function  $F$  depends of the controlling mechanism of the reaction. The parameter  $k$  determines the reaction rate which is dependent on  $P$ ,  $T$  and the sample geometry indicated by  $r$ . Also, in simple cases, it is possible to express  $k$  as a product of three functions:

$$k(P, T, r) = f(r) * g\left(\frac{P}{P_p}\right) * h(T) \quad \text{Ec. 3.2}$$

Where  $f(r)$  is related with the sample geometry,  $g\left(\frac{P}{P_{eq}}\right)$  is the driving force for the reaction meanwhile the function  $h(T)$  is given by:

$$h(T) = k_0 * \exp\left(-\frac{E_a}{R*T}\right) \quad \text{Ec. 3.3}$$

being  $k_0$  a pre-exponential factor,  $E_a$  the activation energy of the overall reaction and  $R$  the gas constant. Experimental data are analyzed according to the former expressions. The functional form of function  $F(\alpha)$  which best fits the data, together with the pressure, temperature and geometry dependence of the reaction rate are used to determine the rate-controlling step for the reaction[12]. Several reaction models  $F(\alpha)$  are listed in Table 3.16.

**Table 3.6.** Kinetic models examined in isothermal sorption curves [13–15]

Symbol	Model	Integral F( $\alpha$ ) form
<i>Diffusion models</i>		
D1	One-dimensional diffusion	$\alpha^2$
D2	Two-dimensional diffusion	$\alpha + (1 - \alpha)\ln(1 - \alpha)$
D3	Three-dimensional diffusion (Jander equation)	$\left[1 - (1 - \alpha)^{1/3}\right]^2$
D4	Three-dimensional diffusion (Ginstling-Braunshtein equation)	$\left(1 - \frac{2\alpha}{3}\right) - (1 - \alpha)^{2/3}$
<i>Geometrical contraction models</i>		
R2	Two-dimensional phase boundary	$1 - (1 - \alpha)^{1/2}$
R3	Three-dimensional phase boundary	$1 - (1 - \alpha)^{1/3}$
<i>Nucleation and growth models</i>		
F1	First-order reaction	$-\ln(1 - \alpha)$
A2	Avrami-Erofe'ev	$[-\ln(1 - \alpha)]^{1/2}$
A3	Avrami-Erofe'ev	$[-\ln(1 - \alpha)]^{1/3}$
A4	Avrami-Erofe'ev	$[-\ln(1 - \alpha)]^{1/4}$

Khawam and Flanagan[11] presented kinetic models and their classification based on the graphical shape of their isothermal curves ( $\alpha$  vs  $t$  or  $d\alpha/dt$  vs  $\alpha$ ) according to their mechanistic assumptions in Table 3.6. Based on their shape, kinetic models can be grouped into deceleratory, or sigmoidal models (Figure 3.19). Deceleratory reaction rates decrease with reaction progress (Figure 3.19 a-c), and sigmoidal models show a bell-shaped relationship between rate and  $\alpha$  (Figure 3.19 d). These methods for graphical presentation are easy means of visually determining the most appropriate model for a particular data set.

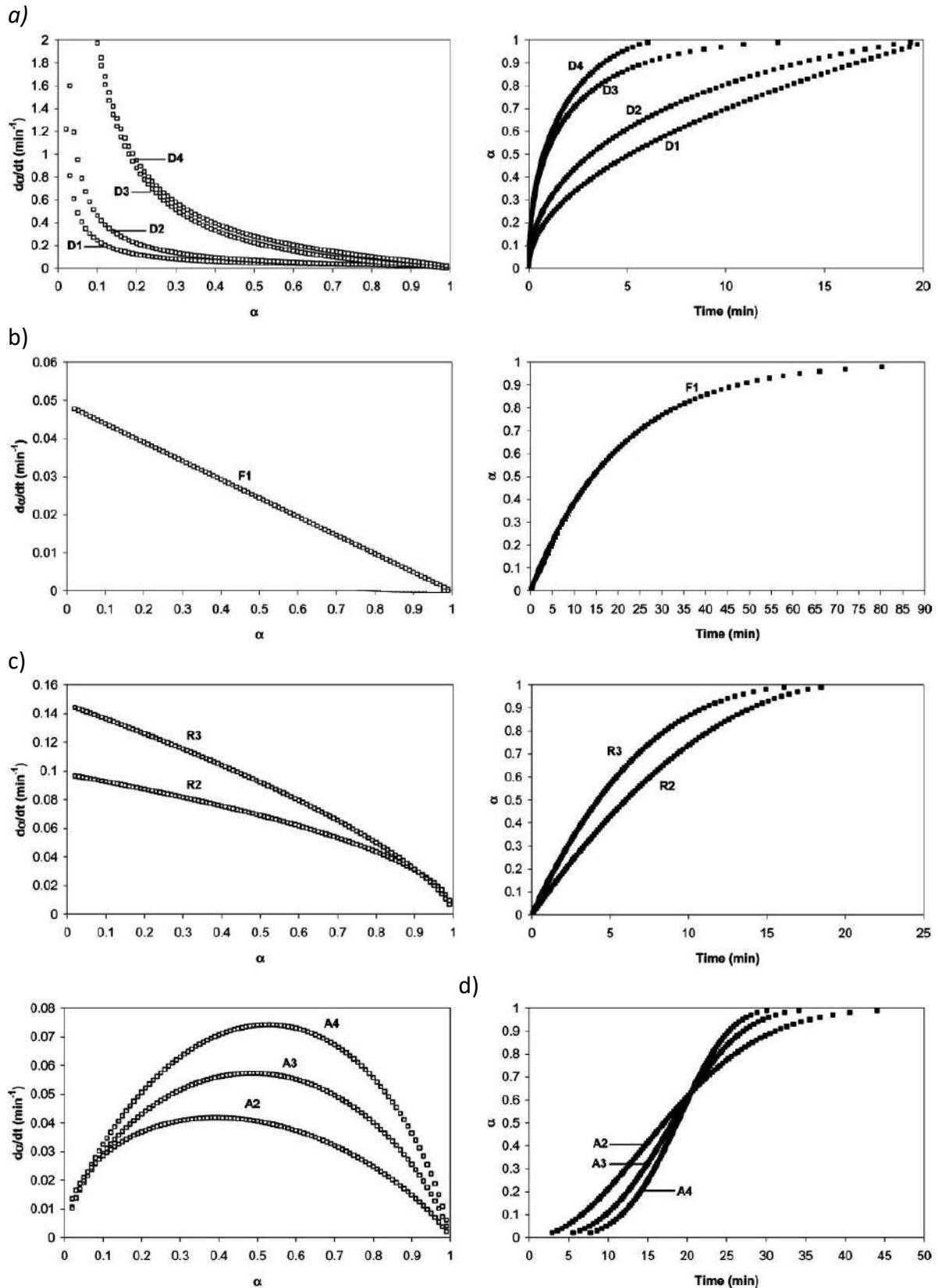


**Figure 3.19.** Isothermal  $d\alpha/dt$  time and  $\alpha$  time plots for solid-state reaction models (Table 3.16); data simulated with a rate constant of  $0.049 \text{ min}^{-1}$ : (a-c) deceleratory; (d) sigmoidal [11].

All models listed in Table 3.6 were used to fit the kinetic data shown in Figs. 3.10 and 3.11. An example is presented in Figure 3.20 for  $y=0.3$  in absorption (left) and desorption (right) in the twentieth cycle. The detailed analysis for each sample is shown in Annex 1. From all the models analyzed in this figure, the best linear relation between  $F(\alpha)$  and time is provided by the model F1; *i.e.* a first order reaction.

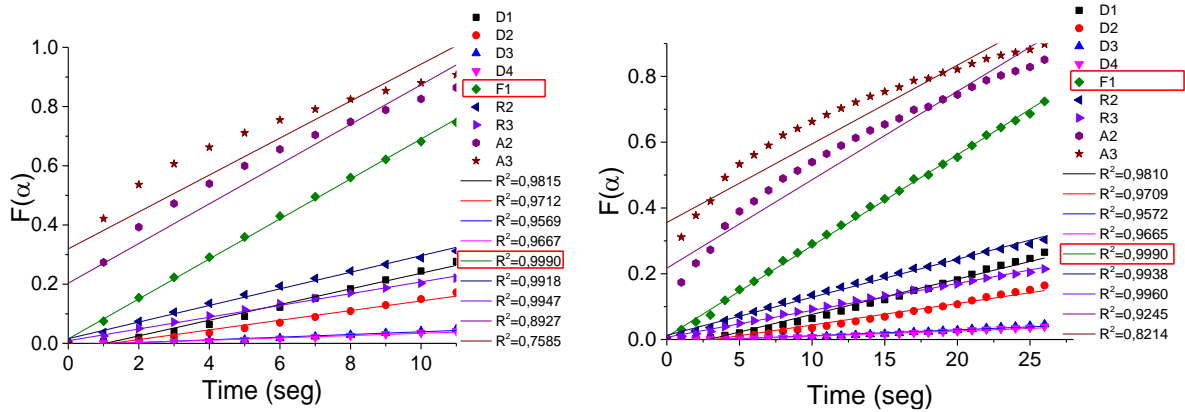


**Figure 3.20.** Function of the reacted fraction vs time and their respective kinetic models in absorption (left) and desorption (right) in cycle 20<sup>th</sup>

The function  $F(\alpha)$  offering the best fit to the sorption data is considered as that for which the plot  $F(\alpha)$  vs.  $t$  offers the coefficient of determination  $R^2$  closest to 1. Table 3.7 presents the kinetic models that offer the best fits to the data extracted from all kinetic experiments. Comments to these results are given in the following.

**Table 3.7.** Best fits of H-sorption curves of  $(1-y)\text{MgH}_2+y\text{TiH}_2$  NCs to kinetic models (when F1 is not the best fitting model, its value is compared with the best fitted one).

$y$	Desorption				Absorption			
	1 <sup>st</sup> Cycle		20 <sup>th</sup> Cycle		2 <sup>nd</sup> Cycle		20 <sup>th</sup> Cycle	
	Model	$R^2$	Model	$R^2$	Model	$R^2$	Model	$R^2$
0	R2	0.9812	R2	0.9504	D3	0.8911	F1	0.9900
	F1	0.9804	F1	0.9500	F1	0.8714		
0.0125	A2	0.9969	A2	0.9939	F1	0.9980	F1	0.9994
	F1	0.9849	F1	0.9911				
0.025	F1	0.9972	R2	0.9961	F1	0.9951	F1	0.9962
			F1	0.9931				
0.05	R2	0.9972	R2	0.9984	F1	0.9961	D4	0.9913
	F1	0.9945	F1	0.9937			F1	0.9865
0.1	F1	0.9928	F1	0.9978	F1	0.9990	D3	0.9925
							F1	0.9426
0.2	R2	0.9970	F1	0.9990	F1	0.9930	D1	0.9931
	F1	0.9927					F1	0.9871
0.3	F1	0.9992	F1	0.9990	F1	0.9990	F1	0.9990

For the first desorption, the pure MgH<sub>2</sub> sample is best fitted with R2 model, but the F1 model is also a good fit with a close  $R^2$  coefficient. For Ti-containing NCs, three different models offer the best fits: A2 for  $y = 0.0125$ , R2 for  $y = 0.05$  and  $0.2$  and F1 for  $y = 0.1$  and  $0.3$ .

However, when F1 is not the best fit, this model cannot be discarded as  $R^2$  remains close to 1. Therefore, the F1 model fits reasonably well all desorption data in the first cycle. For the 20<sup>th</sup> desorption cycle, very similar results are observed leading to the conclusion that the F1 model is the best candidate to fit all desorption data.

As for absorption data, the F1 model fits the best all sorption curves in the 2<sup>nd</sup> cycle for Ti-containing composites. In contrast, for the pure MgH<sub>2</sub> sample ( $y = 0$ ), the D3 model fits better than the others. For the 20<sup>th</sup> cycle, absorption curves of the pure MgH<sub>2</sub> sample and some Ti-containing NCs are best fitted with model F1 ( $y = 0.0125, 0.025$  and  $0.3$ ) while others fit the best to other models: D4, D3 and D1 for  $y = 0.05, 0.1$  and  $0.2$ , respectively. However, the fit of sorption curves to F1 model is always reasonably good.

To summarize, the F1 model offers a good fit for most of the kinetic sorption data obtained in this study. This model corresponds to a first order nucleation and growth model where both nucleation and the subsequent growing of the nuclei, are relevant to understand the kinetic. First, hydride phases are nucleated close to the TiH<sub>2</sub> (catalytic sites) (Figure 3.21 (a)) and the nuclei grow (b). As nuclei grow bigger, they overlap one another (c) to form the hydride layer at the surface of a particle (d). When the hydride layer is thickened, the diffusion distance of the hydrogen atom increases and the hydrogen diffusion through the hydride phase gradually affects the hydriding reaction rate.

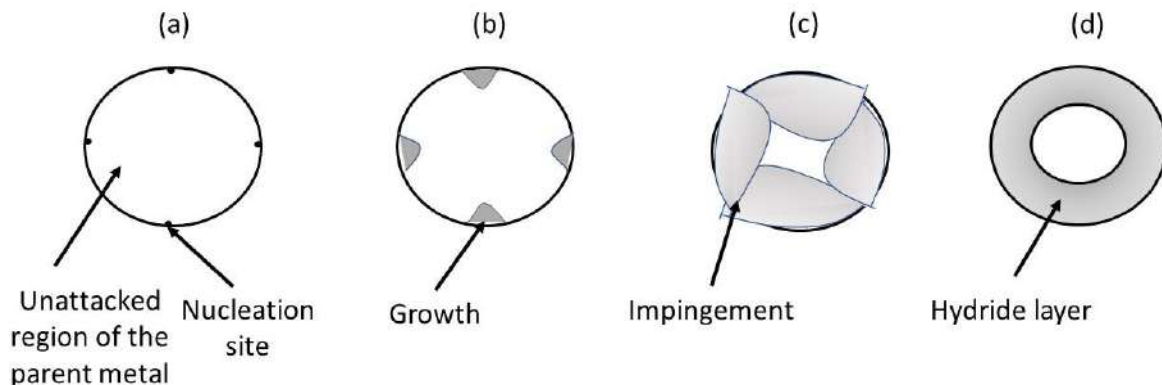


**Figure 3.21.** Schematic diagram of nucleation and growth process

Fernandez and Sanchez [12] explained that, even though there are a great number of papers published about the kinetics of hydrogen-Mg reaction [3,16–19], there is not a proper understanding yet of the slowest step of sorption process. Some authors mention that nucleation and growth mechanism should be taken into account for data analyzing [3,12,20–24], while others have reported that nucleation is insignificant for the kinetics and only the growth of the phase is relevant [16,18]. Zhou *et al.* studied the MgH<sub>2</sub> system with several Ti-based metals [20]. They found the F1 model was perfectly fit with kinetic nucleation and growth process in both absorption and desorption reactions. The MgH<sub>2</sub>-TiH<sub>2</sub> system was studied by Li *et al.* [22], they tested several kinetic models concluding that F1 is the most accurate among them to describe the hydrogenation of MgH<sub>2</sub>-0.1TiH<sub>2</sub>. Zhang *et al.* [25] exposed that R3 model has a good fit for the dehydrogenation of MgH<sub>2</sub>/NbH<sub>x</sub> composites. Fernandez and Sanchez [12] studied the hydrogen kinetic absorption and desorption of Mg, in both cases data seems to obey a rate equation based on nucleation and growth.

### 3.6 Discussion

#### a) MgH<sub>2</sub> system

MgH<sub>2</sub> hydride powder was successfully synthesized by RBM reaching its nominal capacity of 7.6 wt.% at the end of milling. This is supported by the hydrogen uptake curve where the same storage value was determined. Minor Fe content (0.3 at.%) was detected: a common contamination found in milled samples. Fe is coming from the milling jar, because of the collision of the stainless steel balls with the wall jar. The kinetics of hydrogen absorption in Mg by RBM close to RT is remarkably enhanced as compared to classical solid/gas hydrogenation of Mg at 300°C. The latter takes more than 10 hours while the former need less than one hour using in both cases micrometric Mg. This was presented by Vigeholm et al, they showed that full hydrogenation of 90 µm in diameter of Mg particles requires about 1 day at 400 °C and P<sub>H<sub>2</sub></sub> = 2 MPa [26].

By XRD it was possible to identify the two phases contained in the sample, the rutile-type β-MgH<sub>2</sub> phase, and γ-MgH<sub>2</sub>. These phases were also identified by Huot *et al* in ball-milled magnesium hydride [3]. From Rietveld analysis, the abundance of each phase was determined as β-80 wt. % and γ-20 wt. %. This agrees with previous studies. Both phases have a crystal size of ~ 8 nm in close agreement with previous RBM synthesis of MgH<sub>2</sub>[1]. The morphology and particle size were determined by SEM. MgH<sub>2</sub> forms agglomerates with a mean size of 1.2 µm. The agglomerates have a dense aspect and flat rounded surface.

TPD experiments showed that as-milled MgH<sub>2</sub> starts its hydrogen desorption at 280 °C whereas TPA shows that hydrogen absorption starts at 120 °C. These temperatures do not contradict the thermodynamics of the Mg-H system as it was shown in Chapter one.

MgH<sub>2</sub> synthesized by RBM exhibits a poor reversible capacity for reaction time limited to 15 min. This is mainly due to its slow desorption kinetics even at the low initial nanometric crystallite size (8 nm). At 300°C and back-pressure of 0.03 MPa, only 7% of its total capacity is desorbed in 15 min.

After the cycling treatment, the MgH<sub>2</sub> sample was analyzed by XRD both in the absorbed and desorbed state. Only β-MgH<sub>2</sub> phase could be clearly detected. Its crystal size enlarged to 35 ± 5 nm. SEM experiments were done to characterize particle size as well as the morphology. No change in particle size was observed. However, after cycling, surface morphology becomes rougher. The lack of strong changes in particle morphology could be attributed to the poor hydrogen exchange on cycling. In contrast, crystal size growth may explain the increase on surface roughness by the formation of faceted crystals. Crystal growth is attributed to thermal annealing, and not to cycling effects, by holding the sample at 300 °C.

#### b) MgH<sub>2</sub>-TiH<sub>2</sub> system

MgH<sub>2</sub>-TiH<sub>2</sub> NCs with different Ti-contents were successfully synthesized by reactive ball milling. The measured hydrogen absorption capacity was the same or close to the nominal ones. A slight contamination of Fe (0.6 at.%) was also observed.

From XRD it was found that the synthesized materials consist of immiscible MgH<sub>2</sub> and TiH<sub>2</sub>. No ternary Mg-Ti-H hydrides were found. All patterns can be indexed in three phases:  $\beta$ -MgH<sub>2</sub>,  $\gamma$ -MgH<sub>2</sub>, and  $\varepsilon$ -TiH<sub>2</sub>. From Rietveld analysis, the crystal size was measured about  $8 \pm 3$  nm for each phase. Both phase abundance and crystal size agree with the published data [1,27,28]. From SEM, it was determined that MgH<sub>2</sub>-TiH<sub>2</sub> NCs consist of agglomerates 2.3  $\mu$ m in size of  $\sim 100$  nm in size particles and exhibit porous aspect and rough surface.

From PCI measurements, the hydrogenation and dehydrogenation enthalpies of the Mg-MgH<sub>2</sub> transformation were measured as  $-73.6 \pm 0.9$  and  $75.5 \pm 0.6$  kJmolH<sub>2</sub><sup>-1</sup>, respectively. The corresponding entropy values are  $-133 \pm 2$  and  $135 \pm 1$  JK<sup>-1</sup>molH<sub>2</sub><sup>-1</sup> in agreement with literature data for the bulk Mg-H system as was presented in Chapter one. These results can also be compared with previous studies on MgH<sub>2</sub>-TiH<sub>2</sub> NCs. Lu *et al.* obtained for the system MgH<sub>2</sub>-0.1TiH<sub>2</sub> the hydrogenation enthalpy and entropy values of  $-68.2$  kJmolH<sub>2</sub><sup>-1</sup> and  $-127$  JK<sup>-1</sup>molH<sub>2</sub><sup>-1</sup> respectively [27]. Patelli *et al.* calculated enthalpy and entropy values of  $-68.2$  kJmolH<sub>2</sub><sup>-1</sup> and  $-119$  JK<sup>-1</sup>molH<sub>2</sub><sup>-1</sup> respectively for the desorption of the MgH<sub>2</sub>-TiH<sub>2</sub> system [29]. Cui *et al.*, also calculated the desorption enthalpy and entropy of the same system (enthalpy  $-75.1$  kJmolH<sub>2</sub><sup>-1</sup> and entropy  $-136.3$  JK<sup>-1</sup>molH<sub>2</sub><sup>-1</sup>) [30].

TPD curves showed that doped NCs start desorbing at around 150 °C; *i.e.* 130°C lower than for pure MgH<sub>2</sub>. From TPA curves are observed that the hydrogen absorption even starts at room temperature, showing the improvement of hydrogen sorption kinetics in the Mg-H system by TiH<sub>2</sub> additives. Nevertheless, both TPD and TPA results do not contradict the thermodynamics of the Mg-H system

The reversible capacity measured of doped NC is extremely good. NCs with high ( $\gamma \geq 0.1$ ) TiH<sub>2</sub> content shown stable C<sub>rev</sub> through cycling. NCs with low additive amount ( $\gamma \leq 0.05$ ) exhibit fluctuating C<sub>rev</sub>. Lu *et al.* performed eighty complete absorption-desorption cycles of one hour each, any loss of capacity was observed in the system MgH<sub>2</sub>-0.1 TiH<sub>2</sub>[27].

From the kinetic desorption curves, it was identified that hydrogen desorption is accelerated through cycling. In contrast, absorption kinetics does not improve on cycling and likely slow down since the amount of unreacted Mg increases (Fig. 3.12). As a result, NCs with low TiH<sub>2</sub> content are not able to absorb and desorb the initial hydrogen amount during the cycling process having both unreacted Mg and retained MgH<sub>2</sub>. NCs with high TiH<sub>2</sub> content have less unreacted Mg and less retained MgH<sub>2</sub>. However, for these NCs reach in TiH<sub>2</sub> its reversible capacity is not higher than the ones with less additive. Due to if TiH<sub>2</sub> amount increases, also the irreversible part does.

After cycling, the XRD results show that there is an increase in the crystal size in the MgH<sub>2</sub> and Mg phases for all NC in both absorbed and desorbed states. The crystal size of MgH<sub>2</sub> is within the range from 45 to 80 nm, whereas that of Mg is comprised between 65 and 105 nm. It is however remarkable that despite such a significant crystal growth as compared to initial values (8 nm), desorption kinetics do not slow down on cycling. This clearly indicates that H-diffusion in MgH<sub>2</sub> or Mg crystallites is not the rate limiting step for hydrogen desorption in MgH<sub>2</sub>-TiH<sub>2</sub> NCs. In contrast, as discussed later, grain coarsening may contribute to the observed increase of unreacted-Mg (absorption sweeps) on cycling (Fig. 3.12).

SEM-EDS studies were performed to determine particle sizes, morphology and phase distribution. No significant changes on particle size were observed in NCs on cycling. Therefore, this property is not at the origin of kinetic modifications neither induced by TiH<sub>2</sub> content nor by cycling. The morphology of  $\gamma=0.0125$  in absorbed state is like the one as-milled showing a densification which it could be because of the poor cyclability of this. In desorbed state shows the formation of protrusions in its morphology which indicates that even with a poor desorption the morphology is modified.  $\gamma=0.3$ , in both absorbed and desorbed state, shows a main cracked particle, this cracking could be attributed to the stress suffered by the particles during the almost complete absorption-desorption cycling.

As concerns phase distribution, SEM-EDS analysis for NC  $\gamma=0.3$  shows homogenous phases dispersion for the as-milled state. After cycling, the TiH<sub>2</sub> content at the center of the agglomerates is found to be depleted as compared to the average composition. This is assigned to a partial migration of TiH<sub>2</sub> from the core of the agglomerate to the edges on cycling. This migration has been previously observed by Zhou *et al.* [20,31]. The catalytic additives suffer repeating stresses from the surrounding Mg/MgH<sub>2</sub> matrix during the cycling process. The stress might be strong enough so that a “migration” of the catalyst particle is possible (Figure 3.22). Also, the catalyst particle that closely contacted to the Mg/MgH<sub>2</sub> matrix might be detached from the agglomerate due to the shrinkage during dehydrogenation.

These migration and detachment phenomena may explain two hydrogenation facts observed in this thesis: i) as for migration, the acceleration of dehydrogenation kinetics on cycling for all NCs may result from the increased amount of TiH<sub>2</sub> catalytic sites at the agglomerate surface ii) as for detachment, the diminution of reversible capacity in the first cycles for Ti-poor NCs may result from the detachment of TiH<sub>2</sub> additives from the matrix.

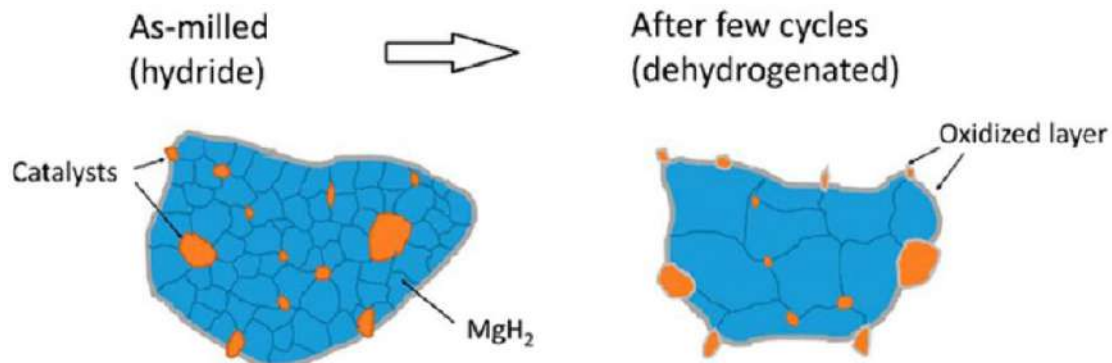


**Figure 3.22.** Schematic depicting the evolution of microstructure of the catalyzed MgH<sub>2</sub> particle during cycling [31]

### c) Comparison between MgH<sub>2</sub> and MgH<sub>2</sub>-TiH<sub>2</sub> systems

RBM is a good technique for the synthesis of MgH<sub>2</sub>-TiH<sub>2</sub> NCs. On increasing the TiH<sub>2</sub> amount, NCs synthesis is accomplished in a shorter time than for pure Mg.

Thermodynamics of the Mg-H system is not altered by TiH<sub>2</sub>-addition and only the MgH<sub>2</sub> counterpart of the nanocomposite can be reversibly ab(de)sorbed at the working temperature,  $T = 300$  °C, and pressure,  $0.01 < P_{H_2} < 1$  MPa, conditions (Figure 3.6). This was confirmed by the similar obtained values of enthalpy and entropy formation than for pure

MgH<sub>2</sub>. Indeed, under these thermodynamic conditions, no significant hydrogen desorption from TiH<sub>2</sub> phase occurs [6]. TPD curves show that the additive facilitates desorption at lower temperature but without crossing the thermodynamic limit. Also, absorption can occur at much lower temperature, even room temperature, for doped NCs.

It has been reported by some researchers that MgH<sub>2</sub> system mixed with additives showed very good stability when cycling at a temperature of 300 °C [32,33], which was confirmed comparing cycle life of the NCs cycled at 300 and 340 °C. Isothermal cycling for 15 min shows that it is possible to get a good reversible capacity adding TiH<sub>2</sub> to the MgH<sub>2</sub>, without this the reversible is practically null. In Figure 3.12, it can be seen that Ti addition increases the weight of the metallic counterpart of the composite since Ti is heavier than Mg which can be clearly seen in NCs with the more TiH<sub>2</sub> amount. This is evidenced in Table 3.1, where the H-content of (1-y)MgH<sub>2</sub>+yTiH<sub>2</sub> NCs gradually decreases from 7.7 to 6.0 wt.% H for y = 0 and 0.3, respectively.

Absorption and desorption kinetics are both accelerated with the incorporation of TiH<sub>2</sub> additive to MgH<sub>2</sub> in the system. TiH<sub>2</sub> has beneficial kinetic effects on the temperature onset for hydrogen absorption and desorption as displayed in TPA and TPD measurements (Figure 3.8). Also, Ti-free MgH<sub>2</sub> sample brings almost negligible desorption at 300°C in 15 min time compared to Ti-doped ones (Figure 3.10). Moreover, sorption rates on absorption (Figure 3.11) and desorption (Figure 3.10) gradually increase with TiH<sub>2</sub> content. Consequently, reacted fractions at the end of cycling sweeps increase with TiH<sub>2</sub> content both on absorption and desorption. As results of these kinetics improvements, the reversible capacity  $C_{rev}$  of MgH<sub>2</sub>-TiH<sub>2</sub> NCs is much higher than that of pure MgH<sub>2</sub> system (Figure 3.9).

The kinetics analysis of sorption curves shows that the F1 model fits the best to both absorption and desorption experimental data. This model corresponds to a first order reaction where both nucleation and the subsequent growing of the nuclei describe sorption kinetics. Figure 3.23 shows the nucleation and growth kinetic model proposed by Ponthieu [34] where nucleation would occur at the TiH<sub>2</sub>/MgH<sub>2</sub> interfaces. Moreover, TiH<sub>2</sub> if present at the particle surface, can act as a gateway for hydrogen gas facilitating hydrogen dissociation (absorption) and recombination (desorption).

Moreover, TiH<sub>2</sub> can also facilitate hydrogen transfer to the Mg phase where MgH<sub>2</sub> nucleates. This is supported by the large diffusion coefficient of H in TiH<sub>2</sub>[35]. In addition, it is proposed that fast H-absorption is possible in nanocomposites because native MgO barriers are bypassed through the TiH<sub>2</sub> phase. This effect seems to be even more important on desorption sweeps (Fig. 3.10): recombination of hydrogen atoms at TiH<sub>2</sub> surfaces will enhance hydrogen desorption kinetics in MgH<sub>2</sub>-TiH<sub>2</sub> nanocomposites as compared to the pure MgH<sub>2</sub> system.

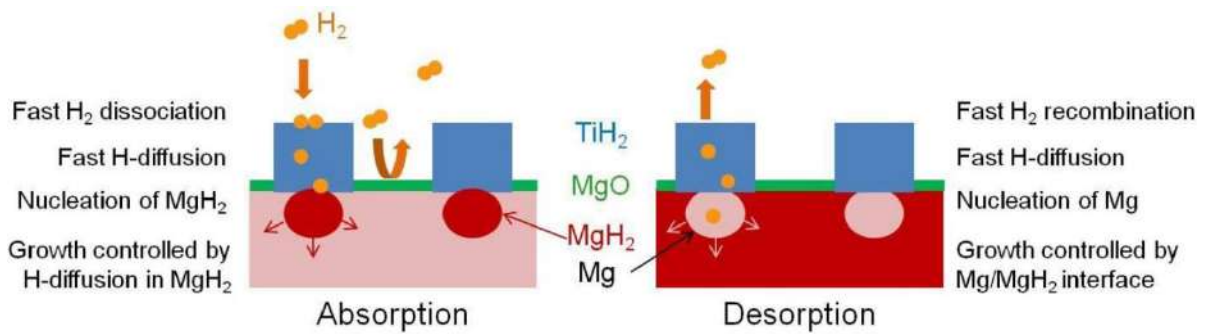


**Figure 3.23.** Schematic representation of hydrogen absorption and desorption mechanisms in MgH<sub>2</sub>-TiH<sub>2</sub> nanocomposites [34].

From the analyzed microstructure by XRD, it has been confirmed that crystallite sizes of Mg and MgH<sub>2</sub> increase up to 100 nm after the cycling process. In contrast, the TiH<sub>2</sub> size remains low and constant around 10 nm. Several authors have proposed that additive inclusions may act as a grain growth inhibitor of Mg and MgH<sub>2</sub> phases [20,24,27,31]. Our study shows that significant grain growth exists after 20 sorption cycles. However, this has no detrimental effect on desorption kinetics but may be at the origin of reduced hydrogen absorption on cycling (*i.e.* increase of unreacted Mg phase). Indeed, as in bulk Mg [12], the growth of MgH<sub>2</sub> nuclei during absorption is likely limited by hydrogen diffusion through MgH<sub>2</sub> crystallites.

#### d) Additive contributions

Ti acts as a gateway for hydrogen transport enabling fast hydrogen dissociation/recombination at the TiH<sub>2</sub> surface and its diffusion towards the bulk as schematically depicted in Figure 3.24. Different authors have reported that TiH<sub>2</sub> can improve the hydrogen sorption kinetics in MgH<sub>2</sub>. For instance, Patelli et al [29] suggest that TiH<sub>2</sub> provides catalytic active sites for surface adsorption and dissociation of H<sub>2</sub>. Hydrogen diffusion is faster in TiH<sub>2</sub> than in MgH<sub>2</sub>, and therefore the TiH<sub>2</sub> nanocrystallites may provide high mobility paths for atomic hydrogen. A similar explanation was given in previous studies performed in our laboratory [1] proposing that TiH<sub>2</sub> is the gateway for the transfer from the gas phase to the bulk. In addition, Jangir et al [36] showed that activation energies for hydrogen desorption from MgH<sub>2</sub> gradually decrease with TiH<sub>2</sub> content.

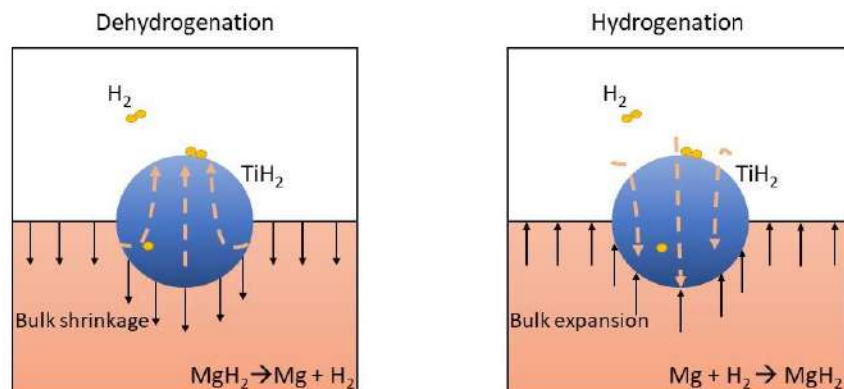


**Figure 3.24.** Schematic shows the TiH<sub>2</sub> role as a gateway for hydrogen transfer (yellow arrows) from the surface to the bulk (black arrows) both on desorption and absorption reactions.

Within the framework of our study, we have demonstrated that TiH<sub>2</sub> addition favorably enhances H-sorption kinetics of the Mg/MgH<sub>2</sub> reaction and cycling stability. The more TiH<sub>2</sub> is added, the more Mg/MgH<sub>2</sub> transformation is accomplished in a given time. This can be clearly observed in Figure 3.12: the higher the TiH<sub>2</sub> amount, the more hydrogen can be reversibly stored through the Mg/MgH<sub>2</sub> reaction. However, as a drawback of TiH<sub>2</sub> addition, it decreases the reversible hydrogenation capacity of Mg/MgH<sub>2</sub> system because of its higher atomic weight (as compared to Mg) and the formation of irreversible TiH<sub>2</sub>. Thus, it exists an optimum TiH<sub>2</sub> content in MgH<sub>2</sub>-TiH<sub>2</sub> nanocomposites to achieve the highest reversible capacity. It was established here at 0.975MgH<sub>2</sub>-0.025TiH<sub>2</sub>, for a limited reaction time of 15 min, leading to a reversible capacity of 4.9 wt.% after 20 sorption cycles.

To summarize, the relative contributions to hydrogen storage in the two-phase (1-y)MgH<sub>2</sub>+yTiH<sub>2</sub> system are presented in Figure 3.25. Starting from pure MgH<sub>2</sub> (y = 0; 7.7 wt.%), the total hydrogen capacity decreases with titanium amount due, firstly to its heavier atomic mass (hatched blue area in Figure 3.25). Secondly, as hydrogen in TiH<sub>2</sub> is not reversible under the working thermodynamic conditions, the reversible hydrogen stored in MgH<sub>2</sub> decreases down to 4.3 wt.% for y = 0.3 (hatched red area in Figure 3.25). From then, the hydrogen that can be reversibly recovered from MgH<sub>2</sub> depends on the H-kinetic properties of the NCs. Without Ti (y = 0), no significant H-amount is recovered from pure MgH<sub>2</sub>. When increasing the Ti-content, such kinetic limitation is minimized, and an optimized value is obtained for the reversible H-capacity of NCs (grey area in Figure 3.25). The fastest kinetics are found at the highest Ti-content (y = 0.3) leading to the highest reversibility in the Mg/MgH<sub>2</sub> reaction (white area in Figure 3.25). However, the negligible hydrogen desorption of TiH<sub>2</sub> restricts the interest of using high Ti-contents. The best compromise between the detrimental effects of increasing TiH<sub>2</sub> content (heavy and irreversible hydride) and its beneficial one (enhancement of Mg/MgH<sub>2</sub> kinetics) leads to an optimum for y = 0.025 with a reversible capacity of 4.9 wt.%.

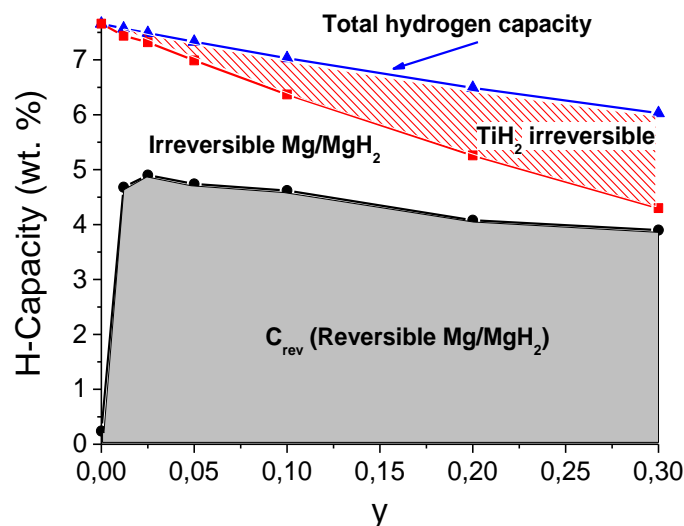


**Figure 3.25.** Reversible and irreversible contributions to hydrogen storage in (1-y)MgH<sub>2</sub>+yTiH<sub>2</sub> nanocomposites with reaction time limited to 15 min (▲ = Total hydrogen capacity, ■ = H-capacity of MgH<sub>2</sub> counterpart, ● = experimental H-reversible capacity).

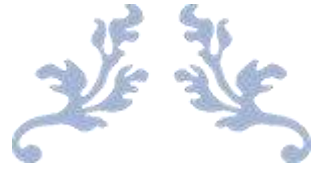
## References

- [1] Cuevas F, Korablov D, Latroche M. Synthesis, structural and hydrogenation properties of Mg-rich MgH<sub>2</sub>-TiH<sub>2</sub> nanocomposites prepared by reactive ball milling under hydrogen gas. *Phys Chem Chem Phys* 2011; 14:1200–11. doi:10.1039/C1CP23030A.
- [2] Zhang J, Cuevas F, Zaïdi W, Bonnet J-P, Aymard L, Bobet J-L, et al. Highlighting of a single reaction path during reactive ball milling of mg and tm by quantitative h<sub>2</sub> gas sorption analysis to form ternary complex hydrides (TM = Fe, Co, Ni). *J Phys Chem C* 2011; 115:4971–9. doi:10.1021/jp2005293.
- [3] Huot J, Liang G, Boily S, Van Neste A, Schulz R. Structural study and hydrogen sorption kinetics of ball-milled magnesium hydride. *J Alloys Compd* 1999; 293–295:495–500. doi:10.1016/S0925-8388(99)00474-0.
- [4] Rueden CT, Schindelin J, Hiner MC, DeZonia BE, Walter AE, Arena ET, et al. ImageJ2: ImageJ for the next generation of scientific image data. *BMC Bioinformatics* 2017; 18:529. doi:10.1186/s12859-017-1934-z.
- [5] San-Martin A, Manchester FD. The H-Mg (Hydrogen-Magnesium) system. *J Phase Equilibria* 1987; 8:431–7. doi:10.1007/BF02893152.
- [6] Arita M, Shimizu K, Ichinose Y. Thermodynamics of the Ti-H system. *Metall Trans A* 1982;13:1329–36. doi:10.1007/BF02642869.
- [7] Lototskyy MV, Davids MW, Tolj I, Klochko YV, Sekhar BS, Chidziva S, et al. Metal hydride systems for hydrogen storage and supply for stationary and automotive low temperature PEM fuel cell power modules. *Int J Hydrog Energy* 2015; 40:11491–7. doi:10.1016/j.ijhydene.2015.01.095.
- [8] Pelletier JF, Huot J, Sutton M, Schulz R, Sandy AR, Lurio LB, et al. Hydrogen desorption mechanism in MgH<sub>2</sub>-Nb nanocomposites. *Phys Rev B* 2001; 63:052103. doi:10.1103/PhysRevB.63.052103.
- [9] Montone A, Aurora A, Gattia DM, Antisari MV. Microstructural and kinetic evolution of Fe doped MgH<sub>2</sub> during H<sub>2</sub> cycling. *Catalysts* 2012;2:400–11.
- [10] Berti N, Cuevas F, Zhang J, Latroche M. Enhanced reversibility of the electrochemical Li conversion reaction with MgH<sub>2</sub>-TiH<sub>2</sub> nanocomposites. *Spec Issue 15th Int Symp Met-Hydrog Syst MH2016 7-12 August 2016 Interlaken Switz* 2017; 42:22615–21. doi:10.1016/j.ijhydene.2017.03.048.
- [11] Khawam A, Flanagan DR. Solid-State Kinetic Models: Basics and Mathematical Fundamentals. *J Phys Chem B* 2006;110:17315–28. doi:10.1021/jp062746a.
- [12] Fernández JF, Sánchez CR. Rate determining step in the absorption and desorption of hydrogen by magnesium. *J Alloys Compd* 2002; 340:189–98. doi:10.1016/S0925-8388(02)00120-2.
- [13] Sharp JH, Brindley GW, Achar BNN. Numerical Data for Some Commonly Used Solid State Reaction Equations. *J Am Ceram Soc* 1966;49:379–82. doi:10.1111/j.1151-2916.1966.tb13289.x.
- [14] Jones LF, Dollimore D, Nicklin T. Comparison of experimental kinetic decomposition data with master data using a linear plot method. *Thermochim Acta* 1975; 13:240–5. doi:10.1016/0040-6031(75)80085-2.
- [15] Hancock JD, Sharp JH. Method of Comparing Solid-State Kinetic Data and Its Application to the Decomposition of Kaolinite, Brucite, and BaCO<sub>3</sub>. *J Am Ceram Soc* 1972;55:74–7. doi:10.1111/j.1151-2916.1972.tb11213.x.

- [16] Ellinger FH, Holley CE, McInteer BB, Pavone D, Potter RM, Staritzky E, et al. The Preparation and Some Properties of Magnesium Hydride 1. *J Am Chem Soc* 1955;77:2647–8. doi:10.1021/ja01614a094.
- [17] Kennelley JA, Varwig JW, Myers HW. Magnesium—Hydrogen relationships 1. *J Phys Chem* 1960; 64:703–4. doi:10.1021/j100834a521.
- [18] Mintz MH, Gavra Z, Hadari Z. Kinetic study of the reaction between hydrogen and magnesium, catalyzed by addition of indium. *J Inorg Nucl Chem* 1978; 40:765–8. doi:10.1016/0022-1902(78)80147-X.
- [19] Karty A, Grunzweig-Genossar J, Rudman PS. Hydriding and dehydriding kinetics of Mg in a Mg/Mg<sub>2</sub>Cu eutectic alloy: Pressure sweep method. *J Appl Phys* 1979; 50:7200–9. doi:10.1063/1.325832.
- [20] Zhou C, Fang ZZ, Bowman RC. Stability of Catalyzed Magnesium Hydride Nanocrystalline During Hydrogen Cycling. Part I: Kinetic Analysis. *J Phys Chem C* 2015; 119:22261–71. doi:10.1021/acs.jpcc.5b06190.
- [21] Liang G, Huot J, Boily S, Schulz R. Hydrogen desorption kinetics of a mechanically milled MgH<sub>2</sub>+5at.%V nanocomposite. *J Alloys Compd* 2000; 305:239–45. doi:10.1016/S0925-8388(00)00708-8.
- [22] Li J, Fan P, Fang ZZ, Zhou C. Kinetics of isothermal hydrogenation of magnesium with TiH<sub>2</sub> additive. *Int J Hydrog Energy* 2014; 39:7373–81. doi:10.1016/j.ijhydene.2014.02.159.
- [23] Ma X, Xie X, Liu P, Xu L, Liu T. Synergic catalytic effect of Ti hydride and Nb nanoparticles for improving hydrogenation and dehydrogenation kinetics of Mg-based nanocomposite. *Prog Nat Sci Mater Int* 2017; 27:99–104. doi:10.1016/j.pnsc.2016.12.013.
- [24] Ponthieu M, Calizzi M, Pasquini L, Fernández JF, Cuevas F. Synthesis by reactive ball milling and cycling properties of MgH<sub>2</sub>–TiH<sub>2</sub> nanocomposites: Kinetics and isotopic effects. *Int J Hydrog Energy* 2014; 39:9918–23. doi:10.1016/j.ijhydene.2014.01.055.
- [25] Zhang L, Xiao X, Xu C, Zheng J, Fan X, Shao J, et al. Remarkably Improved Hydrogen Storage Performance of MgH<sub>2</sub> Catalyzed by Multivalence NbH<sub>x</sub> Nanoparticles. *J Phys Chem C* 2015; 119:8554–62. doi:10.1021/acs.jpcc.5b01532.
- [26] Vigeholm B, Jensen K, Larsen B, Pedersen AS. Elements of hydride formation mechanisms in nearly spherical magnesium powder particles. *J Common Met* 1987; 131:133–41. doi:10.1016/0022-5088(87)90509-1.
- [27] Lu J, Choi YJ, Fang ZZ, Sohn HY, Rönnebro E. Hydrogen Storage Properties of Nanosized MgH<sub>2</sub>–0.1TiH<sub>2</sub> Prepared by Ultrahigh-Energy–High-Pressure Milling. *J Am Chem Soc* 2009; 131:15843–52. doi:10.1021/ja906340u.
- [28] Lu J, Choi YJ, Fang ZZ, Sohn HY, Rönnebro E. Hydrogenation of Nanocrystalline Mg at Room Temperature in the Presence of TiH<sub>2</sub>. *J Am Chem Soc* 2010; 132:6616–7. doi:10.1021/ja910944w.
- [29] Patelli N, Calizzi M, Migliori A, Morandi V, Pasquini L. Hydrogen Desorption Below 150 °C in MgH<sub>2</sub>–TiH<sub>2</sub> Composite Nanoparticles: Equilibrium and Kinetic Properties. *J Phys Chem C* 2017; 121:11166–77. doi:10.1021/acs.jpcc.7b03169.
- [30] Cui J, Wang H, Liu J, Ouyang L, Zhang Q, Sun D, et al. Remarkable enhancement in dehydrogenation of MgH<sub>2</sub> by a nano-coating of multi-valence Ti-based catalysts. *J Mater Chem A* 2013; 1:5603–11. doi:10.1039/C3TA01332D.
- [31] Zhou C, Fang ZZ, Bowman RC, Xia Y, Lu J, Luo X, et al. Stability of catalyzed magnesium hydride nanocrystalline during hydrogen cycling. part II: Microstructure evolution. *J Phys Chem C* 2015; 119:22272–80. doi:10.1021/acs.jpcc.5b06192.

- [32] Dehouche Z, Djaozandry R, Huot J, Boily S, Goyette J, Bose TK, et al. Influence of cycling on the thermodynamic and structure properties of nanocrystalline magnesium based hydride. *J Alloys Compd* 2000; 305:264–71. doi:10.1016/S0925-8388(00)00718-0.
- [33] Dehouche Z, Goyette J, Bose TK, Schulz R. Moisture effect on hydrogen storage properties of nanostructured MgH<sub>2</sub>-V-Ti composite. *Int J Hydrog Energy* 2003; 28:983–8. doi:10.1016/S0360-3199(02)00196-9.
- [34] Ponthieu M. Nouveaux matériaux riches en Mg pour le stockage d'hydrogène : composés Mg<sub>6</sub>Pd<sub>1-x</sub>MT<sub>x</sub> (MT = Ni, Ag, Cu) massifs et nanoconfinés et nanocomposites MgH<sub>2</sub>-TiH<sub>2</sub>. Université Paris-Est, 2013.
- [35] Kaess U, Majer G, Stoll M, Peterson DT, Barnes RG. Hydrogen and deuterium diffusion in titanium dihydrides/dideuterides. *J Alloys Compd* 1997; 259:74–82. doi:10.1016/S0925-8388(97)00124-2.
- [36] Jangir M, Jain A, Agarwal S, Zhang T, Kumar S, Selvaraj S, et al. The enhanced de/re-hydrogenation performance of MgH<sub>2</sub> with TiH<sub>2</sub> additive. *Int J Energy Res* 2017. doi:10.1002/er.3911.





---

# CHAPTER FOUR

---

Effect of hydride-forming *TM* additives (*TM* = Ti, Zr, Sc, Y, V, and Nb) on sorption properties of MgH<sub>2</sub>-based nanocomposites





## 4. Effect of hydride-forming *TM* additives (*TM* = Ti, Zr, Sc, Y, V, and Nb) on sorption properties of MgH<sub>2</sub>-based nanocomposites

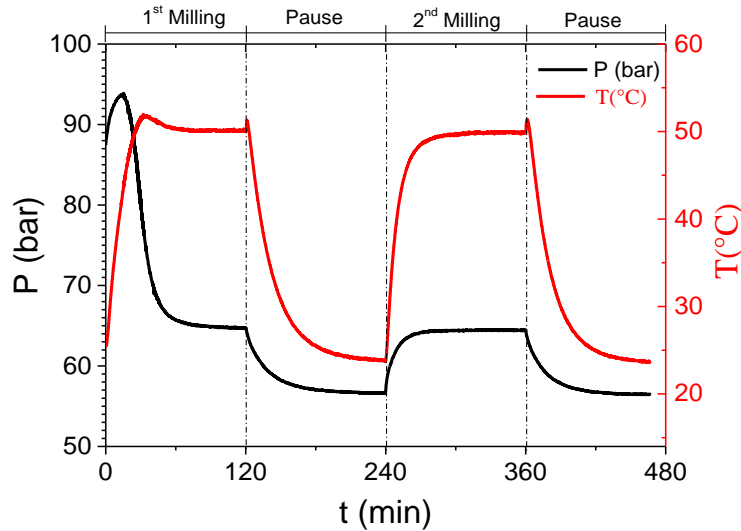
The hydrogen sorption properties of MgH<sub>2</sub>-*TM*H<sub>x</sub> nanocomposites for different transition metals (*TM*= Ti, Zr, Sc, Y, V, and Nb) are analyzed in this chapter. As shown in the previous chapter, there are two ways to successfully improve the MgH<sub>2</sub> kinetics through RBM: by nanostructuring and by additives incorporation. Once that MgH<sub>2</sub>-TiH<sub>2</sub> system was deeply investigated, arose the idea of exploring the effect of other transition metals with properties to close Ti for a better understanding of the additive role. Thus, neighbor elements to Ti in the periodic table were chosen, *i.e.* metals of 3, 4 and 5 groups and 4<sup>th</sup> and 5<sup>th</sup> periods. In the previous chapter, we found out an optimum amount of TiH<sub>2</sub> (2.5 mol%) to have both high  $C_{rev}$  and good cycling in a restricted time of 15 minutes. In this chapter, we decided to fix the *TM* amount to 5 mol% to maintain fast sorption kinetics, while using a significant amount of additive for facilitating characterization purposes (e.g. XRD-studies).

### 4.1 MgH<sub>2</sub> with 4 transition metals Ti and Zr

#### 4.1.1 Synthesis and structural characterization

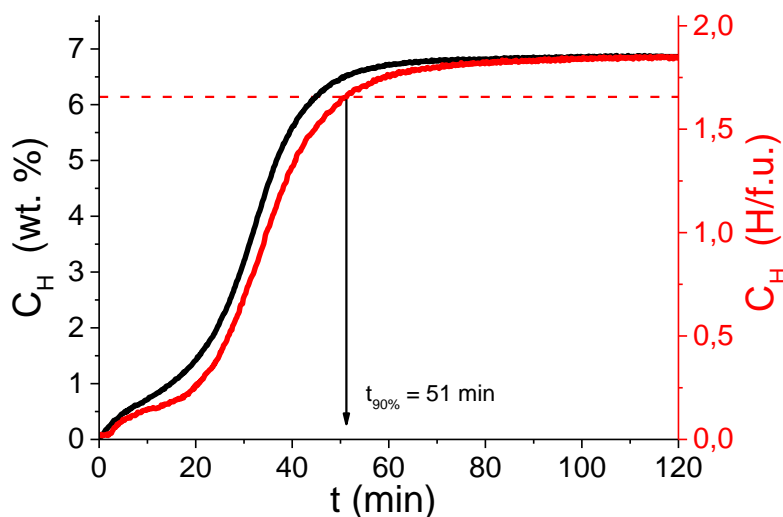
##### a) System 0.95MgH<sub>2</sub>-0.05TiH<sub>2</sub>

Figure 4.1 shows the RBM synthesis of the MgH<sub>2</sub>-TiH<sub>2</sub> composite. An initial pressure closes to 90 bar (9 MPa) at room temperature were the initial conditions for the RBM. As in the previous chapter, the same 5g total mass was used to perform the RBM. The milling program consists of 2 milling cycles of 120 min each with one pause between them of 120 min. At the beginning of the process, the temperature increases because of the frictions and collisions of the stainless-steel balls with the vial walls reaching a maximum value of 50 °C (323 K). This also leads to an increment of the pressure (95 bar (9.5 MPa)) due to gas confinement. Then, the pressure drops down (65 bar (6.5 MPa)) due to the hydrogen absorption of both Mg and Ti metals during the formation of the hydride phases. Once that hydrogenation is completed, a constant pressure is observed. At the end of the first milling cycle, both pressure and temperature decrease to equilibrium values at ambient conditions during the pause time,  $P= 56$  bar (5.6 MPa) and  $T= 24$  °C (297 K). The second cycle did not show any additional hydrogen absorption, is the change in pressure due to thermal variations induced by milling and the pause  $P_{max} = 63$  bar (6.3 MPa) and  $T_{max}= 50$ °C (323 K). Thus, the second cycle can be used to calibrate the gas temperature that differs from the measured vial temperature [1].



**Figure 4.1.** Evolution of the hydrogen pressure (black line) and the vial temperature (red line) as a function of milling time during the synthesis of the composite  $0.95\text{MgH}_2+0.05\text{TiH}_2$

From both pressure and temperature data of the first milling process, the corresponding hydrogen uptake curve was obtained (Figure 4.2). The figure shows the hydrogen uptake during the milling process in both weight percent (wt.%) and hydrogen atoms per formula unit (H/f.u.) scales. The evolution of the hydride phases formation during the first 60 min can be seen then, at the end of 120 min, the maximum uptake capacity is been achieved. Cuevas *et al.* [2] explained that the formation of the nanocomposite  $\text{MgH}_2\text{-TiH}_2$  takes place in two-distinct stages due to the consecutive formation of  $\text{TiH}_2$  and  $\text{MgH}_2$ , during the fast ( $0 < t_m < 15$  min) and long ( $15 < t_m < 50$  min) milling times, respectively (Figure 4.2). The maximum value of  $C_H$  is 1.8 H/f.u. (or 6.8 wt.%) which is close to the one of the targeted material  $0.95\text{MgH}_2+0.05\text{TiH}_2$ , *i.e.* 2.0 H/f.u. or 7.3 wt.% respectively.

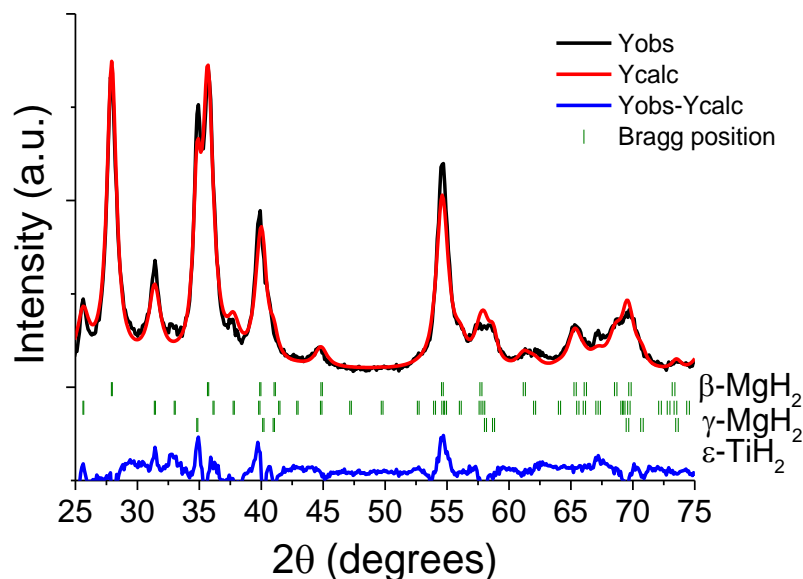


**Figure 4.2.** Hydrogen uptake curves in weight percent (black line) and hydrogen atoms per formula unit (red line) during the first milling cycle of  $0.95\text{MgH}_2+0.05\text{TiH}_2$ .

XRD measurements were used to determine the crystallographic properties of the obtained nanocomposite (NC). Figure 4.3 displays the XRD pattern of as-milled material. The pattern (black line) exhibits broad diffraction peaks evidencing nanostructuring. Three different phases were indexed: two MgH<sub>2</sub> polymorphs ( $\beta$  and  $\gamma$ ) and fluorite-distorted  $\epsilon$ -TiH<sub>2</sub>. The XRD pattern was refined by the Rietveld method [3]. The calculated pattern is shown in Figure 4.3. (red line). Table 4.1 gathers phase amounts and their average crystallite sizes. The ratio between  $\gamma$  and  $\beta$  MgH<sub>2</sub> polymorphs is  $24 \pm 3$  wt.%. TiH<sub>2</sub>-content agrees well as compared to the nominal value. As concerns crystallite sizes, they are evaluated in the interval of 5-7 nm for both  $\beta$ -MgH<sub>2</sub> and  $\gamma$ -MgH<sub>2</sub> polymorphs, and 8 nm for  $\epsilon$ -TiH<sub>2</sub>. It is important to mention that no ternary Mg-Ti-H phase was detected during the synthesis.

**Table 4.1.** Crystallographic properties of as-milled 0.95MgH<sub>2</sub>+0.05TiH<sub>2</sub> and Rietveld agreement factor.

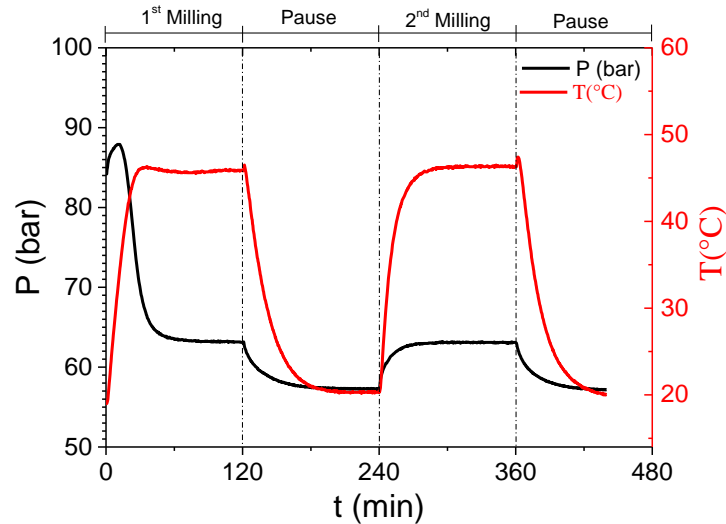
Phase abundance (wt.%)			Crystal size(nm)			
	$\epsilon$ -TiH <sub>2</sub>					
$\gamma$ -MgH <sub>2</sub>	$\beta$ -MgH <sub>2</sub>	meas./nominal	$\gamma$ -MgH <sub>2</sub>	$\beta$ -MgH <sub>2</sub>	$\epsilon$ -TiH <sub>2</sub>	Rwp%
24	65	11/9	5	7	8	15
S.G.			Cell parameters (Å)			
<i>Pbcn</i>	<i>P4<sub>2</sub>/mnm</i>	<i>I4/mmm</i>	<i>a</i> = 4.526 (4)	<i>a</i> = 4.518(1)	<i>a</i> = 3.176(1)	
			<i>b</i> = 5.427(3)	<i>c</i> = 3.028(1)	<i>c</i> = 4.403(1)	
			<i>c</i> = 4.971 (3)			
Theoretical [4]						
Phase label	Prototype	Pearson symbol	Density (mg/m <sup>3</sup> )	Volume (nm <sup>3</sup> )	Cell parameter (Å)	Cell angles (°)
TiH <sub>2</sub> ( $\delta$ )	CaF <sub>2</sub>	cF12 <i>Fm-3m</i>	3.56	0.0932	<i>a</i> = 4.5345 <i>c</i> = 4.5345	$\alpha$ = 90 $\beta$ = 90 $\gamma$ = 90



**Figure 4.3.** Rietveld analysis of XRD pattern of as-milled 0.95MgH<sub>2</sub>+0.05TiH<sub>2</sub> NC

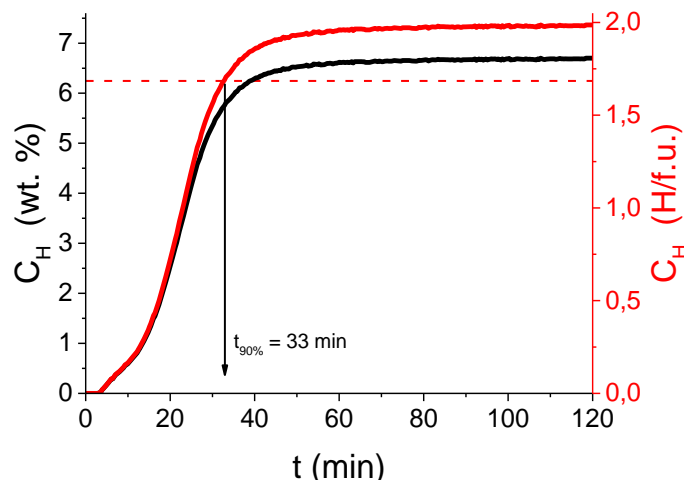
**b) System 0.95MgH<sub>2</sub>-0.05ZrH<sub>2</sub>**

Figure 4.4 shows the evolution of hydrogen pressure and vial temperature during RBM synthesis of MgH<sub>2</sub>-ZrH<sub>2</sub> composite. Variation of these parameters on milling is virtually identical to the Ti-case, so no further description is here given.



**Figure 4.4.** Evolution of the hydrogen pressure (black line) and the vial temperature (red line) as a function of milling time during the synthesis of the composite 0.95MgH<sub>2</sub>+0.05ZrH<sub>2</sub>

Figure 4.5 displays the hydrogen uptake during the milling process in weight percent (wt.%) and hydrogen atoms per formula unit (H/f.u.). The Zr dihydride is formed in less than 20 min. Then, 90 % of the MgH<sub>2</sub> phase formation is obtained after 33 min. Finally, the maximum uptake capacity is achieved after 120 min. The maximum values of  $C_H$  are 1.9 H/f.u. and 6.7 wt.%, which agrees with the nominal ones.



**Figure 4.5.** Hydrogen uptake curves in weight percent (black line) and hydrogen atoms per formula unit (red line) during the first milling cycle of 0.95MgH<sub>2</sub>+0.05ZrH<sub>2</sub>

The XRD pattern of as-synthesized 0.95MgH<sub>2</sub>+0.05ZrH<sub>2</sub> is shown in Figure 4.6. Broad diffraction peaks are detected evidencing nanostructured materials. Three different phases are observed: the two  $\beta$ - and  $\gamma$ -MgH<sub>2</sub> polymorphs and  $\epsilon$ -ZrH<sub>2</sub>. Table 4.2 gathers phase amounts and average crystallite sizes determined by the Rietveld method [3]. The most abundant phase is  $\beta$ -MgH<sub>2</sub>, followed by  $\gamma$ -MgH<sub>2</sub> and finally  $\epsilon$ -ZrH<sub>2</sub>. The crystallite size is identical for all phases (7 nm). No ternary Mg-Zr-H phase was detected.

**Table 4.2.** Crystallographic properties of as-milled 0.95MgH<sub>2</sub>+0.05ZrH<sub>2</sub> sample and Rietveld agreement factor.

Phase abundance (wt.%)			Crystal size(nm)				Rwp%
$\gamma$ -MgH <sub>2</sub>	$\beta$ -MgH <sub>2</sub>	ZrH <sub>2</sub> meas./nominal	$\gamma$ -MgH <sub>2</sub>	$\beta$ -MgH <sub>2</sub>	ZrH <sub>2</sub>		
34	55	11/15	7	7	7	5	
S.G.			Cell parameters (Å)				
<i>Pbcn</i>	<i>P4<sub>2</sub>/mnm</i>	<i>I4/mmm</i>	<i>a</i> = 4.553 (3)	<i>a</i> =4.530(1)	<i>a</i> =3.498 (1)		
			<i>b</i> = 5.405(4)	<i>c</i> = 3.032(1)	<i>c</i> = 4.561(2)		
			<i>c</i> = 5.030 (6)				
Theoretical [5]							
Phase label	Prototype	Pearson symbol	Density (mg/m <sup>3</sup> )	Volume (nm <sup>3</sup> )	Cell parameter (Å)	Cell angles (°)	
ZrH <sub>2</sub> $\epsilon$	ThH <sub>2</sub>	tI6 <i>I4/mmm</i>	5.63	0.055	<i>a</i> = <i>b</i> =3.5179 <i>c</i> =4.4447	$\alpha$ =90 $\beta$ =90 $\gamma$ =90	

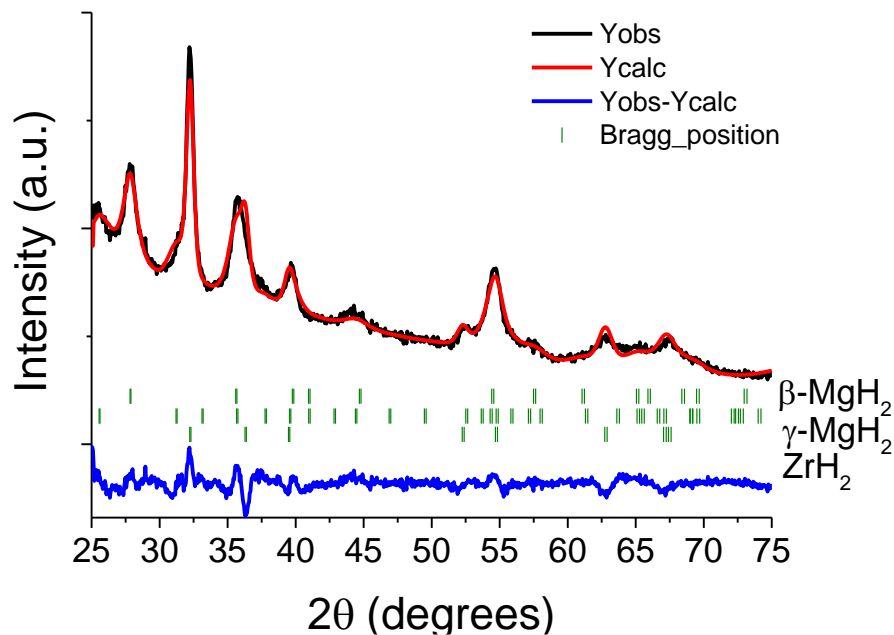


**Figure 4.6.** Rietveld analysis of XRD pattern of 0.95MgH<sub>2</sub>+0.05ZrH<sub>2</sub> nanocomposite

### 4.1.2 Hydrogen sorption properties

#### a) Pressure-composition isotherms

Figure 4.7 shows the PCI isotherms at 300 °C (573 K) of 0.95MgH<sub>2</sub>-0.05TiH<sub>2</sub> (left) and 0.95MgH<sub>2</sub>-0.05ZrH<sub>2</sub> (right) nanocomposites. For Ti, the PCI is characterized by a flat plateau pressure at 0.16 MPa extending from 0.34 to 6.5 wt.%H and exhibiting low hysteresis. For the Zr case, the PCI isotherms show a flat plateau at 0.14 MPa from 0.31 to 6.45 wt.%H. The value of the plateau pressure for both NCs is very close to that of pure MgH<sub>2</sub> (0.16 MPa). This MgH<sub>2</sub> value is obtained by the reported thermodynamic properties of magnesium hydride the hydrogenation and dehydrogenation enthalpies (74.1 and 75.8 kJ mol H<sub>2</sub><sup>-1</sup>), and entropies (133.2 and 135.1 JK<sup>-1</sup>molH<sub>2</sub><sup>-1</sup>)[6].

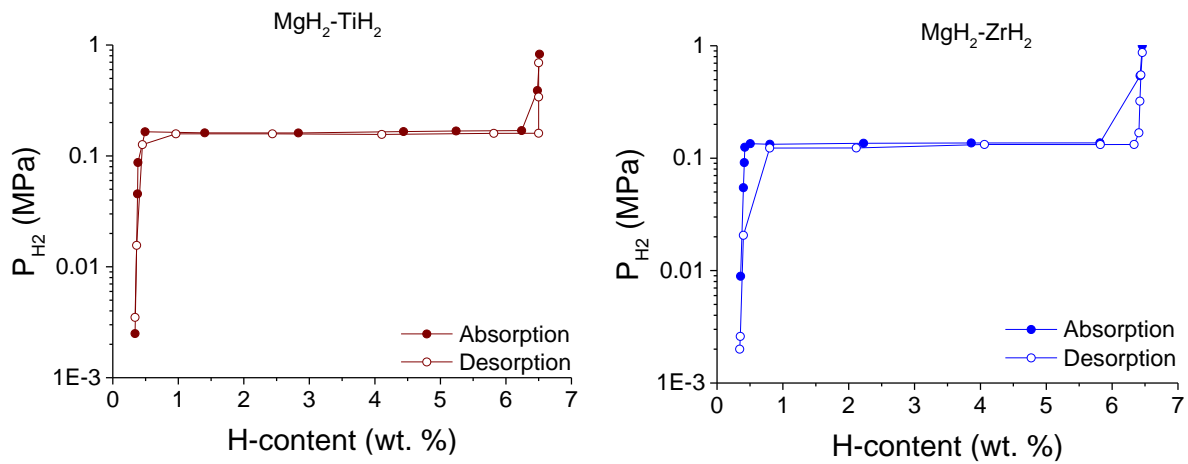


**Figure 4.7.** PCI absorption (full symbols) and desorption (empty symbols) isotherms at 300°C. left) 0.95MgH<sub>2</sub>-0.05TiH<sub>2</sub>, right) 0.95MgH<sub>2</sub>-0.05ZrH<sub>2</sub>

#### b) Evolution of the reversible hydrogen capacity with cycling under constrained reaction time

MgH<sub>2</sub>-TiH<sub>2</sub> and MgH<sub>2</sub>-ZrH<sub>2</sub> nanocomposites have been cycled under a hydrogen atmosphere at 300°C. H-cycling sorption experiments have been arbitrarily constrained to 15 min, a characteristic practical time for refilling hydrogen storage tanks [7]. These sorption measurements were performed using a concept of quasi-constant pressure and equal driving force for absorption and desorption sweeps. The pressures were fixed to P<sub>abs</sub>=8 bar (0.8MPa) and P<sub>des</sub>= 0.03 bar (3x10<sup>-3</sup> MPa) for an equilibrium plateau pressure of P<sub>p</sub> = 0.16 MPa. Twenty manual absorption-desorption cycles were done.

Figure 4.8 shows the evolution of the C<sub>rev</sub>, upon cycling for MgH<sub>2</sub>-TiH<sub>2</sub> and MgH<sub>2</sub>-ZrH<sub>2</sub> nanocomposites. For the Ti-containing NC, C<sub>rev</sub> keeps almost constant during cycling; 5.2 ± 0.03 wt.%H. In contrast, for the Zr-containing-NC, C<sub>rev</sub> is higher for the first cycle (5.6 wt.%) then gradually falls to 3.5 wt.% in 10 cycles and then keeps constant.

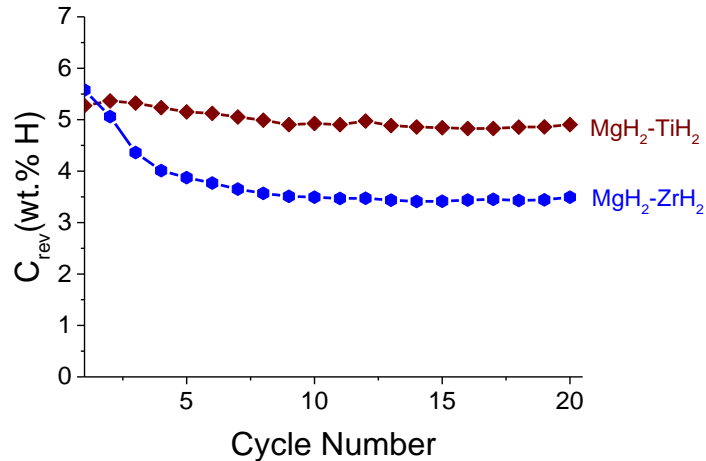


**Figure 4.8.**  $C_{rev}$  on cycling at 300 °C for 0.95MgH<sub>2</sub>-0.05TiH<sub>2</sub> and 0.95MgH<sub>2</sub>-0.05ZrH<sub>2</sub> nanocomposites. Reaction time limited to 15 min,  $P_{abs}=0.8\text{MPa}$ ,  $P_{des}= 3 \cdot 10^{-3} \text{MPa}$ .

### c) Hydrogen sorption curves

Figure 4.9 displays the hydrogen sorption curves for MgH<sub>2</sub>-TiH<sub>2</sub> and MgH<sub>2</sub>-ZrH<sub>2</sub> nanocomposites at initial (1<sup>st</sup> desorption, 2<sup>nd</sup> absorption) and final (20<sup>th</sup> absorption and desorption) sorption cycles. Since both TiH<sub>2</sub> and ZrH<sub>2</sub> are stable hydrides (as it has been explained in Chapter one) under our operation conditions, H-sorption curves are exclusively attributed to MgH<sub>2</sub> to Mg transformation (desorption) and the reverse reaction (absorption). Full MgH<sub>2</sub>-desorption (*i.e.* reacted fraction,  $\alpha = 1$ ) is defined with respect to the nominal H-content stored in MgH<sub>2</sub> in the NCs. For the Ti-containing NC, the reaction fraction at the constrained time (15 min) is limited to 60% for the 1<sup>st</sup> desorption (*i.e.* 40% of MgH<sub>2</sub> is retained in the NC). On the 2<sup>nd</sup> absorption, the absorbed amount is a little more than the half available, meaning that a part of Mg is not reacting to form MgH<sub>2</sub>. At the 20<sup>th</sup> desorption, reaction kinetic is faster than in the initial cycles with  $\alpha \geq 0.80$ . Meanwhile, the absorption looks similar, it can be noted that there is a slight acceleration in the kinetic after 20 cycles.

For the Zr-containing NC (right Fig 4.9), the 1<sup>st</sup> desorption shows faster kinetics than for the Ti-case with ca. 85% of MgH<sub>2</sub> decomposed in 6 min. Moreover, desorption kinetics accelerate on cycling with  $\alpha = 0.85$  in 1.5 min for the 20<sup>th</sup> desorption. In contrast, the 2<sup>nd</sup> absorption is rather fast ( $\alpha = 0.85$  in 2 min) but deteriorates on cycling for a reacted fraction over  $\alpha = 0.4$ . At the end of the 20<sup>th</sup> desorption, the reaction fraction attains 60% only and a large amount of Mg should be unreacted.

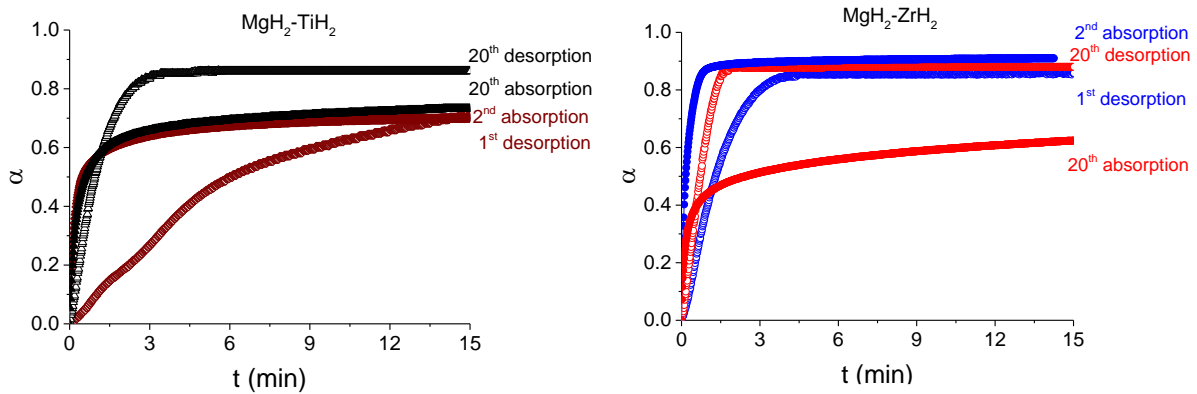


**Figure 4.9.** H-sorption curves at 300°C for cycles one, two and twenty. Left) 0.95MgH<sub>2</sub>-0.05TiH<sub>2</sub>, right) 0.95MgH<sub>2</sub>-0.05ZrH<sub>2</sub>

#### d) Evolution of hydrogen amount in cycling

Figure 4.10 shows the hydrogen content in MgH<sub>2</sub>-TiH<sub>2</sub> and MgH<sub>2</sub>-ZrH<sub>2</sub> nanocomposites after absorption and desorption sweeps and their evolution on cycling. For the Ti-containing NC, the desorption is not completed during the first cycle (*ca.* 2 wt.% not desorbed) and some MgH<sub>2</sub> is retained. The amount of MgH<sub>2</sub> retained gradually decreases on cycling (*ca.* 1 wt.% in cycle 20). This result concurs with the acceleration of desorption kinetics on cycling (Fig. 4.9). As for the absorption state, it contains more hydrogen in the first cycles, while it gradually decreases on long cycling so that the amount of unreacted Mg steadily increases. Consequently, the amount of reversible hydrogen storage keeps constant on cycling at *ca.* 5 wt % in agreement with Fig. 4.8. One can notice that the quantity of hydrogen stored in TiH<sub>2</sub> is supposed to be constant (*ca.* 0.34 wt.%).

For the Zr-containing NC (right Fig 4.10), the hydrogen content strongly decreases for the first four cycles, which concurs with the slowing down of absorption kinetics on cycling (Fig. 4.9. right). Such a decrease leads to a high amount of unreacted Mg. An opposing effect is observed during desorption. The amount of retained MgH<sub>2</sub> decreases on cycling due to an acceleration on hydrogen desorption on cycling (Fig. 4.9. right). After 20 cycles,  $C_{rev}$  is 3.8 wt.%, which is lower than for the Ti-containing NC, losing the most amount of capacity during the hydrogenation.

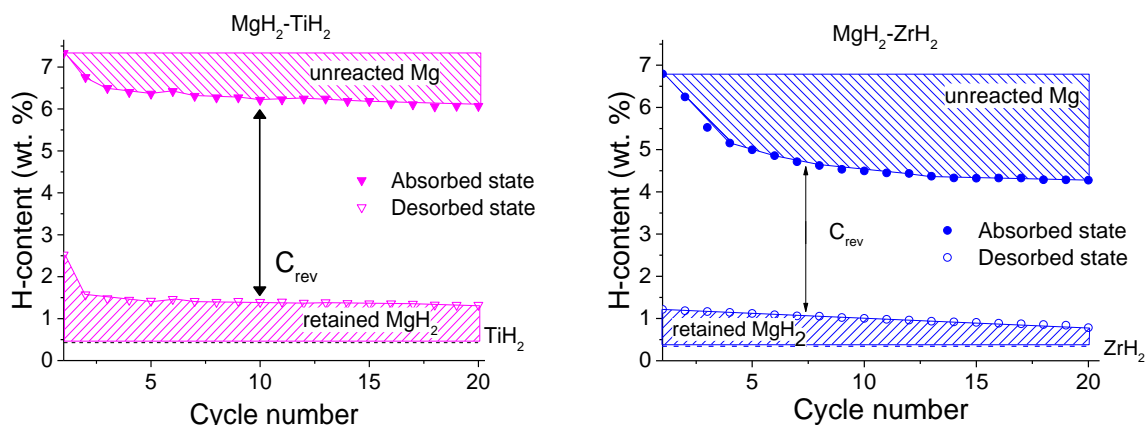


**Figure 4.10.** Evolution of hydrogen content with cycling for 0.95MgH<sub>2</sub>-0.05TiH<sub>2</sub> (left) and 0.95MgH<sub>2</sub>-0.05ZrH<sub>2</sub> (right) nanocomposites. H-content is shown after absorption (full symbols) and desorption (empty symbols). Partial contributions from H-stored in TiH<sub>2</sub> or ZrH<sub>2</sub>, irreversibly retained as MgH<sub>2</sub> and reversibly stored in Mg ( $C_{rev}$ ) are shown.

#### 4.1.3 Effect of hydrogen cycling on the microstructure of MgH<sub>2</sub>-TiH<sub>2</sub> and MgH<sub>2</sub>-ZrH<sub>2</sub> NCs

XRD patterns of MgH<sub>2</sub>-TiH<sub>2</sub> and MgH<sub>2</sub>-ZrH<sub>2</sub> nanocomposites after 20 sorption cycles both in the absorbed and desorbed state are shown in Figure 4.11 and relevant crystallographic data from Rietveld analysis are gathered in Tables 4.3 and 4.4. XRD patterns of both absorbed and desorbed MgH<sub>2</sub>-TiH<sub>2</sub> can be indexed with three phases:  $\beta$ -MgH<sub>2</sub>,  $\epsilon$ -TiH<sub>2</sub>, and Mg. Amount and crystallinity of  $\epsilon$ -TiH<sub>2</sub>, both in absorbed and desorbed states, do not change significantly as compared to the as-synthesized NC. In contrast, MgH<sub>2</sub> undergoes drastic changes in content and crystal size. Taking apart TiH<sub>2</sub>, MgH<sub>2</sub> is the main phase (83 wt.%) in the absorbed state and the minor one in the desorbed one (9 wt.%). A good agreement is found between MgH<sub>2</sub> amount as evaluated from XRD and kinetic data, which validates the hypothesis that incomplete Mg/MgH<sub>2</sub> transformation is due to kinetic effects.

MgH<sub>2</sub>-ZrH<sub>2</sub> diffraction patterns, both in absorbed and desorbed states, can be indexed by three phases:  $\beta$ -MgH<sub>2</sub>, ZrH<sub>2</sub>, and Mg. In the absorbed state, the main phase is  $\beta$ -MgH<sub>2</sub> (51 wt.%) but a significant amount of Mg (34 wt.%) remains unreacted. As it has been shown in the kinetic study, there is a significant amount of unreacted Mg in the sample during absorption. Desorbed state agrees with the kinetic results (Fig. 4.10 right), there is a great amount of Mg (75 wt.%) and a little quantity of retained MgH<sub>2</sub> (5 wt.%). There is no change in the amount and crystallinity of ZrH<sub>2</sub> on cycling as, at the operation conditions, it is a stable hydride.

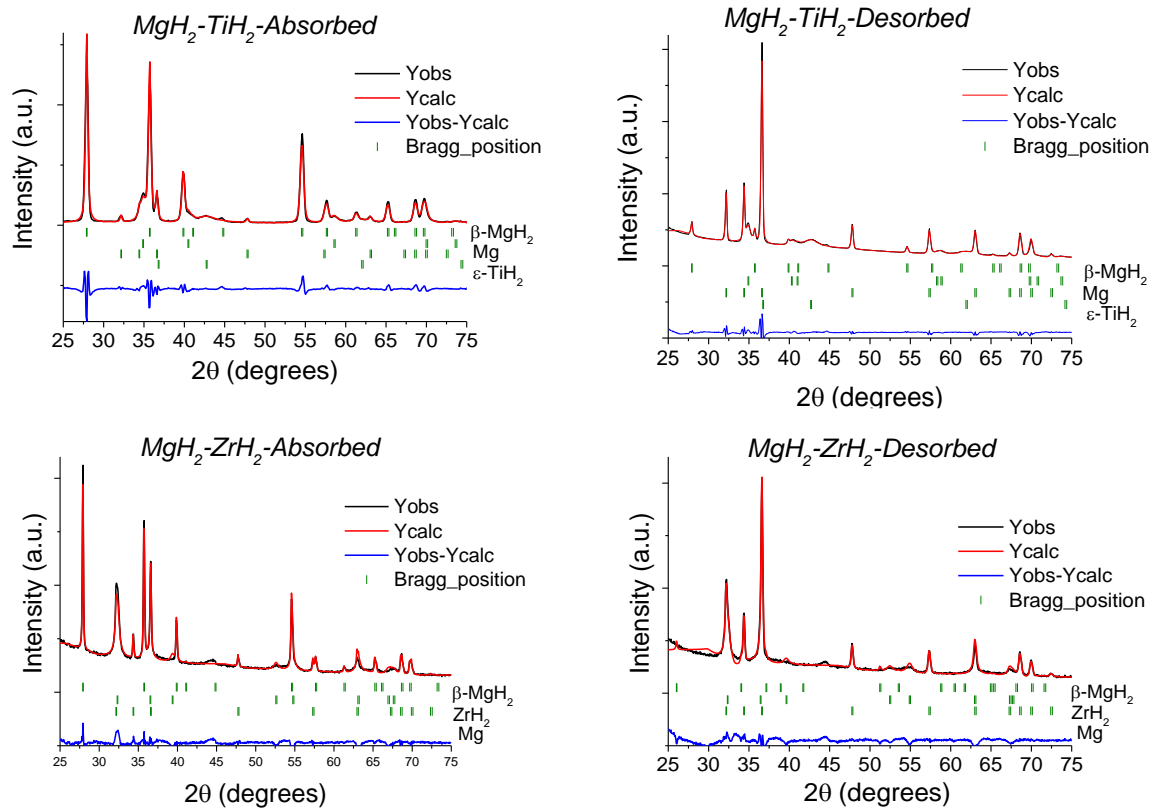


**Figure 4.11.** Rietveld analysis of XRD patterns of 0.95MgH<sub>2</sub>-0.05TiH<sub>2</sub>, (top) and 0.95MgH<sub>2</sub>-0.05ZrH<sub>2</sub> (bottom) nanocomposites after 20 cycles in both absorbed (left) and desorbed (right) states

**Table 4.3.** Crystallographic properties of (des-)absorbed Ti-containing NC after 20 sorption cycles and Rietveld agreement factor.

Absorbed

Phase abundance (wt.%)			Crystal size(nm)			
Mg	β-MgH <sub>2</sub>	meas./nominal	Mg	β-MgH <sub>2</sub>	TiH <sub>2</sub>	Rwp%
8	83	9/11	-	31	8	13
S.G.			Cell parameters (Å)			
<i>P6<sub>3</sub>/mmc</i>	<i>P4<sub>2</sub>/mnm</i>	<i>I4/mmm</i>	<i>a</i> =4.518(1)		<i>a</i> =3.169 (1)	
			<i>c</i> = 3.021(1)		<i>c</i> = 4.606(3)	

Desorbed

Phase abundance (wt.%)			Crystal size(nm)			
Mg	β-MgH <sub>2</sub>	meas./nominal	Mg	β-MgH <sub>2</sub>	TiH <sub>2</sub>	Rwp%
77	9	14/11	87	-	8	14
S.G.			Cell parameters (Å)			
<i>P6<sub>3</sub>/mmc</i>	<i>P4<sub>2</sub>/mnm</i>	<i>I4/mmm</i>	<i>a</i> =3.212(1)		<i>a</i> =3.169 (1)	
			<i>c</i> = 5.215(2)		<i>c</i> = 4.401(1)	

**Table 4.4.** Crystallographic properties (des-)absorbed Zr-containing NC after 20 sorptions and Rietveld agreement factor.

Absorbed

Phase abundance (wt.%)			Crystal size(nm)			
Mg	$\beta$ -MgH <sub>2</sub>	ZrH <sub>2</sub>	Mg	$\beta$ -MgH <sub>2</sub>	ZrH <sub>2</sub>	Rwp%
		meas./nominal				
34	51	15/15	75	75	11	9
S.G.			Cell parameters (Å)			
<i>P6<sub>3</sub>/mmc</i>	<i>P4<sub>2</sub>/mnm</i>	<i>I4/mmm</i>	<i>a</i> =3.213(1) <i>c</i> = 5.220(1)	<i>a</i> =4.519(1) <i>c</i> = 3.022(1)	<i>a</i> =3.478 (1) <i>c</i> = 4.579(1)	

Desorbed

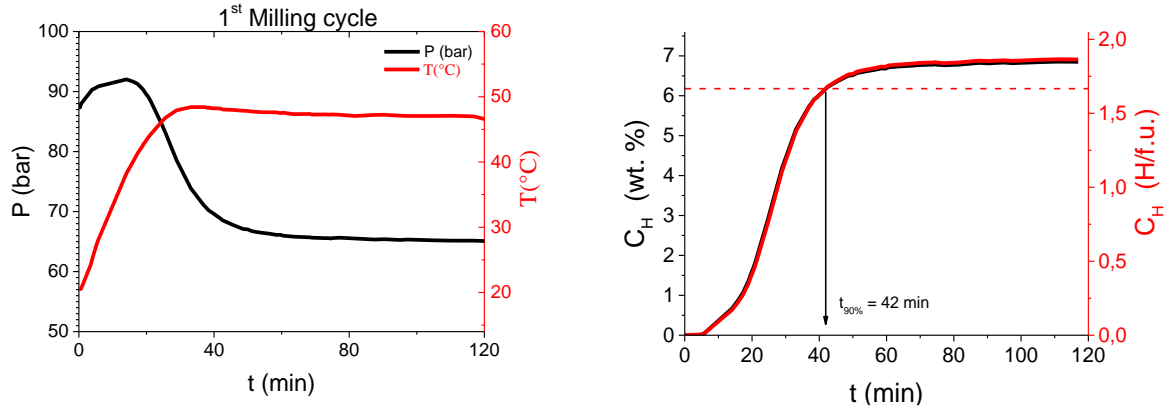
Phase abundance (wt.%)			Crystal size(nm)			
Mg	$\beta$ -MgH <sub>2</sub>	ZrH <sub>2</sub>	Mg	$\beta$ -MgH <sub>2</sub>	ZrH <sub>2</sub>	Rwp%
		meas./nominal				
75	5	15/15	50	-	8	7
S.G.			Cell parameters (Å)			
<i>P6<sub>3</sub>/mmc</i>	<i>P4<sub>2</sub>/mnm</i>	<i>I4/mmm</i>	<i>a</i> =3.212(1) <i>c</i> = 5.216(1)		<i>a</i> =3.485 (1) <i>c</i> = 4.558(1)	

## 4.2 MgH<sub>2</sub> with group 3 transition metals Sc and Y

### 4.2.1 Synthesis and structural characterization

#### a) System 0.95MgH<sub>2</sub>-0.05ScH<sub>2</sub>

The NC 0.95MgH<sub>2</sub>-0.05ScH<sub>2</sub> was synthesized by RBM. A problem in the acquisition data during milling occurred, so it was not possible to measure the second milling cycle. However, we were able to evaluate the hydrogen uptake from the initial and final hydrogen pressure in the jar. The experimental  $C_H$  is 7.0 wt.% which agrees with the theoretical one assuming 0.95MgH<sub>2</sub>-0.05ScH<sub>2</sub> formation. As it has been explained in Chapter one, the metallic Sc was received in lumps. It was performed a first hydrogenation and a simultaneous decrepitation of the hydride. Then, it was sized in 20/100 mesh, and the dihydride was mixed with the Mg powder.



Left: Hydrogen pressure evolution during RBM of Sc-containing NC (black line) and temperature vial (red line) as a function of milling. Right: hydrogen uptake curves in weight percent (black line) and hydrogen atoms per formula unit (red line).

The XRD pattern of as-synthesized 0.95MgH<sub>2</sub>-0.05ScH<sub>2</sub> is shown in Figure 4.12. The pattern can be indexed in three phases:  $\beta$ -MgH<sub>2</sub>,  $\gamma$ -MgH<sub>2</sub>, and ScH<sub>2</sub>. The crystallographic are presented in Chapter 1. The pattern (black line) exhibits broad diffraction peaks evidencing nanostructuring. Table 4.5 summarizes the crystallographic properties of this nanocomposite as evaluated from Rietveld refinement (red line in Fig. 4.12). The most abundant phases are  $\beta$ -MgH<sub>2</sub> (69 wt. %) and  $\gamma$ -MgH<sub>2</sub> (22 wt. %). ScH<sub>2</sub> content (9 wt.%) agrees with the targeted composition of the material 0.95MgH<sub>2</sub>+0.05ScH<sub>2</sub>, in agreement with the fact that no ternary Mg-Sc-H phases were detected. Crystal sizes are the same for  $\beta$ - and  $\gamma$ -MgH<sub>2</sub> phases (7 nm). Interestingly, crystal size for ScH<sub>2</sub> is quite large (23 nm) as compared to previous additives. Several previous studies report this larger crystal size [8,9].

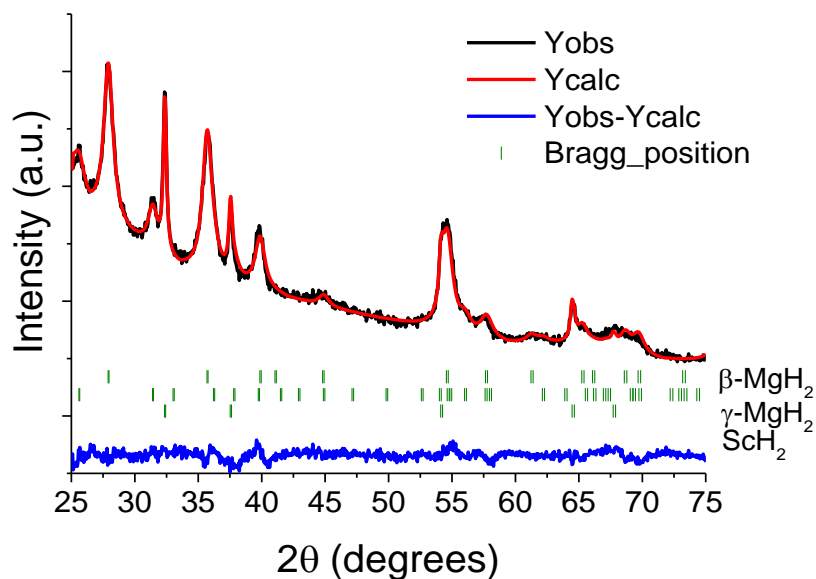


Figure 4.12. Rietveld analysis of XRD patterns for Sc-NC

**Table 4.5.** Crystallographic properties of as-synthesized 0.95MgH<sub>2</sub>+0.05ScH<sub>2</sub> sample and Rietveld agreement factor.

Phase abundance (wt.%)			Crystal size(nm)			
$\gamma$ -MgH <sub>2</sub>	$\beta$ -MgH <sub>2</sub>	ScH <sub>2</sub> meas./nominal	$\gamma$ -MgH <sub>2</sub>	$\beta$ -MgH <sub>2</sub>	ScH <sub>2</sub>	Rwp%
22	69	9/9	7	7	23	3
S.G.			Cell parameters (Å)			
<i>Pbcn</i>	<i>P4<sub>2</sub>/mnm</i>	<i>Fm-3m</i>	<i>a</i> = 4.533 (3)	<i>a</i> =4.519(1)	<i>a</i> =3.789 (1)	
			<i>b</i> = 5.420(2)	<i>c</i> = 3.024(1)		
			<i>c</i> = 4.958 (3)			
Theoretical [10]						
Phase label	Prototype	Pearson symbol	Density (mg/m <sup>3</sup> )	Volume (nm <sup>3</sup> )	Cell parameter (Å)	Cell angles (°)
ScH <sub>2</sub> $\delta$	CaF <sub>2</sub>	cF12 <i>Fm-3m</i>	2.85	0.1095	<i>a</i> =4.7844	$\alpha$ =90 $\beta$ =90 $\gamma$ =90

### b) System 0.95MgH<sub>2</sub>-0.05YH<sub>3</sub>

Synthesis process of Y-containing NC from Mg and Y powders is shown in Figure 4.13. The evolution of hydrogen pressure (left) and hydrogen uptake (right) as a function of milling time is displayed. Qualitative evolution of pressure and temperature on milling is like previous synthesis. Final hydrogen uptake is 1.9 H/f.u. and 6.8 wt.% which reasonably agrees with the expected values: 2.05 H/f.u and 6.9 wt.%, respectively.

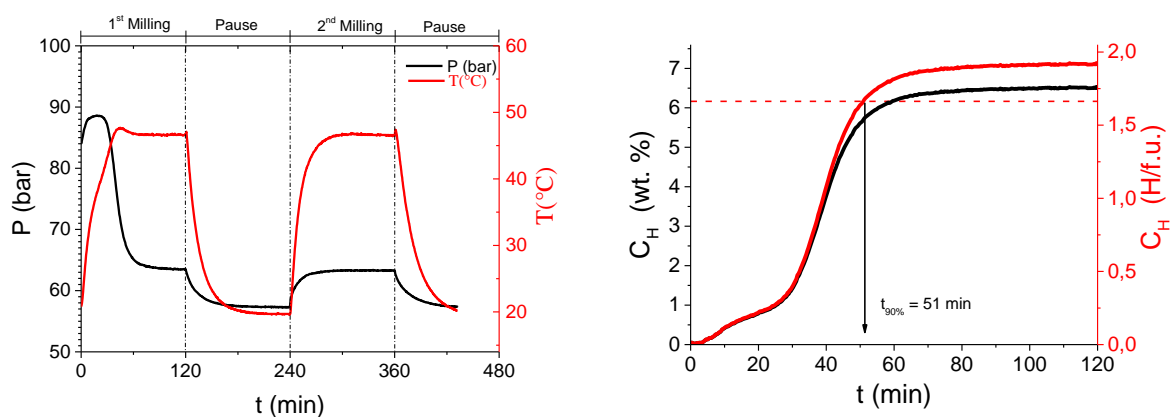
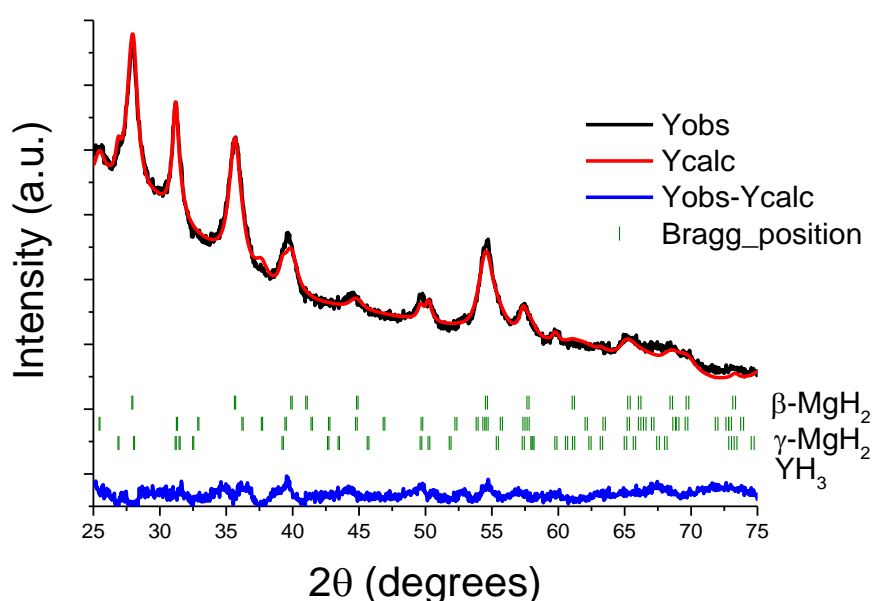

**Figure 4.13.** Left: Hydrogen pressure evolution during RBM of Y-containing NC (black line) and temperature vial (red line) as a function of milling. Right: hydrogen uptake curves in weight percent (black line) and hydrogen atoms per formula unit (red line).

Figure 4.14 shows the XRD pattern of the as-synthesized Y-containing NC. The pattern can be indexed with three phases  $\beta$ -MgH<sub>2</sub>,  $\gamma$ -MgH<sub>2</sub>, and YH<sub>3</sub>. No ternary Mg-Y-H phase was detected. Rietveld refinement was carried out and the main crystallographic properties are gathered in Table 4.6. The main phase is  $\beta$ -MgH<sub>2</sub> (70 wt. %). Minor phases are  $\gamma$ -MgH<sub>2</sub> (20 wt.

%) and YH<sub>3</sub> (10 wt. %). The crystal sizes are the same for both MgH<sub>2</sub> polymorphs (7 nm) and a little larger for YH<sub>3</sub> (13 nm).

**Table 4.6.** Crystallographic properties of as-milled 0.95MgH<sub>2</sub>+0.05YH<sub>3</sub> sample and Rietveld agreement factor.

Phase abundance (wt.%)			Crystal size(nm)				Rwp%
$\gamma$ -MgH <sub>2</sub>	$\beta$ -MgH <sub>2</sub>	YH <sub>3</sub> meas./nominal	$\gamma$ -MgH <sub>2</sub>	$\beta$ -MgH <sub>2</sub>	YH <sub>3</sub>		
20	70	10/16	7	7	13	3	
S.G.			Cell parameters (Å)				
<i>Pbcn</i>	<i>P4<sub>2</sub>/mnm</i>	<i>P-3c1</i>	$a=4.567(3)$ $b=5.447(3)$ $c=4.960(3)$	$a=4.519(1)$ $c=3.033(1)$	$a=6.3617(1)$ $c=6.635(2)$		
Theoretical							
Phase label	Prototype	Pearson symbol	Density (mg/m <sup>3</sup> )	Volume (nm <sup>3</sup> )	Cell parameter (Å)	Cell angles (°)	
YH <sub>3</sub>	HoH <sub>3</sub>	hP24 <i>P-3c1</i>	3.96	0.2313	$a=6.3587$ $c=6.6068$	$\alpha=90$ $\beta=90$ $\gamma=120$	



**Figure 4.14.** Rietveld analysis of XRD pattern of as-milled 0.95MgH<sub>2</sub>+0.05YH<sub>3</sub> NC

#### 4.2.2. Hydrogen sorption properties

##### a) Pressure-composition isotherms

Isothermal PCI curves at 300 °C of Sc-containing and Y-containing NC are depicted in Figure 4.15. Their isotherms are very similar. For Sc-containing NC, the isotherm exhibits a flat plateau pressure at 0.14 MPa with a width of 6 wt.%. No significant hysteresis is observed between absorption and desorption isotherms. For the Y-containing NC, the plateau pressure, which exhibits low hysteresis is located at 0.15 MPa. The width of the plateau is also 6 wt. %.

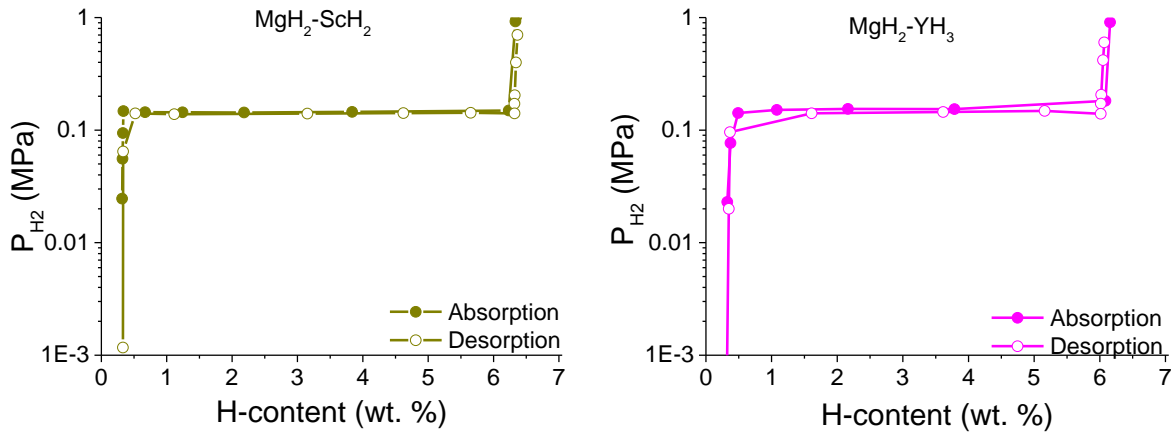


**Figure 4.15.** PCI absorption (full symbols) and desorption (empty symbols) isotherms at 300°C. Left) 0.95MgH<sub>2</sub>-0.05ScH<sub>2</sub>, right) 0.95MgH<sub>2</sub>-0.05YH<sub>3</sub>

**b) Evolution of the reversible hydrogen capacity with cycling under constrained reaction time**

H-cycling sorption experiments are carried out at 300 °C with 15 min absorption/desorption sweeps. The evolution of the reversible capacity on cycling  $C_{rev}$  for both Sc- and Y-containing NC is shown in Fig. 4.16 and compared to that of the Ti-containing one. The initial  $C_{rev}$  capacity for Sc-containing NC is quite small (3.5 wt. %) but improves on cycling to attain 4.8 wt.% after 7 cycles and gradually decrease down to 4.1 wt.% after 20 cycles. For the Y-containing compound, the initial  $C_{rev}$  is extremely low (1 wt.%) and it further decreases down to 0.6 wt.% after 20 cycles. A similar behavior has been observed in the NC of pure magnesium (Fig. 3.9 Chapter 3) where  $\gamma = 0$  exhibited in the first cycle very low reversible capacity,  $C_{rev} = 0.5$  wt.%, with a gradual decrease after 20 cycles:  $C_{rev} = 0.2$  wt.%. The Ti-containing composite exhibits higher reversible capacity and more stable cycling behavior as compared to both Sc- and Y-containing NCs.

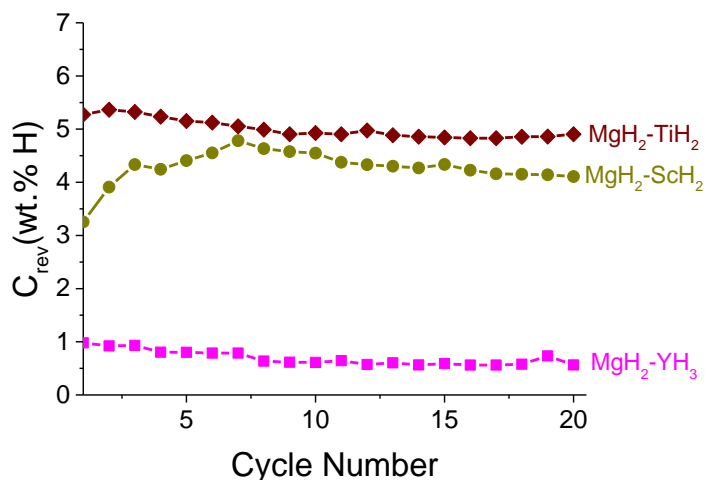


**Figure 4.16.**  $C_{rev}$  on cycling at 300 °C for 0.95MgH<sub>2</sub>-0.05ScH<sub>2</sub> and 0.95MgH<sub>2</sub>-0.05YH<sub>3</sub> and 0.95MgH<sub>2</sub>-0.05TiH<sub>2</sub> nanocomposites. Reaction time limited to 15 min.

### c) Hydrogen sorption curves

Figure 4.17 displays the hydrogen sorption curves for MgH<sub>2</sub>-ScH<sub>2</sub> and MgH<sub>2</sub>-YH<sub>3</sub> nanocomposites at initial (1<sup>st</sup> desorption, 2<sup>nd</sup> absorption) and final (20<sup>th</sup> absorption and desorption) sorption cycles. For Sc-containing NC (left), kinetics of the 1<sup>st</sup> desorption is sluggish. Only 47% of the reaction fraction takes place in 15 min, leaving 53% of retained MgH<sub>2</sub>. On the 2<sup>nd</sup> absorption, kinetics is, however, faster and 97% of the previously formed Mg is converted into MgH<sub>2</sub>. At the 20<sup>th</sup> desorption, kinetics is faster than for the first desorption sweep but the transformed fraction only attains 64%. At the 20<sup>th</sup> absorption, kinetics is very close to the 2<sup>nd</sup> sweep but the final reaction fraction is much lower:  $\alpha = 0.75$  and 0.97 for 2<sup>nd</sup> and 20<sup>th</sup> absorption, respectively.

For Y-containing NC (Fig. 4.17 right), the desorption kinetics are similar and extremely slow at cycles one and twenty, leading to a large amount of retained MgH<sub>2</sub>. On the other hand, H-absorption of the previously formed Mg is fast: after 15 min., more than 90% of the formed Mg returns to MgH<sub>2</sub>. Comparing both NCs with TiH<sub>2</sub>, the kinetics of the latter one is getting faster in both absorption and desorption, this also happened in desorption for Sc-NC. However, the absorption is slowing down for in Sc-NC, as for Y-NC in a slightly way.

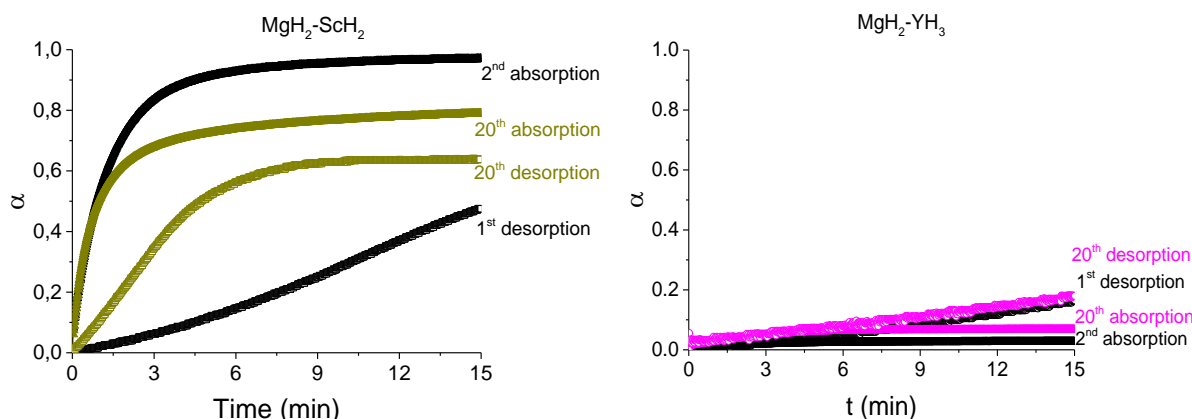


**Figure 4.17.** H-sorption curves at 300°C for cycles one, two and twenty. Left) 0.95MgH<sub>2</sub>-0.05ScH<sub>2</sub>, right) 0.95MgH<sub>2</sub>-0.05YH<sub>3</sub>

### d) Evolution of hydrogen amount on cycling

Figure 4.18 shows the evolution of hydrogen content in MgH<sub>2</sub>-ScH<sub>2</sub> and MgH<sub>2</sub>-YH<sub>3</sub> NCs upon cycling both after absorption and desorption sweeps. For the Sc-containing NC, the retained amount of MgH<sub>2</sub> in the first desorption is high because of the sluggish desorption kinetic described before (Fig. 4.17 left). Nevertheless, absorption kinetics in the first cycles is fast, and low amount of Mg remains unreacted. As cycling proceeds, desorption kinetics accelerate and the retained MgH<sub>2</sub> decreases. In contrast, the amount of unreacted Mg increases on cycling. As a result, the reversible capacity increases on cycling particularly within the first cycles (see also Fig. 4.16). For the Y-containing NC (Figure 4.18 right), the amount of retained MgH<sub>2</sub> is extremely high (above 5 wt.%) due to the very slow desorption kinetics of Y-containing NC (Fig. 4.17 right). In contrast, the absorption kinetics are relatively high and almost full reformation of MgH<sub>2</sub> occurs. However, the reversible capacity does not surpass 1 wt. % on cycling. As it has been discussed above the Ti-NC  $C_{rev}$  is 5 wt %, for Sc-NC and Y-NC,

$C_{rev}$  = 4.4 and 1 wt %, respectively. Ti-NC shows higher value due to the improvement of the kinetic.

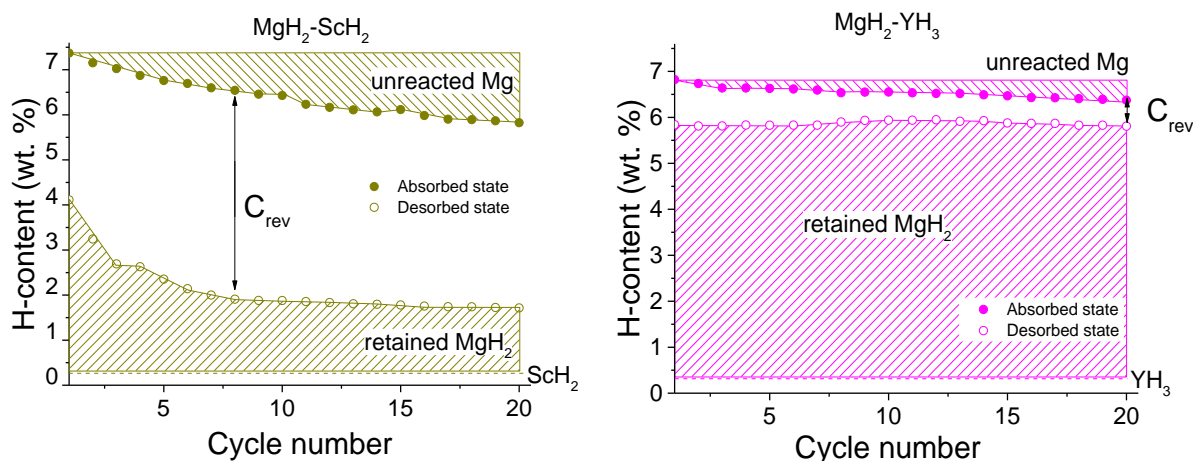


**Figure 4.18.** Evolution of hydrogen content with cycling for 0.95MgH<sub>2</sub>-0.05ScH<sub>2</sub> (left) and 0.95MgH<sub>2</sub>-0.05YH<sub>3</sub> (right) nanocomposites. H-content is shown after absorption (full symbols) and desorption (empty symbols). Partial contributions from H-stored in ScH<sub>2</sub>, YH<sub>3</sub>, irreversibly retained as MgH<sub>2</sub> and reversibly stored in Mg ( $C_{rev}$ ) are shown.

#### 4.2.3 Effect of hydrogen cycling on the microstructure of MgH<sub>2</sub>-ScH<sub>2</sub> and MgH<sub>2</sub>-YH<sub>3</sub>

##### NCs

XRD patterns of MgH<sub>2</sub>-ScH<sub>2</sub> and MgH<sub>2</sub>-YH<sub>3</sub> nanocomposites after 20 sorption cycles both in the absorbed and desorbed state are shown in Figure 4.19 and relevant crystallographic data from Rietveld analysis are gathered in Tables 4.7 and 4.8. XRD patterns of both absorbed and desorbed MgH<sub>2</sub>-ScH<sub>2</sub> can be indexed with three phases:  $\beta$ -MgH<sub>2</sub>, Mg and ScH<sub>2</sub>. Phase amount and crystallinity of ScH<sub>2</sub> in both absorbed and desorbed state remain the same as for the as-synthesized NC. In contrast, MgH<sub>2</sub> and Mg change in content and crystal size. MgH<sub>2</sub> is the main phase (70 wt.%) in the absorbed state and the minor one (5 wt.%) in the desorbed one showing rather high reversibility for hydrogen storage. A good agreement is found between XRD and kinetic data, which validates the hypothesis that incomplete Mg/MgH<sub>2</sub> transformation is due to kinetic limitations. Crystal sizes of MgH<sub>2</sub> and Mg are quite close and do not exhibit significant change between absorbed and desorbed states (60±10 nm).

MgH<sub>2</sub>-YH<sub>3</sub> diffraction patterns (Fig. 4.19 bottom) after 20 cycles in absorbed and desorbed states can be indexed with three phases:  $\beta$ -MgH<sub>2</sub>, YH<sub>3</sub>, and Mg. As discussed in the previous kinetic section, the main phase in both states is  $\beta$ -MgH<sub>2</sub>. Its crystal size is practically the same in both states (ca. 50 nm). Comparing both NCs with Ti-NC, this last one shows an increase of the  $\beta$ -MgH<sub>2</sub> phase in the absorbed state as well as, Mg phase in the desorbed state, because of the improved kinetic, that is not observed for Sc-NC and Y-NC.

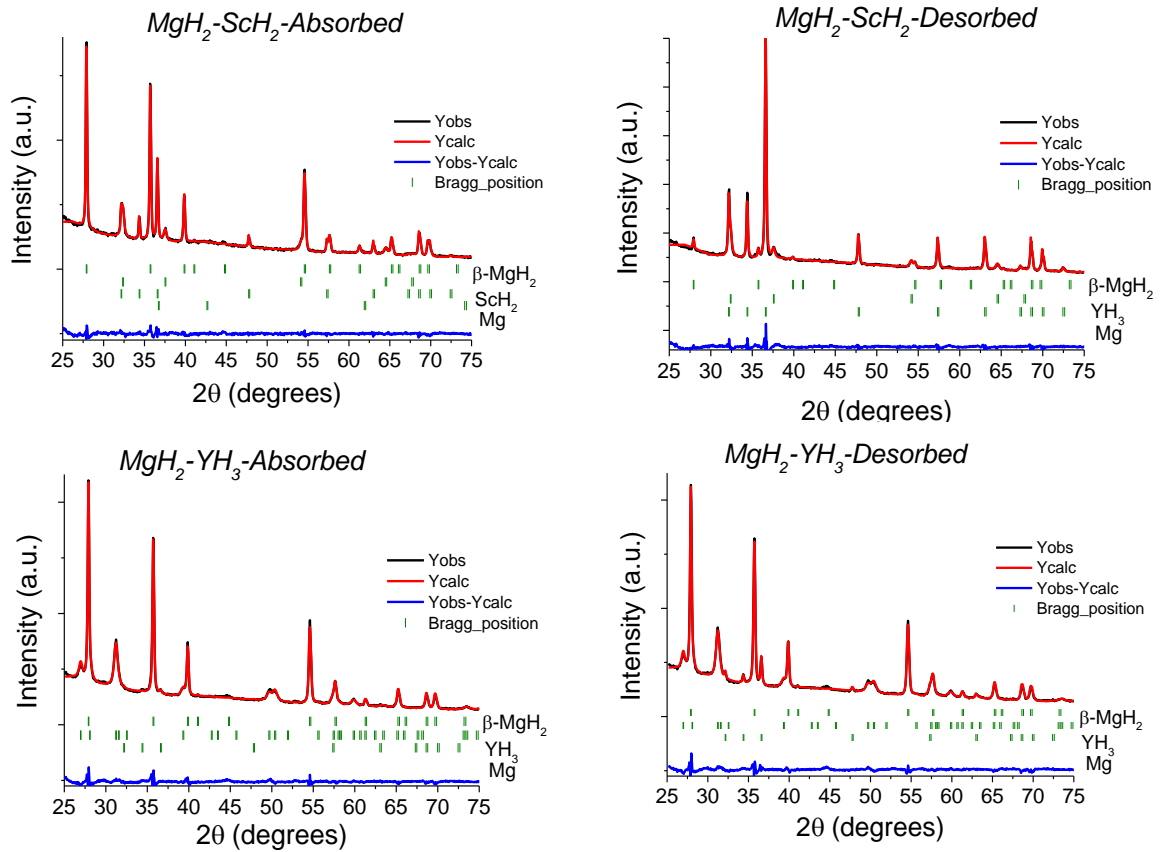


**Figure 4.19.** Rietveld analysis of XRD patterns of 0.95MgH<sub>2</sub>-0.05ScH<sub>2</sub> (top) and 0.95MgH<sub>2</sub>-0.05YH<sub>3</sub> (bottom) nanocomposites after 20 cycles in both absorbed (left) and desorbed (right) states

**Table 4.7.** Crystallographic properties (des)absorbed Sc-containing NC after 20 sorption cycles and Rietveld agreement factor.

Absorbed

Phase abundance (wt.%)			Crystal size(nm)				Rwp%
Mg	β-MgH <sub>2</sub>	ScH <sub>2</sub> meas./nominal	Mg	β-MgH <sub>2</sub>	ScH <sub>2</sub>		
20	70	10/10	70	70	20	3	
S.G.			Cell parameters (Å)				
<i>P6<sub>3</sub>/mmc</i>	<i>P4<sub>2</sub>/mnm</i>	<i>Fm-3m</i>	<i>a</i> = 3.213 (3) <i>c</i> = 4.960 (3)	<i>a</i> = 4.521(1) <i>c</i> = 3.023(1)	<i>a</i> = 4.791 (1)		

Desorbed

Phase abundance (wt.%)			Crystal size(nm)				Rwp%
Mg	β-MgH <sub>2</sub>	ScH <sub>2</sub> meas./nominal	Mg	β-MgH <sub>2</sub>	ScH <sub>2</sub>		
85	5	10/10	55	-	20	5	
S.G.			Cell parameters (Å)				
<i>P6<sub>3</sub>/mmc</i>	<i>P4<sub>2</sub>/mnm</i>	<i>Fm-3m</i>	<i>a</i> = 3.211 (1) <i>c</i> = 5.214 (3)	<i>a</i> = 4.518(1) <i>c</i> = 3.023(1)	<i>a</i> = 4.787 (1)		

**Table 4.8.** Crystallographic properties of abs(desorbed) Y-NC after 20 cycles and Rietveld agreement factor. Absorbed

Phase abundance (wt.%)			Crystal size(nm)			
Mg	$\beta$ -MgH <sub>2</sub>	YH <sub>3</sub> meas./nominal	Mg	$\beta$ -MgH <sub>2</sub>	YH <sub>3</sub>	Rwp%
1	84	15/16	-	56	13	3
S.G.			Cell parameters (Å)			
<i>P6<sub>3</sub>/mmc</i>	<i>P4<sub>2</sub>/mnm</i>	<i>P-3c1</i>	<i>a</i> =4.520(1)		<i>a</i> = 6.355 (1)	
			<i>c</i> = 3.023(1)		<i>c</i> = 6.610(1)	

Phase abundance (wt.%)			Crystal size(nm)			
Mg	$\beta$ -MgH <sub>2</sub>	YH <sub>3</sub> meas./nominal	Mg	$\beta$ -MgH <sub>2</sub>	YH <sub>3</sub>	Rwp%
7	77	16/16	-	50	15	3
S.G.			Cell parameters (Å)			
<i>P6<sub>3</sub>/mmc</i>	<i>P4<sub>2</sub>/mnm</i>	<i>P-3c1</i>	<i>a</i> =4.519(1)		<i>a</i> = 6.354 (1)	
			<i>c</i> = 3.023(1)		<i>c</i> = 6.608(1)	

### 4.3 MgH<sub>2</sub> with group 5 transition metals V and Nb

#### 4.3.1 Synthesis and structural characterization

##### a) System 0.95MgH<sub>2</sub>-0.05VH

Figure 4.20, left, shows the synthesis of V-containing NC with typical profiles of both vial temperature and hydrogen pressure. On the right, the hydrogen uptake curve is depicted and consists of two steps. The first uptake, at  $t < 30$  min with ca. 1 wt.% absorption is assigned to VH<sub>2</sub> formation. Later, Mg absorbs hydrogen with 90% of the reaction completed at 53 min. The total hydrogen content after 120 min of milling is  $C_H = 7.3$  wt.%, 1.9 H/f.u.

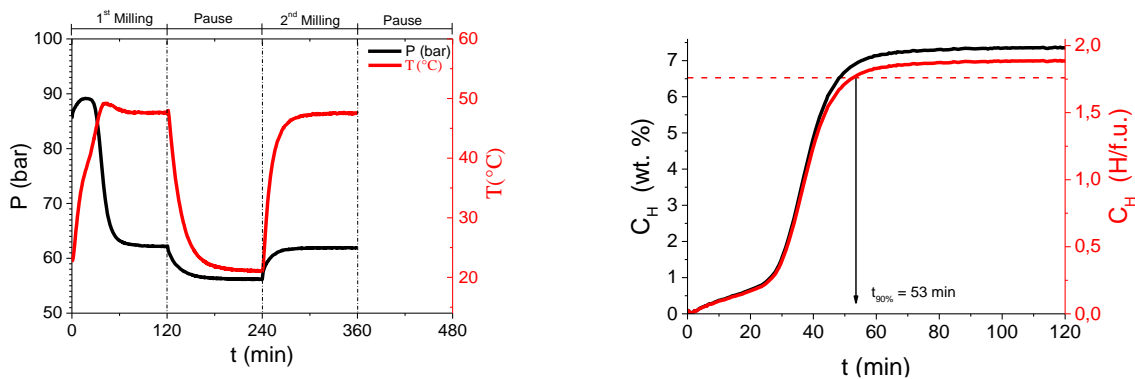


**Figure 4.20.** Left: Hydrogen pressure evolution and temperature vial (red line) as a function of milling during RBM (black line) of V-containing NC. Right: Hydrogen uptake curves in weight percent (black line) and hydrogen atoms per formula unit (red line).

The XRD pattern of the as-milled V-containing NC is shown in Figure 4.21. It can be indexed with three phases:  $\beta$ -MgH<sub>2</sub>,  $\gamma$ -MgH<sub>2</sub>, and VH. As it was explained in Chapter one VH<sub>0.8</sub> is where the  $\beta_1$  phase disappears and the  $\beta_2$  (VH<sub>0.9-2</sub>) phase exists from a pressure of 0.1 MPa

[11]. Table 4.9 gathers the main crystallographic properties for all phases as evaluated by the Rietveld method. The most abundant phase is  $\beta$ -MgH<sub>2</sub> (80 wt. %), followed by,  $\gamma$ -MgH<sub>2</sub> (10 wt. %) and, VH (10 wt. %). The crystal sizes are very small for all phases: 6 nm for both MgH<sub>2</sub> polymorphs and 10 nm for VH.

**Table 4.9.** Crystallographic properties of as-milled V-containing NC and Rietveld agreement factor.

Phase abundance (wt.%)			Crystal size(nm)			
$\gamma$ -MgH <sub>2</sub>	$\beta$ -MgH <sub>2</sub>	VH meas./nominal	$\gamma$ -MgH <sub>2</sub>	$\beta$ -MgH <sub>2</sub>	VH	Rwp%
10	80	10/10	6	6	10	3
S.G.			Cell parameters (Å)			
<i>Pbcn</i>	<i>P4<sub>2</sub>/mnm</i>	<i>I4/mmm</i>	<i>a</i> = 4.531 (2)	<i>a</i> =4.519(1)	<i>a</i> =3.034 (1)	
			<i>b</i> = 5.425(2)	<i>c</i> = 3.020(1)	<i>c</i> = 3.396(2)	
			<i>c</i> = 4.963(2)			
Theoretical [12]						
Phase label	Prototype	Pearson symbol	Density (mg/m <sup>3</sup> )	Volume (nm <sup>3</sup> )	Cell parameter (Å)	Cell angles (°)
VH <sub>0.9</sub>	-	-	-	0.0729	<i>a</i> =4.46 <i>c</i> =3.66	$\alpha$ =90 $\beta$ =90 $\gamma$ =120

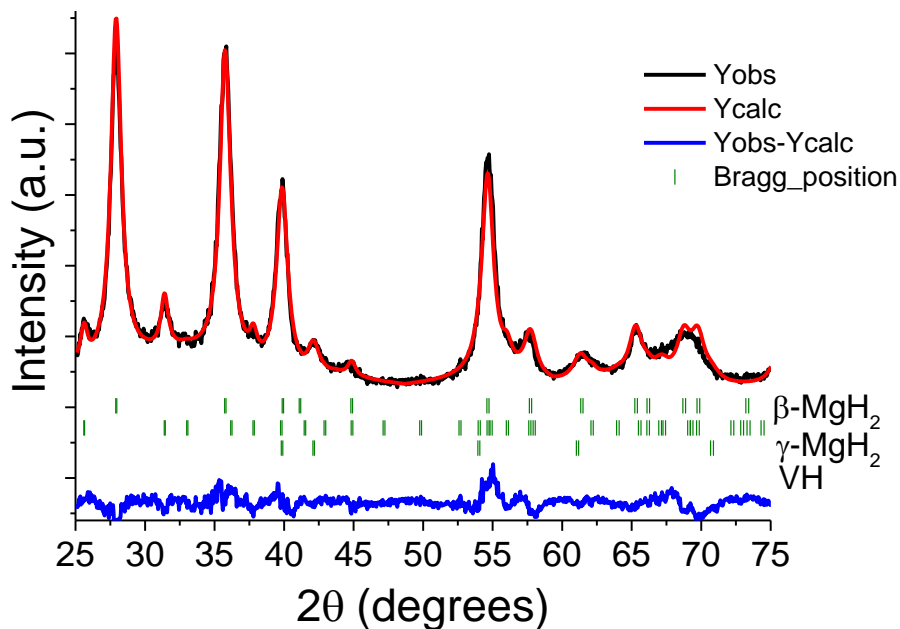


**Figure 4.21.** Rietveld analysis of XRD patterns for V-NC

**b) System 0.95MgH<sub>2</sub>-0.05NbH**

Figure 4.22 (left) shows the evolution of hydrogen pressure and vial temperature during RBM of Nb and Mg powders under hydrogen to synthesize Nb-containing NCs. The corresponding hydrogen uptake curve for the first milling cycle is displayed in Figure 4.20. Hydrogenation of Nb occurs at  $t < 10$  min as suggested by the fast hydrogen uptake in the first minutes of milling. Then Mg hydrogenation occurs on longer milling time with 90% of the reaction accomplished in 46 min. At the end of the first milling cycle,  $C_H$  attains 1.9 H/f.u. and 6.4 wt.% which agrees well with the nominal values according to the formation of 0.95MgH<sub>2</sub>-0.05NbH<sub>2</sub>.

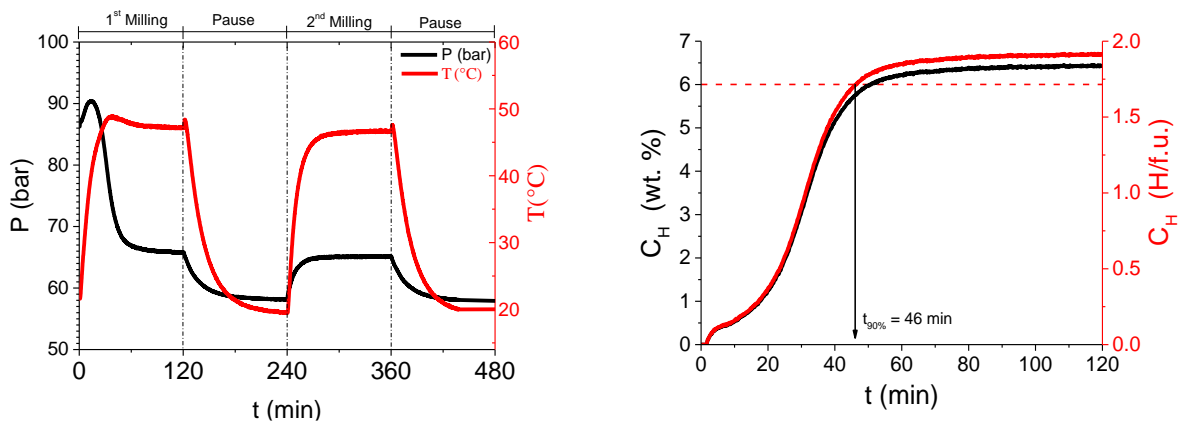


**Figure 4.22.** Left: Hydrogen pressure evolution and temperature vial (red line) as a function of milling during RBM (black line) of Nb-containing NC. Right: Hydrogen uptake curves in weight percent (black line) and hydrogen atoms per formula unit (red line).

**4.3.2 Hydrogen sorption properties****a) Pressure-composition isotherms**

Figure 4.23 shows isothermal PCI curves at 300 °C for V-containing (left) and Nb-containing (right) NCs. Both nanocomposites exhibit a flat plateau at close hydrogen pressure:  $P_p = 0.16$  and 0.14 MPa for V- and Nb-containing composites, respectively. In the first case, the width of the plateau pressure is ca. 7 wt.%, while in the second extends over ca. 6 wt.% at  $P_p = 0.16$ . This difference can be explained by the higher atomic weight of Nb as compared to V. Also, it can be noticed that there is minimal hysteresis between absorption and desorption curves.

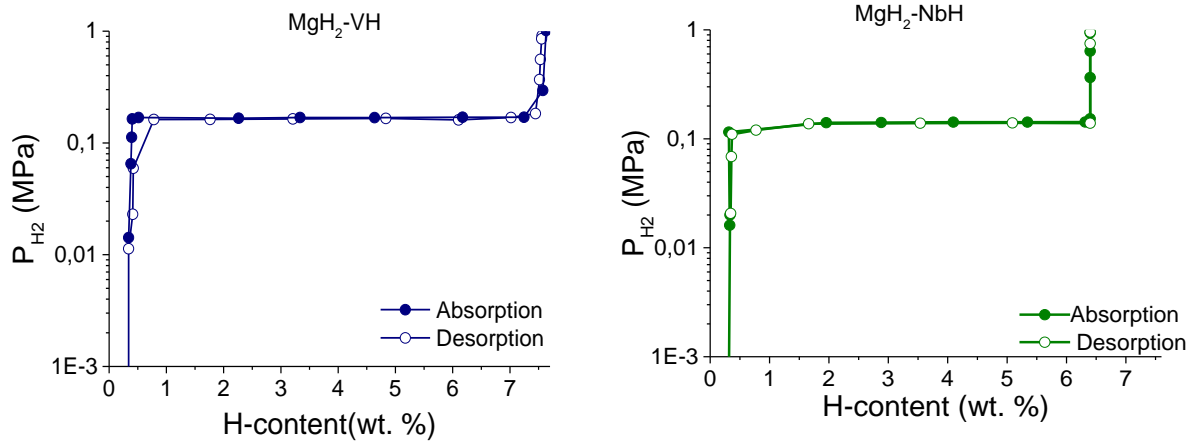


**Figure 4.23.** PCI absorption (full symbols) and desorption (empty symbols) isotherms at 300°C. Left) 0.95MgH<sub>2</sub>-0.05VH, right) 0.95MgH<sub>2</sub>-0.05NbH

**b) Evolution of the reversible hydrogen capacity with cycling under constrained reaction time**

Figure 4.24 shows H-cycling sorption experiments for V- and Nb-containing NCs carried at 300°C with 15 min absorption/desorption sweeps.  $C_{rev}$  was measured for both NCs and compared to Ti-containing one. For both V- and Nb-NCs the same tendency is observed with a gradual decrease of  $C_{rev}$  on cycling: they lose ca. 35 % of the initial capacity on 20 cycles, being initial values 6.1 and 5.7 wt.% for V- and Nb-NCs, respectively. In contrast,  $C_{rev}$  for Ti-containing NC is rather stable with a capacity loss of only 7 % in 20 cycles.

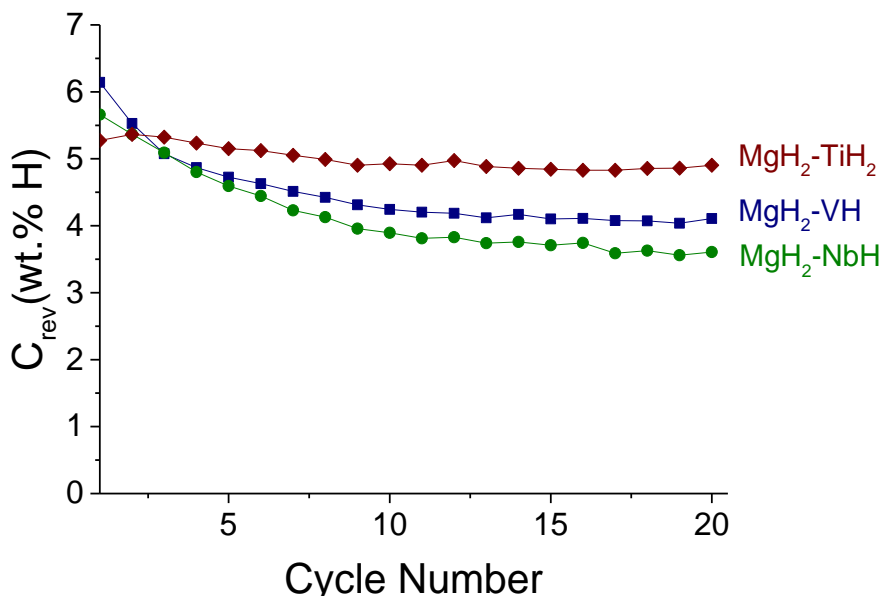


**Figure 4.24.**  $C_{rev}$  on cycling at 300 °C for 0.95MgH<sub>2</sub>-0.05VH and 0.95MgH<sub>2</sub>-0.05NbH and 0.95MgH<sub>2</sub>-0.05TiH<sub>2</sub> nanocomposites. Reaction time limited to 15 min.

### c) Hydrogen sorption curves

Figure 4.25 displays the hydrogen sorption curves for MgH<sub>2</sub>-VH and MgH<sub>2</sub>-NbH nanocomposites at initial (1<sup>st</sup> desorption, 2<sup>nd</sup> absorption) and final (20<sup>th</sup> absorption and desorption) sorption cycles. For V-containing NC (left), kinetics of the 1<sup>st</sup> desorption is very fast at short reaction time and 75% of the reacted fraction  $\alpha$  is attained in 6 min. However, the reaction slows down at longer time and  $\alpha$  only attains 80% after 15 min. After twenty cycles, the desorption kinetic is even faster at short times with  $\alpha = 0.65$  in 3 min but saturating at this reacted fraction for longer reaction time. As concerns absorption kinetics, they are extremely fast in the 2<sup>nd</sup> absorption with 85% of the reacted fraction in 3 min, saturating at long reaction time ( $\alpha = 0.9$  at 15 min). For the 20<sup>th</sup> cycle, reaction kinetics at short reaction time are as fast as in the 2<sup>nd</sup> sweep ( $\alpha = 0.6$  for  $t < 1$ min) but then it slows down as reaction proceeds with only 75% of the reaction accomplished after 15 min.

For the Nb-containing NC (Fig. 4.25, right), the first desorption curve resembles that of the V-one with 80% of the reaction rapidly accomplished in 6 min. but slowing down at longer reaction time ( $\alpha = 0.83$  at 15 min.). After 20 cycles, desorption kinetics are slightly faster at short reaction time ( $t < 2$  min) but for long reaction time, the reaction fraction saturates at  $\alpha = 0.6$ . Comparing both NCs with Ti-NC, these V-NC and Nb-NC show a faster desorption kinetic through cycling but a reduction in the reacted fraction, on the other hand, Ti-NC exhibits slower desorption kinetic but the reacted fraction increases. For the three NCs, the speed in absorption kinetic is the same in cycles one and twenty, nevertheless, Ti-NC keeps the same reacted fraction, V-NC and Nb-NC reduce this value through cycling.

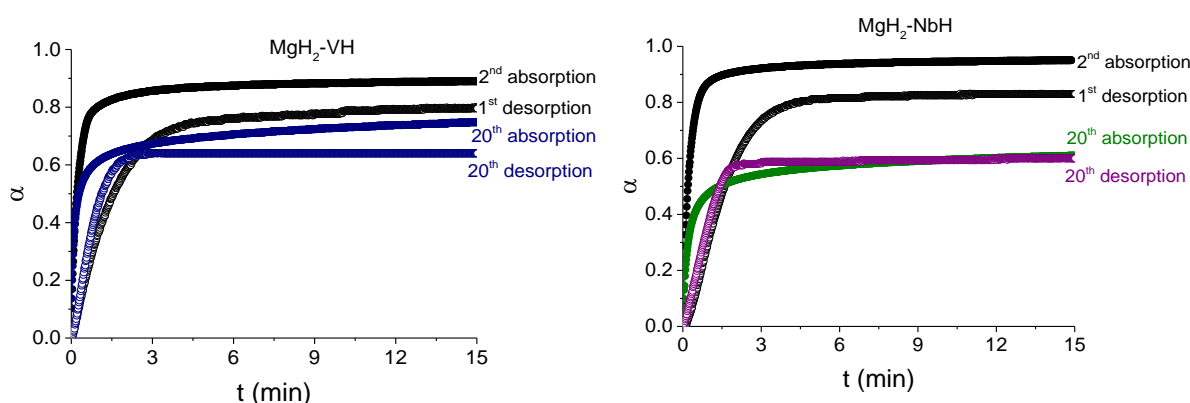


**Figure 4.25.** H-sorption curves at 300°C for cycles one, two and twenty. Left) 0.95MgH<sub>2</sub>-0.05VH, right) 0.95MgH<sub>2</sub>-0.05NbH

### d) Evolution of hydrogen amount in cycling

For the V-containing NC, the desorption is not completed during the first cycle (*ca.* 2 wt.% not desorbed) and some MgH<sub>2</sub> is retained. The amount of MgH<sub>2</sub> retained gradually decreases on cycling (*ca.* 1 wt.% in cycle 20). This result concurs with the acceleration of desorption kinetics on cycling (Fig. 4.9). As for the absorption state, it contains more hydrogen in the first cycles, while it gradually decreases on long cycling so that the amount of unreacted Mg steadily increases. As a consequence, the amount of reversible hydrogen storage keeps

constant on cycling at ca. 5 wt % in agreement with Fig. 4.8. One can notice, that the quantity of hydrogen stored in TiH<sub>2</sub> is supposed to be constant (ca. 0.34 wt.%).

Figure 4.26 shows the hydrogen content in MgH<sub>2</sub>-VH (left) and MgH<sub>2</sub>-NbH (right) nanocomposites both after absorption and desorption sweeps and their evolution on cycling. For the V-containing NC,  $C_{rev}$  decreases gradually due to increasing amount of unreacted Mg on cycling. Based on the previous kinetic measurements (Figure 4.25 b), this is attributed to the sluggish absorption kinetics (*i.e.* saturation of reacted fraction) at long reaction time. In contrast, there is no significant influence of desorption kinetics since the amount of MgH<sub>2</sub> retained remains unchanged during cycling. For the Nb containing-NC (Fig. 4.26, right), a rather similar behavior is observed.  $C_{rev}$  decreases due to sluggish absorption kinetics at long reaction time with the expected occurrence of a high amount of unreacted Mg after 20 cycles. In contrast, the amount of retained MgH<sub>2</sub> tends to steadily decrease due to the slight enhancement of desorption kinetics on cycling. Doing a comparison of Ti-NC with these NCs; Ti-NC keeps constant  $C_{rev}$  through cycling because of the improvement of the kinetic during cycling. On the other hand, V-NC and Nb-NC lose  $C_{rev}$  during absorption state due to sluggish kinetic.

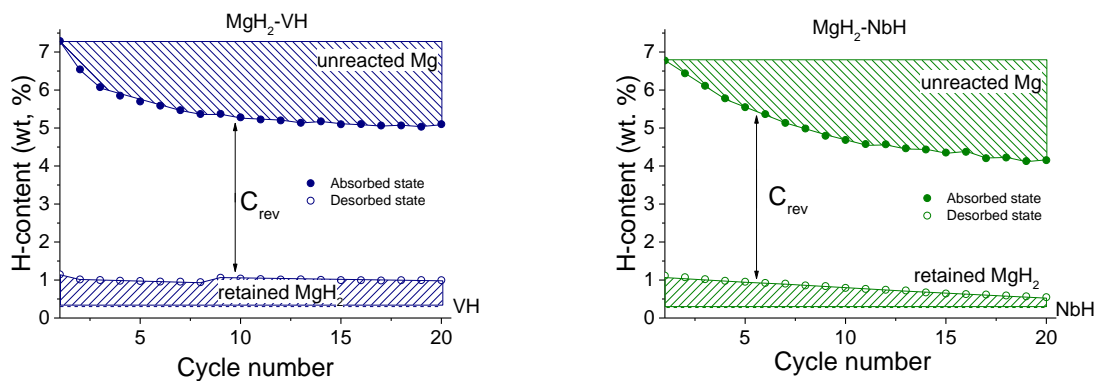


**Figure 4.26.** Evolution of hydrogen content with cycling for 0.95MgH<sub>2</sub>-0.05VH, (left) and 0.95MgH<sub>2</sub>-0.05NbH (right) nanocomposites. H-content is shown after absorption (full symbols) and desorption (empty symbols). Partial contributions from H-stored in VH, NbH, irreversibly retained as MgH<sub>2</sub> and reversibly stored in Mg ( $C_{rev}$ ) are shown.

#### 4.3.3 Effect of hydrogen cycling on the microstructure of MgH<sub>2</sub>-VH

XRD patterns of MgH<sub>2</sub>-VH nanocomposite after 20 sorption cycles both in absorbed and desorbed state are shown in Figure 4.19 and relevant crystallographic data from Rietveld analysis are gathered in Table 4.10. XRD pattern of both absorbed and desorbed MgH<sub>2</sub>-VH composites can be indexed with three phases:  $\beta$ -MgH<sub>2</sub>, VH, and Mg.  $\beta$ -MgH<sub>2</sub> is the major phase (65 wt.%) in the absorbed state, while Mg is the major one (58 wt.%) in the desorbed state. In both states, the crystal size is the same (50 nm) for MgH<sub>2</sub> and Mg. VH<sub>0.9</sub> amount and crystal size remain unchanged as compared to the as-synthesized nanocomposite.

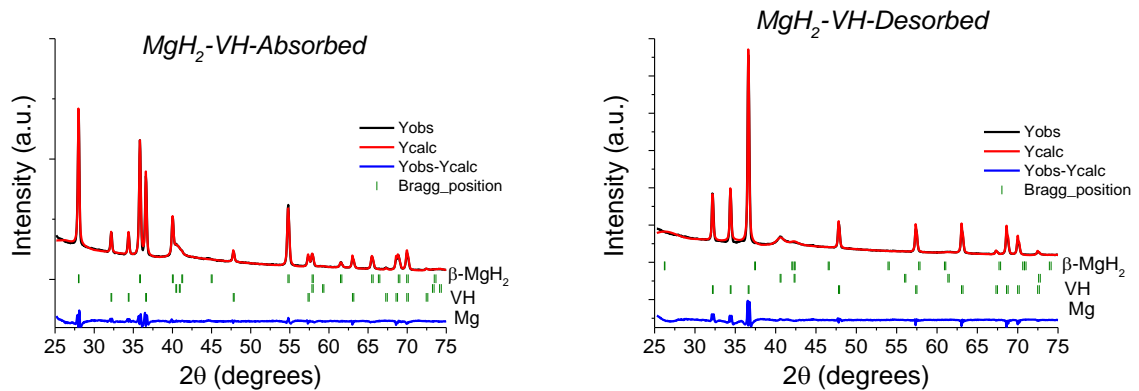


**Figure 4.27.** Rietveld analysis of XRD patterns for V-NC, in both absorbed and desorbed state

**Table 4.10.** Crystallographic properties of abs sample V-NC and Rietveld agreement factor.

#### Absorption

Phase abundance (wt.%)			Crystal size(nm)			
Mg	$\beta$ -MgH <sub>2</sub>	VH meas./nominal	Mg	$\beta$ -MgH <sub>2</sub>	VH	Rwp%
25	65	10/10	50	50	7	4
S.G.			Cell parameters (Å)			
<i>P6<sub>3</sub>/mmc</i>	<i>P4<sub>2</sub>/mnm</i>	<i>I4/mmm</i>	<i>a</i> = 3.211 (1)	<i>a</i> = 4.504(1)	<i>a</i> = 3.119 (1)	
			<i>c</i> = 5.215(1)	<i>c</i> = 3.013(1)	<i>c</i> = 3.185(1)	

#### Desorption

Phase abundance (wt.%)			Crystal size(nm)			
Mg	$\beta$ -MgH <sub>2</sub>	VH meas./nominal	Mg	$\beta$ -MgH <sub>2</sub>	VH	Rwp%
58	32	10/10	50	50	5	5
S.G.			Cell parameters (Å)			
<i>P6<sub>3</sub>/mmc</i>	<i>P4<sub>2</sub>/mnm</i>	<i>I4/mmm</i>	<i>a</i> = 3.209 (1)	<i>a</i> = 4.804(1)	<i>a</i> = 3.019(2)	
			<i>c</i> = 5.211(1)	<i>c</i> = 2.381(1)	<i>c</i> = 3.282(3)	

## 4.4 Discussion

The following discussion is presented analyzing each MgH<sub>2</sub>-*transition metal* system, their main results and their comparison with the literature results. Finally, it is shown a comparison and analysis among them.

### MgH<sub>2</sub>-ZrH<sub>2</sub>

The system MgH<sub>2</sub>-ZrH<sub>2</sub> shows the faster milling kinetic among all the NCs. In 33 min, 90% of the hydrogenation reaction is achieved. After synthesis, the crystallite size was measured and the three phases  $\gamma$ -MgH<sub>2</sub>,  $\beta$ -MgH<sub>2</sub>, and ZrH<sub>2</sub> have a uniform size of 7 nm. After 20 sorption cycles, it is observed that  $C_{rev}$  decreases through the first cycles then keeps constant. Regarding kinetic, it is observed that desorption improves during cycling and reversibility loss is attributed to the poor absorption kinetic. The same behavior was already shown by Zaluska et al [13]. They studied several additives for improving the MgH<sub>2</sub> sorption kinetics. They observed that vanadium markedly improves the kinetics of hydrogen absorption. Even more effective is 5 wt.% of zirconium, which can lead to desorption occurring

at lower temperatures than pure magnesium (280°C). However, the best kinetic results are reported for mixtures of additives, for example, Zr-Ti or Mn-Zr. The addition of Mn and Zr was found to be especially effective, leading to hydrogen absorption at much lower temperatures (190 and 170°C). Csujko et al [14] compared the effects of catalytic metal additives on the hydrogen desorption properties of magnesium hydride formed after hydrogenation of the Mg + 10 wt.%X (X = V, Zr, or Y) composites. They found that the desorption is much better for Mg + 10 wt.%V, then Zr and finally Y. The difference is particularly marked at lower temperatures (300 and 325 °C). Other studies have been done with ZrF<sub>4</sub> to improve the sorption kinetic [15]. Yamanaka et al [16] studied the thermal properties of zirconium hydride in the range of 25 to 500 °C, detecting that the thermal diffusivity decreased with increasing temperature and was almost independent of the hydrogen content, also observing that the temperature dependence of the heat capacity of the zirconium hydride is small.

After cycling the particle size was measured and it was noted that there is no change in the crystal size for the ZrH<sub>2</sub> phase whereas Mg and MgH<sub>2</sub> phases have grown larger. This growth was also observed by Csujko et al [14], they explained that during the hydrogenation stage, the powder particles lose their nanostructured character since the particles do not contain nanosized β-MgH<sub>2</sub> hydride grains (crystallites) anymore. Therefore, during the desorption stage, the β-MgH<sub>2</sub> hydride is already sub-microcrystalline rather than nanocrystalline. The grain growth of MgH<sub>2</sub> is also more substantial, apparently due to higher employed activation or hydrogenation temperature (350 °C).

### MgH<sub>2</sub>-ScH<sub>2</sub>

RBM shows a maximum hydrogen uptake is achieved (7 wt. %). After synthesis, the NC was analyzed by XRD, where three phases are found: γ-MgH<sub>2</sub>, β-MgH<sub>2</sub> and ScH<sub>2</sub>. By the Rietveld method, the abundance and crystal size were calculated. The most abundant phase is β-MgH<sub>2</sub>, then, γ-MgH<sub>2</sub> and finally ScH<sub>2</sub>. Both Mg phases showed a crystal size of 7nm and the ScH<sub>2</sub> was 23 nm. The ScH<sub>2</sub> crystal size is the largest one compared with the other additives, a fact characteristic on this dihydride. Luo et al [9] synthesized by RBM the xMgH<sub>2</sub>+(1-x)ScH<sub>2</sub> (x=0.65-1) system at different times, they calculated a crystal size for ScH<sub>2</sub>= 40 nm after 40h of milling. In this study, the researchers found that Mg do not react during ball milling for milling time larger than 20 h. They indicate that there is an optimum of 6h milling to reach the full MgH<sub>2</sub> formation; also mentioning the good dispersion among the phases observed by SEM analysis. Figure 4.12 shows that the full absorption is carried out in only 40 min having the main phases described above. From this study, an optimum synthesis time could be proposed in 60 min.

After carrying out twenty sorption cycles, the hydrogen reversible capacity is enhanced from the first cycles, then reaches a maximum (C<sub>rev</sub>= 4.5 wt. %H) and finally fluctuates around this maximum. This good cycling performance was also observed by Luo et al [8], they perform hydrogen sorption cycles of 0.65MgH<sub>2</sub>+0.35ScH<sub>2</sub>, in thin films at 290 °C and 2 MPa. After 55 cycles, they observed a good cyclability of the NC, reaching C<sub>rev</sub>= 4.2 wt% H. They measured a hydrogen absorption of 3.2 wt. % H in 5 min and hydrogen desorption 3 wt. % H in 15 min. As can be seen in Figure 4.16 after 20 cycles, C<sub>rev</sub>= 4.1 wt% H, which agrees with the previous study exposed above.

From kinetic results it is noticed that kinetic absorption improves during when desorption kinetic is lessening. This could be attributed to ScH<sub>2</sub>, being a transition metal hydride, only helping the dissociation of H<sub>2</sub> to H during absorption. This is in agreement with Ogawa et al [17]. They studied the hydrogen desorption of Mg—10at%ScH<sub>2</sub>, at several temperatures (350, 375 and 400 °C) at 1MPa founding that even at 400°C the system shows a sluggish desorption kinetic. For the cycling reported by Luo et al [8], after 55 sorption cycles, they conclude a kinetic improvement occurs after 20 hydrogen sorption cycles.

After the cycling process, the crystal size for Mg/MgH<sub>2</sub> phases reaches 62±7 nm in both absorbed and desorbed state, ScH<sub>2</sub> remaining the same. This could be understood if ScH<sub>2</sub> is only a gateway, having a fluorite structure allowing a higher mobility of H than MgH<sub>2</sub>/Mg. Also, the large crystal size of ScH<sub>2</sub> limits the growth of the MgH<sub>2</sub>/Mg phases.

### MgH<sub>2</sub>-YH<sub>3</sub>

After RBM, three phases were identified by XRD, two polymorphs of MgH<sub>2</sub> and YH<sub>3</sub>. Zlotea et al. [18] reported on the heats of enthalpy formation ( $\Delta H_f$ ) for YH<sub>2</sub>, YH<sub>3</sub> and MgH<sub>2</sub> with -114, -89 and -37 KJ·mol<sup>-1</sup>H respectively. They explained that the formation of YH<sub>2</sub> is the most favorable at moderate pressures, however, at higher pressures, both MgH<sub>2</sub> and YH<sub>3</sub> are always formed, which agrees with the heats of formation.

Absorption-desorption cycles were carried out in a constraint time of 15 min. The Y-NC shows the poorest  $C_{rev}$  value among all the tested materials with  $C_{rev}$  only slightly higher than pure MgH<sub>2</sub>, Ogawa et al [17] tried to study the hydrogen desorption properties of Mg-10at.%Y.

However, they explain that they were not successful because of the limited solubility of yttrium in the magnesium host. They observed that the desorption kinetic is very sluggish by comparison with other additives. Borgschulte et al [19] explained that the morphology dependence of the catalytic activity of supported metal clusters in heterogeneous catalysis is attributed to a so-called strong metal-support interaction (SMSI). They demonstrate that the SMSI state of deposited Pd clusters is also the physical origin of the thickness dependence of the hydrogen uptake of switchable mirrors and the same effect is also expected to play a role in hydrogen storage. They investigated the morphology and the electronic structure of Pd clusters grown on oxidized yttrium surfaces, both as deposited and after hydrogenation, founding a strong Pd thickness dependence for yttrium hydrogenation. Chacon et al [20] studied the hydrogen uptake in Pd/Mg<sub>1-x</sub>Y<sub>x</sub> thin films ( $x= 0-17$  at. %). They found that yttrium atoms are substitutionally included into the magnesium lattice giving rise to an extended solution, as compared to bulk alloys. They also found that for low Y content, the hydrogen uptake is like that of pure magnesium. This latter result agrees with the ones explained above. They concluded that the hydrogen uptake can be described with a nucleation and growth model. After cycling, the crystal size was measured, and it was found that there is no change in the sizes while the NC totally absorbs and desorbs. They have similar phase abundance and YH<sub>3</sub> does not change its crystallite size. This can be explained by the poor reversibility of the reaction, as a result, the material remains like its initial state, the growth of MgH<sub>2</sub> before and after cycling can be attributed to the increase of the temperature.

### MgH<sub>2</sub>-VH

MgH<sub>2</sub>-VH NC was successfully synthesized by RBM. The mechanically milled MgH<sub>2</sub>+5 at.%V composite exhibits much better hydrogen sorption kinetics than non-milled and mechanically milled MgH<sub>2</sub>, reported previously by Huot et al [21]. A PCI curve was plotted with only one plateau observed, which corresponds to MgH<sub>2</sub>, and agrees with [22].

$C_{rev}$  was measured during cycling, and a loss of the reversible capacity is observed for the first sorption cycles, then remains constant. This is attributed to the sluggish absorption kinetics. However, desorption kinetic is fast, it is in line with the results of Liang et al. [22] who observed that MgH<sub>2</sub>-5at.%V is able to desorb hydrogen at 300 °C under vacuum (0.015 MPa) with fast kinetics. Ren et al [23] tested different MgH<sub>2</sub>-V-based mixtures observing dehydrogenation at 240 °C and 0.001 MPa, the binary system MgH<sub>2</sub>-5at.% showing the slowest desorption kinetic among all the composites. Sorption kinetic worsening was observed during 20 cycles, which could be related to the migration of catalyst particles to the edge as it was described in Chapter 3. Worsening was also observed by Tan et al [24]. They carried out hundreds of sorption cycles for MgH<sub>2</sub>-5 at.%V and worsening were observed from the first cycles. They attributed this fact to the growth of the Mg/MgH<sub>2</sub> particles through cycling, which increases the hydrogen diffusion path. This disagrees with our results because from XRD analysis, we conclude that Mg/MgH<sub>2</sub> growth is limited for the additive phase provoking a coarsening limitation effect [2]. Finally, Liang et al. [25] analyzed the desorption kinetic mechanism. They concluded that it follows a nucleation and two-dimensional growth at temperatures below 300 °C and an interface controlled, two-dimensional growth for temperatures above 300 °C

### MgH<sub>2</sub>-NbH

The synthesis of MgH<sub>2</sub>-NbH NC was successfully achieved, the hydrogenation during the synthesis reached 90% yield in only 46 minutes, which is shorter than other NCs except for Zr. The PCI curve is very close to the homolog MgH<sub>2</sub>-VH, the smaller hydrogen capacity is explained by the fact that at 5at. % translates into 10 wt.% vanadium and 15 wt.% niobium NCs. The  $C_{rev}$  was measured during cycling. After of twenty cycles, a loss of 2 wt.% H. is observed. The dehydrogenation kinetics of MgH<sub>2</sub>-NbH is as fast as that of MgH<sub>2</sub>-VH, and hydrogenation curves have the same shape. This was also observed by Huot et al. [26] that suggested that having the same curve shape, they have the same dehydrogenation rate-limiting step. The capacity loss is seen in absorption, where the kinetic is sluggish. Liu et al [27] carried out absorption of Mg-7.5 wt.% Nb at 4MPa and 200 °C, pointing out that the complete hydrogenation should be done in 60 min. Kinetic worsening through cycling was also observed the, which explains the reduction of  $C_{rev}$ . A large hydrogen storage capacity loss (3 wt. %) was also observed by Tan et al [28]. As this system is like MgH<sub>2</sub>-VH with comparable shape curves, it can be assumed that nucleation and two-dimensional growth is the kinetic model which can better explain the experimental data.

### Effect of *TM* additives on MgH<sub>2</sub>

MgH<sub>2</sub>-based NCs with 5 mol% of different additives (Ti, Zr, Sc, Y, V, and Nb) were successfully synthesized by RBM. Under our milling conditions, all additives formed hydrides with the following stoichiometry: TiH<sub>2</sub>, ZrH<sub>2</sub>, ScH<sub>2</sub>, YH<sub>3</sub>, VH<sub>2</sub>, and NbH<sub>2</sub>, in agreement with their thermodynamic properties [11,29–34]. Each NC reached the nominal capacity within the first milling cycle. This was confirmed by XRD analysis with 10 wt % for the additives of period four and 15wt.% for those of the fifth period, according to their atomic number (Table 4.11). For TiH<sub>2</sub> and ZrH<sub>2</sub>, as presented in Figures 4.1 and 4.4, these hydrides are stable at around 8 MPa and temperature close to 60°C (inner vial temperature). ScH<sub>2</sub> was hydrogenated before milling as it explained in section 4.2.1 a, so this NC remains stable during the RBM. For YH<sub>3</sub>, the trihydride formation is explained by Huiberts et al [35] : during hydrogen absorption of YH<sub>2</sub>, at higher concentration of hydrogen, the material resistivity quickly increases, first due to an increase of octahedral occupation in the fcc dihydride, followed for a further increase due to the transformation of the hcp trihydride. The NC VH<sub>2</sub> and NbH<sub>2</sub> are obtained after RBM, according to their thermodynamic properties as explained in Chapter one. However, after RBM, the milling vial is unloaded, and the pressure is decreased to 0.03 MPa. At this point, a desorption of the dihydride occurs leading to the formation of the monohydride VH and NbH.

**Table 4.11.** RBM results for doped nanocomposites

NC	Measured (wt. %)	Nominal (wt. %) (expected)	Atomic number (metal)
TiH <sub>2</sub>	11	9	22
ZrH <sub>2</sub>	11	15	40
ScH <sub>2</sub>	9	9	21
YH <sub>3</sub>	10	16	39
VH <sub>2</sub>	10	10	23
NbH <sub>2</sub>	-	15	41

Depending on *TM*, by RBM, a variation of the hydrogenation time is observed. For instance, 90% hydrogenation is completed in 40 min for MgH<sub>2</sub>-ZrH<sub>2</sub>, MgH<sub>2</sub>-ScH<sub>2</sub>, and MgH<sub>2</sub>-NbH<sub>2</sub>. On the other hand, MgH<sub>2</sub>-TiH<sub>2</sub>, MgH<sub>2</sub>-YH<sub>3</sub>, and MgH<sub>2</sub>-VH<sub>2</sub> need 50 min to reach 90%. These results indicate that the nature of the additive has an influence on the nanocomposites synthesis and, depending on the additive, synthesis time can be improved. The more stable dopants, belonging to the 5<sup>th</sup> period, allows a faster hydrogenation than the NCs of period four, with two exceptions: the ones who belong to group 3, Sc because it was previously hydrogenated and Y due to its poor dopant contribution.

From XRD data, it is observed that the main phase after synthesis is  $\beta$ -MgH<sub>2</sub>, followed by Y-MgH<sub>2</sub>, and finally the additive phase. Formation of any ternary phase Mg-*TM*-H has not been detected. From XRD analysis, the crystallite size of each phase was determined. The two ( $\beta$  and  $\gamma$ ) MgH<sub>2</sub> phases exhibit a crystallite size of  $6 \pm 1$  nm with all additives. The crystallite size of the additive phases ranges between 7 to 13 nm, except for ScH<sub>2</sub> with a larger crystallite size of 23 nm (explained above).

Figure 4.28 shows both the absorption and desorption plateau pressures, for each NC compared with pure MgH<sub>2</sub> data [36]. The addition of TM leads to almost the same plateau pressure value  $P_p$  than pure MgH<sub>2</sub> for absorption and desorption. This assures that the thermodynamic of MgH<sub>2</sub> is not changed and agrees with some other systems already studied. For instance, Cuevas et al.[2] studied the 70MgH<sub>2</sub>+30TiH<sub>2</sub> at 300°C with  $P_{abs}=0.8$  Mpa,  $P_{des}= 0.03$  MPa, there was no evidence for a change in the MgH<sub>2</sub> thermodynamic. Liang et al. [30] assessed 95MgH<sub>2</sub>+5VH<sub>2</sub>, at 200°C and  $P_{abs}= 0.1$  Mpa,  $P_{des}= 0.015$  MPa, measuring both the enthalpy and entropy of hydride formation which is exactly the same than MgH<sub>2</sub>. Desorption of 90MgH<sub>2</sub>+10ScH<sub>2</sub> was carried out by Ogawa et al. [17] at 350°C and 1MPa. They calculate the enthalpy and entropy of hydride formation which is like pure MgH<sub>2</sub>.

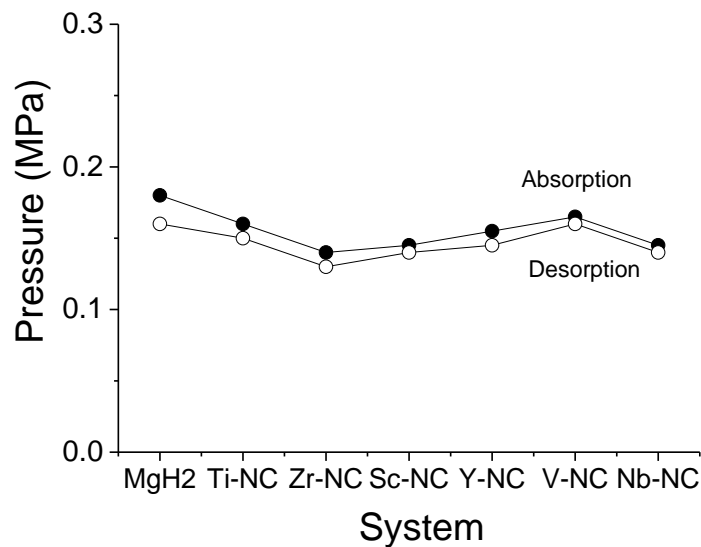


**Figure 4.28.** Half-plateau pressures on absorption and desorption for each synthesized NC

Figure 4.29 depicts the evolution of  $C_{rev}$  during 20 cycles for all studied NCs. Four different behaviors can be distinguished. The most commonly observed is for Zr-, Nb- and V-containing nanocomposites for which the reversible capacity gradually decreases on cycling. As for Sc-containing NC, it starts with low  $C_{rev}$  (3.2 wt.%), increases up to a maximum after 7 cycles and then gradually decreases on long-cycling, as for the previous additives. A unique behavior is seen for Y-containing system, for which the reversible capacity is very low at the first cycle (1 wt.%) and gradually decreases upon cycling. Finally, the best and most interesting behavior is observed for Ti. It exhibits a high capacity from the first cycle (5.3 wt.%) which remains almost unchanged on cycling (4.9 wt.% after 20 cycles).

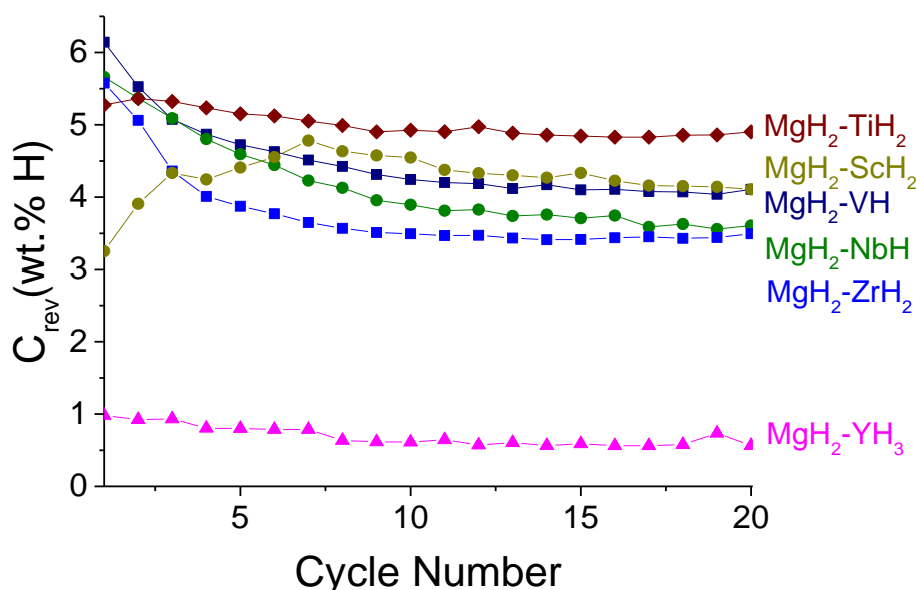


Figure 4.29.  $C_{rev}$  on cycling at 300 °C for reaction time limited to 15 min

The low reversible capacity of the MgH<sub>2</sub>-YH<sub>3</sub> composite from the first cycle deserves particular interest despite its poor performances. This Y-NC forms similarly to the other NCs by RBM (Fig. 4.13) and consists as usual of two MgH<sub>2</sub> polymorphs in nanostructured state. However, though microstructural properties are favorable, hydrogen desorption is extremely slow and resembles to that of nanometric MgH<sub>2</sub> prepared by RBM (Fig. 3.9 Chapter 3). This fact can be attributed to surface barriers, such as formation of yttrium oxides leading to slow recombination of hydrogen atoms at the yttrium hydride surface as compared to the other studied *TM* hydrides.

Low reversible capacity at the first sorption cycles also occurs for MgH<sub>2</sub>-ScH<sub>2</sub>, belonging both to the same group 3. It can be argued from their close chemical properties that reaction barriers may also form at the ScH<sub>2</sub> surface limiting hydrogen recombination. Indeed, slow desorption kinetics in the first cycle is detected for MgH<sub>2</sub>-ScH<sub>2</sub> composite (Fig.4.17). However, contrary to Y-containing NC, the reversible capacity of Sc-NC significantly increases on cycling and therefore both cases differ. Another singular property of Sc-NC is the large crystallite size of ScH<sub>2</sub> phase (23 nm), due to its preparation method by the solid-gas reaction, as compared to other *TM*-hydride additives (ca. 10 nm). Thus, one may tentatively attribute the low reversible capacity of MgH<sub>2</sub>-ScH<sub>2</sub> at first H-cycles to a less efficient dispersion of ScH<sub>2</sub> in the MgH<sub>2</sub> matrix or at its surface as compared to other *TM*-hydride additives.

The cases of Zr-, Nb- and V- containing nanocomposites, for which the reversible capacity gradually decreases on cycling, are all characterized by the similar evolution of reaction kinetics on cycling (Figures 4.9, 4.25 left and 4.25 right, respectively). For desorption sweeps, kinetics accelerates on cycling in the three cases. In contrast, for absorption sweeps, reaction kinetics slow down on cycling for reacted fraction exceeding ca. 0.4, leading to a large amount of unreacted Mg (Figures 4.10 right and 4.26). This evidences that the gradual

diminution of  $C_{rev}$  on cycling relates to the absorption process because of the kinetic exposed above.

The MgH<sub>2</sub>-TiH<sub>2</sub> composite offers the best behavior in  $C_{rev}$  for all NCs with stable reversible capacity on cycling. As it happens for Zr-, Nb- and V-NCs, reaction kinetic accelerates on desorption (Fig. 4.9b) but absorption kinetics after 20<sup>th</sup> cycles are better for MgH<sub>2</sub>-TiH<sub>2</sub> than for the other NCs. Indeed, one can notice in the 20<sup>th</sup> absorption sweep, that the reacted fraction at which the absorption kinetics slow down is higher for Ti-NC ( $\alpha = 0.6$ ) than for Zr-, Nb- and V-NCs ( $\alpha = 0.4$ ).

From the XRD and Rietveld's analysis after the cycling process, some facts must be pointed out: additive phases were identified for the NCs in the absorbed and desorbed state as follows: TiH<sub>2</sub>, ZrH<sub>2</sub>, ScH<sub>2</sub>, VH<sub>0.8</sub>, NbH<sub>0.8</sub>, and YH<sub>3</sub>. In the case of YH<sub>3</sub>, the phase YH<sub>2</sub> was never observed as explained above. The Mg/MgH<sub>2</sub> crystallite size increases after absorption and desorption in all cases at the end of 20 cycles. The crystal size of Mg and MgH<sub>2</sub> increases about 10 times after 20 hydrogen cycles at 300 °C which could be attributed to thermal effects between the Mg metal and MgH<sub>2</sub> after cycling process for each NC.

To summarize the hydrogen storage properties of 0.95MgH<sub>2</sub>-0.05*TM*H<sub>x</sub> (*TM*= Ti, Zr, Sc, Y, V, and Nb) NCs for practical applications, the hydrogen content contributions after twenty cycles of the different counterparts in the NC are displayed in Figure 4.30. The total hydrogen content of the NCs is given by blue triangles assuming the formation of MgH<sub>2</sub> TiH<sub>2</sub>, ZrH<sub>2</sub>, ScH<sub>2</sub>, VH<sub>2</sub>, NbH<sub>2</sub> and YH<sub>3</sub> during RBM synthesis. It is slightly larger for *TM* belonging to the period 4 (ca. 7.3 wt.%) than for the period 5 (6.8 wt.%). The available capacity of the nanocomposites is given by red squares assuming that reversible hydrogen storage only occurs for the MgH<sub>2</sub> counterpart, *i.e.* *TM* hydrides are not reversible at the operating conditions.

Based on the kinetic performance of the nanocomposites, some reversible (grey area) and irreversible (white area) Mg/MgH<sub>2</sub> contributions are detected. Their relative extent depends on the additive. Starting from MgH<sub>2</sub>-YH<sub>3</sub> exhibits very poor desorption kinetics and therefore a high irreversible contribution. MgH<sub>2</sub>-ZrH<sub>2</sub> and MgH<sub>2</sub>-NbH<sub>2</sub> have the similar reversible capacity (3.5 wt.%), which value is low due to the sluggish absorption kinetic at high reacted fraction. Like these latter NCs, MgH<sub>2</sub>-VH<sub>2</sub> exhibits slow absorption kinetics but the lighter weight of the *TM* confers a high reversible capacity (4 wt.%). After 20 sorption cycles, MgH<sub>2</sub>-ScH<sub>2</sub> has a similar behavior to h MgH<sub>2</sub>-VH<sub>2</sub> though it was characterized by sluggish desorption kinetics in the first cycles. Finally, MgH<sub>2</sub>-TiH<sub>2</sub> offers the larger amount of reversibility (4.9 wt.%) thanks not only to its fast kinetics on absorption and desorption but their good stability on cycling.

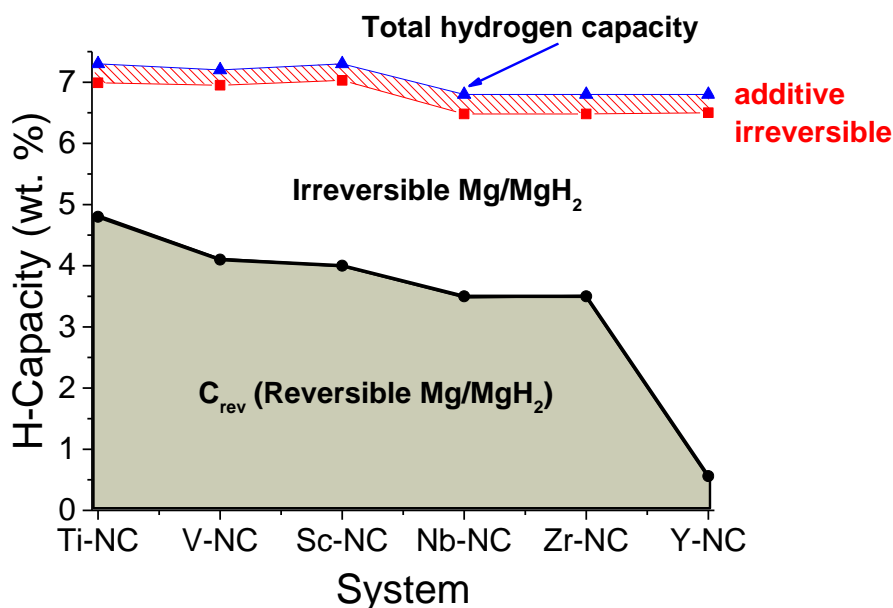


Figure 4.30. Reversible and irreversible contributions to hydrogen storage in 0.95MgH<sub>2</sub>-0.05TM NCs after 20 sorption cycles ( $\blacktriangle$  = Total hydrogen capacity,  $\blacksquare$  = H-capacity of MgH<sub>2</sub> counterpart,  $\bullet$  = experimental H-reversible capacity)

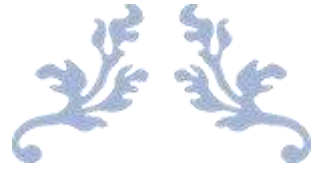
## References

- [1] Zhang J, Cuevas F, Zaïdi W, Bonnet J-P, Aymard L, Bobet J-L, et al. Highlighting of a Single Reaction Path during Reactive Ball Milling of Mg and TM by Quantitative H<sub>2</sub> Gas Sorption Analysis To Form Ternary Complex Hydrides (TM = Fe, Co, Ni). *J Phys Chem C* 2011;115:4971–9. doi:10.1021/jp2005293.
- [2] Cuevas F, Korablov D, Latroche M. Synthesis, structural and hydrogenation properties of Mg-rich MgH<sub>2</sub>-TiH<sub>2</sub> nanocomposites prepared by reactive ball milling under hydrogen gas. *Phys Chem Chem Phys* 2011;14:1200–11. doi:10.1039/C1CP23030A.
- [3] Ares JR, Cuevas F, Percheron-Guégan A. Mechanical milling and subsequent annealing effects on the microstructural and hydrogenation properties of multisubstituted LaNi<sub>5</sub> alloy. *Acta Mater* 2005;53:2157–67. doi:10.1016/j.actamat.2005.01.030.
- [4] A Handbook of Lattice Spacings and Structures of Metals and Alloys. Elsevier; 1958. doi:10.1016/C2013-0-08243-6.
- [5] Okamoto H, editor. Desk handbook: phase diagrams for binary alloys. 2nd ed. Materials Park, Ohio: ASM International; 2010.
- [6] San-Martin A, Manchester FD. The H-Mg (Hydrogen-Magnesium) system. *J Phase Equilibria* 1987;8:431–7. doi:10.1007/BF02893152.
- [7] Lototskyy MV, Davids MW, Tolj I, Klochko YV, Sekhar BS, Chidziva S, et al. Metal hydride systems for hydrogen storage and supply for stationary and automotive low temperature PEM fuel cell power modules. *Int J Hydrog Energy* 2015;40:11491–7. doi:10.1016/j.ijhydene.2015.01.095.
- [8] Luo X, Grant DM, Walker GS. Hydrogen storage properties of nano-structured 0.65MgH<sub>2</sub>/0.35ScH<sub>2</sub>. *Int J Hydrog Energy* 2013;38:153–61. doi:10.1016/j.ijhydene.2012.10.025.
- [9] Luo X, Grant DM, Walker GS. Catalytic effect of nano-sized ScH<sub>2</sub> on the hydrogen storage of mechanically milled MgH<sub>2</sub>. *J Alloys Compd* 2015;622:842–50. doi:10.1016/j.jallcom.2014.10.161.
- [10] Venturini EL, Morosin B. Low temperature anomaly in Sc<sub>0.995</sub>Gd<sub>0.005</sub>H<sub>1.9</sub>. *Phys Lett A* 1977;61:326–8. doi:10.1016/0375-9601(77)90630-2.
- [11] Reilly JJ, Wiswall RH. Higher hydrides of vanadium and niobium. *Inorg Chem* 1970;9:1678–82. doi:10.1021/ic50089a013.

- [12] Dolukhanyan S. Synthesis of novel compounds by hydrogen combustion. *J Alloys Compd* 1997;253–254:10–2. doi:10.1016/S0925-8388(96)03071-X.
- [13] Zaluska A, Zaluski L, Ström–Olsen JO. Nanocrystalline magnesium for hydrogen storage. *J Alloys Compd* 1999;288:217–25. doi:10.1016/S0925-8388(99)00073-0.
- [14] Czujko T, Varin RA, Chiu C, Wronski Z. Investigation of the hydrogen desorption properties of Mg+10wt.%X (X=V, Y, Zr) submicrocrystalline composites. *J Alloys Compd* 2006;414:240–7. doi:10.1016/j.jallcom.2005.07.009.
- [15] Malka IE, Bystrzycki J, Płociński T, Czujko T. Microstructure and hydrogen storage capacity of magnesium hydride with zirconium and niobium fluoride additives after cyclic loading. *Proc 12th Int Symp Met-Hydrog Syst Fundam Appl MH2010* 2011;509:S616–20. doi:10.1016/j.jallcom.2010.10.122.
- [16] Yamanaka S, Yamada K, Kurosaki K, Uno M, Takeda K, Anada H, et al. Thermal properties of zirconium hydride. *10th Int Symp Thermodyn Nucl Mater* 2001;294:94–8. doi:10.1016/S0022-3115(01)00457-3.
- [17] Ogawa K, Aoki H, Kobayashi T. Hydrogen absorption and electronic structure of magnesium-based yttrium and scandium dilute alloys. *J Common Met* 1982;88:283–8. doi:10.1016/0022-5088(82)90233-8.
- [18] Zlotea C, Sahlberg M, Moretto P, Andersson Y. Hydrogen sorption properties of a Mg–Y–Ti alloy. *J Alloys Compd* 2010;489:375–8. doi:10.1016/j.jallcom.2009.09.085.
- [19] Borgschulte A, Westerwaal RJ, Rector JH, Dam B, Griessen R, Schoenes J. Effect of the strong metal-support interaction on hydrogen sorption kinetics of Pd-capped switchable mirrors. *Phys Rev B* 2004;70:155414. doi:10.1103/PhysRevB.70.155414.
- [20] Chacon C, Johansson E, Hjörvarsson B, Zlotea C, Andersson Y. Growth and hydrogen uptake of Mg–Y thin films. *J Appl Phys* 2005;97:104903.
- [21] Huot J, Liang G, Boily S, Van Neste A, Schulz R. Structural study and hydrogen sorption kinetics of ball-milled magnesium hydride. *J Alloys Compd* 1999;293–295:495–500. doi:10.1016/S0925-8388(99)00474-0.
- [22] Liang G, Huot J, Boily S, Van Neste A, Schulz R. Hydrogen storage properties of the mechanically milled MgH<sub>2</sub>–V nanocomposite. *J Alloys Compd* 1999;291:295–9. doi:10.1016/S0925-8388(99)00268-6.
- [23] Ren C, Fang ZZ, Zhou C, Lu J, Ren Y, Zhang X. Hydrogen Storage Properties of Magnesium Hydride with V-Based Additives. *J Phys Chem C* 2014;118:21778–84. doi:10.1021/jp504766b.
- [24] Tan X, Zahiri B, Holt CMB, Kubis A, Mitlin D. A TEM based study of the microstructure during room temperature and low temperature hydrogen storage cycling in MgH<sub>2</sub> promoted by Nb–V. *Acta Mater* 2012;60:5646–61. doi:10.1016/j.actamat.2012.06.009.
- [25] Liang G, Huot J, Boily S, Schulz R. Hydrogen desorption kinetics of a mechanically milled MgH<sub>2</sub>+5at.%V nanocomposite. *J Alloys Compd* 2000;305:239–45. doi:10.1016/S0925-8388(00)00708-8.
- [26] Huot J, Pelletier JF, Lurio LB, Sutton M, Schulz R. Investigation of dehydrogenation mechanism of MgH<sub>2</sub>–Nb nanocomposites. *J Alloys Compd* 2003;348:319–24. doi:10.1016/S0925-8388(02)00839-3.
- [27] Liu T, Ma X, Chen C, Xu L, Li X. Catalytic Effect of Nb Nanoparticles for Improving the Hydrogen Storage Properties of Mg-Based Nanocomposite. *J Phys Chem C* 2015;119:14029–37. doi:10.1021/acs.jpcc.5b03442.
- [28] Tan X, Wang L, Holt CMB, Zahiri B, Eikerling MH, Mitlin D. Body centered cubic magnesium niobium hydride with facile room temperature absorption and four weight percent reversible capacity. *Phys Chem Chem Phys* 2012;14:10904–9. doi:10.1039/C2CP42136D.
- [29] Arita M, Shimizu K, Ichinose Y. Thermodynamics of the Ti–H system. *Metall Trans A* 1982;13:1329–36. doi:10.1007/BF02642869.
- [30] Edwards RK, Levesque P, Cubicciotti D. Solid Solution Equilibria in the Zirconium–Hydrogen System1. *J Am Chem Soc* 1955;77:1307–11. doi:10.1021/ja01610a074.

- [31] Manchester FD, Pitre JM. The h- sc (Hydrogen- Scandium) system. *J Phase Equilibria* 1997;18:194–205. doi:10.1007/BF02665706.
- [32] Alefeld G, Völkl J, editors. *Hydrogen in Metals II: Application-Oriented Properties*. Berlin Heidelberg: Springer-Verlag; 1978.
- [33] J A Pryde and C G Titcomb. Phase equilibria and kinetics of evolution of dilute solutions of hydrogen in niobium. *J Phys C Solid State Phys* 1972;5:1293.
- [34] Yannopoulos LN, Edwards RK, Wahlbeck PG. The Thermodynamics of the Yttrium-Hydrogen System1. *J Phys Chem* 1965;69:2510–5. doi:10.1021/j100892a004.
- [35] Huiberts JN, Griessen R, Rector JH, Wijngaarden RJ, Dekker JP, Groot DG de, et al. Yttrium and lanthanum hydride films with switchable optical properties. *Nature* 1996;380:231–4. doi:10.1038/380231a0.
- [36] Crivello J-C, Dam B, Denys RV, Dornheim M, Grant DM, Huot J, et al. Review of magnesium hydride-based materials: development and optimisation. *Appl Phys A* 2016;122. doi:10.1007/s00339-016-9602-0.





---

# CHAPTER FIVE

---

Conception of an automatic cycling device to measure the cycle-life of metal hydrides





## Chapter 5. Conception of an automatic cycling device to measure the cycle-life of metal hydrides

The target of this chapter is the conception and assembly of an Automatic Hydrogen Cycling device (AC-device) prototype. It has been carried out in different steps which are explained in this chapter. First, the thermodynamic operation conditions have been established. Second, a hydride forming alloy that will act as a source and sink of hydrogen has been selected according to operating conditions. Third, a blueprint has been drawn before the assembly. The conception of hydride reservoirs, pressure, flow and temperature sensors, automatic valves and connectors have been considered in this step. Fourth, a coupling with commercial software has been adapted to the automatic control and data acquisition.

### 5.1 Principle of the Automatic cycling device

#### 5.1.1 Thermochemical hydride compressors

The AC-device will be based on the use of metal hydrides as thermochemical compressors of hydrogen gas. As shown in Figure 5.1, the temperature dependence of the plateau pressure of a hydride forming alloys can be used to compress hydrogen gas. By heating the hydride from a low temperature,  $T_L$  to a high-temperature  $T_H$ , its equilibrium pressure increases from a low-pressure plateau,  $P_L$ , and the high-pressure plateau,  $P_H$ . Thus, in operation, a reservoir filled with a hydride that is repeatedly heated and cooled between  $T_L$  and  $T_H$  will follow the thermodynamic path  $ABCD$  (solid line, absorption; dashed line, desorption) shown at Fig. 5.1 (right). The compression ratio depends on the alloy selected, on the temperature range  $\Delta T = T_H - T_L$ , and on the overall system dynamics. The thermal energy needed to do the work of compression can be produced from waste heat or solar energy [1].

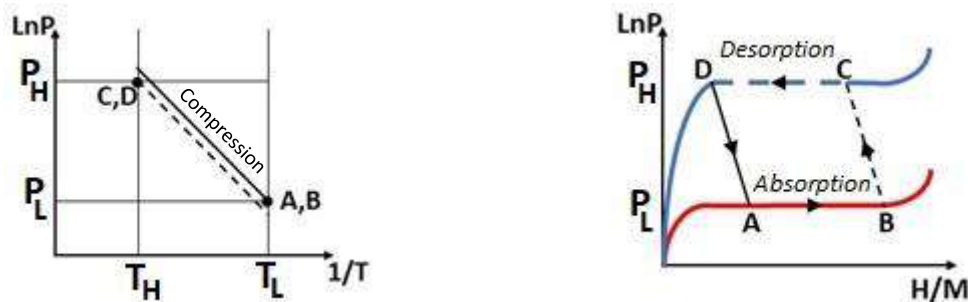


Figure 5.1 Principle of the hydride compressor, van't Hoff plot (left) and ideal P-c-I [1]

##### 5.1.1.1 Development of hydride compressors

In the early 70's, Reilly *et al.* described one of the first applications of hydrides compressors [2]. The compressor used vanadium hydride. It was built to drive periodically a mercury column acting as a pump for other gases. The first commercial hydride compressor was developed by Golben in 1983 [3]. The device is a four-stage metal/hydrogen compressor that uses hot water at 75 °C as an energy source. Four stages filled with different alloys from the  $\text{LaNi}_5$  family are assembled in series in two different beds inside a reservoir. Based on this work, in the 80's, two models are commercially proposed by Ergenics, a single electrically

powered unit that is able to compress H<sub>2</sub> between 0.5 and 3.5 MPa, and a four-stage hot water (75 °C) heated unit that compresses H<sub>2</sub> from 0.4 to 4.1 MPa for a weight system of 64 kg [4].

### 5.1.1.2 Hydrogen cycling devices

Hydrogen cycling in manual hydrogenation systems is time-consuming and strict manipulations must be considered to keep the purity of the gas. Usually, these experiments are carried out in standard Sieverts' type volumetric devices [5,6]. This kind of equipment is not optimized for performing extended absorption/desorption cycles. Even when automatic devices are designed specifically for cycling, such as PCTPro system from Setaram[7], other problems arise. Typical designs of these devices involve the use of high purity hydrogen as a gas source and a vacuum pump used as a gas sink. The compound under study is held at constant temperature while high-pressure and low-pressure sweeps (*i.e.* pressure cycling) are imposed from a hydrogen source (usually, 20 MPa tank inlet) and a hydrogen sink (vacuum connected reservoir outlet). Thus, large quantities of high purity gas are unfortunately wasted as cycling proceeds. A second issue is related to gas purity itself. Hydride-forming materials can be poisoned by impurities such as O<sub>2</sub>, CO<sub>2</sub>, and water. This gas can be further purified, for example, up to 99.99% grade by means of a hydriding/dehydriding sorption process using a suitable metal hydride. Even in such a case, as the gas is pumped out of the system on every cycle, fresh gas must be constantly added to the system through a gas inlet. This operation increases the risk of leakage and subsequent contamination. In addition, the open sink concept (usually a mechanical vacuum pump) also introduces risk of contamination due, for example, to oil fumes from the pump and gas upstream diffusion. Most of these issues can be solved if decomposition/formation of metal hydrides by thermal cycling is used as a source/sink of hydrogen gas. Purified H<sub>2</sub> is only introduced into the equipment's volume at the beginning of the experiment. If all device components are properly sealed, external impurities will not appear and residual ones will likely be dissolved in the metal hydride.

Alternatively, another way to cycle hydride materials is to impose thermal cycles at fixed external pressure. However, this implies using wide temperature ranges to achieve full hydride decomposition and formation. Thus, cycle-life degradation will result not only from hydrogen absorption/desorption processes but also from thermally induced changes. Moreover, to facilitate hydriding/decomposition, the sample could be thermally cycled out from technological working conditions, making the association of results with real applications difficult.

Taking into account last drawbacks, Meyer *et al* [8]. designed an automated equipment for pressure cycling. The basic idea was to use a single hydride reservoir filled with a hydride forming alloy as a hydrogen source/sink by programmed heating/cooling to generate pressure sweeps. The highest/lowest temperatures are selected so that the generated pressures by a hydride forming alloy are above/below the formation/decomposition pressure of the sample under study, which will be kept at constant temperature. Thus, thermal cycles are applied to the hydrogen source/sink compound and not to the sample under study. The pressure sweeps were used to fill (or empty) a calibrated intermediate volume up to a desired pressure. The gas contained in this volume was then automatically expanded to the sample volume like in a classical Sieverts' apparatus and the amount of hydrogen absorbed in each sweep could be determined. Using a forming hydride material LaNi<sub>5</sub>, as a source and sink of hydrogen, the equipment eradicated hydrogen waste and ensure high purity gas during the experimentation.

Using this apparatus, 1000 uptake/release cycles were performed in a  $Mm_{0.8}Ca_{0.2}Ni_5$  (Mm: 50% cerium, 25% lanthanum, and 15-18% neodymium) sample kept at 25°C. Absorption and desorption pressures were about 5 and 2 MPa. A full absorption-desorption cycle took 12 min. Such a fast cycling was achieved thanks to an effective heating/cooling (internal cartridge heater/external cold-water flow) system.

To study the cycle-life of hydrides, Challet [9] developed a simpler pressure cycling equipment which was able to work autonomously without interruption (Figure 5.2). The hydrogen source/sink was provided by a reservoir filled by a hydride forming alloy:  $LaNi_{4.6}Sn_{0.4}$ . Thermal cycling was imposed on this reservoir to generate pressure cycles. To supply hydrogen to the studied sample (absorption), the reservoir is heated so that the plateau pressure  $P_H$  of  $LaNi_{4.6}Sn_{0.4}$  exceeds that of the studied sample ( $P_S$ ). The sample then absorbs hydrogen. By cooling the reservoir down to a temperature  $T_L$  for which the plateau pressure  $P_L$  of  $LaNi_{4.6}Sn_{0.4}$  drops below that of the sample, the latter desorbs the hydrogen. Cycling absorption/desorption of the sample is therefore carried out by pressure cycling. The studied sample was maintained at constant temperature. With this system, no measurement of the quantity of hydrogen exchanged between the reservoir and the sample was available. It was used for cycling a  $La_{0.55}Y_{0.45}Ni_5$  sample at -5°C over 100 cycles in the pressure range from 0.05 to 2 MPa. Each cycle took as much as 5 hours since low-efficient classical tubular oven and ambient air was used as heating/cooling systems.

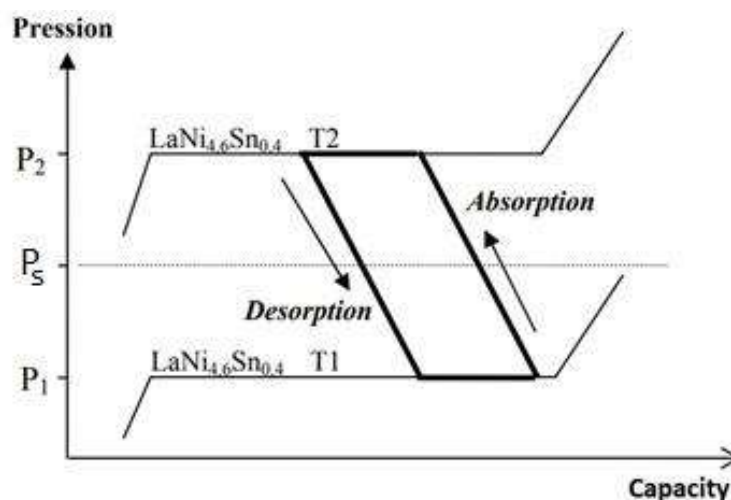


Figure 5.2 Thermodynamic principle of the device developed by Challet [9]

### 5.1.2 Principle of AC-device

Taking into consideration the previous works, there is a strong interest to build an AC-device to measure the cycling-life of hydrides. More specifically, we aimed to determine the cycle-life of  $MgH_2$ -based NCs which operate at 300°C and possess fast kinetics as shown in Chapters 3 and 4.

The ideal thermodynamic principle of the designed system is schematically described in Figure 5.3. The sample S, a  $MgH_2$ -TMH<sub>x</sub> nanocomposite, will be cycled through  $MgH_2 \leftrightarrow Mg$

transformation with the help of two equivalent reservoirs filled up with the same hydride forming alloy. These reservoirs will be heated up at different temperatures  $T_H$  and  $T_L$  to act as hydrogen source and hydrogen sink, respectively. The reservoir at  $T_H$  will be initially hydrogenated in an external apparatus at the onset of the  $\beta$ -hydride branch (point 1 in Fig. 5.3). The reservoir at  $T_L$  will be initially hydrogenated at the end of the  $\alpha$ -solution branch (point 4 in Fig. 5.3). Temperatures  $T_H$  and  $T_L$  will be set so that the corresponding equilibrium plateau pressures  $P_H$  and  $P_L$  of the hydride forming alloy enclose that of the studied  $\text{MgH}_2\text{-TMH}_x$  sample  $P_S$ . The sample temperature will be kept constant (typically at 300 °C). Reservoirs and sample holder will be put in contact alternatively. Thus, connection between the high-temperature reservoir and the sample holder will hydrogenate sample  $P_S$  (arrow from 2 to 3 in Fig. 5.3), whereas connection between the sample holder and the low-temperature reservoir will dehydrogenate it (reverse arrow from 3 to 2 in Fig. 3.5). This results in a complete hydrogenation/dehydrogenation cycle for sample  $S$  at constant temperature. Sample mass will be much lower than that of the hydride forming alloy in the sinks as schematically represented in Fig. 3.5 by a large difference in plateau width. It will allow tens of cycling sweeps before all hydrogen from the high-temperature reservoir is transferred to the low temperature one. Once this happens, the temperature between both reservoirs will be inverted.

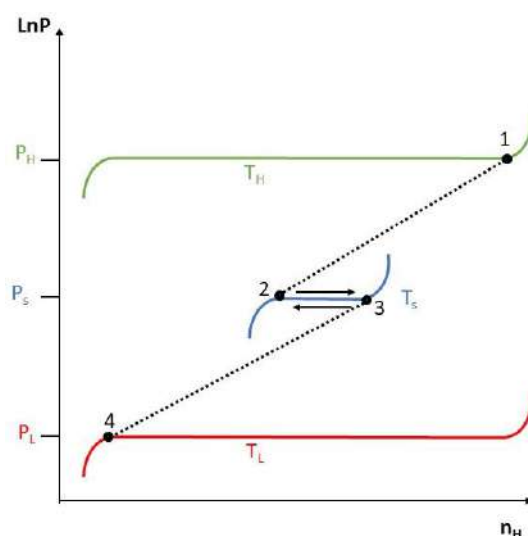


**Figure 5.3** Schematic operation principle of the AC-device based on the PCT properties of a hydride forming alloy. Temperatures  $T_H$  and  $T_L$  correspond to the equilibrium plateau pressures  $P_H$  and  $P_L$  of the hydride forming alloy,  $P_S$  and  $T_S$  correspond to the  $\text{MgH}_2\text{-TMH}_x$  pressure and temperature sample.

## 5.2 Setting of the operation conditions

The purpose of the AC-device within the framework of this Thesis is to perform extended hydrogen cycles for  $\text{MgH}_2\text{-TMH}_x$  NCs. Therefore, it is necessary to consider the thermodynamics of  $\text{Mg/MgH}_2$ . The PCI curves in Chapter 3, Figure 3.7, showed that at 300 °C the  $Pp$  of  $\text{MgH}_2\text{-TMH}_x$  NCs in both absorption and desorption is 0.16MPa. Thus, the pressure

and temperature conditions of the AC-device can be fixed considering these thermodynamic data as well as kinetic, safety and thermal management issues. Values are presented in Table 5.1. Thus, absorption ( $P_H$ ) and desorption ( $P_L$ ) pressures were fixed to similar values than those used in chapters 3 and 4 to get high enough driving forces for the reversible  $\text{MgH}_2 \leftrightarrow \text{Mg}$  reaction and ensure fast kinetics. The temperature sink reservoir was fixed at  $T_L = 50^\circ\text{C}$  for using ambient air for thermal management while operating close to RT. The temperature of the source reservoir was fixed at  $T_H \leq 200^\circ\text{C}$  for safety issues.

**Table 5.1** Thermodynamic operation conditions of the AC-device

Variable	Value
Sample mass, $m_s$	0.1 g
Sample temperature, $T_s$	300 °C
Sample plateau pressure, $P_s$	0.16 MPa
H <sub>2</sub> source pressure, $P_H$	~1 MPa
H <sub>2</sub> sink pressure, $P_L$	~0.05 MPa
H <sub>2</sub> source temperature, $T_H$	$\leq 200^\circ\text{C}$
H <sub>2</sub> sink temperature, $T_L$	50°C
Sample holder volume	2.25 cm <sup>3</sup>

### 5.3 Selection of the hydride forming alloy

There are four important facts to consider for selecting the hydride forming alloy used to fill up the source and sink reservoirs according to the previous operation settings: storage capacity, thermodynamic properties (plateaus), kinetics and cycle-life. First, the alloy must have a high reversible storage capacity to ensure the autonomy of the system. The amount should be much larger than that of the cycled sample. Second, flat plateaus with moderate hysteresis are needed to guarantee a good efficiency of the system and stable driving forces during cycling. Third, alloy kinetics should be as fast as those of the cycled sample for not limiting its absorption/desorption rate and minimizing the time needed for cycling. Forth, the alloy must have a long-cycle life for maintaining the thermodynamic operation conditions of the AC-device over thousands of cycles. An additional fact for this work is a safety issue, because of the device autonomy the hydride material should work at a relatively low temperature ( $T \leq 200^\circ\text{C}$ ) and pressure ( $P \leq 3\text{ MPa}$ ).

Hydride-forming alloys of  $AB_5$  and  $AB_2$  types are suitable for the compression of hydrogen due to their thermodynamic properties: they exhibit moderate hysteresis and almost flat pressure plateaux. Hydrogen absorption in these intermetallic compounds is characterized by a hydrogen capacity of about one atom per metal atom (H/M).

Van Vught et al. [10] reported that  $\text{LaNi}_5$  could reversible absorb 6 H/f.u. at room temperature under a  $P_P$  about 0.2 MPa. Thus,  $\text{LaNi}_5$  forms a too unstable hydride for being used as hydrogen sink at  $T_L = 50^\circ\text{C}$ . To adapt its plateau pressure to these thermodynamic conditions part of B-type atoms (Ni) can be replaced by other transition metals [11,12]. Indeed, plateau pressures of substituted  $\text{LaNi}_5$ -type compounds depend on the nature and amount of the substituting elements [13]. Unfortunately, there is a price to pay for this

adaptation. The substituted compounds show smaller capacity than  $\text{LaNi}_5$ . Capacities of several substituted compounds are presented in Table 5.2.

**Table 5.2** Hydrogen capacity at 40 °C for various substituted  $\text{LaNi}_5$ -type alloys and their  $P_p$  [14]

Composition	Storage capacity (H/f.u.)	$P_p$ (MPa)
$\text{LaNi}_5$	6.24	0.2
$\text{LaNi}_{4.7}\text{Al}_{0.3}$	5.85	0.1
$\text{LaNi}_{4.25}\text{Co}_{0.75}$	6.23	0.1
$\text{LaNi}_{4.6}\text{Mn}_{0.4}$	6.21	0.1
$\text{LaNi}_{4.5}\text{Sn}_{0.5}$	5.25	0.1

Many studies have been carried out to determine and understand the kinetic properties of  $AB_5$  alloys. One of the best advantages of  $AB_5$  alloys is the selective oxidation of the  $A$  metal, leaving catalytic  $B$  species at the surface to promote adsorption and dissociation of the hydrogen molecules [15]. Thus, Ni segregation at the alloy surface provides fast surface reactions and high resistance against poisoning from gas impurities. Schlapbach *et al* [16] have emphasized the fact that  $\text{LaNi}_5$  kinetics are extremely fast, they present a diffusion coefficient value for  $\text{LaNi}_{4.9}\text{Cu}_{0.1}$  of  $2 \times 10^{-9} \text{cm}^2 \text{s}^{-1}$  at 20 °C, which shows the fast hydrogen mobility in bulk. Also, they pointed out that the thermal conductivity of both the hydride and the  $\text{LaNi}_5$  in powder form is poor. In many engineering applications, heat transfer between the hydride bed and the reservoir controls the system kinetics.

Cycle-life properties have been investigated for many  $AB_5$  alloys. In general, the reduction of the capacity through cycling is attributed to the disproportionation of the alloy upon hydrogen absorption into  $AH_x$  and  $B$ -enriched compounds [17]. This causes losses in reversible storage capacity and modifies the PCT isotherms. This issue is particularly severe in  $\text{LaNi}_5$  alloy. As shown in Figure 5.4, the partial substitution of Ni by Sn greatly reduces the rate of degradation [18]. Similar improvements have been found for Al, Ge, and Si substitution [15].

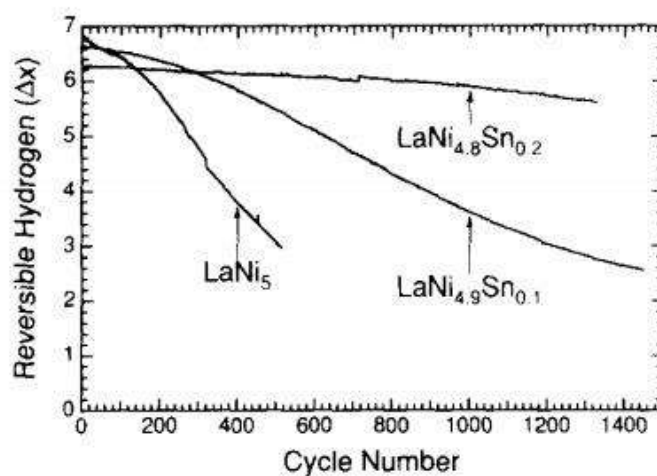


**Figure 5.4** Effect of Sn substitution on the cycle-life of  $\text{LaNi}_{5-x}\text{Sn}_x$  alloys

Percheron-Guégan *et al.* reported that the partial replacement of Ni for other transition metals and semi-metals generally leads to a lowering of  $P_p$  [19]. This is clearly evidenced in Fig. 5.5. The extent of this stabilization depends strongly on the type and the rate of substitution. For instance, manganese and aluminum substituted compounds form very stable hydrides: at 40 °C:  $P_p = 5 \times 10^{-4}$  and  $1.6 \times 10^{-4}$  MPa for  $\text{LaNi}_4\text{MnH}_6$  and  $\text{LaNi}_4\text{AlH}_{4.8}$ , respectively, compared to with  $P_p = 0.37$  MPa for  $\text{LaNi}_5\text{H}_{6.4}$ . Exceptions to this rule occur with platinum and palladium[20,21].

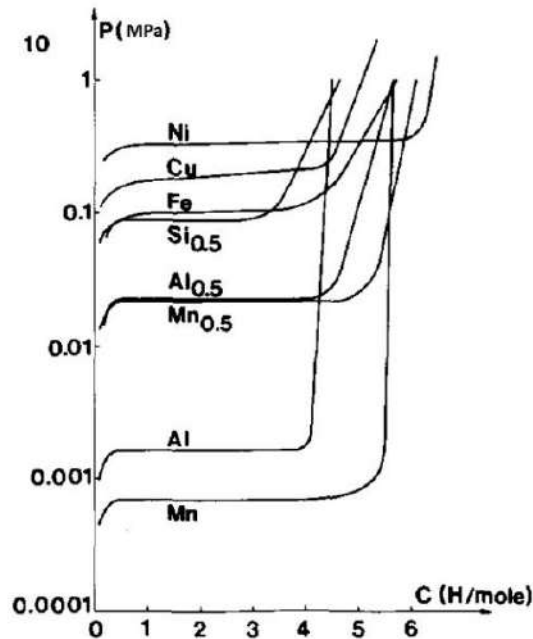


**Figure 5.5** Desorption isotherms at 40 °C for some substituted  $\text{LaNi}_{5-x}\text{M}_x$  compounds [19].

Considering the operation conditions given before (particularly,  $P_L = 0.05$  MPa at  $T_L = 50^\circ\text{C}$ ) several stabilizing substitutions are of interest:  $M = \text{Mn}, \text{Al}, \text{Si},$  and  $\text{Sn}$ . To make a choice between these possibilities, capacity, kinetics, and cycle-life should be considered. All the four substituted systems exhibit good hydrogen reversibility and fast kinetics [19]. Nevertheless, the desorption capacity for Al, Si, and Sn is lower than for Mn. On the other hand, Mn substituted alloy has poor cycle-life as compared to the others. Indeed,  $\text{LaNi}_{4.7}\text{Al}_{0.3}$  has good cycle-life with a loss of 12% in hydrogen uptake after 2500 cycles [22]. Even better, Lambert *et al.* [23] reported that the hydrogen capacity of  $\text{LaNi}_{4.8}\text{Sn}_{0.2}$  remains virtually unaffected after 10 000 thermal cycles with a very low hysteresis during the absorption/desorption cycling. Taking the cycle-life as a key factor of choice, the  $\text{LaNi}_{5-x}\text{Sn}_x$  system has been selected. The substitution amount  $x$  is determined in the following from thermodynamic considerations.

Using the Van't Hoff equation 1.1 Chapter 1, the composition of the alloy can be determined from the defined thermodynamic properties as well as enthalpy and entropy values of the reaction. For  $P_p = 0.05$  MPa at  $T = 50^\circ\text{C}$ , the required formation enthalpy can be calculated as  $\Delta H = -38.11 \text{ kJ mol}^{-1}\text{H}_2$  for an entropy of reaction fixed at  $112 \text{ J K mol}^{-1}\text{H}_2$ [24], which is a typical value for hydrogen absorption in the  $\text{LaNi}_{5-x}\text{Sn}_x$  system. Lartigue [25]

tabulated  $\Delta H$  values using literature data for different Sn-contents [24,26,27]. They are gathered in Table 5.3 and plotted in Figure 5.7. The data can be fit by the linear equation:

$$\Delta H = -30.28 - 23.87 x$$

For  $\Delta H = -38.11 \text{ kJ mol}^{-1}\text{H}_2$ , the content of Sn,  $x$ , is 0.34. The composition of the defined alloy is  $\text{LaNi}_{4.66}\text{Sn}_{0.34}$ .

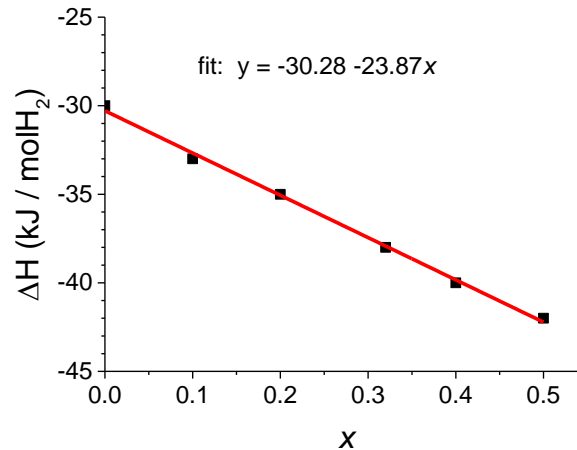


**Figure 5.6.** Formation enthalpy of  $\text{LaNi}_{5-x}\text{Sn}_x$  hydrides as a function of substitution ratio

**Table 5.3** Enthalpy of hydride formation for different alloys in the  $\text{LaNi}_{5-x}\text{Sn}_x$  system

$x$ value	$\Delta H$ ( $\text{kJ mol}^{-1}\text{H}_2$ )
0	30
0.10	33
0.20	35
0.32	38
0.40	40
0.50	42

Following this selection, it is worth noting that Sn-content also reduces the capacity of the alloy as compared to the parent compound. This has been evidenced by Joubert *et al.* who reported the *PCI* curves of the  $\text{LaNi}_{5-x}\text{Sn}_x$  system for  $0 \leq x \leq 0.5$  [26]. As shown in Fig. 5.6. not only the plateau pressures decrease with Sn-content but also the plateau width reduces in length.

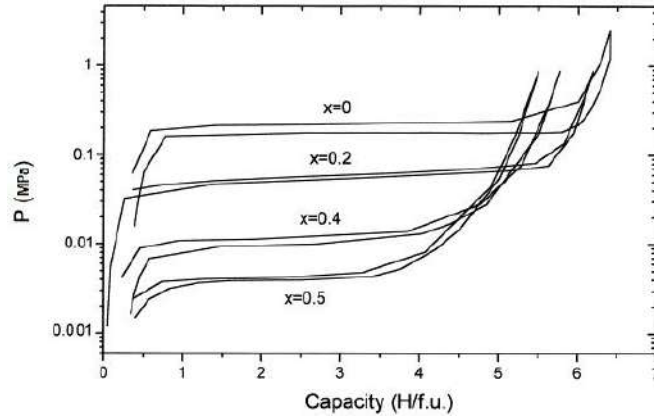


Figure 5.7 PCI curves at 25°C for  $\text{LaNi}_{5-x}\text{Sn}_x$  compounds [26]

Using the calculated thermodynamic data of the selected alloy  $\text{LaNi}_{4.66}\text{Sn}_{0.34}$  (i.e.,  $\Delta H = -38.11 \text{ kJ mol}^{-1}\text{H}_2$ ,  $\Delta S = -112 \text{ JK}^{-1}\text{mol}^{-1}\text{H}_2$ ) we could estimate suitable thermodynamic parameters for the high-temperature hydrogen source reservoir. For a temperature of  $T_H = 150 \text{ }^\circ\text{C}$ , the plateau pressure  $P_H$  is evaluated as 1.38 MPa, within the range of the thermodynamic operation conditions defined in Table 5.1. Moreover, these conditions allow to obtaining relatively close driving forces ( $DF$ ) for hydrogen absorption (Ec. 5.1) and desorption (Ec.5.2) at 300°C in  $\text{MgH}_2\text{-TMH}_x$  NCs:

$$DF_{abs} = \ln \frac{P_H}{P_S} = \ln \frac{1.38}{0.16} = 2.15 \quad \text{Eq. 5.1}$$

$$DF_{des} = \ln \frac{P_S}{P_L} = \ln \frac{0.16}{0.05} = 1.16 \quad \text{Eq. 5.2}$$

As a next step, the amount of  $\text{LaNi}_{4.66}\text{Sn}_{0.34}$  needed for each reservoir was estimated. This calculation was based on the number of moles,  $n_{\text{H,MgH}_2}$ , needed to hydrogenate a given amount of Mg. This amount was fixed to 100 mg leading to  $n_{\text{H,Mg}} = 0.008$ . The Mg amount was selected as a compromise between having high enough material for subsequent microstructural characterization after cycling but low enough for minimizing the quantity of hydrogen transferred in each cycle.  $\text{LaNi}_{4.66}\text{Sn}_{0.34}$  was considered to form  $\text{LaNi}_{4.66}\text{Sn}_{0.34}\text{H}_5$  as a hydride (see Fig. 5.7). The needed amount of  $\text{LaNi}_{4.66}\text{Sn}_{0.34}$  was overestimated by a factor of 25 ( $n_{\text{H, LaNi}_{4.66}\text{Sn}_{0.34}\text{H}_5} = 0.2$ ) to supply enough hydrogen to hydrogenate the Mg sample 25 times. The estimated quantity of  $\text{LaNi}_{4.66}\text{Sn}_{0.34}$  was 35 g.

As a final remark, the thermic conductivity of  $\text{LaNi}_5$  alloys is reported to be low ( $1.32 \text{ Jm}^{-1}\text{s}^{-1}\text{K}^{-1}$ ) [28,29]. To overcome this issue and based on the studies of Meyer *et al.* [7] and Suda *et al.* [30],  $\text{LaNi}_{4.66}\text{Sn}_{0.34}$  was mixed to Cu (20 wt. %) powders. Cu powder was previously subjected to a reduction treatment (7h at 350°C under Ar/H<sub>2</sub> flowing) for getting rid of native surface oxides.

### 5.3.1 Synthesis of $\text{LaNi}_{4.66}\text{Sn}_{0.34}$

In 1972, Buschow and van Mal [31] published the La-Ni phases diagram (Fig 5.8, left). In the range of 50 to 100 % of nickel atoms, there are six compounds:  $\text{LaNi}$ ,  $\text{LaNi}_x$  ( $x \approx 1.4$ ),  $\text{LaNi}_2$ ,  $\text{LaNi}_7$ , and  $\text{LaNi}_5$ . The binary diagram La-Ni shows a wide homogeneity domain for the phase  $\text{LaNi}_5$ . Also, the ternary La-Ni-Sn system at 400 °C is shown (Figure 5.8 right) [32]. Beside eight ternary compounds ( $\text{LaNi}_5\text{Sn}$ ,  $\text{LaNi}_4\text{Sn}_2$ ,  $\text{LaNi}_2\text{Sn}_2$ ,  $\text{La}_3\text{Ni}_2\text{Sn}_6$ ,  $\text{La}_3\text{Ni}_2\text{Sn}_7$ ,  $\text{La}_3\text{Ni}_8\text{Sn}_{16}$ ,  $\text{LaNiSn}$ , and  $\text{La}_5\text{Ni}_{24}\text{Sn}$ ) the pseudobinary phase  $\text{La}(\text{Ni}, \text{Sn})_5$  with  $\sim 8$  at.% Sn solubility limit exists. The Sn-content in  $\text{LaNi}_{4.66}\text{Sn}_{0.34}$  is 6 at.%.

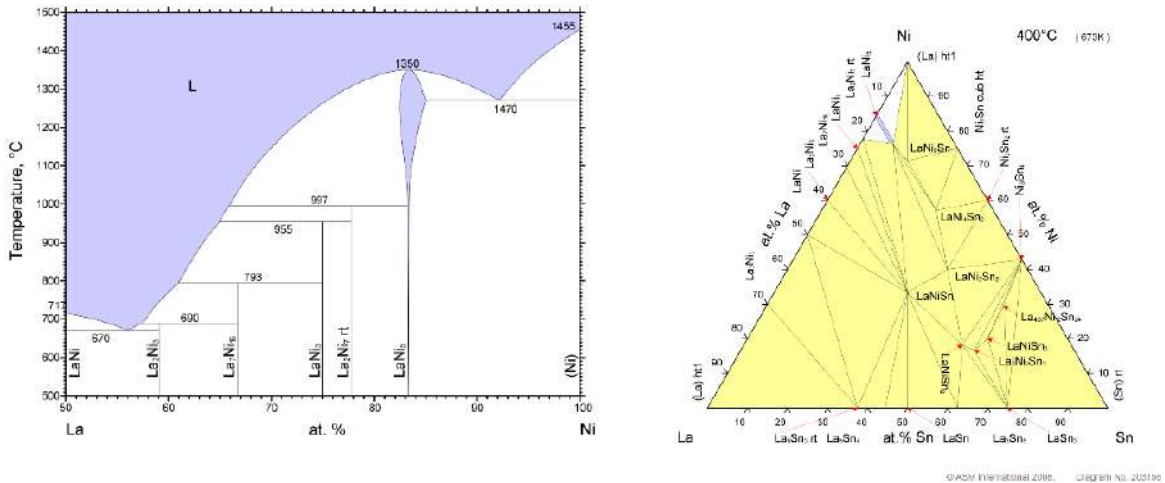


**Figure 5.8.** Binary Phase Diagram of La-Ni (left), ternary Phase Diagram La-Ni-Sn at 400°C (right)

#### 5.3.1.1 Characterization of $\text{LaNi}_{4.66}\text{Sn}_{0.34}$

##### a) Structural properties

A representative BSE image of the sample is shown in Figure 5.9. The sample is a single phase (uniform grey color). The average atomic composition as obtained by EPMA measurements on 50 random points at the ingot surface is  $\text{La}_{1.00 \pm 0.02}\text{Ni}_{4.67 \pm 0.02}\text{Sn}_{0.34 \pm 0.02}$ .

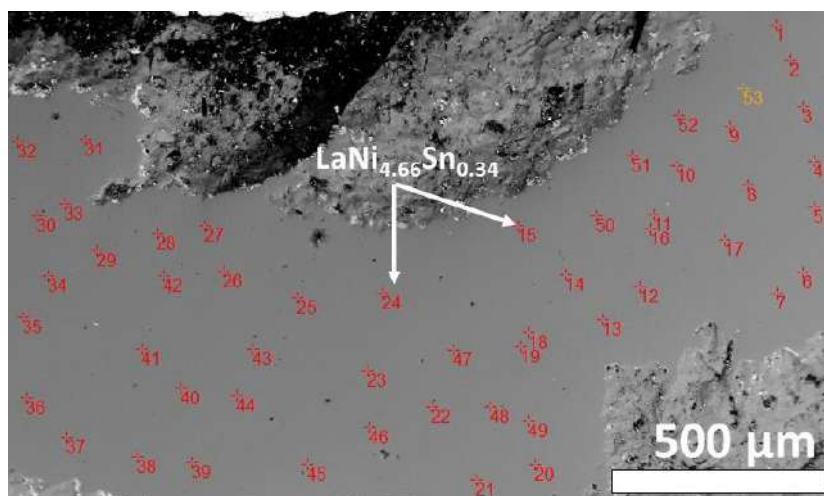


**Figure 5.9.** BSE image of  $\text{LaNi}_{4.66}\text{Sn}_{0.34}$  alloy

### b) Structural properties

XRD analysis confirmed that the alloy consists of a single  $\text{LaNi}_5$ -type phase. The obtained diffractogram and the corresponding Rietveld refinement output are represented in Figure 5.10. The refined lattice parameters are  $a = 5.077(2) \text{ \AA}$  and  $c = 4.043(2)$ . Sn atoms were placed on Ni Wyckoff position  $3g (\frac{1}{2}, 0, \frac{1}{2})$  and refined composition is  $\text{LaNi}_{4.69(5)}\text{Sn}_{0.31(5)}$  in agreement with the chemical analysis

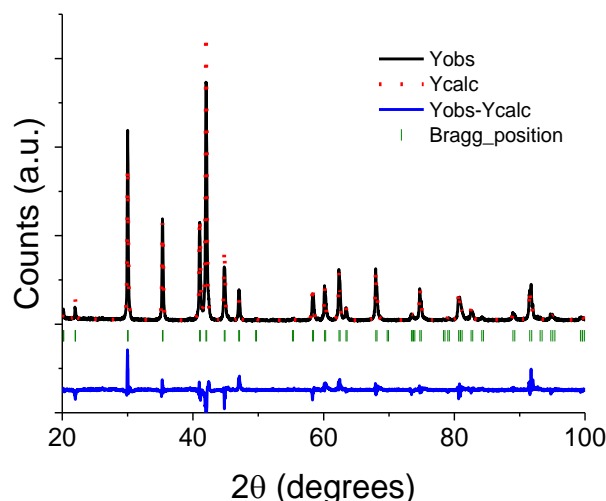


Figure 5.10 Rietveld refinement of  $\text{LaNi}_{4.66}\text{Sn}_{0.34}$  alloy

### c) Thermodynamic properties

The hydrogenation properties of the  $\text{LaNi}_{4.66}\text{Sn}_{0.34}$  alloy were characterized by *PCI* isotherms at 50, 100, 125 and 150 °C in the pressure range  $10^{-3}$  to 2.5 MPa (Figure 5.12). The maximum capacity is 5.5 H/f.u. with a plateau width around 4 H/u.f. *PCI* curves exhibit small hysteresis between hydrogen uptake and release with a sloping plateau.

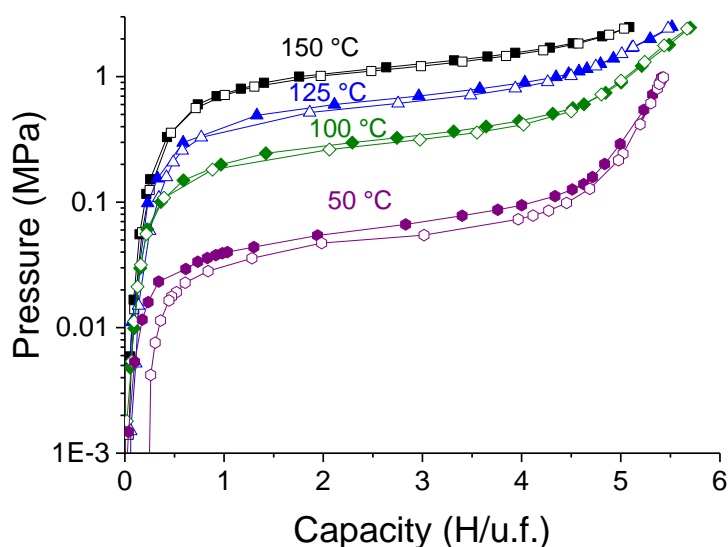


Figure 5.11 *PCI* isotherms of  $\text{LaNi}_{4.66}\text{Sn}_{0.34}$  alloy at several temperatures. Empty and full symbols stand for desorption and absorption, respectively.

From the  $P_p$  at half-plateau, the van't Hoff plot has been obtained as shown in Figure 5.12. Enthalpy and entropy values both on absorption and desorption are shown. The formation enthalpy,  $\Delta H_{\text{abs}} = -33.4 \text{ kJ mol}^{-1}\text{H}_2$ , is slightly lower (in absolute value) than the targeted one,  $\Delta H = -38.11 \text{ kJ mol}^{-1}\text{H}_2$ . Note also that a deviation in the same direction occurs for the entropy, which counterbalances this effect. Indeed, the plateau pressures at selected temperatures match well with targeted values (Table 5.1). At  $T_L = 50^\circ\text{C}$ , the plateau pressure on absorption (*i.e.* to act as a hydrogen sink) is  $P_L = 0.06 \text{ MPa}$ . At  $T_H = 50^\circ\text{C}$ , the plateau pressure on desorption (*i.e.* to act as a hydrogen source) is  $P_H = 1.2 \text{ MPa}$ .

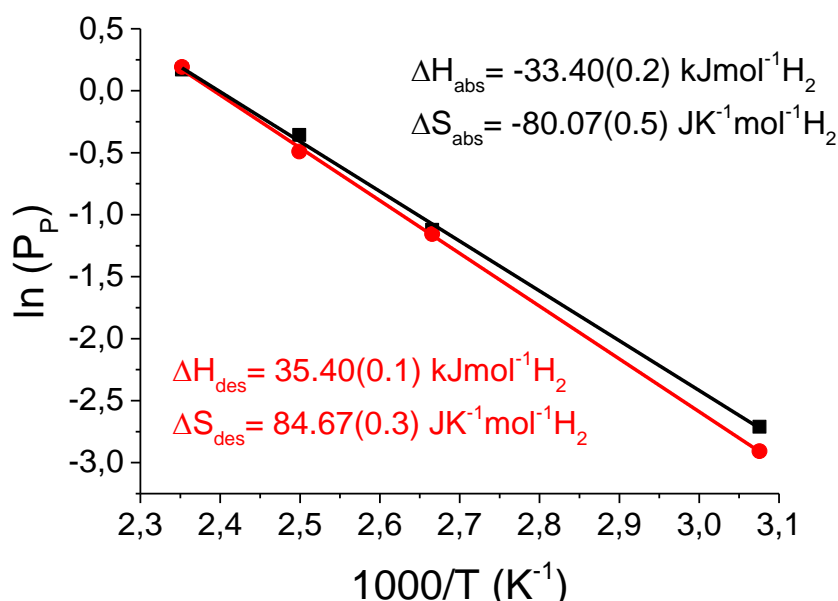


Figure 5.12 van't Hoff plots corresponding

#### 5.4 Blueprint of AC-device

Once that both hydrogen source and sink hydrides have been chosen, the reservoir or reactor where the hydrides are going to take place it has been selected. Knowing the mass of  $\text{LaNi}_{4.66}\text{Sn}_{0.34}$  (35 g), and density ( $8.28 \text{ g/cm}^3$ ) the volume occupied by the hydride forming alloy can be calculated ( $4.22 \text{ cm}^3$ ) (Cu volume was also considered). With these data and the supplier availability, it was chosen a Swagelok double-ended cylinders, of  $50 \text{ cm}^3$ , able to work at pressures up to  $34.4 \text{ MPa}$ , stainless steel 304L materials resist to intergranular corrosion. The double-ended was considered to set a thermocouple on one side and the other is the out/in gas. The heat provided to the reactor is coming from a heating tight mica collar. The maximum reachable temperature is  $375^\circ\text{C}$ . The supply voltage is  $230 \text{ V}$ . The electric connection is done by cable isolated of the sink from glass under flexible braid steel. A T-type thermocouple was plugged in the heating collar and connected to a PID controller, for temperature control of the reactor.

According to the operating conditions, two Bronkhorst thermal mass flow meters made on stainless steel 304L, with maximum flow values (1000 mg/h), temperature (70 °C) and pressure (10 MPa), were selected. To work in an automatic way, two Swagelok 3-way solenoid valves were acquired. These valves open when receiving an electrical signal, allowing air to enter the actuator. When the signal stops, the solenoid valves close and vents pressure from the actuator. A pressure indicator is also used in the system likewise a safety valve limiting to a maximum of 25 bar pressure operation into the system. Swagelok stainless steel ball valves (7) has been added to the system for manual operation at the beginning or end of the process. The tubing fitting material is from stainless steel with 4 mm of internal diameter. The volume of the system (out of the two reservoirs) was measured to be 21.24 cm<sup>3</sup>.

A diagram of the AC-device is drawn in Figure 5.13, acronyms are explained from left to right in Table 5.4.

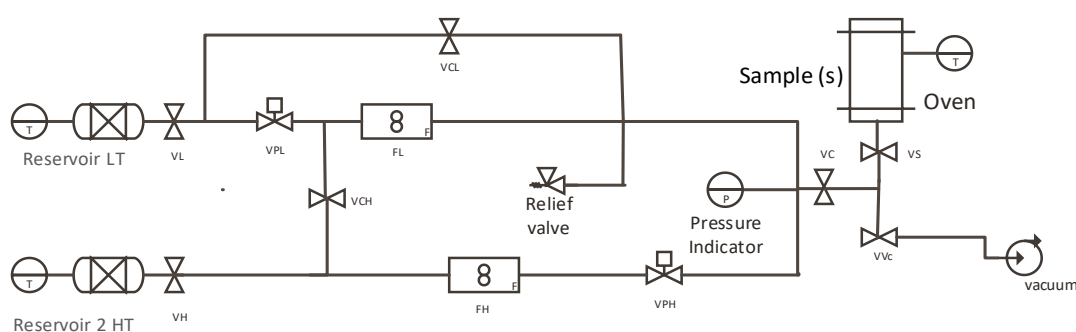


**Figure 5.13.** AC-device diagram

**Table 5.4** Acronyms used for AC-device diagram

Acronym	Meaning
Reservoir LT	Reactor at low temperature
Reservoir HT	Reactor at high temperature
VL	Valve of low-pressure reactor
VH	Valve of high-pressure reactor
VPL	Solenoid valve to low-pressure reactor
VPH	Solenoid valve to high-pressure reactor
FL	Flux-meter to low-pressure reactor
FH	Flux-meter to high-pressure reactor
VCH	Internal recirculation valve
VCL	External recirculation valve
RV	Relief valve
PI	Pressure indicator
VC	Valve to system
VS	Valve to sample
VVc	Valve to vacuum system

The working steps can be explained with different pictures. For instance, Figure 5.14 depicted in yellow the very first step, vacuum procedure. The vacuum is applied to system or stationary parts.

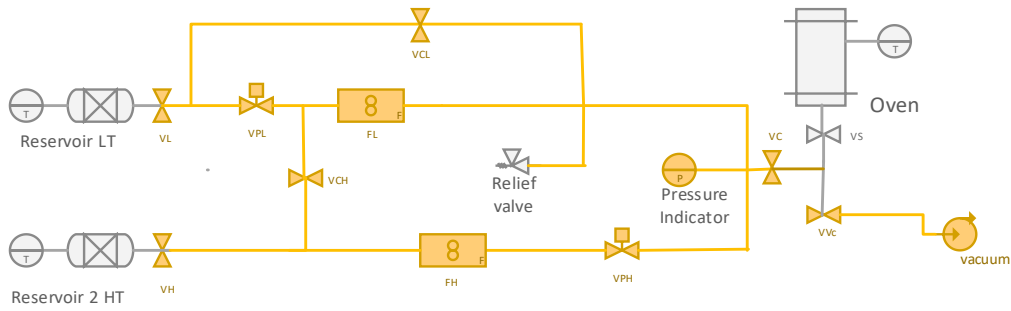


Figure 5.14. AC-device vacuum process diagram

Figure 5.15 shows the parts involved during the hydrogen release of  $AB_5$  and hydrogen uptake of Mg. Reservoir HT, release hydrogen which flows through the flux meter and solenoid valve and goes directly to the sample reservoir to be absorbed by Mg for 15 min.

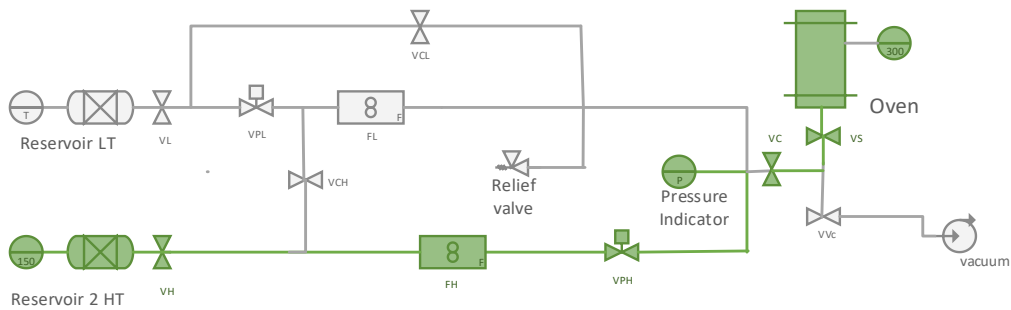


Figure 5.15. AC-device Mg hydrogen uptake process diagram

Then, VPH valve is closed and VPL valve is opened, hydrogen release from  $MgH_2$  starts and  $AB_5$  low-temperature hydrogen absorption begins (Figure 5.16). This process is also scheduled for 15 min.

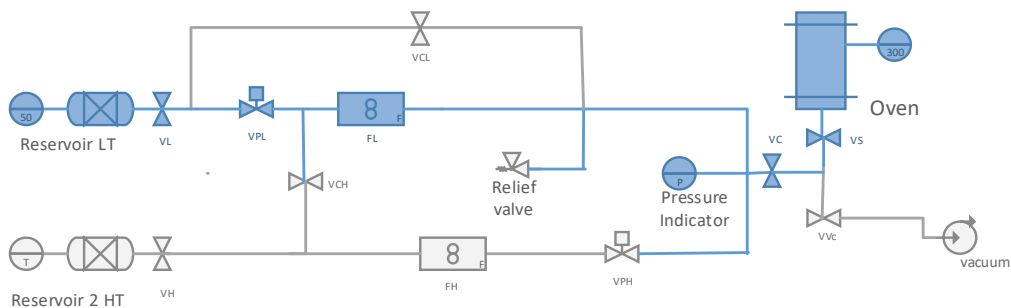


Figure 5.16. AC-device  $MgH_2$  hydrogen release process diagram

After tens of cycles, the hydrogen source is going to be empty and the hydrogen sink is close to being full. At that time the temperature of both reservoirs is inverted, and the source starts refilling as shown in Figure 5.17.

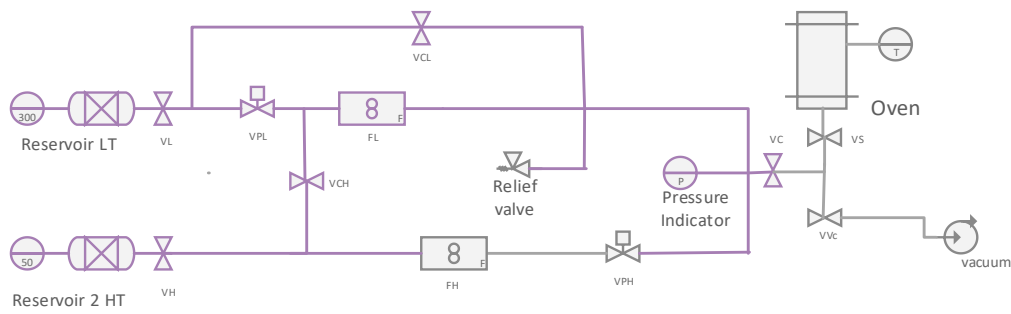


Figure 5.17. AC-device hydrogen source refilling process diagram

The AC-device is physically depicted in Figure 5.18.

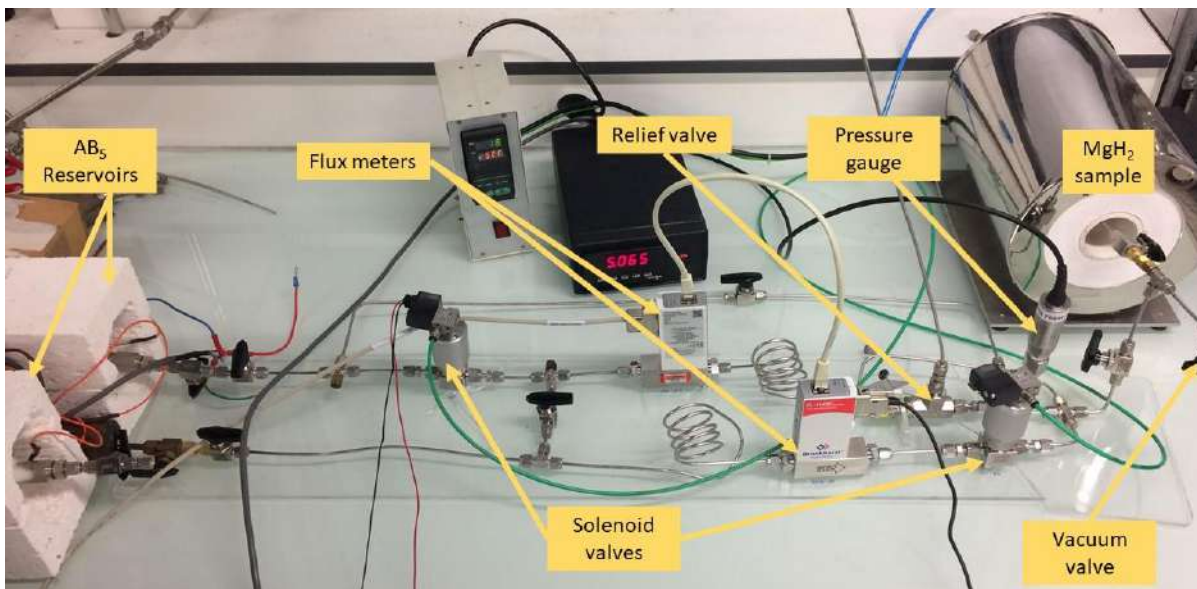


Figure 5.18. AC-device

## 5.5 Connections and software of control and measure

Tubing, electric signal converters, and activators have been fixed on an acrylic surface as can be seen in figure 5.18. An interface box containing the relays controlling each valve and the DC power supplies for the pressure sensors was made. A desktop computer records the pressure data and flux meters. In accordance with these measurements, the computer also controls the opening and closing of the electrically controlled valves. The interface to the computer is performed through a DAQPad-6211 external acquisition board from the company National Instruments, connected to the USB port of the computer.

The control program (Figure 5.19) is performed with the *LabView*<sup>®</sup> 12 software from National Instruments. The operator can assign a name to outputs (valves) an input (pressure gauge). The state of the valves is displayed by indicator lights, text or gauge indicator of pressure, representing the measurements on the screen. The measured data and the state of the valves can be saved on file in real time. The control can be performed either with the mouse or the keyboard.

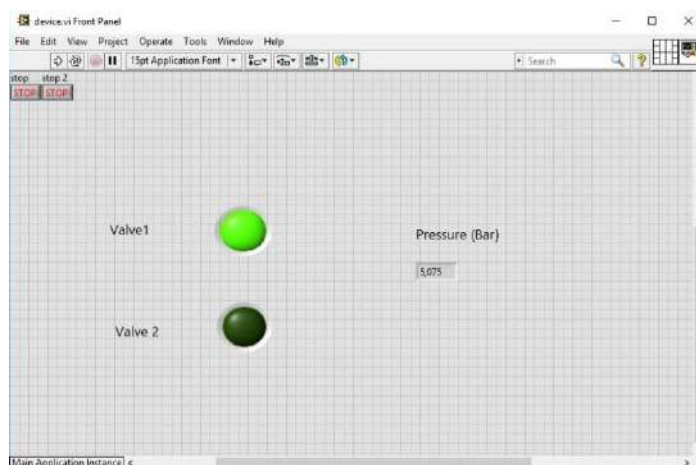


Figure 5.19 Control panel in LabView® 12

For the Bronkhorst® flux meters, a commercial software developed by the same company is available freely. *Flowplot* (Fig. 5.20) is an application meant for service purposes on Bronkhorst® digital instruments and readout units. It gives a good insight into the dynamic behavior of digital instruments. Features are signal monitoring, up to eight plots of value versus time, and an easy way to adjust instrument settings, like controller, alarm and counter parameters in real time.

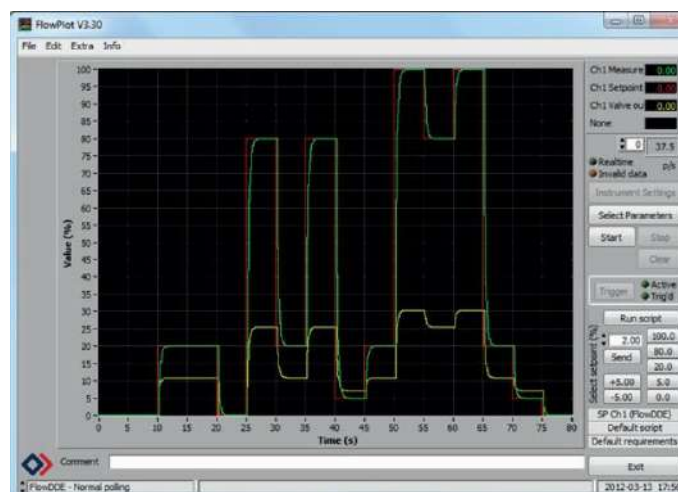


Figure 5.20 Flowplot main window by Bronkhorst®

## 5.6 Measurements

The system was initially tested without any sample to validate the cycling acquisition data. Before starting with the test, it was carried out a leaking checkup, which assured that the system is completely tight and isolated. It was also possible to measure the intern volume of the pipelines and accessories ( $v = 21.240 \pm 0.001 \text{ cm}^3$ ). Then, the cycling simulation was run. During this operation, both flux-meters were saving data through the cycling simulation. At the end, the data were recovered from the *Flowplot* software and treated in OriginPro® software. The recording information of both flux-meters is shown in Figure 5.21a. The flux-meter one records the absorption, meanwhile the flux-meter two records the desorption. The

*Flowplot* software gives the time and value data. From that information, a plot with two axes is drawn: the time as  $x$  (s) and the flux value  $y$  (%), this percent value corresponds at one basis of 1 % for 10 mg<sub>H2</sub>/second.

During this first test, it was possible to simulate more than 40 absorption-desorption cycles. Due to the fact that the sample holder was empty, the hydrogen flux was constant for absorptions, and desorptions. Figure 5.21b, shows the hydrogen flux during the first sorption cycle (black curves) and the integrated flux (red curves). From the integrated data, it is possible to calculate the mole number that went through the flux meters. These values are 0.002 mole for absorption and 0.004 mole for desorption. Taking on account that there is no hydride forming sample for the sorption process, the same quantity is measured for absorption and desorption. After 43 cycles all the hydrogen contained in the source tank was transferred to the sink.

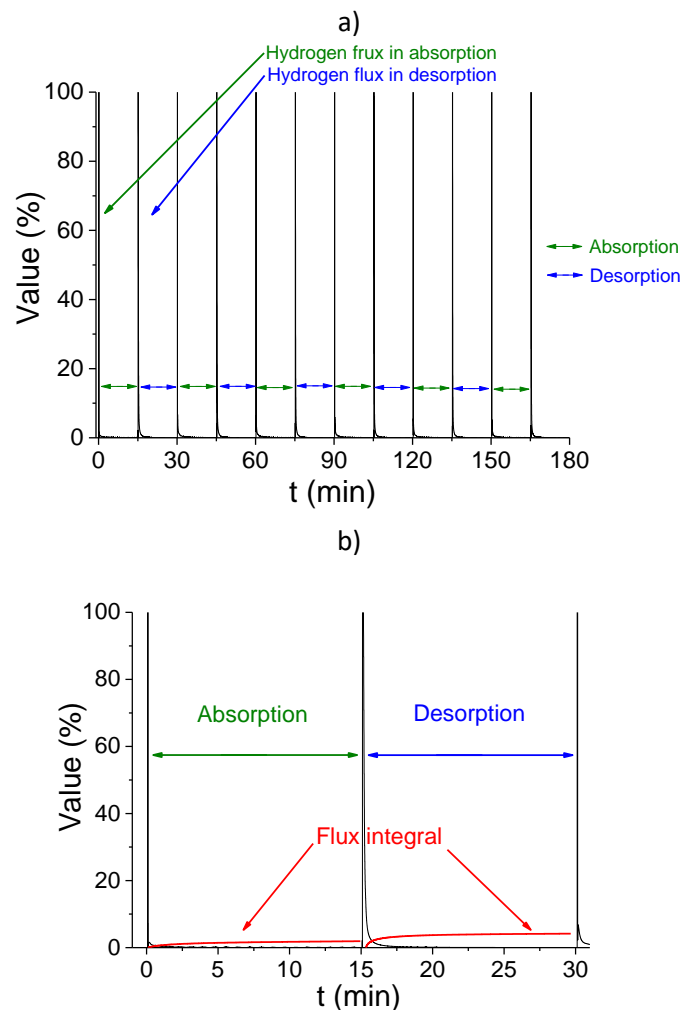


**Figure 5.21** Acquisition data plot (a), first sorption cycle (b)

Once the system has been tested, an experimentation was carried out with a hydride-forming sample NC: 95MgH<sub>2</sub>-5TiH<sub>2</sub>. More than 50 sorption cycles were carried out during this study. The NC used for the experiment was obtained directly from the synthesis, which means that it was already hydrogenated. The sample mass was 0.0995 g. Then, it was introduced into

the sample holder (volume=  $2.250 \pm 0.001 \text{ cm}^3$ ) inside a glove-box (argon atmosphere). Once the sample was inside the sample holder, the free volume was calculated ( $2.181 \text{ cm}^3$ ). The sample holder was plugged to the AC-device and heated up to  $300 \text{ }^\circ\text{C}$ . Thus, the sample releases a small amount of hydrogen leading to a slight increase in gas pressure. After the sample reached  $300^\circ\text{C}$ , and the reservoirs were at their respective temperatures ( $50$  and  $150 \text{ }^\circ\text{C}$ ), the cycling setup was started (cycling time  $15 \text{ min}$ . absorption and  $15 \text{ min}$ . desorption). During the sorption process, it was necessary to stand-by the process 4 times and to refill the source reservoir with the hydrogen contained in the sink. This was performed when the sink pressure was close to the  $95\text{MgH}_2\text{-5TiH}_2$  plateau pressure ( $1.6 \text{ bar}$ ). The refill procedure took in average  $3 \text{ h}$ . Figure 5.22 shows the first 12 cycles, for both absorption and desorption. As the absorption rate is faster than the desorption one, a peak for desorption is clearly detected. An intensity decrease of the desorption peak is also observed.

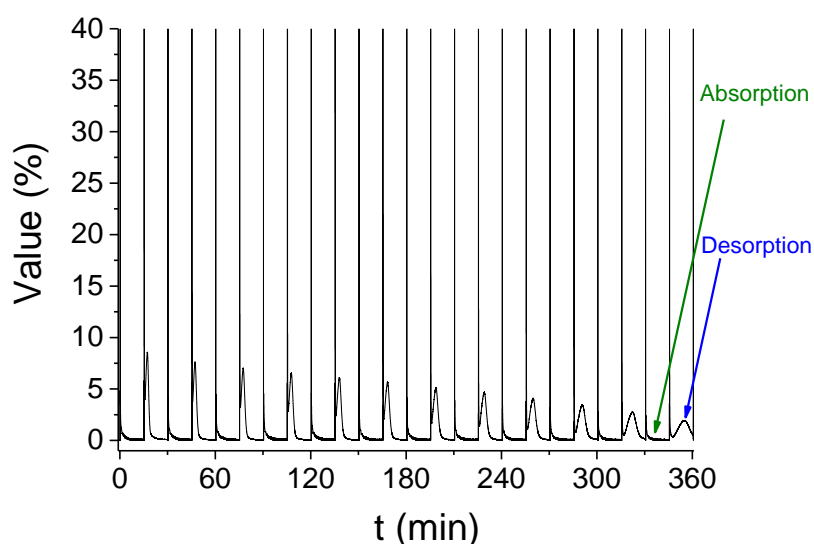


**Figure 5.22** Hydrogen uptake-release in AC-device

At the end of the cycling process, measured flux data is obtained from *Flowplot* software. Then, the hydrogen moles number can be calculated for both absorption and desorption. In Figure 5.23 left, the first cycle is shown in detail for absorption and desorption. The shadowed desorption curve can be integrated to calculate the number of moles that have been desorbed for this first step. Figure 5.23 (right) shows the integration curve that corresponds to  $0.02$  moles of hydrogen that have been desorbed by the  $95\text{MgH}_2\text{-5TiH}_2$  NC in  $15 \text{ min}$ , at  $300^\circ\text{C}$ . The same process is repeated through the full cycling process.

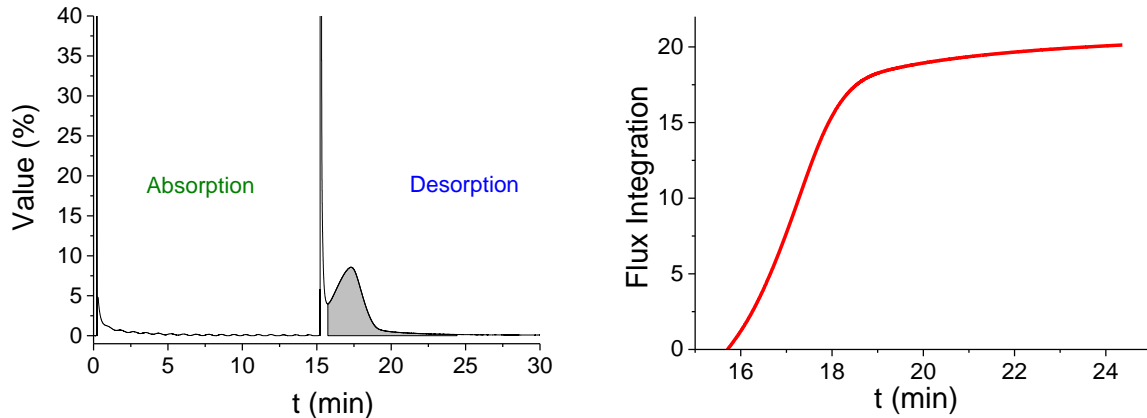


**Figure 5.23** First absorption and desorption steps (left), integral of the desorbed curve (right)

## 5.7 Conclusion

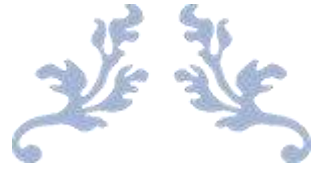
From this experiment, it was possible to carry out tens of uptake-release hydrogen cycling with the automatic cycling device designed and assembled in the laboratory. To build this device, a study of the cycling operation conditions has been done. A bibliography research was performed to choose the best hydride that would work as both source and sink, and an  $AB_5$ -type intermetallic alloy was chosen. The alloy  $\text{LaNi}_{4.66}\text{Sn}_{0.33}$  was synthesized and was characterized both structurally and thermodynamically. Considering all the main parts of the device (reservoirs, sensors, automatic valves, and connectors), a piping and instrumentation diagram was drawn. Manipulation and safety tests were performed before starting up. The automatization and operation with a commercial software were performed to operate the system from a computer. In the end, this prototype allows performing tens of uptake/release cycles in a safe and automatic way. These cycles are carried out at high hydrogen purity as well as economizing the hydrogen consumption. In comparison with manual cycling process or some commercial cycling machines, this prototype is working with a constant amount of hydrogen, only transferring the gas from the source to the sink passing through the sample of interest. Very first test on the sample  $95\text{MgH}_2\text{-}5\text{TiH}_2$  have shown that sorption cycles can be conducted successfully, and quantitative measurements of hydrogen exchanged during the cycling can be obtained from the flux meters. Further works are needed to fully calibrate the device and to perform accurate measurements. However, first trials have shown that such device can efficiently conduct large-scale cycling of metallic hydride with high safety and low cost.

## References

- [1] Helmut W. Hydrogen in Metals III. vol. 73. 1997.
- [2] Reilly JJ, Holtz A, Wiswall Jr RH. A new laboratory gas circulation pump for intermediate pressures. *Rev Sci Instrum* 1971;42:1485–6.
- [3] Golben PM. Multi-stage hydride-hydrogen compressor. *IECEC83 Proc. Eighteenth Intersoc. Energy Convers. Eng. Conf. Vol. 1, 1983, p. 1746–53.*
- [4] Ishikawa H, Oguro K, Kato A, Suzuki H, Ishii E. Preparation and properties of hydrogen storage alloys microencapsulated by copper. *J Common Met* 1986;120:123–33. doi:10.1016/0022-5088(86)90634-X.
- [5] Sieverts A. Absorption of Gases by Metals. *Z Für Met* 1929;21:37–46.
- [6] Blach TP, Gray EM. Sieverts apparatus and methodology for accurate determination of hydrogen uptake by light-atom hosts. *J Alloys Compd* 2007;446–447:692–7. doi:10.1016/j.jallcom.2006.12.061.
- [7] Gas sorption station: PCTPro, gas analyzer - Setaram Instrumentation n.d. <https://www.setaram.com/setaram-products/gas-sorption/pctpro-8/> (accessed October 22, 2018).
- [8] Meyer G, Arneodo Larochette P, Baruj A, Castro FJ, Lacharmoise P, Zacur E, et al. Equipment for hydrogen absorption-desorption cycling characterization of hydride forming materials. *Rev Sci Instrum* 2007;78:023903. doi:10.1063/1.2437160.
- [9] Challet S. Stockage de l'hydrogène dans les hydrures métalliques pour l'alimentation en hydrogène de véhicules à pile à combustible. UNIVERSITE PARIS XII – VAL DE MARNE, 2005.
- [10] Van Vucht JHN, Kuijpers Fa, Bruning H. Reversible room-temperature absorption of large quantities of hydrogen by intermetallic compounds. *Philips Res Rep* 25 133-40 Apr 1970
- [11] Lartigue C, Percheron-Guégan A, Achard JC, Tasset F. Thermodynamic and structural properties of  $\text{LaNi}_{5-x}\text{Mn}_x$  compounds and their related hydrides. *J Common Met* 1980;75:23–9. doi:10.1016/0022-5088(80)90365-3.
- [12] Diaz H, Percheron-Guégan A, Achard JC, Chatillon C, Mathieu JC. Thermodynamic and structural properties of  $\text{LaNi}_{5-y}\text{Al}_y$  compounds and their related hydrides. *Int J Hydrog Energy* 1979;4:445–54. doi:10.1016/0360-3199(79)90104-6.
- [13] Achard J., Lartigue C, Percheron-Guégan A, Dianoux A., Tasset F. Hydrogen mobility in  $\text{LaNi}_5$  hydride and its aluminium-and manganese-substituted hydrides. *Int Symp Prop Appl Met Hydrides* 1982;88:89–96. doi:10.1016/0022-5088(82)90018-2.
- [14] Cuevas F, Joubert J-M, Latroche M, Percheron-Guégan A. Intermetallic compounds as negative electrodes of Ni/MH batteries. *Appl Phys A* 2001;72:225–38. doi:10.1007/s003390100775.

- [15] Bowman RC, Fultz B. Metallic Hydrides I: Hydrogen Storage and Other Gas-Phase Applications. *MRS Bull* 2002;27:688–93. doi:10.1557/mrs2002.223.
- [16] Bowman RJ, Gerard N, Hempelmann R, Jacob I, Mintz MH, Ono S, et al. Hydrogen in Intermetallic Compounds II: Surface and Dynamic Properties, Applications. vol. 67. Springer Science & Business Media; 2006.
- [17] Friedlmeier G, Manthey A, Wanner M, Groll M. Cyclic stability of various application-relevant metal hydrides. *J Alloys Compd* 1995;231:880–7. doi:10.1016/0925-8388(95)01776-3.
- [18] Bowman RC, Luo CH, Ahn CC, Witham CK, Fultz B. The effect of tin on the degradation of  $\text{LaNi}_{5-y}\text{Sn}_y$  metal hydrides during thermal cycling. *J Alloys Compd* 1995;217:185–92. doi:10.1016/0925-8388(94)01337-3.
- [19] Percheron-Guégan A, Lartigue C, Achard JC. Correlations between the structural properties, the stability and the hydrogen content of substituted  $\text{LaNi}_5$  compounds. *J Common Met* 1985;109:287–309. doi:10.1016/0022-5088(85)90061-X.
- [20] Prigent J, Joubert J-M, Gupta M. Investigation of modification of hydrogenation and structural properties of  $\text{LaNi}_5$  intermetallic compound induced by substitution of Ni by Pd. *J Solid State Chem* 2011;184:123–33. doi:10.1016/j.jssc.2010.10.037.
- [21] Prigent J, Joubert J-M, Gupta M. Modification of the hydrogenation properties of  $\text{LaNi}_5$  upon Ni substitution by Rh, Ir, Pt or Au. *J Alloys Compd* 2012;511:95–100. doi:10.1016/j.jallcom.2011.08.094.
- [22] Park J-M, Lee J-Y. The intrinsic degradation phenomena of  $\text{LaNi}_5$  and  $\text{LaNi}_{4.7}\text{Al}_{0.3}$  by temperature induced hydrogen absorption-desorption cycling. *Mater Res Bull* 1987;22:455–65. doi:10.1016/0025-5408(87)90255-8.
- [23] Lambert SW, Chandra D, Cathey WN, Lynch FE, Bowman RC. Investigation of hydriding properties of  $\text{LaNi}_{4.8}\text{Sn}_{0.2}$ ,  $\text{LaNi}_{4.27}\text{Sn}_{0.24}$  and  $\text{La}_{0.9}\text{Gd}_{0.1}\text{Ni}_5$  after thermal cycling and aging. *J Alloys Compd* 1992;187:113–35. doi:10.1016/0925-8388(92)90527-G.
- [24] Luo S, Flanagan TB, Bowman R. Hydrogen isotherms for  $\text{LaNi}_{4.6}\text{M}_{0.4}$  alloys where M=group 4A elements. *Proc Int Symp Met-Hydrog Syst Fundam Appl MH2000* 2002;330–332:531–5. doi:10.1016/S0925-8388(01)01623-1.
- [25] Lartigue C. Etude structurale et thermodynamique du système  $\text{LaNi}_{5-x}\text{Mn}_x$ -hydrogène. PhD Thesis. Paris VI, 1979.
- [26] Joubert J-M, Latroche M, Černý R, Bowman R., Percheron-Guégan A, Yvon K. Crystallographic study of  $\text{LaNi}_{5-x}\text{Sn}_x$  ( $0.2 \leq x \leq 0.5$ ) compounds and their hydrides. *J Alloys Compd* 1999;293–295:124–9. doi:10.1016/S0925-8388(99)00311-4.
- [27] Luo S, Clewley J., Flanagan TB, Bowman R., Wade L. Further studies of the isotherms of  $\text{LaNi}_{5-x}\text{Sn}_x\text{-H}$  for  $x=0\text{--}0.5$ . *J Alloys Compd* 1998;267:171–81. doi:10.1016/S0925-8388(97)00536-7.

- [28] Nagel M, Komazaki Y, Suda S. Effective thermal conductivity of a metal hydride bed augmented with a copper wire matrix. *J Common Met* 1986;120:35–43. doi:10.1016/0022-5088(86)90625-9.
- [29] Goodell PD. Thermal conductivity of hydriding alloy powders and comparisons of reactor systems. *J Common Met* 1980;74:175–84. doi:10.1016/0022-5088(80)90088-0.
- [30] Suda S, Komazaki Y, Kobayashi N. Effective thermal conductivity of metal hydride beds. *J Common Met* 1983;89:317–24. doi:10.1016/0022-5088(83)90340-5.
- [31] Buschow KH, Van Mal HH. Phase relations and hydrogen absorption in the lanthanum-nickel system. *J Common Met* 1972;29:203–10. doi:10.1016/0022-5088(72)90191-9.
- [32] Zhuang Y, Deng H, Liu J, Yao Q. The 673 K isothermal section of the La–Ni–Sn ternary system. *J Alloys Compd* 2004;363:228–31. doi:10.1016/S0925-8388(03)00475-4.



---

# CONCLUSIONS

---

Conclusions and future works





## Conclusions and future works

This final chapter aims to point out the main results achieved throughout this Ph.D. Thesis. Different strategies have been implemented through different Mg-based materials to improve the hydrogen sorption properties of Mg. The kinetic properties were enhanced by nanostructuring and addition of early transition metals. Besides kinetics enhancement, hydrogen reversibility and cyclic stability at short time (15 min) of the magnesium-based materials were analyzed and discussed. Additional efforts were dedicated to making a proof-of-concept, design and build an automatic hydrogen uptake/release cycling device for future extended cycle-life studies. It is now essential to consider the relevance of these strategies to correctly orientate future investigations.

### Conclusions

In this Ph.D. thesis, it was experimentally shown that by reactive ball milling, it is possible to reach hydrogen uptake in microcrystalline Mg in shorter times than for bulk material. The synthesized nanocomposites have a high density of grain boundaries which improves the hydrogen diffusion in the particle. Also, this work demonstrates that hydride-forming early transition metals enhance hydrogen sorption kinetics in Mg, in some cases showing a high hydrogen reversibility for short reaction time (15 min) and stable capacity on cycling. Most significant and detailed results are given in the following.

#### (1-y)MgH<sub>2</sub>+yTiH<sub>2</sub> system

- Reaction time for MgH<sub>2</sub> formation decreases with TiH<sub>2</sub> addition during reactive ball milling synthesis, which reveals that TiH<sub>2</sub> enhances hydrogen absorption rates of Mg.
- PCI measurements show that the hydrogenation and dehydrogenation enthalpies of the Mg-MgH<sub>2</sub> transformation ( $-73.6 \pm 0.9$  and  $75.5 \pm 0.6$  kJmolH<sub>2</sub><sup>-1</sup>) are not modified by Ti addition. This concurs with the lack of formation of ternary Mg-Ti-H phases.
- TPD measurements show that Ti-containing NCs start desorbing at a lower temperature than pure MgH<sub>2</sub>. TPA measurements demonstrate that hydrogen absorption in Mg even starts at room temperature.
- NCs with high TiH<sub>2</sub> content (0.1<y<0.3 mol.) showed stable hydrogen reversible capacity through cycling.
- Kinetics of the reversible Mg ↔ MgH<sub>2</sub> transformation speed with TiH<sub>2</sub> addition. The more Ti is added, the faster the reaction takes place.
- Morphological SEM studies proved that no significant changes in NCs particle size occur by Ti addition nor in sorption cycling. Therefore, changes in particle size are not at the origin of the observed kinetic modifications.
- XRD results show that there is a significant increase in the crystal size both for MgH<sub>2</sub> and Mg phases for all NC.
- SEM-EDS analysis on cycled NCs revealed migration of TiH<sub>2</sub> from the core of the agglomerate particles to the edges upon cycling.
- Hydrogen desorption from MgH<sub>2</sub> is accelerated through cycling. This is attributed to surface effects: faster hydrogen recombination at NC surface on cycling which is promoted by surface migration of TiH<sub>2</sub>. Bulk effects are discarded since Mg and MgH<sub>2</sub>

crystal size increases on cycling which should slow-down reaction kinetics by H-diffusion if it would be the rate limiting step.

- No improvement of hydrogen absorption kinetics occurs on cycling.
- Hydrogen sorption curves both on absorption and desorption can be fitted with a first-order reaction nucleation and growth model.
- $\text{TiH}_2$  acts as a gateway for hydrogen transport enabling fast hydrogen dissociation/recombination at the  $\text{TiH}_2$  surface and its diffusion towards the bulk.
- $\text{TiH}_2$  enhances the reversible hydrogen uptake of Mg but remains an irreversible hydride at moderate temperatures (300 °C). As a consequence, there is an optimum amount of  $\text{TiH}_2$  for getting the highest reversible capacity in  $(1-y)\text{MgH}_2+y\text{TiH}_2$  NCs. This optimum is set to  $y = 0.025$  for a reaction time of 15 min, with a reversible capacity of 4.9 wt.% at the twentieth cycle.

### Effect of *TM* additives on $\text{MgH}_2$

- All early transition metals formed hydride phases during RBM synthesis of  $\text{MgH}_2$ - $\text{TMH}_x$  NCs. These hydrides have the following stoichiometry:  $\text{TiH}_2$ ,  $\text{ZrH}_2$ ,  $\text{ScH}_2$ ,  $\text{YH}_3$ ,  $\text{VH}_2$ , and  $\text{NbH}_2$ .
- Depending on the additive, the synthesis time of  $\text{MgH}_2$ - $\text{TMH}_x$  NCs can be reduced from 50 to 30 min.
- The addition of *TM* leads to equivalent plateau pressures than for pure  $\text{MgH}_2$ , showing that the thermodynamics of  $\text{MgH}_2$  is not changed.
- After sorption cycling, XRD analysis showed that the hydrogen content of transition metal hydrides is the same as in the as-synthesized state except for V and Nb. The composition of these is  $\text{VH}_{0.8}$  and  $\text{NbH}_{0.8}$ .
- The order of the hydrogen reversible capacity after 20 cycles is as follows:  $\text{Ti} > \text{Sc} > \text{V} > \text{Nb} > \text{Zr} > \text{Y}$ .

### Automatic cycling device

- A closed-loop experimental device has been designed for automatic hydrogen cycling of  $\text{MgH}_2$ -based composites with high-purity hydrogen gas.
- The thermodynamic operation parameters aim to characterize reversible hydrogen absorption systems within the range pressure  $0.05 \leq P_{\text{H}_2} \leq 2$  MPa. These parameters were used to define the composition and amount of an  $\text{AB}_5$  hydride ( $\text{LaNi}_{4.33}\text{Sn}_{0.66}$ ) which is used as a hydrogen source and sink in the cycling device.
- The cycling device was successfully assembled and operated with a software monitoring.
- Many sorption cycles were performed showing the good operation and convenience of the automatic device.
- The device allows to perform cycling in a safe way and at high hydrogen purity.

### **Future work**

The automatic cycling device design in this Thesis will allow extending the current studies to much longer cycling ranges, which is of high interest for real applications. Considering the materials synthesized in this work, it will be worth to analyze the extended cycle-life of the optimized nanocomposite  $0.975\text{MgH}_2+0.025\text{TiH}_2$  with a reversibility capacity of 4.9 wt.%. Similarly, the extended cycle-life study of the  $\text{MgH}_2\text{-ScH}_2$  system, which shows good stability over 20 cycles, deserves interest.

In chapter 3, it was observed by SEM that it exists a partial migration of  $\text{TiH}_2$  from the core of the agglomerate to the edges on cycling. This phenomenon is relevant to understand the efficiency and role of the additive. A more detailed high-resolution characterization of this migration by Transmission Electron Microscopy as a function of cycling and nature of the additive is required.

The kinetic study of  $0.95\text{MgH}_2\text{-}0.05\text{TMH}_x$  NCs revealed that the reversible capacity of  $\text{MgH}_2\text{-ZrH}_2$ ,  $\text{MgH}_2\text{-VH}$ ,  $\text{MgH}_2\text{-NbH}$  NCs diminishes at the very first sorption cycles because of their poor absorption kinetic. Future work on the influence of additive amount on kinetic and cycling properties, as well as on microstructural modifications (particle morphology and phase distribution), is of interest to gain a better understanding of additive effects.

The kinetic model here used for the analysis of sorption curves in  $\text{MgH}_2\text{-TiH}_2$  NCs can be further pushed to extract rate constants and activation energies using the Arrhenius equation. Results can be compared to pure  $\text{MgH}_2$  for a better understanding of kinetic properties of  $\text{MgH}_2\text{-TMH}_x$  NCs,

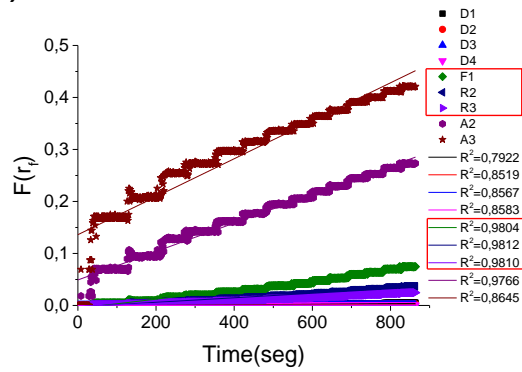
The performances of the implemented automatic cycling device can be improved. The hydrogen capacity of the reservoirs can be improved by increasing the mass of the hydride-forming alloy. The Labview® program needs improvement to enrich simultaneous data acquisition of flow, pressure and temperature signals as well as further automatization of some manual parts.



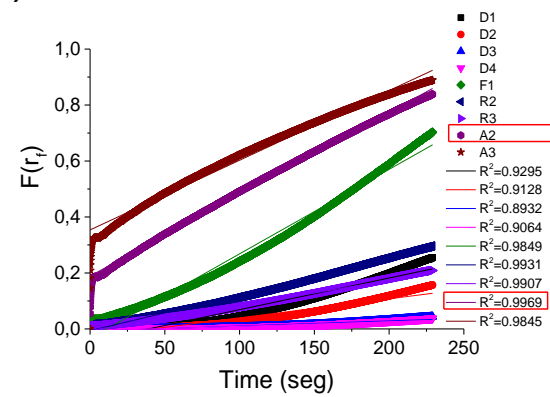
## Annex Fitting kinetic models

Function of the reacted fraction vs time and their respective kinetic models in first desorption of  $(1-y)\text{MgH}_2+y\text{TiH}_2$ .

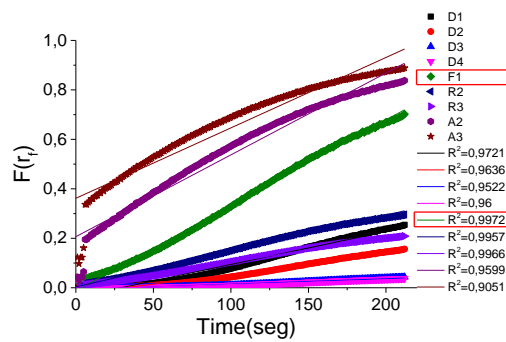
$y=0$



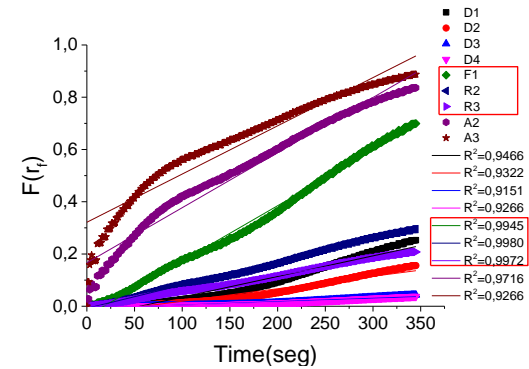
$y=0.0125$



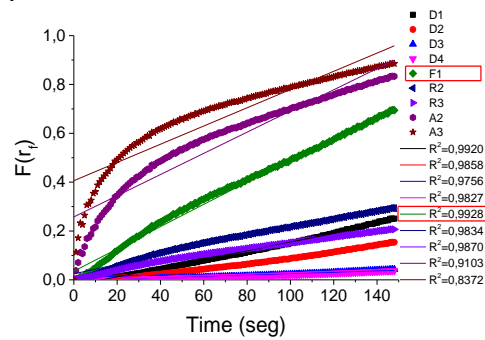
$y=0.025$



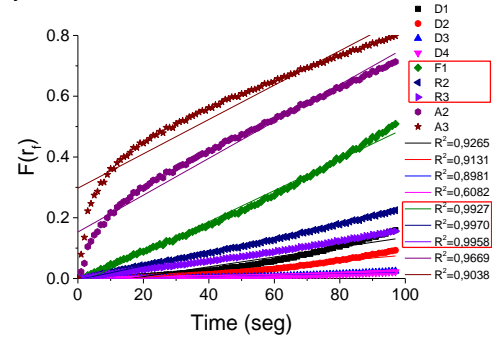
$y=0.05$



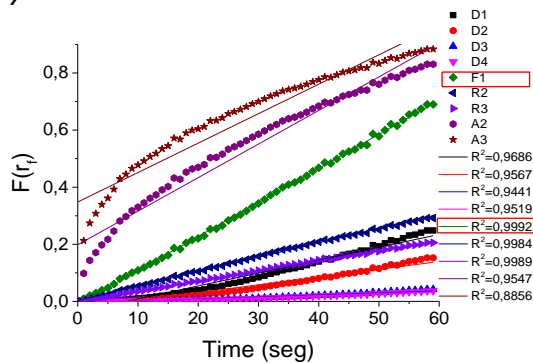
$y=0.1$



$y=0.2$

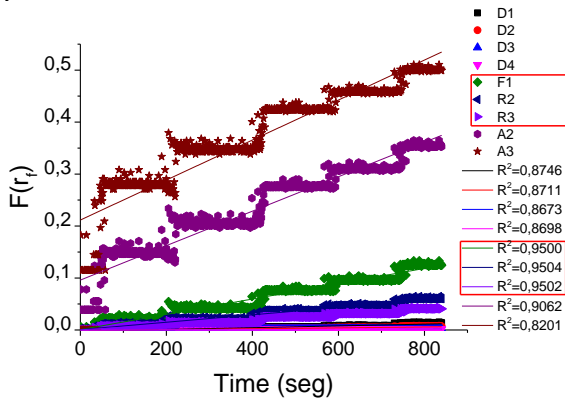


$y=0.3$

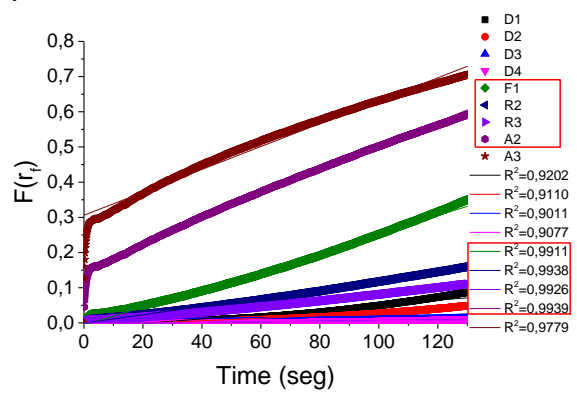


Function of the reacted fraction vs time and their respective kinetic models in twentieth desorption of  $(1-y)\text{MgH}_2+y\text{TiH}_2$ .

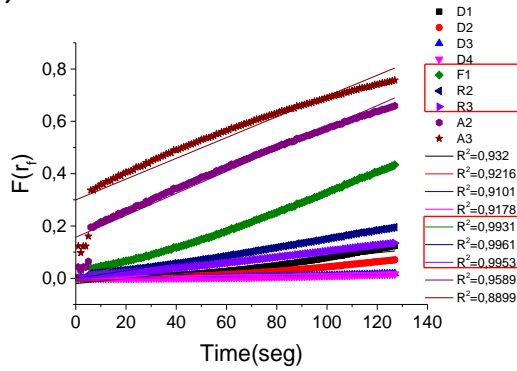
$y=0$



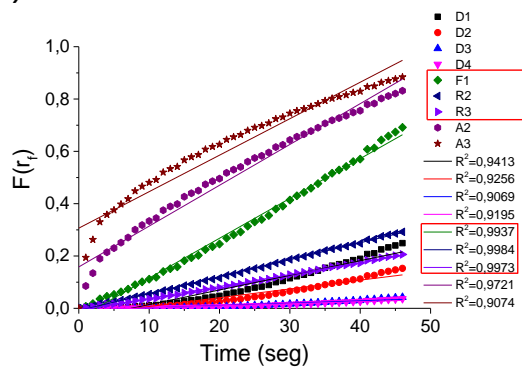
$y=0.0125$



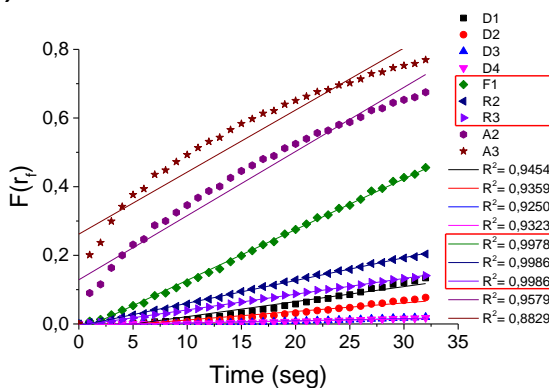
$y=0.025$



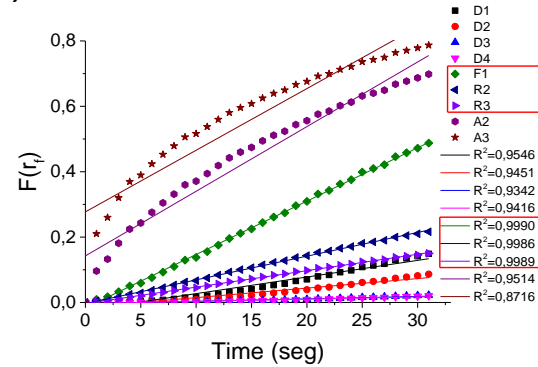
$y=0.05$



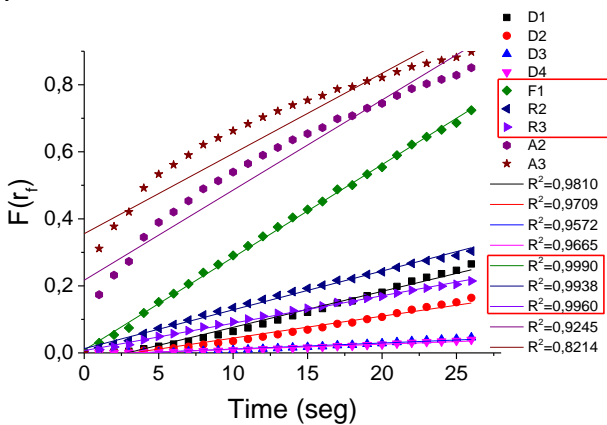
$y=0.1$



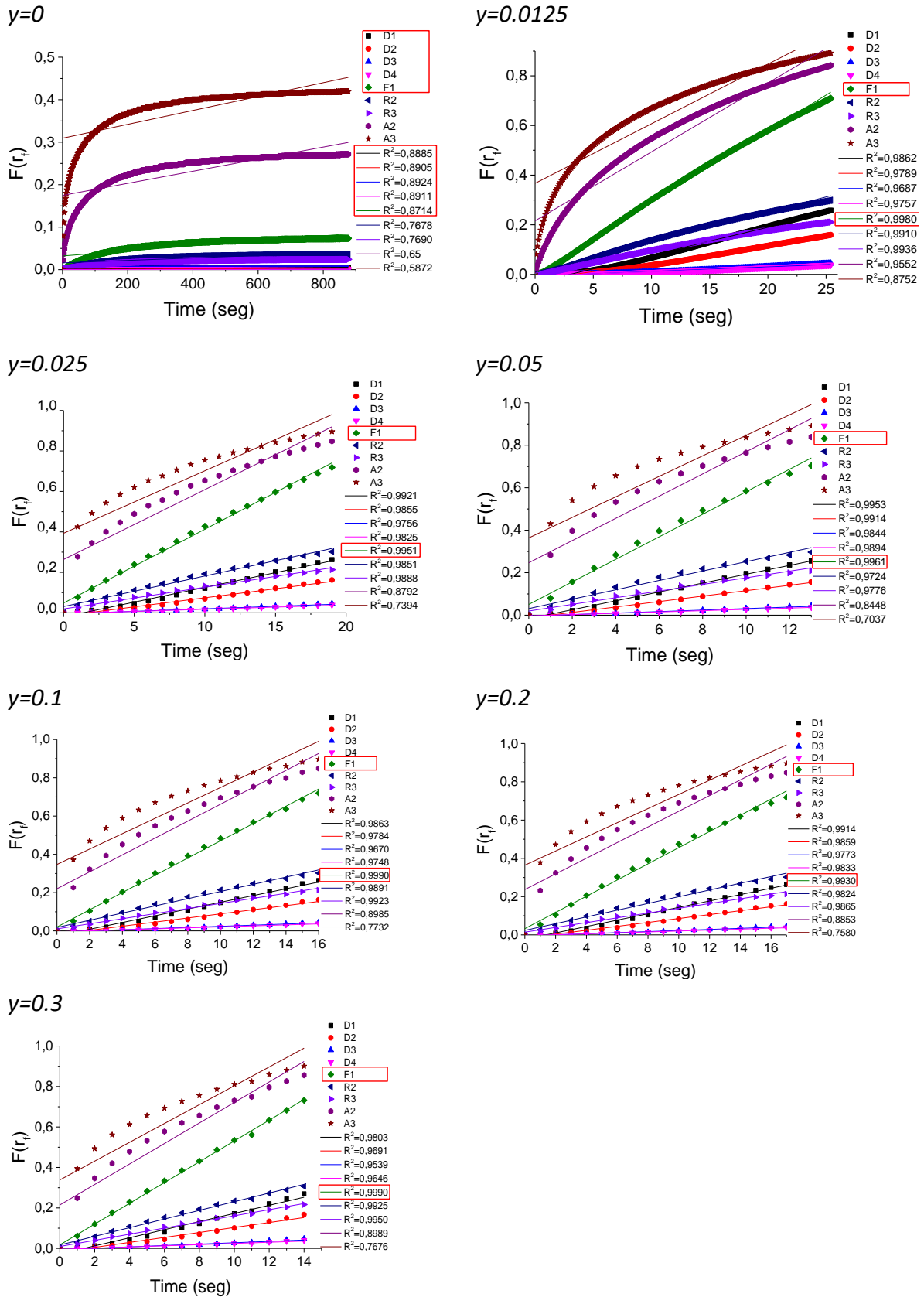
$y=0.2$



$y=0.3$

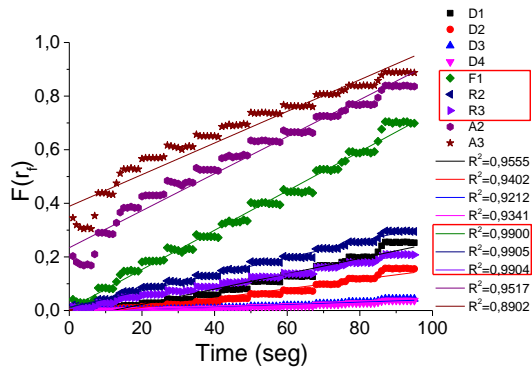


Function of the reacted fraction vs time and their respective kinetic models in second absorption of  $(1-y)\text{MgH}_2+y\text{TiH}_2$ .

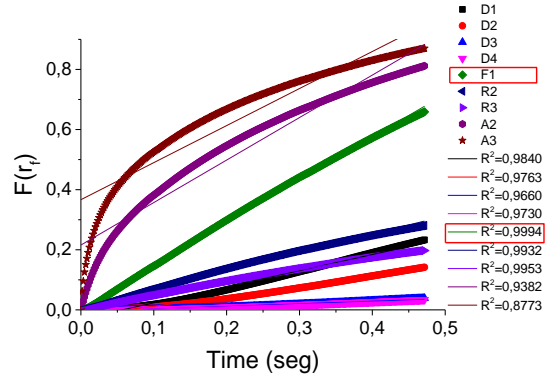


Function of the reacted fraction vs time and their respective kinetic models in twentieth absorption of  $(1-y)\text{MgH}_2+y\text{TiH}_2$ .

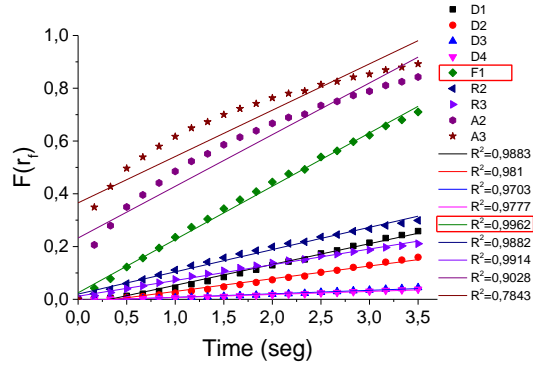
$y=0$



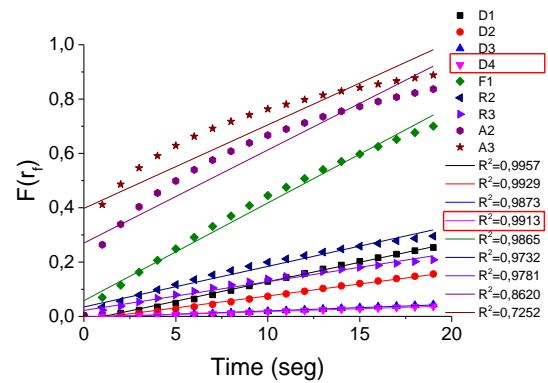
$y=0.0125$



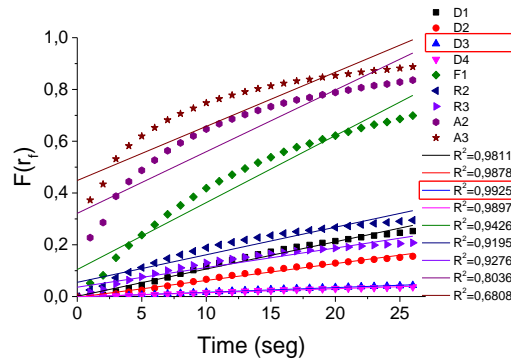
$y=0.025$



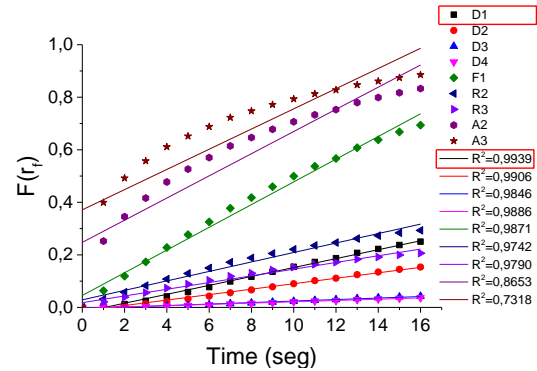
$y=0.5$



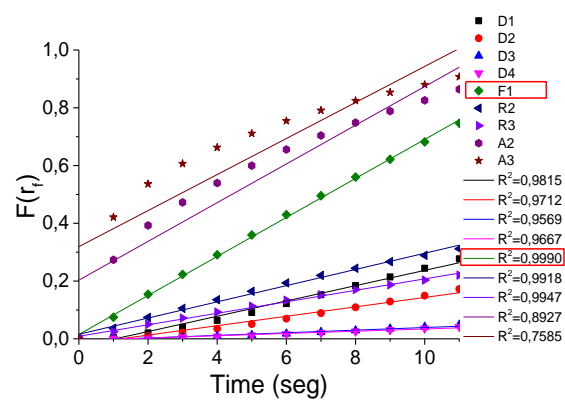
$y=0.1$



$y=0.2$



$y=0.3$





## Mg/transition-metal nanomaterials for efficient hydrogen storage

Magnesium metal is a prominent element for solid-state hydrogen storage due to its large abundance in earth's crust and its high weight and volumetric hydrogen uptakes. However, hydrogen sorption suffers from sluggish kinetics and the formed hydride is too stable for applications working under ambient conditions. The former issue can be solved by developing composites combining two hydrides,  $\text{MgH}_2$  and  $\text{TiH}_2$  at the nanoscale. These materials are synthesized by mechanical milling under reactive atmosphere. By this technique, the formation of nanocomposites and their hydrogenation can be obtained in a single-step. Moreover, these materials can be produced at large scale for application purposes. The work focused on three topics: i) the optimization of the  $\text{TiH}_2$  content in the  $(1-y)\text{MgH}_2+y\text{TiH}_2$  system. This was accomplished by optimizing the titanium content ( $0.0125 \leq y \leq 0.3$  mole), while keeping good kinetics, hydrogen reversibility and cycle-life. The data show that  $y=0.025$  is the best compromise to fulfill the most practical properties; ii) the extension to other transition metals for the system  $0.95\text{MgH}_2+0.05\text{TMH}_x$  (TM: Sc, Y, Ti, Zr, V and Nb), evaluating the contribution of each additive to kinetics, hydrogen reversibility and cycle-life; iii) the conception of an automatic cycling device able to carry out hundreds of sorption cycles with the aim of measuring the cycle-life of metal hydrides. The work was done using manifold experimental methods. For synthesis, reactive ball milling under hydrogen atmosphere was primarily used. The crystal structure and the chemical composition of nanomaterials was determined from X-ray diffraction (XRD) analysis. Particle size and morphology were obtained by Scanning Electron Microscopy / Energy Dispersive X-Ray Spectroscopy (SEM/EDS). Thermodynamic, kinetic and cycling properties toward hydrogen sorption were determined by the Sieverts method.

Keywords : magnesium hydride, hydrogen storage, nanocomposites, metal hydrides.

---

## Nanomatériaux à base de magnésium et de métaux de transition pour un stockage efficace de l'hydrogène

Le magnésium est un élément de choix pour le stockage de l'hydrogène à l'état solide en raison de sa grande abondance dans la croûte terrestre et de ses fortes capacités de sorption massique et volumétrique de l'hydrogène. Cependant, la réaction de sorption souffre d'une cinétique lente et l'hydrure formé est trop stable pour des applications fonctionnant sous conditions ambiantes. Le premier problème peut être résolu en développant des composites associant deux hydrures,  $\text{MgH}_2$  et  $\text{TiH}_2$ , à l'échelle nanométrique. Ces matériaux sont synthétisés par broyage mécanique sous atmosphère réactive. Cette technique permet la formation des nanocomposites et leur hydrogénation en une seule étape. De plus, ces matériaux peuvent être produits à grande échelle pour les besoins des applications. Les travaux ont été menés en trois parties : i) l'optimisation de la teneur en  $\text{TiH}_2$  dans le système  $(1-y)\text{MgH}_2+y\text{TiH}_2$ . Ceci a été accompli en ajustant la teneur en titane ( $0,0125 \leq y \leq 0,3$  mole), tout en conservant une bonne cinétique, une réversibilité de l'hydrogène et une durée de vie utile. Les données montrent que la valeur  $y = 0,025$  offre le meilleur compromis pour développer les propriétés les plus adéquates; ii) l'extension à d'autres métaux de transition pour le système  $0,95\text{MgH}_2 + 0,05\text{TMH}_x$  (TM: Sc, Y, Ti, Zr, V et Nb), en évaluant la contribution de chaque additif sur la cinétique, sur la réversibilité de l'hydrogène et sur la durée de vie en cyclage; iii) la conception d'un dispositif de cyclage automatique capable de réaliser des centaines de sorption/désorption dans le but de mesurer la durée de vie des hydrures métalliques. Le travail a été effectué à l'aide de nombreuses méthodes expérimentales. Pour la synthèse, le broyage réactif sous atmosphère d'hydrogène a été principalement utilisé. La structure cristalline et la composition chimique des nanomatériaux ont été obtenues à partir de l'analyse par diffraction des rayons X (DRX). La taille et la morphologie des particules ont été déterminées par microscopie électronique à balayage et spectroscopie de rayons X à dispersion d'énergie (SEM/EDS). Les propriétés thermodynamiques, cinétiques et cycliques de la sorption d'hydrogène ont été déterminées par la méthode de Sieverts.

Mots clés : hydrure de magnésium, stockage de l'hydrogène, nanocomposites, hydrures métalliques.